Karlsruher Institut für Technologie

ETP-KA/2023-4

Qualification of Silicon Sensors for the Phase-2 Upgrade of the CMS Outer Tracker

Zur Erlangung des akademischen Grades eines

Doktors der Naturwissenschaften (Dr. rer. nat.)

von der KIT-Fakultät für Physik des
Karlsruher Instituts für Technologie (KIT)

angenommene

DISSERTATION

von

M.Sc. Florian Wittig

aus Öhringen

Tag der mündlichen Prüfung: 26.05.2023

Referent:	Prof. Dr. Ulrich Husemann	Institut für Experimentelle Teilchenphysik
Korreferent:	Prof. Dr. Günter Quast	Institut für Experimentelle Teilchenphysik

Florian Wittig:
Qualification of Silicon Sensors for the Phase-2 Upgrade of the CMS Outer Tracker
May 2023

Contents

Part I.

Introduction and Basics

1 Introduction

In 2008, the *Large Hadron Collider* (LHC), the world's largest and most powerful particle accelerator, was commissioned at the *European Organization for Nuclear Research* (CERN) near Geneva, Switzerland. The LHC accelerates two counter-rotating beams of protons or heavy ions and brings them to collision at four different interaction points that are distributed along the 27 km circumference accelerator ring. Analyzing the collision fragments with specialized detectors allows for examining predictions of the *Standard Model* (SM) of particle physics that describes all known elementary particles and their interactions. In 2012, the discovery of the Higgs boson, the last missing particle in the Standard Model, which was predicted by Peter Higgs in the 1960s, was announced by the CMS[1] and ATLAS[2] experiments. However, the overall picture is not yet completed, as the Standard Model fails to explain the existence of dark matter and dark energy as well as the observed magnitude of the asymmetry between matter and antimatter, just to mention a few aspects. This indicates that there must be physics beyond the Standard Model and emphasizes the need to further improve accelerators and experiments to be capable of validating different Standard Model extensions such as Supersymmetry, which could resolve some of the open questions. Therefore, the LHC will be upgraded to the *High Luminosity LHC* (HL-LHC) with the start of operation scheduled for early 2029. The instantaneous luminosity, a measure of the particle interaction rate per unit area and time, will be increased by a factor of five to seven compared to its initial design value. As a result, the amount of data collected during the HL-LHC operation period with a duration of at least ten years will increase drastically and enlarge the probability to find new physics, and will also reduce the uncertainties on already known processes.

The intensified particle flux through the detectors resulting from the luminosity increase implies new challenges for the experiments regarding radiation tolerance and event filtering. To fully exploit the physics potential of the HL-LHC phase, experiments must be fundamentally revised. For the CMS experiment the revision is referred to as Phase-2 Upgrade and affects all its sub-detector systems. A central part of the upgrade is the full replacement of the silicon tracker. The new CMS tracker is divided in an inner part (Inner Tracker) that will be equipped with highly granular pixel modules, while in the outer region (Outer Tracker) less granular p_T-modules made of two closely spaced silicon sensors will be installed. To keep the CMS trigger system efficient, the Outer Tracker must provide track information to the Level-1 track finder at the bunch crossing frequency of 40 MHz. Due to bandwidth limitations a pre-selection of tracks based on the particles' transverse momentum (p_T) at module level is required in order to efficiently reduce the amount of track data forwarded to the Level-1 track finder. Trajectories of charged particles crossing the detector volume are differently bent by the CMS magnetic field, with the bending radii being smaller for higher p_T particles. Thus, the displacement of hits in the two sensor layers of the modules is a measure of the particles' p_T. The displacement is determined on module level by a dedicated logic implemented on the chips reading out the sensors. Applying a spatial cut on the hit displacement ensures that only track information of

[1] **C**ompact **M**yon **S**olenoid
[2] **A** **T**oroidal **L**HC **A**pparatus

particles exceeding a certain p_T-threshold is forwarded to the CMS trigger system. Thus, the number of tracks per event is reduced by one order of magnitude without losing interesting particles. The full event hit data is buffered in the meantime and can be read out from the modules in case of a positive CMS trigger decision. In Chapter 2 and 3, the LHC and the CMS experiment, together with the HL-LHC and the CMS Phase-2 Outer Tracker upgrade are introduced.
In total, there will be about 13 200 p_T-modules in the Outer Tracker, divided in two different flavours. PS modules consisting of a macro-pixel and a strip sensor will be installed at the innermost layers, while less granular 2S modules made of two identical strip sensors will be placed in the outer region. All Outer Tracker sensors are based on float-zone (FZ) silicon with n-doped strip/pixel implants in a p-doped bulk. The active and physical sensor thickness is 290 µm and 320 µm, respectively. Based on the active thickness and the sensor base material, the sensors are also referred to as FZ290 sensors. The introductory part of this thesis is concluded with Chapter 4, where the general design, the manufacturing process and working principle of silicon sensors is discussed in detail.

In mid 2020 the mass production of the silicon sensors for the Outer Tracker p_T-modules has started and is expected to be completed by the end of 2024 with a total production quantity of roughly 28 000 sensors. One main part of this thesis is dedicated to the sensor quality control (SQC) during the mass production. The *Karlsruhe Institute of Technology* (KIT) is one of six test centers responsible for the SQC, receiving monthly shipments with sensors whose quality must be validated. Monitoring the sensor quality by electrically characterizing sensors with specialized setups is essential to detect deviations at an early stage and to take appropriate measures if needed. Thus, it can be assured that the sensors delivered by the manufacturer *Hamamatsu Photonics K.K.* (HPK) meet the requirements set by the CMS Collaboration and can be used to assemble p_T-modules without any restrictions. Chapter 5 gives an overview of the overall quality assurance strategy, motivates and discusses the different sensor parameters that are monitored and introduces the setups used at KIT for the sensor qualification. Afterwards, the results collected at KIT after finishing about 50 % of the sensor production are discussed.

The second part of this thesis is dedicated to beam test measurements conducted at the DESY[3] test beam facility in Hamburg, Germany. The facility provides the infrastructure for validating the sensor performance in modules by illuminating them with a highly energetic electron beam of energies up to 6 GeV. Placing the modules in the middle of a beam telescope allows for reconstructing the tracks of the electrons traversing the module. Thus, it is possible to measure the particle detection efficiency of the modules and to resolve potential inefficient areas. In Chapter 6, the test beam facility and the different software frameworks used for analyzing the beam test data are introduced.
Beam test measurements with miniature versions of the PS module macro-pixel sensor based on the final FZ290 material were performed in the scope of this thesis. Sensors with different design approaches regarding the pixel biasing structures were tested. In order to read out the sensors they were assembled with a matching readout chip, the *Macro Pixel ASIC* (MPA), forming a single *Macro-Pixel SubAssembly* (MaPSA). The single MaPSAs were irradiated with protons to radiation levels as they are expected after ten years of CMS operation to investigate the impact of radiation damage on the detection efficiency. Furthermore, the beam test measurements focused on the inefficient sensor regions that are caused by the pixel biasing structures at perpendicular particle incidence. Particles traversing the sensor at an angle can overcome

[3] Deutsches Elektronen-Synchrotron

these inefficient regions and the global sensor efficiency is recovered. Thus, the assemblies were rotated with respect to the beam in steps to study the impact of different particle incidence angles on the sensor efficiency. Results collected during the beam test are summarized and discussed in Chapter 7.
In the course of the CMS Phase-2 Outer Tracker Upgrade KIT also takes part as a 2S module assembly center and has pledged to build up to 2000 2S modules. The module production is expected to start in mid 2023. In order to validate the 2S module design and functionality several prototype modules have been built and tested in the past by the CMS community. Since mid 2021, a new module iteration is available, and KIT was one of the first assembly centers that received the component to build and validate the new prototypes. In addition to intensive laboratory tests presented in [Kop22] the prototypes were tested at the DESY test beam facility. Besides a 2S module with unirradiated components a second module with irradiated sensors and frontend hybrids was tested. Thus, the module performance regarding the particle detection efficiency at the beginning and the end of the CMS detector lifetime can be studied. Furthermore, modules were rotated with respect to the beam, emulating particles with different transverse momenta to validate the module p_T discrimination mechanism. Results of the 2S module beam tests are presented in Chapter 8.

2

The Large Hadron Collider and the CMS Experiment

High energy physics (HEP) aims to understand and describe the most fundamental building blocks of matter. Particle accelerators are key instruments in HEP, allowing to accelerate particles to large energies and to bring them to collision. Detectors are used to analyze the resulting collision products and, thus, to draw conclusions about the properties of these particles. The *Large Hadron Collider* (LHC), located at the *European Organization for Nuclear Research* (CERN) in Geneva, is the currently world's largest and most powerful particle accelerator. It is designed to accelerate two counter-rotating beams of protons or heavy ions and to bring them to collision at four dedicated interaction points. This section briefly introduces the CERN accelerator complex and gives an overview of the *Compact Muon Solenoid* (CMS) detector, which is one of the four main experiments at CERN.

2.1. The Large Hadron Collider (LHC)

The Large Hadron Collider is located inside a circular tunnel with a circumference of 26.7 km running 50 m to 175 m underneath the surface. It forms the last link in a multi-stage accelerator chain that is located at the CERN accelerator complex, shown in Figure 2.1. Before particles can be injected into the LHC ring, they must pass various pre-accelerator stages to reach the required LHC injection energy.
Proton acceleration starts at *Linear Accelerator 4* (LINAC 4), which accelerates hydrogen ions (H^-) to an energy of 160 MeV. Electrons are removed from the ions by using stripping foils and the remaining protons are passed to the *Proton Synchrotron Booster* (BOOSTER). The BOOSTER supplies 1.4 GeV protons to the *Proton Synchrotron* (PS), that further increases the energy to 25 GeV. As a last step, the *Super Proton Synchrotron* (SPS) accelerates the protons to 450 GeV, which is the LHC proton injection energy. In contrast to protons, heavy ions are first accelerated by the *Linear Accelerator 3* (LINAC 3) and the *Low Energy Ion Ring* (LEIR) before they are injected into the Proton Synchrotron. [CER22a]
For particle acceleration, radiofrequency cavities are used featuring high-frequency oscillating electric fields. Depending on the time stamp at which the particles are passing the cavity with respect to the phase of the oscillating electric field, the particles are accelerated or decelerated. Thus, the beam is split into spatially separated packets of particles with the same energy, called *bunches*. In total 2808 bunches containing about $1.15 \cdot 10^{11}$ protons each can be filled into each of the two LHC beam pipes. The resulting bunch to bunch distance is about 7.5 m, corresponding to a time spacing of 25 ns [EB08]. Superconducting niobium-titanium based dipole magnets operated at a temperature of 1.9 K bent the particles on a circular orbit. Particle bunches injected into the LHC are further accelerated using 16 superconducting cavities with an electromagnetic field oscillating at 400 MHz. The particle energy is increased by slowly ramping up the magnetic field of the dipole magnets. Hence, the radius of the circular orbit becomes smaller, and particle bunches enter the cavities at a different phase of the oscillating

electric field, gaining additional energy. Higher order magnetic multipoles continuously shape and focus the counter-rotating beams. The beam energy is limited by the maximum magnetic field of the dipole magnets at 8.3 T, resulting in a proton peak energy of 7 TeV. The center of mass energy of two colliding beams with identical particles and energies is given by the sum of the energies of the individual beams. Thus, the maximum center of mass energy that can be reached at the LHC is 14 TeV. Kicker magnets are used to deflect the counter-rotating beams and to bring them to collision at four dedicated interaction points distributed along the LHC ring. [EB08] Four major experiments with different detector design approaches are installed at the interaction points, focusing on different topics of particle physics.

- The Compact Muon Solenoid (CMS) [CMS08] detector is a general purpose detector and is introduced in more detail in Section 2.2.
- The ALICE (A Large Ion Collider Experiment) detector aims for the investigation of quark-gluon plasma, created from heavy-ion collisions [ALI08].
- The ATLAS (A Toroidal LHC ApparatuS) detector, which is like the CMS detector a general purpose detector, studies a broad spectrum of particle physics topics based on proton-proton collisions [ATL08].
- The Large Hadron Collider beauty (LHCb) experiment investigates rare decays of charm and beauty hadrons as well as CP violation [LHC08].

The production rate of a particular physics process p at a particle collider is given by

$$\frac{\mathrm{d}N_p}{\mathrm{d}t} = \mathcal{L} \cdot \sigma_p \ , \tag{2.1}$$

where σ_p indicates the cross-section of the process and $\mathcal{L}$ represents the *instantaneous luminosity*. To investigate rare physics processes with small cross-sections a collider with high instantaneous luminosity is needed to create a sufficient number of events within a certain time interval. The total number of events of a process p, generated in the time interval $[0, T]$ is derived by integrating Equation (2.1) over time

$$N_p = \int_0^T \mathcal{L}(t) \cdot \sigma_p \, \mathrm{dt} = \mathcal{L}_{\mathrm{int}} \cdot \sigma_p \ , \tag{2.2}$$

with $\mathcal{L}_{\mathrm{int}}$ describing the *integrated luminosity*, measured in inverse femtobarn (fb^{-1}). The integrated luminosity is a measure of the total amount of data that have been delivered by the collider. Thus, besides the center-of-mass energy, the instantaneous luminosity is a central parameter to characterize the performance of particle colliders. Assuming two beams with Gaussian beam profile colliding head-on, $\mathcal{L}$ can be approximated by

$$\mathcal{L} = \frac{n_b N_1 N_2 f}{4\pi \sigma_x \sigma_y} \ , \tag{2.3}$$

where N_1 and N_2 represent the number of protons in the two colliding bunches with the spatial extensions σ_x and σ_y. The total number of bunches circulating with the orbital frequency f is indicated by n_b. [HM18]

Originally the LHC has been designed to be operated at an instantaneous luminosity of $1 \cdot 10^{34}\,\mathrm{cm}^{-2}\,\mathrm{s}^{-1}$, resulting in about 25 simultaneous proton-proton interactions per bunch crossing, called *pileup* [EB08]. By optimizing machine parameters and reducing the overall beam size, the LHC operators managed to increase the luminosity to twice its design value with

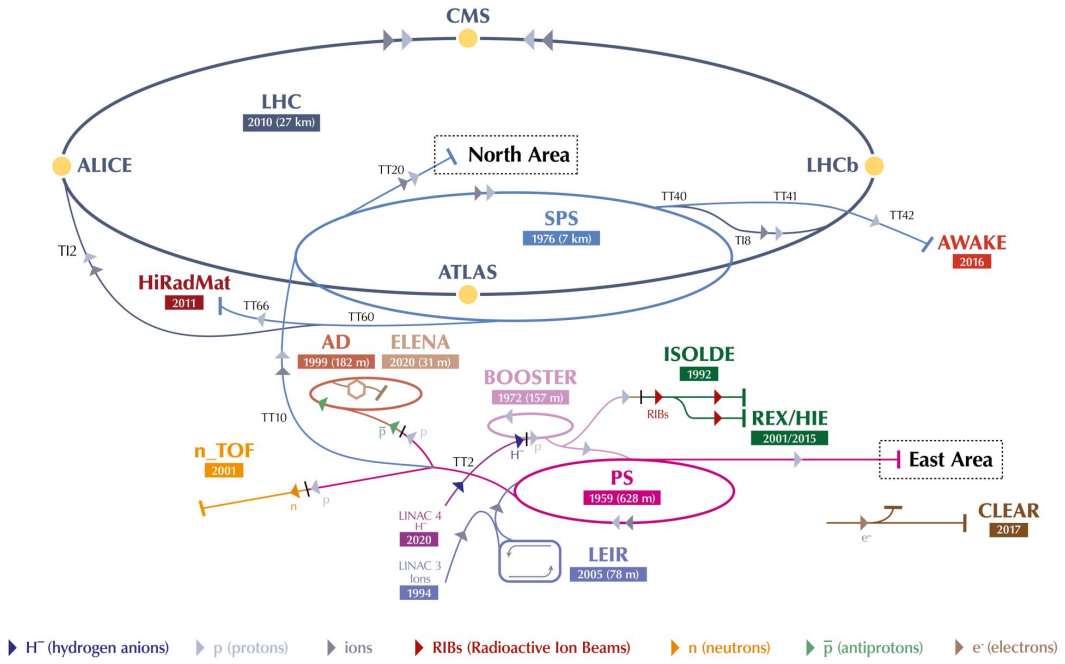

Figure 2.1.: The CERN accelerator complex. Protons or heavy ions pass different pre-accelerator stages before being injected into the LHC storage ring. The four interaction points together with the corresponding experiments are marked with yellow circles. [Mob19]

an average pileup of 60 [Pra17] in 2017. Regarding proton-proton collisions, a total integrated luminosity of 193 fb^{-1} has been collected by the LHC in two data-taking runs at 7 TeV, 8 TeV and 13 TeV center of mass energy until 2019 [CMS17b]. With the start of Run 3 in July 2022, the LHC delivered first proton collisions at 13.6 TeV center of mass energy after about three years of upgrading and maintenance work.

2.2. The Compact Muon Solenoid (CMS) Experiment

The CMS detector is a general purpose detector and is located in a cavern 90 m below the surface at one of the four LHC interaction points. With a weight of 14 000 t, a length of 21 m and a diameter of 15 m, CMS is the heaviest, and next to ATLAS, the second-largest LHC experiment [CER22d]. It studies a broad range of particle physics objectives, ranging from standard model precision measurements to beyond standard model physics, such as the search for dark matter or supersymmetry. Since its completion and commissioning in 2008, the greatest success so far has been the discovery of the Higgs boson in 2012, together with the ATLAS experiment [CMS12], [ATL12]. A schematic view of the CMS detector is shown in Figure 2.2. Various sub-detector systems, each specialized in detecting particular types of particles, are arranged cylindrically around the beam pipe. Endcaps at each end spatially seal the cylinder to achieve an almost complete coverage of the volume around the interaction point. The individual sub-detector components are briefly described in the following starting from the inside. A more detailed overview is given in [CMS08].

Silicon Tracker

The silicon based *tracker* is the innermost subdetector of the CMS experiment and has an active area of about 200 m^2, making it the largest silicon tracker ever built. Its main purpose is to provide spatial coordinates along the trajectory of charged particles that are traversing the tracker and interact with its individual layers. Based on these coordinates the full particle trajectory is reconstructed.
The inner part of the tracker, which is closest to the interaction point, is equipped with pixel modules that enclose the beam pipe within four cylindrical barrel layers and additional three endcap disks, covering a pseudo rapidity range of up to ± 2.5[1]. In total, the pixel modules provide about 124 million readout channels distributed among an active area of roughly 2 m^2, whereby each of the modules features 66 560 pixels with a pixel size of $100 \times 150\,\mu m^2$. The high readout channel density of the inner tracker is required to reliably resolve the individual particle tracks despite the high particle density[2] at the interaction point and, thus, to precisely reconstruct primary and secondary vertices. [Ada+21b]
As the particle flux decreases with increasing distance to the interaction point, less granular modules using silicon strip sensors are installed in the outer region of the tracker. Depending on the module position, different sensor geometries with strip pitches ranging from 80 µm to 205 µm and strip lengths between 8.5 cm and 20 cm are used to achieve the best possible tracking performance. In total, the outer tracker comprises 15 148 strip sensor modules distributed among ten barrel layers and nine endcap layers with a total of about 9.3 million readout channels. More information about the inner and outer CMS tracker can be found in [Ada+21b] and [Col08], respectively.

Electromagnetic Calorimeter (ECAL)

The *electromagnetic calorimeter* (ECAL) is made of 75'848 lead tungstate ($PbWO_4$) crystals and encloses the silicon tracker [Col08]. Due to its high density of $\rho = 8.28\,g\,cm^{-3}$ and the resulting short radiation length of $X_0 = 0.89$ cm, $PbWO_4$ is a perfect material for a homogenous calorimeter fitting inside the solenoid magnet. Scintillation light coming from shower processes of particles, that are interacting electromagnetically with the transparent crystal material, is detected by avalanche and vacuum photodiodes. The emitted light intensity is a measure of the particle energy. Crystals installed in the barrel region have a length of 23 cm, whereas slightly shorter crystals (22 cm) are installed in the endcaps. Thus, the thickness of the ECAL equals about 25 to 26 radiation lengths, absorbing most of the particles interacting electromagnetically. Further information about the ECAL design can be found in [CMS97a].

Hadronic Calorimeter (HCAL)

The *hadronic calorimeter* (HCAL) surrounds the ECAL and measures the energy of hadrons by absorbing them. In contrast to the ECAL, the HCAL is a sampling calorimeter consisting of alternating layers of brass absorber plates and plastic scintillators. Hadrons entering the calorimeter interact with the absorber layers generating showers. Secondary shower particles also interact with the scintillator material, which emits light that gets wavelength-shifted and is detected by photodiodes. Since the HCAL volume is limited by the surrounding solenoid magnet, additional tail catcher scintillators are installed outside the solenoid, whereby the solenoid and return yoke act as absorber material. To reliably detect hadronic forward jets,

[1] Pseudoprapidity: $\eta = -\ln\left(\tan\left(\frac{\Theta}{2}\right)\right)$ with Θ being the angle between the particle trajectory and the beam axis (z-axis).

[2] Assuming an instantaneous luminosity of $1 \cdot 10^{34}\,cm^{-2}\,s^{-1}$ with about 25 pile-up events results in about 1 000 charged particles that emerge from the interaction point at each bunch crossing. [Col08]

a supplementary forward calorimeter is installed along the beam pipe at a distance of about 11 m from the interaction point covering pseudorapidities ranging from $3 \leq |\eta| \leq 5$. Additional information about the HCAL can be found in [CMS97b] and [Man+12].

Superconducting Solenoid

The four layer niobium-titanium (NbTi) based superconducting solenoid, enclosed by a 12 500 t return yoke, is the key component of the CMS experiment and surrounds the tracker and calorimeters. Inside the 12.5 m and 6 m wide cylindrical volume, the homogenous 3.8 T magnetic field runs parallel to the beam pipe and is returned by the steel return yoke. Operating the solenoid at 3.8 T requires a current of about 19 kA, while the energy stored inside the magnet is about 2.6 GJ. Charged particles traversing the CMS detector are deflected by the magnetic field due to the Lorentz force, allowing to determine the charge sign and momentum from the trajectory curvature. Detailed information about the superconducting solenoid can be found in [CMS08] and [CMS97c].

Muon System

In the momentum range relevant for CMS, muons are *minimum ionizing particles* (MIPs). They are the only charged particles that can pass the entire CMS detector with hardly any energy loss. Therefore, the muon system forms the outermost detector part and is based on three different types of gaseous detectors that are integrated into the magnet return yoke. Additionally, the return yoke absorbs all other particles besides the muons, leading to a clear muon signature measured by the chambers. Drift tubes and resistive plate chambers are installed in the barrel region, whereas a combination of cathode strip chambers and resistive plate chambers are installed in the endcaps. Varying technologies were chosen to meet the requirements in terms of particle rates and resolution at different regions of the CMS detector. More information about the muon system can be found in [CMS97d].

Different particle types traversing the CMS detector can be distinguished based on their signatures in the individual sub-detector systems. Figure 2.3 shows a slice of the CMS experiment, including detector signatures originating from differently interacting particles. For optimal event reconstruction, CMS makes use of the particle-flow approach which correlates all sub-detector information in order to determine the physical particle properties of the underlying event in the best possible way [CMS17a].
Electrically neutral particles such as photons or neutral hadrons penetrate the tracker on a straight line without generating a signal and are stopped at the calorimeters. Photons interact electromagnetically with the ECAL, creating showers of secondary particles. However, some photons might already interact with the tracker material forming electron-positron pairs, leading to secondary vertices inside the tracking volume. Neutral hadrons, on the other hand, penetrate the ECAL and are stopped inside the HCAL. In both cases, the shower orientation hints to the direction of particle incidence.
In contrast to electrically neutral particles, leptons such as electrons or positrons, as well as charged hadrons, generate hits in the individual tracker layers that are combined to tracks by dedicated tracking algorithms. Depending on their charge sign and momentum, charged particles are deflected differently by the magnetic field. The sign polarity defines the orientation of the track curvature and the particle *transverse momentum* (p_T) affects the track radius, whereby higher momenta reduce the trajectory curvature. By linking particle tracks to associated energy depositions in the calorimeters, the best possible information concerning the momentum and energy of the underlying particle is achieved.

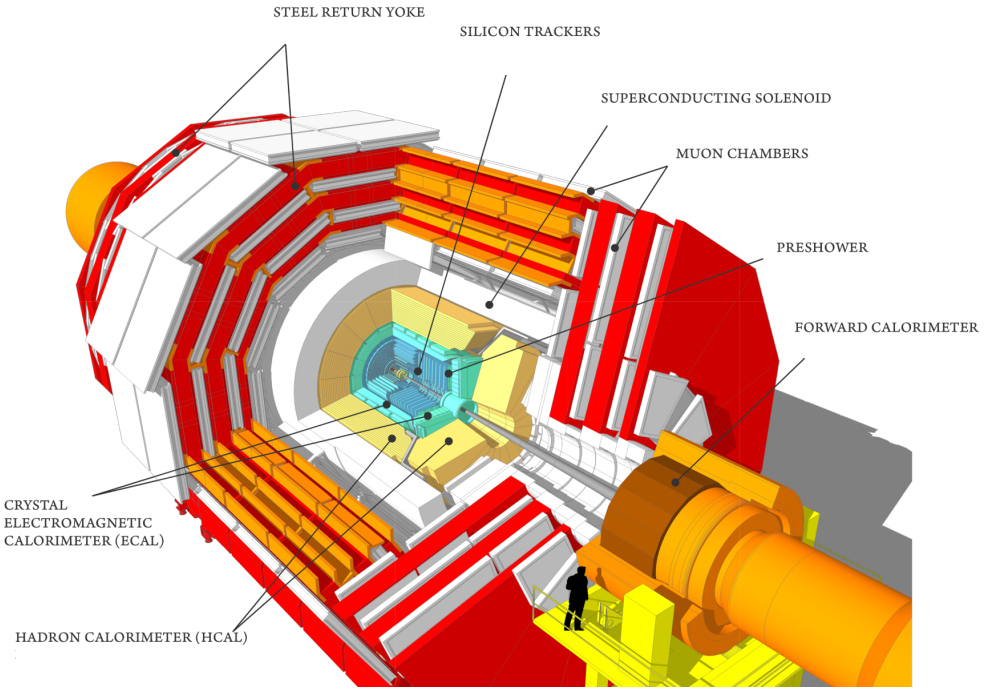

Figure 2.2.: Illustration of the Compact Muon Solenoid (CMS) detector. Sub-detector systems from the outside to the inside: muon chambers embedded in the return yoke, superconducting solenoid, hadronic calorimeter, electromagnetic calorimeter and silicon tracker. Adapted from [Tay11].

Muons pass the entire detector without being stopped by the calorimeters or the magnet system. Therefore, they are easy to identify due to their unique signature consisting of hit signals in the tracker and a matching track in the muon system. Since the orientation of the magnetic field is inverted by the return yoke, the projection of the combined tracks has a sinusoidal shape.
Neutrinos are the only standard model particles that leave the detector without any signatures. In general, the transverse momentum of particles colliding at the LHC is zero in the reference frame of the detector. Thus, by summing up the transverse momenta measured from all particles originating from a specific event, neutrinos can be indirectly identified by missing transverse momentum. [CMS17a]

2.2.1. CMS Trigger Concept

Running at an instantaneous luminosity of $1 \cdot 10^{34}\,\mathrm{cm}^{-2}\,\mathrm{s}^{-1}$, the LHC delivers about 20 to 25 simultaneous proton-proton interactions per bunch crossing with an average of roughly 1000 secondary particles creating signals in the detector. At a bunch crossing frequency of 25 ns, this results in 1 MB of zero-suppressed data being produced by the CMS readout systems, which equals $40\,\mathrm{TB}\,\mathrm{s}^{-1}$. It is technically not feasible to read out and store this enormous amount of data, nor is it necessary from the physics point of view, as only a small fraction contains interesting events. Higher luminosities increase the amount of data even further. Therefore, CMS features a two stage trigger system that identifies relevant events and triggers their readout to store the corresponding data on hard drive. [CMS08]
The CMS Level-1 Trigger (L1) forms the first stage and has a maximum output rate of 100 kHz. Field Programmable Gate Arrays (FPGAs) combined with custom designed Application-Specific Integrated Circuits (ASICs) process coarse data from the calorimeters and muon system and

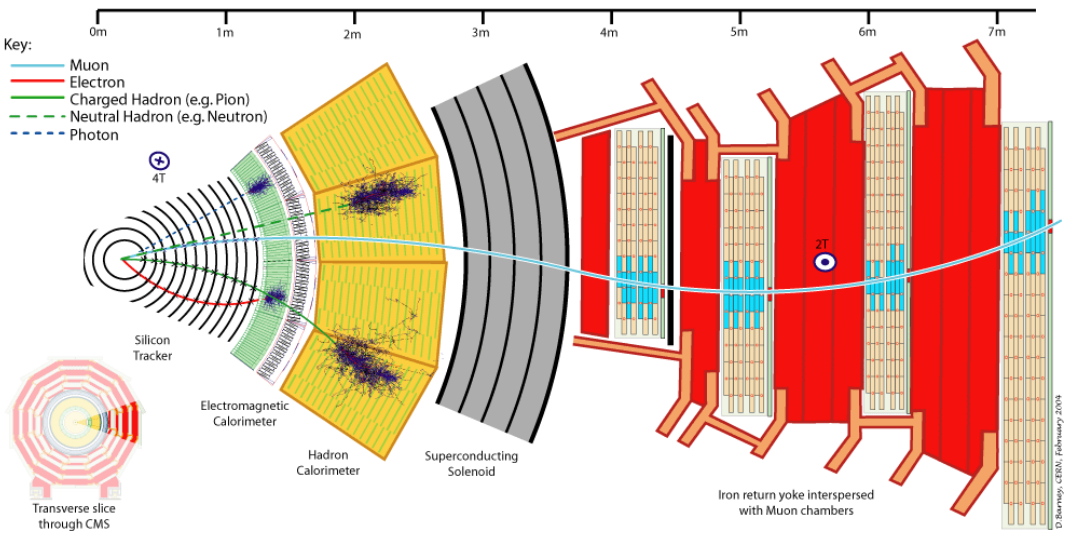

Figure 2.3.: CMS detector slice with signatures of particles interacting differently with the detector. Trajectories of charged particles are reconstructed by the silicon tracker. The electromagnetic and hadronic calorimeters measure particle energies by absorbing them. Only muons can leave the detector, due to their MIP character, creating signals in the tracker and the muon system. [Dav16]

search for predefined signatures. Within 3.2 µs, a decision is made whether to read out the detector frontends, which are buffering the full set of data, or to discard the data and clear the buffers. [CMS00]
Events selected by the L1 trigger are forwarded to the software-based High Level Trigger (HLT) running on a computer farm with thousands of CPU cores. For each event, physics objects such as muons, electrons and jets are reconstructed using the information of all subdetector systems. The HLT event reconstruction and selection is based on dedicated trigger paths that use algorithms similar to the ones used for the offline event reprocessing. Each path represents a sequence of predefined processing steps with increasing complexity. Overall, the HLT trigger menu comprises different paths to be sensitive to many different physics processes analyzed by the CMS Collaboration. The average rate of events passing the HLT is 400 Hz. [CMS17c]

3

The High Luminosity LHC (HL-LHC) and the CMS Outer Tracker Phase-2 Upgrade

Since the LHC commissioning, physicists and engineers have been working on continuously improving the performance of the accelerator in terms of instantaneous luminosity and center of mass energy. Maintenance and optimization work over the last few years have been carried out during regularly scheduled *Year-End Technical Stops* (YETS), *Extended Year-End Technical Stops* (EYETS) and *Long Shutdowns* (LS). These operational breaks are also used by the experiments for maintenance and to upgrade their detectors. In Figure 3.1 a chronological overview of the LHC performance and the improvements that have been implemented, as well as the future upgrade plans is given. With the start of Run 3 in mid 2022, the LHC is running at 13.6 TeV centre-of-mass energy and an instantaneous luminosity of $2 \cdot 10^{34}\,\mathrm{cm}^{-2}\,\mathrm{s}^{-1}$, which is twice the initial design value. Until the end of 2025, the total integrated luminosity delivered by the LHC is expected to be increased up to $450\,\mathrm{fb}^{-1}$. During the subsequent Long Shutdown 3, the LHC will be further upgraded to the *High Luminosity LHC* (HL-LHC). [CER22e], [Apo+17] A brief overview of the HL-LHC upgrade as well as the upgrade of the CMS tracker is given in this chapter.

3.1. The High Luminosity LHC (HL-LHC)

As indicated in Figure 3.1, HL-LHC operation is scheduled to start in early 2029. Running at center of mass energies of up to 14 TeV, the HL-LHC will deliver instantaneous luminosities of 5 to $7.5 \cdot 10^{34}\,\mathrm{cm}^{-2}\,\mathrm{s}^{-1}$ with a maximum average pileup of about 200 events. Assuming an operation time of at least ten years, the amount of collected data will be in the order of $3000\,\mathrm{fb}^{-1}$ with the option to be increased to $4000\,\mathrm{fb}^{-1}$ in the ultimate runtime scenario. The search for rare processes that might hint towards new physics beyond the Standard Model, but also the minimization of statistical uncertainties on already investigated processes will strongly benefit from the vast increase of data. [Apo+17]
In order to achieve the increase in luminosity and to ensure safe operation during the upcoming years, various LHC components have to be upgraded or replaced. The inner triplet magnets, responsible for focusing the beams shortly before they are brought to collision, are exposed to particularly high radiation doses due to their small distance to the interaction point. It is required to replace the magnet system, since it would not withstand the HL-LHC phase, posing the risk of sudden failure resulting in severe damage to the machine. New quadrupole magnets with a more powerful magnetic field of up to 12 T will be installed, improving the overall beam focusing.
To reduce the aging of the new magnets but also to limit the peak pileup inside the experiments, luminosity leveling has to be implemented for the HL-LHC. Instead of having a high instantaneous luminosity at the beginning, which decreases over time, the luminosity is kept on a constant level by continuously adjusting the beam parameters. Thus, an almost identical average pileup is obtained over time. Furthermore, the number of collimators that protect

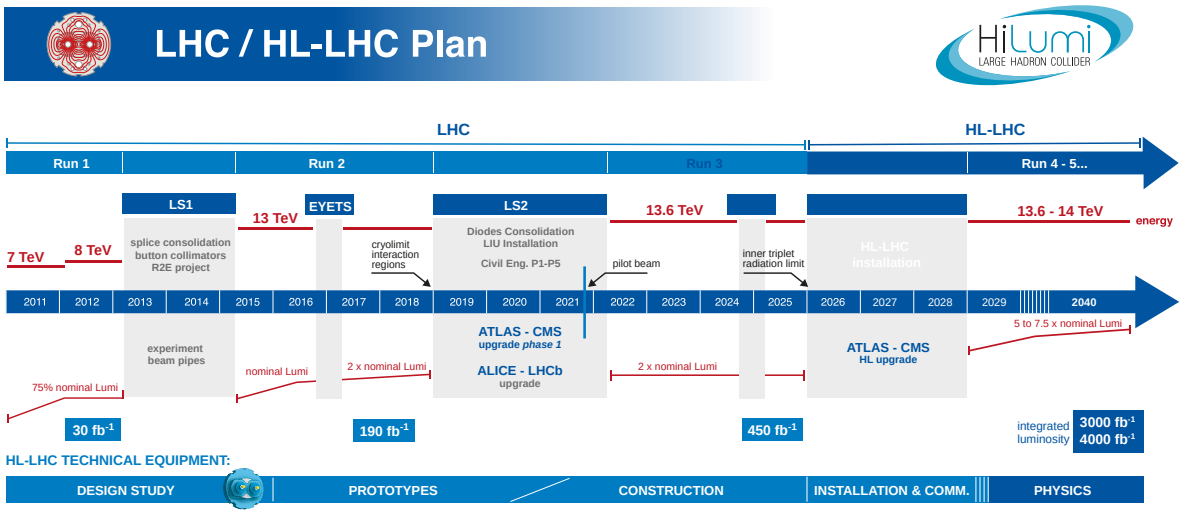

Figure 3.1.: The LHC and HL-LHC upgrade schedule. After passing Long Shutdown 2, the Run 3 period has started in mid 2022. The LHC is currently running at twice its design luminosity and a center of mass energy of 13.6 TeV. With the Long Shutdown 3 starting in early 2026, the LHC will undergo major upgrades to enter its high luminosity phase starting in 2029. Modified from [CER22e].

superconducting components from quenching by absorbing stray particles will be increased and a large fraction of the already existing collimators will be exchanged.
The installation of superconducting crab cavities at the interaction points is another central part of the upgrade. Two bunches crossing each other at an angle only see a fraction of each other. The crab cavities will tilt the bunches into the collision point by deflecting their head and tail. Improving the bunch overlap maximizes the probability of proton-proton interactions and, thus, significantly increases the luminosity. [CER22f] A full overview of the HL-LHC upgrade can be found in [Apo+17].

3.2. The CMS Phase-2 Tracker Upgrade

As a consequence of the HL-LHC upgrade, the CMS experiment needs to be fundamentally revised during Long Shutdown 3 to ensure efficient operation within the upcoming high luminosity phase. The so-called *Phase-2 Upgrade* affects all CMS sub-detector systems including the silicon tracker, which has to be completely replaced. The main requirements for the new tracker together with the overall tracker concept is summarized in this section, following the *Technical Design Report* (TDR) of the CMS Phase-2 Tracker [CMS17d].

Radiation Tolerance: Components of the new tracker will face unprecedented radiation exposures due to the intensified particle flux inside the detector. Since the *Outer Tracker* (OT) will not be accessible for maintenance, the sensors and readout electronics have to resist the harsh radiation environment and stay fully functional within the whole CMS operation period. However, the small distance to the interaction point and the associated higher radiation exposure requires to keep the *Inner Tracker* (IT) accessible, allowing to replace components during regular shutdowns.

Increased Granularity: With an average pileup of 140 to 200, the track density in the detector volume rises dramatically. High channel occupancies would cause inefficient tracking due to the

enlarged number of possible hit combinations. Additionally, the separation of closely spaced tracks becomes more difficult. Therefore, the number of readout channels in the Outer and Inner Tracker has to be enlarged to keep the channel occupancy at a moderate level.

Reduced Material Budget: Multiple scattering negatively affects the tracking performance as well as the performance of the calorimeters and, thus, deteriorates the global event reconstruction. The new tracker will feature an overall lower material budget compared to the current tracker while having a larger geometrical acceptance of up to $|\eta| = 4$.

Level-1 Trigger Contribution: The currently used CMS Level-1 trigger, as introduced in Section 2.2.1, is not operable within the high pileup environment. Firstly, the overall trigger rates would reach a non-feasible level and secondly, the selection algorithms would become inefficient. Track information from the Outer Tracker has to be supplied to the Level-1 track finder to reduce the overall trigger rates without losing interesting events. Hence, a new module concept has been developed, allowing to reject tracks from low p_T particles on module level and to forward the corresponding track information to the Level-1 trigger at the bunch crossing frequency of 40 MHz. The p_T-module concept is described in more detail in Section 3.2.2.

3.2.1. The CMS Phase-2 Tracker Layout

The projection of one quarter of the new CMS Phase-2 Tracker is schematically shown in Figure 3.2 with the interaction point located in the lower left corner and the beam pipe running parallel to the z-axis. The Inner Tracker, indicated by the green and orange lines, is the part closest to the interaction point and will be equipped with about 4 000 highly granular silicon pixel modules. The module design is based on two different sensor layouts with pixel sizes of $25 \times 100\,\mathrm{mm}^2$ and $50 \times 50\,\mathrm{mm}^2$. Depending on the module type, the sensors are read out by either two or four readout chips fabricated in a 65 nm CMOS process that are flip chipped onto the sensor. Besides the four module layers in the barrel region, the Inner Tracker is elongated along the forward direction by twelve additional disc layers, extending the acceptance to $|\eta| \approx 4$. In total, the Inner Tracker has about two billion readout channels and covers an active silicon area of $4.9\,\mathrm{m}^2$. [CMS21]
The Outer Tracker surrounds the Inner Tracker and will be equipped with about 13 000 p_T modules made of two closely spaced silicon sensors, whereby two types of modules can be distinguished: PS modules (blue), comprising a macro-pixel and a strip sensor, and less granular 2S modules (red) consisting of two identical strip sensors. The module designs are discussed in more detail in Section 3.4 and Section 3.3, respectively. As indicated in Figure 3.2, the barrel area consists of six layers and is subdivided into the *Tracker Barrel PS* (TBPS) region, housing three layers of PS modules, and the *Tracker Barrel 2S* (TB2S) region with additional three layers of 2S modules. In order to achieve full geometrical coverage at minimal material budget, a fraction of the PS modules in the TBPS is tilted with respect to the beam. Furthermore, the tilting ensures efficient detection of high p_T particles crossing the barrel region. Five *Tracker Endcap Double-Discs* (TEDD), each equipped with overlapping layers of PS modules at smaller radii and 2S modules at larger radii, adjoin the barrel area and cover the forward direction. [CMS17d]

3.2.2. The Outer Tracker p_T-Module Concept

As mentioned in Section 3.2, the Outer Tracker has to provide track information to the Level-1 track finder in order to efficiently select interesting events at manageable trigger rates. Track

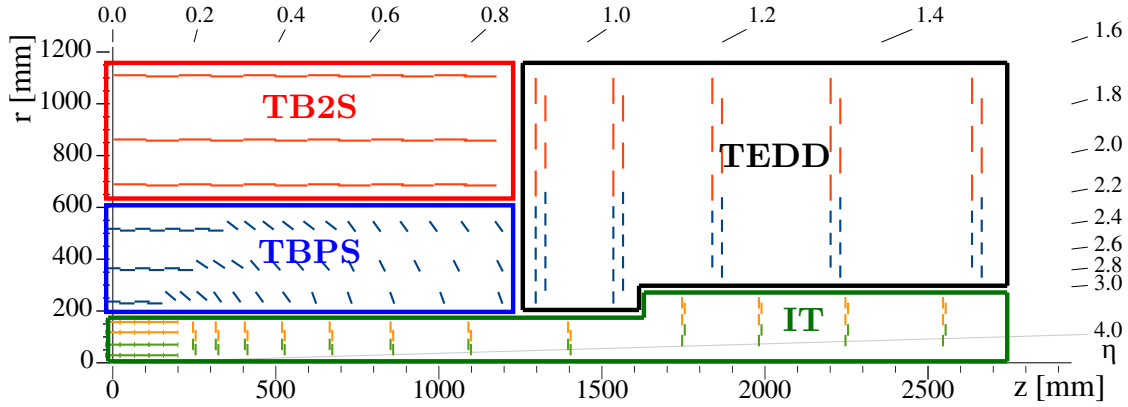

Figure 3.2.: Schematic illustration showing an r-z projection of one quarter of CMS Phase-2 Tracker. The interaction point is located at $r, z = 0$ with the beam pipe in parallel to the z-axis. Each colored line represents a layer of modules. The Inner Tracker (orange and green) is located as close as possible to the interaction point. The Outer Tracker is subdivided into three areas, represented by colored boxes and described in the text and is equipped with PS (blue) and 2S (red) modules. Adapted from [CMS17d].

information has to be directly provided by the modules at the bunch crossing rate of 40 MHz. However, it is technically not feasible to forward all hit information due to limited bandwidths. Thus, the Outer Tracker modules feature a *transverse momentum* (p_T) discrimination logic and only forward hit information of particles with transverse momenta exceeding a programmable threshold value. Figure 3.3 schematically shows the concept of the on-module p_T discrimination. Charged particles crossing the tracker are differently deflected by the magnetic field depending on their transverse momenta. As a result, the hits generated in the two closely spaced sensor layers of the module have a certain displacement which, in turn, is a measure of the particle's transverse momentum assuming that the particle comes from the interaction point. Higher transverse momenta result in smaller displacements. The module readout chips search for hit combinations with a seed hit in the lower sensor (seed layer) and a matching hit in the upper sensor (correlation layer). Combinations of hits are only matched, if the upper hit is located within a programmable correlation window. Matched hits form a *stub signal* that is directly forwarded to the Level-1 track finder containing information about seed hit position as well as the hit displacement, called *stub bend*. Changing the window size allows to modify the p_T threshold of the module. Simulations have shown that a p_T threshold of 2 GeV is sufficient to reduce the number of tracks per event by several orders of magnitude, allowing to supply track information to the trigger at 40 MHz without losing interesting events [Pes+10].
Different geometrical aspects have to be taken into account to achieve efficient and homogenous p_T discrimination among all modules inside the tracker. Modules located closer to the interaction point are hit at smaller incidence angles resulting in a deteriorated p_T resolution. Increasing the sensor spacing for these modules keeps the discrimination of high and low p_T particles efficient. Hence, PS modules will be built with sensor distances of 1.6 mm, 2.6 mm and 4 mm, while the 2S modules will come with sensor spacings of 1.8 mm and 4 mm. Furthermore, it is required to shift the correlation window with respect to the seed position to compensate for the inherent shift of the particle tracks depending on the module position with respect to the interaction point. [CER22e]

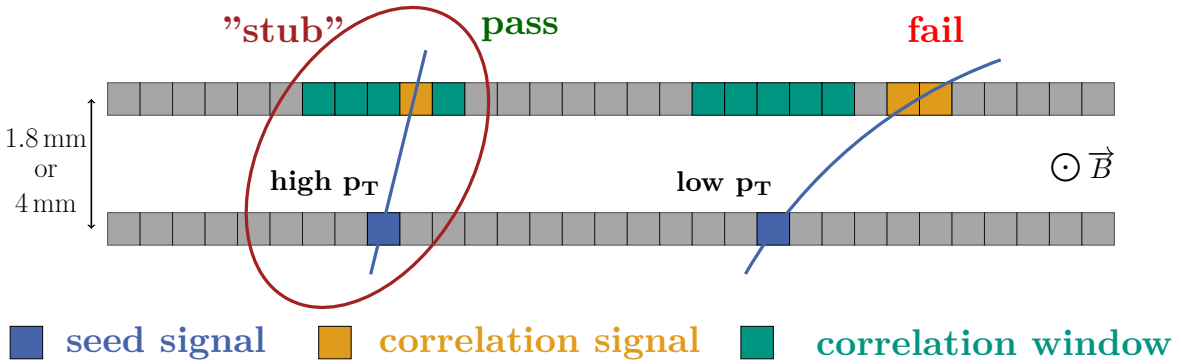

Figure 3.3.: The hit pattern of charged particles crossing the module depends on the particle's transverse momentum (p_T). The higher the p_T, the smaller the deflection by the magnetic field and, consequently, the smaller the displacement of the hit signals in the two sensor layers. By defining an adjustable correlation window in the upper sensor, low p_T particles can be rejected. Correlated hits form a stub signal and the corresponding information is forwarded to the CMS Level-1 trigger.

3.2.3. Radiation Environment

The intensified particle flux during the HL-LHC phase will drastically increase the radiation exposure of all detector components. Dedicated radiation simulations using the FLUKA simulation tool have been performed by the CMS *Beam Radiation Instrumentation and Luminosity* (BRIL) group. Within the Monte Carlo simulations, primary proton-proton collision events are generated, and the resulting secondary particles are propagated through the detector. The individual particle interactions with the detector material and the corresponding radiation exposure are evaluated based on different physics models taking into account the particle type and energy. Thus, it is possible to predict the radiation exposure of individual components in dependence of their location in the tracker. [Fer+05][CMS17d]
Radiation exposure is quantified by two parameters, the *total ionizing dose* (TID) that is a measure of the total energy absorbed due to ionization, and the 1 MeV neutron equivalent fluence, which quantifies the absorbed energy due to nuclear interactions based on the *non ionizing energy loss* (NIEL) hypothesis (see Section 4.5.1). Figure 3.4 shows the tracker fluence distribution in units of 1 MeV neutron equivalent per cm^2 that is expected after collecting $3000\,fb^{-1}$ of data. Due to the immediate proximity to the interaction point and the resulting higher particle density, the Inner Tracker will face the highest fluences with a maximum of $2.45 \cdot 10^{16}\,cm^{-2}$ at the first module layer. The particle density drops with increasing distance to the interaction point and consequently, the maximum expected fluences in the Outer Tracker region are significantly lower. Depending on the module type, different maximum fluences are expected for the PS and 2S modules. PS modules will face a maximum of $1.07 \cdot 10^{15}\,cm^{-2}$, whereas the maximum 2S fluence is $4.22 \cdot 10^{14}\,cm^{-2}$. In the ultimate CMS runtime scenario with $4000\,fb^{-1}$ of collected data the respective fluences increase by a factor of $1.\overline{3}$. [CMS23a]

3.3. The 2S Module

In total, 7680 2S modules will be installed in the CMS Outer Tracker [CMS17d]. The *Karlsruhe Institute of Technology* (KIT), which is one of eight CMS Outer Tracker module assembly centers, pledged to build up to 2000 of these modules. Besides the 2S module production starting in 2023, KIT is also involved in the testing of 2S module prototypes in order to validate

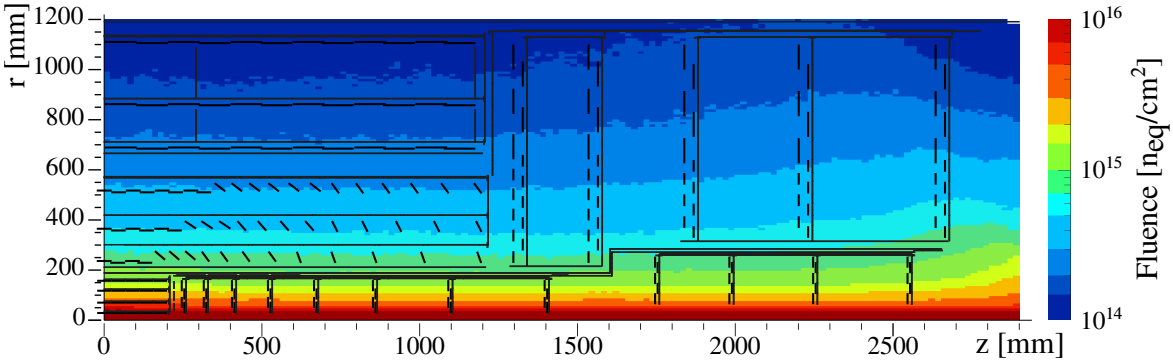

Figure 3.4.: Distribution of the expected total fluence in the CMS Phase-2 Tracker after taking 3000 fb^{-1} of data. The fluence levels are given in 1 MeV neutron equivalent per cm^2, assuming proton-proton collisions at 14 TeV center of mass energy. [CMS17d]

the unrestricted functionality of the module design and its components before entering mass production. In the scope of this thesis, beam test measurement with the latest 2S module prototypes have been performed, investigating the overall module performance but also the impact of radiation damage. The module design and its main components corresponding to the prototypes tested in this thesis is introduced in the following. A detailed description of the module assembly procedure can be found in [Mai19].

3.3.1. Module Components and Mechanics

Figure 3.5a shows an exploded view of the 2S module with all its main components. Two silicon strip sensors (2S sensors), each measuring approximately $10 \times 10\,cm^2$, form the center part of the module. The sensors are segmented into two rows of 1016 strips arranged in parallel with a strip-to-strip distance of 90 µm. Carbon-fiber reinforced aluminum (Al-CF) bridges, on which the sensors are glued back to back, serve as the main structural element of the module and provide the precise sensor spacing that is required for the p_T discrimination described in Section 3.2.2. Different bridge thicknesses are available to achieve sensor distances of 1.8 mm or 4 mm. The bridges also serve as the main cooling path to dissipate the heat generated by the sensors and readout electronics during module operation. In order to electrically isolate the Al-CF bridges from the sensor backside, which is set to high voltage during module operation, 25 µm thick Kapton MT® polyimide strips are placed in between the sensor backside and the bridges. High voltage is applied through HV-tails that are glued on the sensor backside with wire bonds serving as interconnection between the tail and the sensor. Two frontend hybrids (FH) are placed along the opposing sensors edges next to the pads of the strips. Each frontend hybrid houses eight *CMS Binary Chips* (CBC) for the sensor readout and an additional *Concentrator Integrated Circuit* (CIC) that further processes the individual CBC data streams. The service hybrid (SEH) is connected to both FEHs and is responsible for the module powering and optical data transmission. All hybrids are glued onto the L-shaped extensions of the Al-CF bridges. Thermal simulations have shown that, depending on the module spacing and the individual location in the tracker, additional cooling points (stump bridges) are required. All modules will feature a stump bridge located in the middle of the sensor edge next to the service hybrid to improve the heat dissipation from the SEH electronics. A second stump bridge at the opposite sensor edge (not visible in Figure 3.5a) will be installed for all 4 mm modules, as well as selected 1.8 mm modules that are exposed to particularly high radiation levels. [CMS17d]

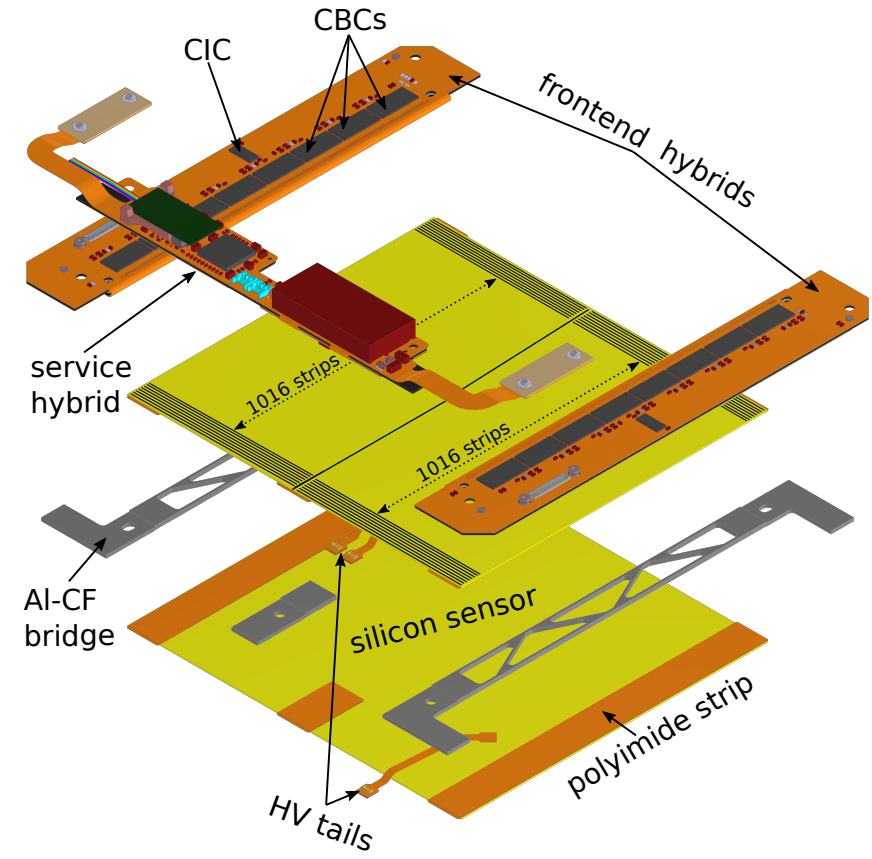

(a)

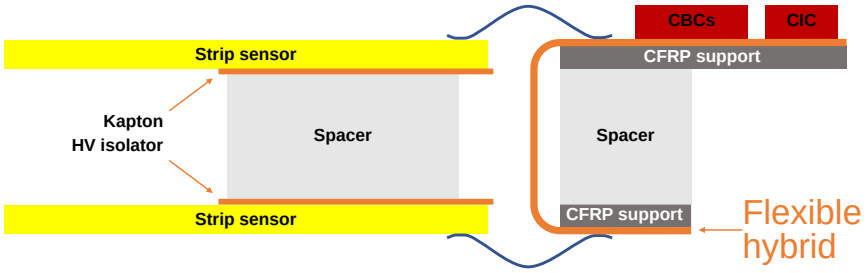

(b)

Figure 3.5.: (a): Exploded view of a 2S module. Two silicon strip sensors arranged in parallel are spaced out by two carbon-fiber reinforced aluminum (Al-CF) bridges. Polyimide strips electrically isolate the sensor backsides from the bridges. Two frontend hybrids, each housing eight CBC readout chips, are glued onto the L-shaped extensions of the bridges. The module is powered by the service hybrid, which is also responsible for the optical data transmission. Modified from [CMS17d]. (b): Concept of the flexible 2S frontend hybrids. The hybrids are laminated on carbon-fiber reinforced polymer (CFRP) supports (stiffeners) and folded around spacers that match the sensor spacing. With this configuration wire bonds connecting the strips with the CBC readout channels can be placed on both sides of the hybrid. [CMS17d]

3.3.2. Module Electronics and Data Processing

After the general 2S module design has been introduced in the previous section, the individual components of the module prototype version investigated in this thesis are described in more detail in the following. Furthermore, the hit and stub data paths and processing, which were tested in the scope of beam test measurements, are briefly introduced.

The Frontend Hybrid (FEH)

Figure 3.5b shows a cross-section of the frontend hybrid design. Eight CBCs together with a CIC are bump bonded onto the hybrid, which is realized in a flexible technology. The flexible part is laminated onto carbon-fiber reinforced polymer (CFRP) supporting structures (stiffeners) and folded around spacers to match the spacing of the sensor sandwich. With this approach, the CBC readout channels can be partly routed to the hybrid backside so that the strips of the bottom sensor can be easily connected to the CBCs via wire bonds. [CMS17d]

CMS Binary Chip (CBC)

This part gives a brief overview of the latest CBC version (CBC3.1) based on the corresponding manual [Pry19], where a much more detailed description can be found. Each CBC has 254 readout channels that are alternately wire bonded to strips of the lower and upper sensor of the module. Thus, one CBC handles two sets of 127 strips, allowing to search for correlated signals in the two sensor layers. Figure 3.6a shows the block diagram of the CBC architecture. Charge signals from the sensor strips are first processed by the analog frontends of the respective channels. Since the 2S sensors are AC-coupled, the CBC does not feature a leakage current compensation circuit. As shown in Figure 3.6b, the analog frontend consists of a pre-amplifier and a subsequent capacitive gain post-amplifier, that shape and amplify the incoming strip signal. The amplifier output is further processed by the comparator stage, returning a digital 1 (0), if the signal exceeds (stays below) a defined threshold that is given in the DAC unit V_{cth}. The comparator threshold is set globally for all channels of the chip. In order to compensate for nonuniform post-amplifier outputs among the individual channels due to process variations, an offset can be added to the comparator input signal. The individual channel offsets are set via programmable 8-bit offset registers. Additionally, the CBC features a test pulse generator, allowing to inject defined charge pulses into the analog frontend for testing and calibration procedures.
As indicated by the pink and green background colors in Figure 3.6a, there are two different clock domains running on the CBC. The 320 MHz domain (green) is provided via a differential scalable low-voltage signaling (SLVS) input and is used for data transmission and fast control. Logic blocks for hit and stub detection run on the 40 MHz domain (pink), which is recovered from the Fast Control Interface (FCI). All measurements presented in this thesis have been carried out using the default readout mode of the hit detection circuit. Within this mode, the output of the analog frontends is sampled by the 40 MHz clock and only comparator signals during the rising edge of the clock are captured. The resulting hit signal stays high till the comparator output returns to zero at the following rising clock edge. Thus, the minimum output width is one clock cycle, corresponding to 25 ns. Individual channels of the chip can be masked by using a programmable 254-bit register to disable the hit detection circuit of the respective channels by keeping the output at logic 0. In order to align the 40 MHz sampling clock relative to the data generated at each LHC bunch crossing, the CBC features a Delay Locked Loop (DLL), allowing a phase adjustment of up to 25 ns with a step size of 1 ns.
After the hit detection block, the data path is split up. Full hit information of all 254 channels is stored in a static random-access memory (SRAM), waiting to be read out following a trigger

signal from the Level-1 trigger. With an SRAM depth of 512 clock cycles and a sampling rate of 40 MHz, hit data is only available for 12.8 µs before events are overwritten. While full hit data is stored, the corresponding events are processed by the stub logic in parallel. Adjacent hits in each sensor layer are summarized to clusters. Cluster widths exceeding a programmable size are rejected, whereas all clusters larger than four adjacent channels are rejected by default as they usually originate from low p_T particles crossing the sensor at large angles. Cluster combinations fulfilling the correlation principle explained in Section 3.2.2 are searched, and the corresponding stub signal is sent out. Neighboring CBCs share their edge channel hit information, so that stub signals originating from clusters located in the transition region between two chips are reliably detected. In case there is more than one clusters within the correlation window, the one located closer to the seed cluster is selected, representing the configuration with the highest p_T. The correlation window size is programmable in half channel steps up to a maximum of ± 7 channels. To compensate for geometrical effects due to the individual module positions and orientations in the CMS tracker, the stub finding procedure features further logic blocks to swap the seed and correlation layers and to apply an offset correction on the correlation window position. Valid stubs are described by two parameters: the seed cluster position and the stub bend information, which is defined as the offset between the respective centers of the seed and correlation cluster. Data rate limitations constrain the number of stubs that can be detected and forwarded by each CBC to a total of three stubs per bunch crossing. However, the stub output is not prioritized, and in case there are more than three stub signals it is not guaranteed that the transmitted stubs are those with the smallest bend (the highest momentum). Stub data is continuously sent out by the data assembly logic using five SLVS output lines running on the 320 MHz clock domain. Another SLVS line serves as output path for the buffered level-1 hit data (L1 data), that is sent out after a positive L1 trigger decision.

Concentrator Integrated Circuit (CIC)

The *Concentrator Integrated Circuit* (CIC) located on each frontend hybrid acts as the interface between the CBCs and the service hybrid. All 2S modules investigated in the scope of this thesis feature frontend hybrids equipped with the chip version CIC2. The CIC is connected to all eight CBCs via 48 (8×6) SLVS lines and buffers, aggregates and formats stub and L1 data from the individual chips. Stub data emitted by the CBCs at the bunch crossing frequency of 40 MHz is buffered for eight consecutive bunch crossings, and the respective stub signals are sorted by their bend code, prioritizing high p_T events with small bends. Thus, in case of a stub buffer overflow only information of lower p_T events is lost. L1 data from the CBCs enters the CIC without sparsification and two CIC operation modes can be configured. Within the sparsified mode, L1 data is compressed by forming clusters from hits of neighboring channels in both sensor layers. Only the corresponding cluster position and width is forwarded, reducing the overall amount of data and allowing trigger rates of up to 750 kHz. In contrast, the deserialized debug mode transmits the CBC raw data without any sparsification, which reduces the maximum trigger rate down to 100 kHz. Data transmission from the CIC to the Low Power Gigabit Transceiver (LpGBT) placed on the service hybrid, is accomplished by a total of six SLVS lines, each operating at 320 Mbit s^{-1}. Five of these lines transmit stub trigger data while the remaining one transmits L1 data. More information about the CIC2 can be found in [Ber+22] and [CMS17d].

The Service Hybrid (SEH)

The Service Hybrid (SEH) is based on the same flex technology as the FEHs and has two flexible tails with fine-pitch connectors that are plugged into their counterparts sitting on each

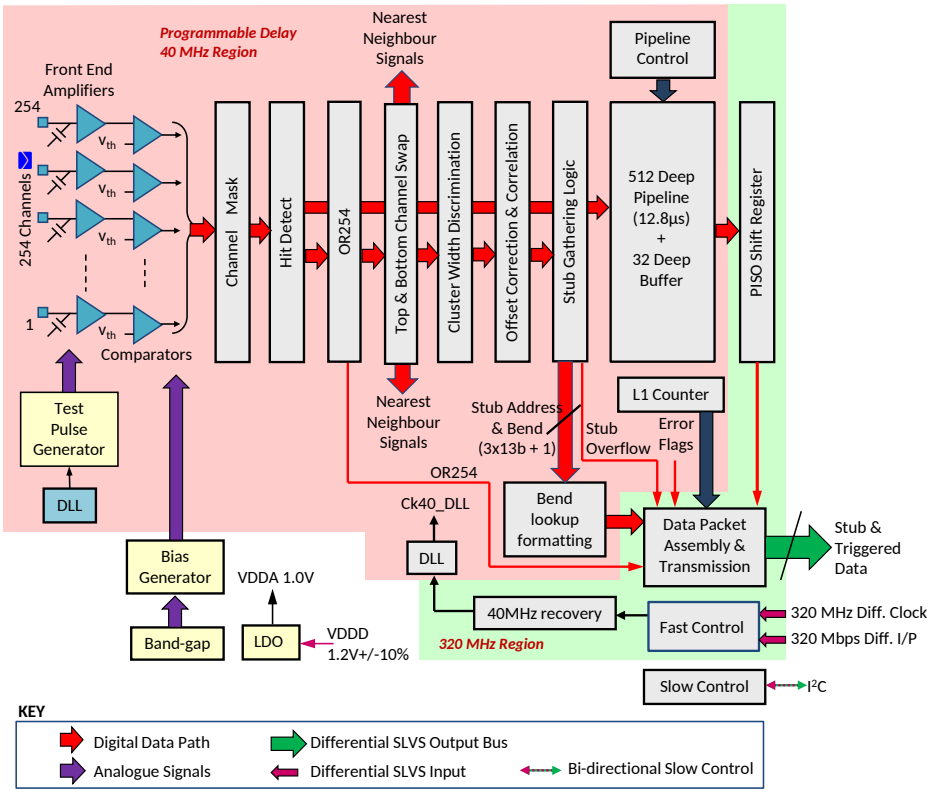

(a)

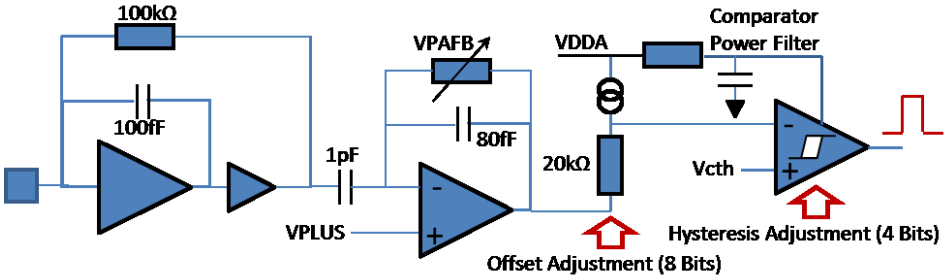

(b)

Figure 3.6.: (a): Block diagram showing the CBC architecture. Binary hit data coming from the 254 frontend channels is processed by the hit and stub detection logic running on a 40 MHz domain. The data transmission logic and Fast Control runs on a 320 MHz domain. (b): Analog CBC frontend of one readout channel. Charge signals coming from the sensor strips are shaped and amplified by two amplifier stages. The amplifier output is adjusted by a constant offset defined by an 8-bit offset register before entering the comparator stage. A binary output signal, 1 (0) if the signal exceeds (stays below) the globally applied threshold, is returned by the comparator. Both figures taken from [Pry19].

FEH. As mentioned previously, the LpGBT receives the CIC data via six SLVS lines at a bandwidth of 320 Mbit s^{-1}. The two incoming data streams are serialized and formatted before the data is forwarded at 5.12 Gbit s^{-1} to the Versatile Transceiver plus (VTRx+) [Tro+18] for opto-electrical conversion and finally transmitted via an optical fiber to the-off module detector backend. Additionally, the LpGBT generates the 320 MHz clock for the FEHs and

configures the CICs, CBCs and the VTRx+ via I^2C. A two-stage DC-DC converter scheme, covered by an electromagnetic shield, provides all the low voltage levels needed by the module electronics. Within the first DC-DC stage, the 10 V module input voltage is converted to 2.55 V by the bPOL12V [CER22b] and provided to the VTRX+, while the bPOL2V5 [CER22c] further reduces the voltage to 1.25 V needed by the CICs, CBCs, the lpGBT and the VTRx+. Sensor high voltage is supplied by the HV-circuit implemented on the SEH backside featuring connectors for the HV-tails of the sensors. Bias voltages of up to 800 V can be applied. More information about the 2S module service hybrid can be found in [Kle+19].

3.4. The PS Module

For the complete CMS Outer Tracker a total of 5616 PS modules are required [CMS17d]. These PS modules will be assembled by four out of the eight CMS Outer Tracker module centers. The start of production is scheduled for 2023, similar to the 2S module production. Although the ETP as a pure 2S module assembly center will not be directly involved in the PS module production, it has contributed to the development and testing of prototype versions of the PS module macro-pixel sensor (PSp sensor) [Sch19]. In the context of this thesis, additional efficiency studies with irradiated PSp sensor prototypes featuring the final sensor design and sensor material were performed (see Chapter 7). PS module characteristics relevant for this thesis are introduced in the following, while a more detailed description can be found in [CMS17d].

3.4.1. Module Design and Components

An exploded view of the PS module showing its main components is depicted in Figure 3.7a. With about $10 \times 5\,\mathrm{cm}^2$, the PS module sensors have half the size of a 2S sensor. Two sensor versions with different granularity are assembled in the PS module: A macro-pixel sensor (PSp sensor) and a strip sensor (PSs sensor). The PSp sensor forms the lower module layer and is segmented in 30208 pixel cells arranged in 32 rows with 944 pixels each. Thus, the cell size of a single pixel is about $100 \times 1467\,\mu\mathrm{m}^2$. In order to read out the complete sensor, 16 *Macro Pixel ASICs* (MPAs) [CER17a] are required. The MPAs are flip-chipped and bump bonded onto the PSp sensor, following a matrix configuration with two rows of eight chips each. All 16 MPAs together with the PSp sensor form the *Macro-Pixel Sub-Assembly* (MaPSA). In contrast, the less granular PSs sensor is placed at the module top side and is segmented into 1920 strips with a length of about 2.4 cm. The strips are grouped into two rows with 960 strips each, as indicated by the black lines in Figure 3.7a. With a strip-to-strip distance of 100 µm, the PSs sensor strip pitch is identical to the pixel pitch of the PSp sensor. More information about the individual sensors can be found in Section 5.1.1. Four aluminum nitride bridges serve as structural elements for the sensor sandwich consisting of the MaPSA and the PSs sensor. Bridges with three different thicknesses will be available for the PS module assembly, providing sensor spacings of 1.6 mm, 2.6 mm and 4 mm. Two frontend hybrids (FEH), each housing eight *Short Strip ASICs* (SSA) [CER17b] and one *Concentrator Integrated Circuit* (CIC) [Ber+22], are placed along the longer edges of the sensor sandwich. The SSA is the binary readout chip of the PSs sensor and provides 120 readout channels per chip. As shown in Figure 3.7b, the PS module frontend hybrids are based on the same flex technology as the hybrids of the 2S module, allowing to place wire bond connections to the readout chips from both hybrid sides. Wire bonds connecting the SSAs with strips of the PSs sensor are placed at the hybrid top side, while the MPAs are connected to the hybrid backside. Since the SSA does not feature any stub finding logic blocks, it passes the processed hit information to the MPA using dedicated routes implemented on the FEH. The MPAs search for valid stub signals by correlating clusters

detected in both sensor layers, following the principle introduced in Section 3.2.2. Data streams form the MPAs are collected and serialized by the CICs sitting on the FEHs, which then forward the data to the readout hybrid. Due to space limitations, the module powering and data transmission is split between two service hybrids, each of them placed along one of the short edges of the sensor sandwich. The PS readout hybrid [Ras+20] is responsible for the optical data transmission to the FPGA detector backend and provides clock and control signals to the readout ASICs. As with the 2S module, the two main components fulfilling these tasks are the *Low Power Gigabit Transceiver* (LpGBT) and the *Versatile Transceiver Plus* (VTRx+). All voltage levels required by the module electronics and the readout ASICs are provided by the two stage DC-DC converter sitting on the PS power hybrid. An additional powering connector runs across the module top to ensure uniform distribution of the ground and voltage levels among the module. In order to effectively remove heat from the individual components generated the during module operation, the whole module is built onto a 200 µm thick carbon-fiber reinforced polymer (CFRP) baseplate, providing large-surface cooling contacts for the sensor sandwich and the hybrids. Heat generated by the MPAs and the PSs sensor is conducted to the PSp sensor through the bump bond connections and the sensor spacers. Thus, all heat has to be removed via the PSp sensor, whose backside is directly glued onto the baseplate with a thin polyimide foil in between for electrical isolation. In the tracker, the PS module baseplate will be glued onto supporting structures with embedded cooling pipes, ensuring sufficient heat dissipation. [CMS17d] [Zog+22]
Sensor efficiency studies presented in this thesis (see Chapter 7) were performed with single MaPSAs consisting of one MPA and a matching miniature PSp sensor. Thus, the size of a single MaPSA equals the size of one sixteenth of the full-size MaPSA, indicated by the red frame in Figure 3.7a.

3.4.2. The Macro Pixel ASIC (MPA)

The *Macro Pixel ASIC* (MPA) is briefly introduced in the following based on the MPA manual [CER17a], where a more detailed description can be found.
The MPA block diagram is shown in Figure 3.8. One MPA handles the readout of a pixel matrix consisting of 16 rows with 118 pixels each. Charge signals coming from the sensor pixels are first processed by the analog frontends, which are based on a preamplifier-shaper stage and a subsequent comparator stage. In contrast to the Outer Tracker strip sensors, the PSp sensor is DC coupled and the MPA frontends, therefore, feature leakage current compensation circuits for pixel currents up to 200 nA. The comparator threshold, given in steps of the least significant bit (LSB), is applied via a differential voltage offset that can be set by an internal 8-bit threshold DAC (thDAC). In order to achieve uniform response throughout the whole pixel matrix, each frontend channel has an additional 5-bit trimDAC to apply individual threshold voltage offsets that compensate for fabrication variations. For testing and calibration purposes charge pulses, initiated by a dedicated calibration circuit, can be injected into the individual pixel frontends.
Like the CBC (see Section 3.3.2), the MPA uses a 320 MHz and a 40 MHz clock domain, indicated the blue and pink color in Figure 3.8. The 320 MHz clock is supplied externally via a SLVS line and is used for fast control, data de/serialization and data transmission, while the 40 MHz domain is mainly used to processes the outputs of the analog frontends. In total, three different MPA readout modes, two synchronous and one asynchronous, are available. Within the synchronous modes, the binary output from the analog frontends is sampled by the 40 MHz clock. The *edge sensitive* mode generates a high signal (1) with a duration of one clock cycle (25 ns) for each pulse coming from the analog frontend. In contrast, the output of the *level sensitive* mode remains high for subsequent clock cycles as long as the analog discriminator

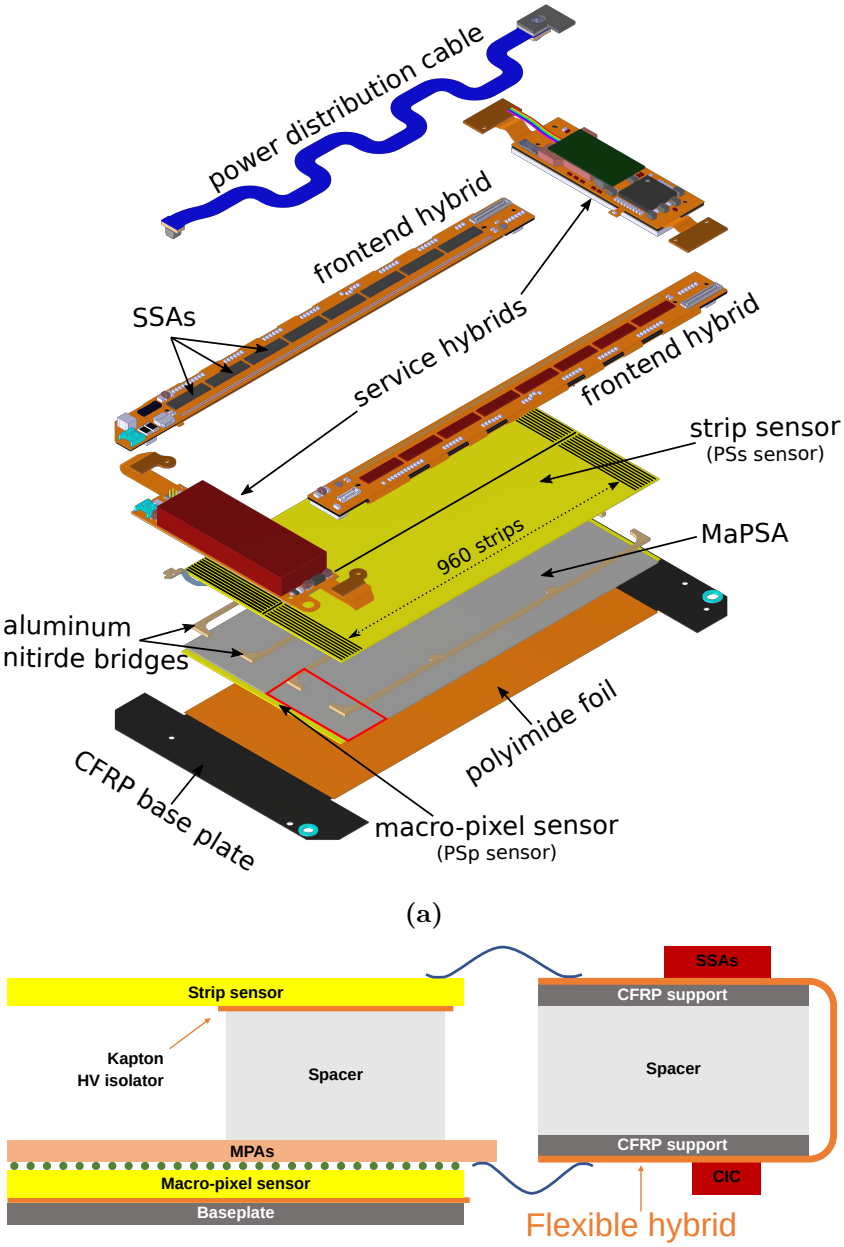

Figure 3.7.: (a): Exploded view of the PS module. The Macro-Pixel Sub-Assembly (MaPSA) comprises 16 MPAs and a macro-pixel sensor, with the MPAs being flip-chipped and bump-bonded onto the sensor. Aluminum nitride bridges connect the MaPSA to the strip sensor forming the sensor sandwich. Two frontend hybrids, each housing eight SSAs and one CIC are wire bonded to the PSs sensor and the MPAs. Additional two service hybrids power the module and transmit the data to the detector backend. The whole module is glued onto a carbon-fiber reinforced polymer (CFRP) baseplate. Modified from [CMS17d]. (b): Concept of the flexible PS frontend hybrids. The hybrids are laminated on CFRP supports (stiffeners) and folded around spacers that match the sensor spacing. With this configuration, wire bonds connecting the PSs sensor strips with the SSA readout chips can be placed the hybrid top while wire bond connections to the MPAs are placed on the backside. [CMS17d]

output stays high. However, the duration of the output pulse within the *level sensitive* mode can be limited to a specific number of clock cycles that is defined by the *HipCut* register. As the name indicates, applying a *HipCut* allows suppressing signals originating from highly ionizing particles (HIPs), which would keep the digital output high for several clock cycles. All beam test measurements presented in Chapter 7 were performed using the *level sensitive* mode. The *asynchronous* readout mode is based on the 15-bit ripple counters of each pixel frontend and is only used for the calibration and testing routines of the MPA. Commands provided via fast control initiate and terminate the data acquisition by opening and closing the internal shutters of each counter. Once activated, the ripple counter simply counts the number of pulses coming from the analog frontend. Data from the individual counters can be read out via I^2C or the stub data path after closing the shutter and triggering the readout.
In contrast, data streams generated within the synchronous readout mode split up into the stub data path and the L1 data path. Within the stub data path the individual pixel hits are combined to clusters and the corresponding cluster center positions are determined. The stub finding logic receives the cluster positions of the pixels, as well as the strip cluster positions provided by the SSAs and searches for combinations fulfilling the correlation criteria explained in Section 3.2.2. Stub information is continuously generated and sent to the Level-1 track finder at the bunch crossing frequency of 40 MHz. In parallel, the L1 data of each pixel row are stored in a 512 clock cycle deep SRAM, corresponding to the 12.8 µs L1 latency. When a positive L1 trigger signal is received within this time frame, the L1 data is passed to the data formatting block where they are further processed for transmission and sent out.

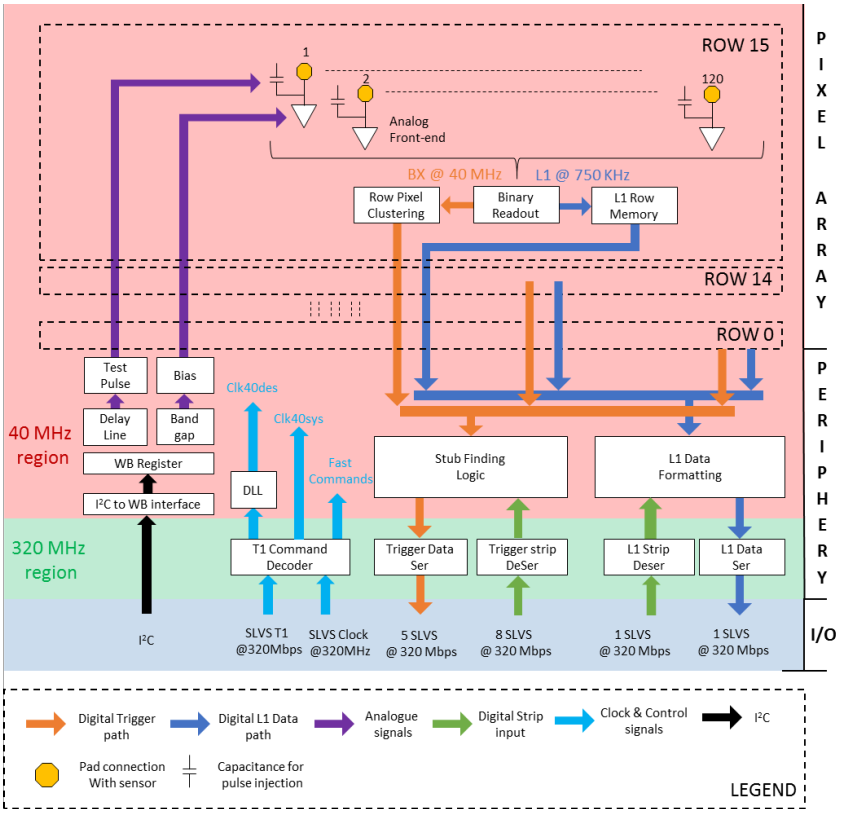

Figure 3.8.: Block diagram showing the MPA architecture. Sensor signals are processed by the analog frontend channels and transformed into binary data. L1 data (blue) containing the full event information are stored in dedicated row memories for a maximum duration of 12.8 µs. In parallel, the hit data are further processed within the stub data path (orange) and combinations of pixel and strip clusters forming valid stub signals are searched by the stub finding logic, whereby the strip data are provided by the SSA. While the stub data is provided at the bunch crossing frequency of 40 MHz to the L1 track finder, L1 data are only sent out after being requested by a positive L1 trigger signal. Figure taken from [CER17a].

4
The Concept of Silicon Sensors

4.1. The Physics of Semiconductors

This section provides a brief overview of the physical principles of semiconductors and how they can be manipulated to make them suitable for detector applications in high energy physics. However, the section is by no means a complete summary. The focus is rather on introducing essential concepts that are important for understanding the structures investigated in the scope of this thesis. Reference for further readings is provided throughout this section.

4.1.1. The Band Model

Individual atoms in solid state materials are arranged in a periodical lattice. The lattice structure can be described by a characteristic unit cell that contains all the information so that any lattice can be built by attaching the corresponding unit cells to each other. Silicon, for example, crystallizes in a diamond structure and its unit cell consists of tetrahedrons with each atom having four equidistant nearest neighbors. The four outer silicon shell electrons form covalent bonds, whereby each electron is shard with one of the adjacent atoms. At low temperatures, all electrons are bound and no free charge carriers are available. Thus, silicon is not conductive, whereas its conductivity improves with increasing temperature as more and more electrons are ionized from the covalent bond by thermal vibrations. Generally, electrical properties of solid states, such as the conductivity, can be described by the band model, which is motivated in the following. A more detailed derivation by solving the Schrödinger equation for electrons that are affected by a periodic potential can be found in the standard literature such as [Hun22] and [Kit04]. For a single atom, the energy levels that are occupied by shell electrons can be derived by following the rules of quantum mechanics. Starting with a configuration of two atoms, the individual energy levels are identical if the distance between the atoms is sufficiently large so that they do not interact with each other. Bringing them closer together, they form a system that must comply with the Pauli exclusion principle. Hence, the individual energy levels split up as it is not allowed to have more than two fermions within the same energy state. Transferring this consideration to a crystal lattice with a huge number of atoms interacting with each other, the individual energy levels smear out and form continuous energy bands. These bands are interrupted by gaps that correspond to forbidden energy states, which cannot be occupied.
At a given temperature T and in thermal equilibrium, the Fermi-Dirac distribution describes the probability that a state with the energy E is occupied by an electron

$$F(E) = \frac{1}{1 + \exp\left(\frac{E - E_\mathrm{F}}{k_\mathrm{B} T}\right)} \ . \tag{4.1}$$

In the above equation k_B denotes the Boltzmann constant and E_F represents the Fermi level that describes the energy at which the probability of electron occupation is exactly one-half.
As shown in Figure 4.1, materials can be divided into three different groups based on the energy gap width: conductors, insulators and semiconductors. Here, the term valence band refers to

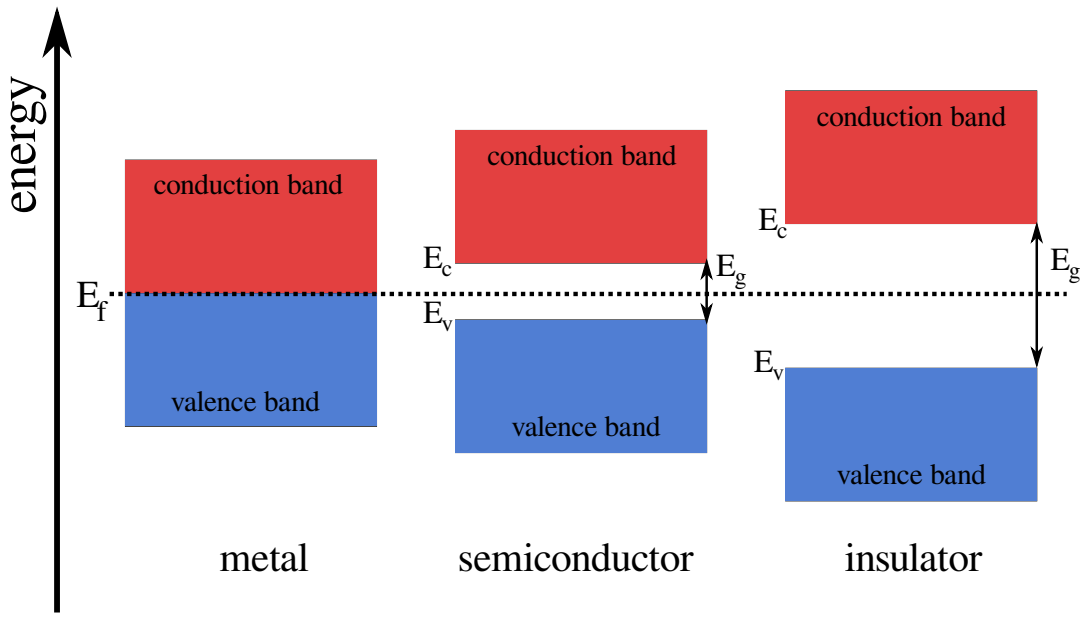

Figure 4.1.: Illustration of the energy band model for different materials.

the energy band that is fully filled with electrons up to the energy level E_v at a temperature of absolute zero. In contrast, the conduction band is completely empty, and its lowest energy level is given by E_c. Thus, the energy gap E_g is defined by the difference of E_c and E_v and corresponds to the energy that is needed to lift an electron from the valence into the conduction band. For any material, electrical conduction is only possible if bands are partly filled, whereas completely filled or empty bands do not contribute to the conductivity as electrons cannot become mobile. Regarding conductors, the valence and conduction band are either overlapping (e.g. Pb) with no band gap in between, or the conduction band is partly filled (e.g. Cu), resulting in good conductivity as there are many unoccupied states that can be easily occupied with little energy effort. Insulators on the other hand exhibit band gaps that cannot be overcome by thermal excitation and the valence band, therefore, remains empty. In contrast, the band gap of semiconductors is in the order of 1 eV to 4 eV and electrons can be lifted into the conduction band via thermal excitation, leaving an electron deficiency in the valence band behind. This is indicated on the left-hand side of Figure 4.2. The electron deficiency position is not fixed as it can be filled by a neighboring electron, which in turn creates a deficiency at the former electron position. In the following, the electron deficiencies are called holes. In general, holes carry an effective positive charge and move in the opposite direction to the electrons. Thus, regarding the semiconductor, electrons lifted to the conduction band, but also the remaining holes in the valence band contribute to the overall conductivity.

4.1.2. Doping

Semiconductors in their intrinsic form are neither suitable for applications in the electronics sector nor for the construction of charge sensitive detectors in the field of high energy physics. However, the electrical properties of the intrinsic material can be manipulated by deliberately introducing foreign atoms into the silicon lattice. This process is called doping and is explained in the following based on the example of silicon.
As described above, silicon as an element of the fourth main group of the periodic table has four valence electrons, where each of them forms a covalent bond with the electrons of the neighboring atoms, so that no unbound electrons remain. This configuration changes if silicon

atoms are replaced by elements of the fifth main group, e.g. phosphorus. Only four valence electrons can form covalent bonds while the fifth remains unbound and can move almost freely through the lattice. Since additional electrons are added as majority charge carriers, the process is called n-doping, resulting in n-type silicon. In contrast, p-type silicon is obtained by replacing silicon atoms with elements of the third main group, e.g. boron. This process is called p-doping accordingly due to the excess of holes that represent the majority charge carriers in p-type silicon. As only three electrons can contribute to the covalent bonds, a hole remains that can be filled by electrons of neighboring atoms. In the picture of the band model, the doping process introduces new energy levels within the band gap, as it is shown Figure 4.2. Donor states located close to the conduction band originate from the nearly unbound electrons, introduced by n-doping. These electrons can be lifted into the conduction band with little energy effort, e.g. thermal excitation. In contrast, acceptor states located just above the valence band are introduced by p-doping and correspond to holes that can be easily filled with electrons from the valence band. As a consequence of the additional states, the Fermi level shifts towards the conduction band for n-doped silicon, whereas for p-type silicon it moves towards the valence band. In both cases the actual shift depends on the doping concentration. Independent on the doping type, the introduced energy levels improve the silicon conductivity σ as they can be easily ionized at room temperature. [Hun22] [SL12]
The semiconductor resistivity ρ is inversely proportional to the conductivity and can be described as

$$\rho = \frac{1}{\sigma} = \frac{1}{e(\mu_\mathrm{e} n + \mu_\mathrm{p} p)} \ , \tag{4.2}$$

with e being the electron charge, μ_e and μ_h the electron and hole mobility (see Section 4.1.3) and n and p the density of electrons and holes in the material. If one type of impurities dominates in the material, e.g. acceptors in p-doped silicon, for which the acceptor dopant density N_A is significantly larger than the intrinsic carrier concentration, Equation (4.2) simplifies to

$$\rho = \frac{1}{\sigma} = \frac{1}{e(\mu_\mathrm{p} N_\mathrm{A})} \ . \tag{4.3}$$

For intrinsic silicon the resistivity at room temperature is in the order of 235 kΩ cm, while for doped silicon as it is used in the detectors of high energy physics experiments, typical resistivities are in the range of 2 kΩ cm and 10 kΩ cm. [Har17]

4.1.3. Charge Carrier Transport

For semiconductors in the equilibrium state, the mean charge carrier velocity is about $10^7\,\mathrm{cm\,s^{-1}}$ at room temperature. However, the movement is continuously interrupted by scattering processes with lattice vibrations and imperfections, resulting in an average free path of roughly 10^{-5} cm and a mean free time of $\tau_c \approx 10^{-12}$ s. On average, the carrier displacement is zero since the motion is random and there is no preferred direction. The situation changes if the equilibrium is disturbed by an external voltage that initiates *drift* processes.
Charge carriers are accelerated in a defined direction in between the individual collisions as a consequence of the electric field. The resulting average drift velocity is proportional to the electric field $\vec{E}$ and is given by

$$\vec{v_\mathrm{n}} = -\frac{e\tau_\mathrm{c}}{m_\mathrm{n}}\vec{E} = -\mu_\mathrm{n}\vec{E} \quad \text{and} \quad \vec{v_\mathrm{p}} = \frac{e\tau_\mathrm{c}}{m_\mathrm{p}}\vec{E} = \mu_\mathrm{p}\vec{E} \ , \tag{4.4}$$

where $m_\mathrm{n/p}$ denote the effective charge carrier mass of electrons and holes and $\mu_\mathrm{n/p}$ represent the corresponding charge carrier mobilities. In general, the mobilities depend on the temperature

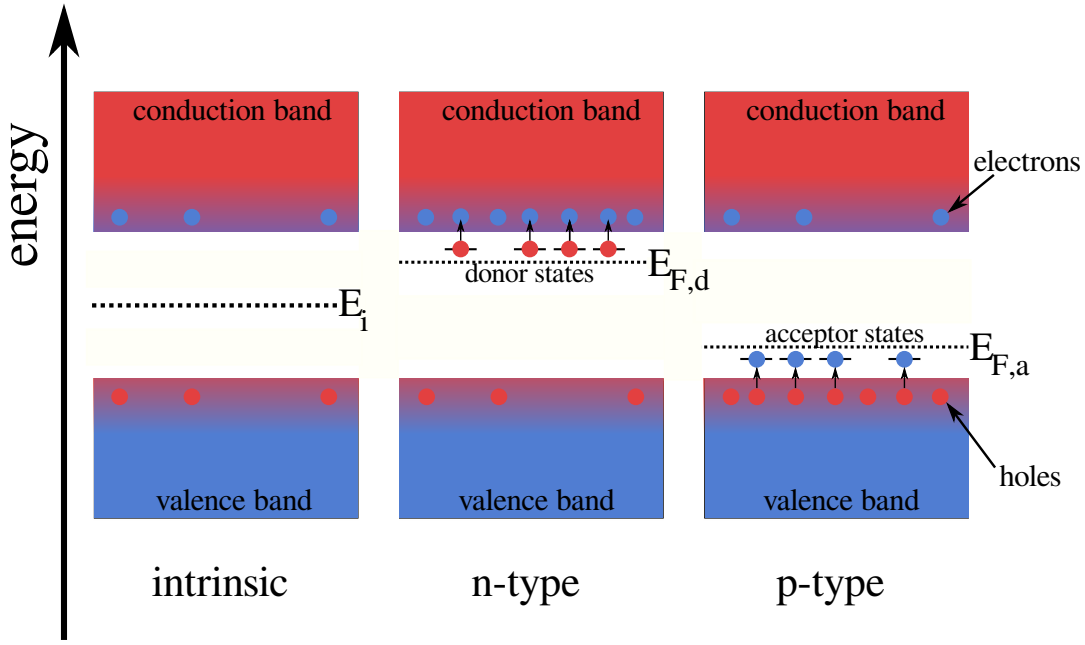

Figure 4.2.: Band model representation for an intrinsic semiconductor, compared to the n- and p-doped configuration. Additional donor states are introduced underneath the conduction band by n-doping, while p-doping introduces acceptor states just above the valence band. As a consequence of the additional energy states introduced by the dopant atoms, the Fermi level shifts accordingly. Illustration following [Hin17].

as well as the doping and defect concentration in the material. However, the above relation is only valid for velocity changes which are small compared to the thermal velocity. At high fields charge carriers start to interact with the lattice via phonon emission, which becomes the dominant process, resulting in velocity saturation. [Lut07] [Spi06]

In case the equilibrium state is disturbed by inhomogeneous charge carrier concentrations within the semiconductor, *diffusion* processes take place to compensate for the inhomogeneity. Statistically, it is more likely that on average more charge carriers from regions with high densities move to the lower density region, although the individual movement is random. Thus, the inhomogeneous charge carrier distribution is smoothed out. The diffusion process can be described by

$$\vec{F_{\mathrm{n}}} = -D_{\mathrm{n}}\vec{\nabla}_{\mathrm{n}} \text{ and } \vec{F_{\mathrm{p}}} = -D_{\mathrm{p}}\vec{\nabla}_{\mathrm{p}} \ , \tag{4.5}$$

where $\vec{F}_{\mathrm{n/p}}$ represents the flux of electrons/holes with the diffusion constants $D_{\mathrm{n/p}}$ and the carrier concentration gradients $\vec{\nabla}_{\mathrm{n/p}}$.

The total current densities are obtained by summing up the contributions of the drift and diffusion processes, which might take place at the same time.

$$\vec{I_{\mathrm{n}}} = e\mu_{\mathrm{n}} n\vec{E} + D_{\mathrm{n}}\vec{\nabla}_{\mathrm{n}} \text{ and } \vec{I_{\mathrm{p}}} = e\mu_{\mathrm{p}} p\vec{E} - D_{\mathrm{p}}\vec{\nabla}_{\mathrm{p}} \tag{4.6}$$

In thermal equilibrium, the current densities have to be zero at any point, leading to the Einstein equations

$$D_\mathrm{n} = \frac{kT}{e}\mu_\mathrm{n} \text{ and } D_\mathrm{p} = \frac{kT}{e}\mu_\mathrm{p} \,, \tag{4.7}$$

which directly link the carrier diffusion to the corresponding carrier mobility. [Lut07]

4.1.4. The pn-Junction

The simplest electronic component that can be made from differently doped silicon is the pn-junction or diode, shown in Figure 4.3. It consists of a p- and an n-doped part, which are directly connected to each other. The Fermi levels of the individual parts are affected by the doping and do differ from each other as shown in Figure 4.2. However, regarding a pn-junction in thermal equilibrium the Fermi levels of both regions must be equal, resulting in bent energy bands across the junction. The equalization is established by charge carrier diffusion (see Equation (4.5)) between the differently doped regions. Electrons diffuse from the n-part into the p-part, while the holes diffuse in the opposite direction. Consequently, the electrons and holes recombine in the junction region and a fixed charge density arises that is caused by the remaining ionized dopant atoms. The resulting electric field initiates charge carrier drift processes (see Equation (4.4)) that counteract the diffusion and a state of equilibrium is reached with an intrinsic space charge region that is free of mobile charge carriers. Mathematically, the system can be described by solving the Poisson equation under consideration of the present charge densities. In the following, only parameters relevant for the understanding of the pn-junction and position sensitive sensors (see Section 4.3) are summarized. A detailed derivation can be found in [Har17] or [Spi06]. It can be shown that at a fixed temperature T the potential difference in the space charge region, which is described by the built-in voltage V_bi, only depends on silicon properties

$$V_\mathrm{bi} = \frac{k_B T}{e} \ln\left(\frac{N_A \cdot N_D}{n_i^2}\right) \,, \tag{4.8}$$

where k_B denotes the Boltzmann constant, e the elementary charge, N_A (N_D) the acceptor (donor) density and n_i the intrinsic density[1]. As shown in Figure 4.3 the built-in voltage defines the deformation of the energy band in the transition region. Doping concentrations of the structures investigated in this thesis can be approximated with $N_A \approx 5 \cdot 10^{12}\,\mathrm{cm}^{-3}$, and $N_D \approx 1 \cdot 10^{19}\,\mathrm{cm}^{-3}$, V_bi for the bulk and the implants, respectively [Mül21]. This yields a built-in voltage of about 0.7 V. The width of the space charge w is directly correlated with the built-in voltage and is constant, if no external voltage V_ext is applied.

$$w = \sqrt{\frac{2\epsilon_s}{e}\left(\frac{1}{N_A} + \frac{1}{N_D}\right)(V_\mathrm{bi} + V_\mathrm{ext})} \xrightarrow[\text{p-type structures}]{N_A << N_D} w \approx \sqrt{\frac{2\epsilon_s}{e|N_\mathrm{eff}|}(V_\mathrm{bi} + V_\mathrm{ext})} \tag{4.9}$$

Here, ϵ_s indicates the product of the vacuum permittivity ϵ_0 and the dielectric constant of silicon ϵ_{Si}. As mentioned above, the donor and acceptor concentrations of the structures investigated in this thesis differ by several orders of magnitude. Hence, only the acceptor doping concentration $N_A \approx |N_\mathrm{eff}|$ of the lower doped part is relevant and has to be taken into account for further considerations.
Equation (4.9) indicates that the width of the space charge can be manipulated by applying an external voltage V_ext across the junction. Depending on the voltage polarity, the width is

[1] n_i =1.45 $\cdot 10^{10}\,\mathrm{cm}^{-3}$ at 27 °C

either enlarged or reduced. Applying positive potential to the n-doped part while setting the p-doped part to negative potential increases the width. If the applied voltage is sufficiently high, the space charge region grows to the size of the diode so that the complete volume is free of mobile charge carriers. This operation mode is called reverse bias mode and is the standard mode to operate semiconductor-based particle detectors.
Since the space charge region is free of charge carriers, it forms a capacitor that is surrounded by the conducting n- and p-doped silicon part. Thus, the diode capacitance depends on the width of the depletion region

$$C = \epsilon_{\mathrm{s}} \frac{A}{w} = A \sqrt{\frac{\epsilon_s e |N_{\mathrm{eff}}|}{2(V_{\mathrm{bi}} + V_{\mathrm{ext}})}} \ , \tag{4.10}$$

with A describing the diode area. The voltage at which the space charge region reaches its maximum size is called *full depletion voltage* V_{FD} and is given by the voltage above which the diode capacitance stays constant.

$$\frac{C_{\mathrm{diode}}}{A} = \begin{cases} \sqrt{\dfrac{\epsilon_{\mathrm{s}} e |N_{\mathrm{eff}}|}{2(V_{\mathrm{bi}} + V_{\mathrm{ext}})}} & , V_{\mathrm{ext}} \leq V_{\mathrm{FD}} \\ \dfrac{\epsilon_0 \epsilon_{\mathrm{Si}}}{D} = \mathrm{const.} & , V_{\mathrm{ext}} > V_{\mathrm{FD}} \end{cases} \tag{4.11}$$

As can be seen by rearranging Equation (4.9), the depletion voltage only depends on the diode thickness D and the effective doping concentration N_{eff}

$$V_{\mathrm{FD}} = \frac{e |N_{\mathrm{eff}}| D^2}{\epsilon_{\mathrm{si}}} \ . \tag{4.12}$$

Thus, according to equation Equation (4.3), the depletion voltage is inversely proportional to the resistivity ρ of the material.

In order to describe the current flow through the diode, two contributions must be considered: currents originating from diffusion processes, as well as generation currents. The diffusion current is given by the Shockley equation

$$I_{\mathrm{diff}} = I_0 \cdot \left(e^{\frac{eV_{\mathrm{ext}}}{k_B T}} - 1 \right) = e \left(\frac{n_{p0} D_n}{L_n} + \frac{p_{n0} D_p}{L_p} \right) \cdot \left(e^{\frac{eV_{\mathrm{ext}}}{k_B T}} - 1 \right) \ , \tag{4.13}$$

with n_{p0} (p_{n0}) describing the electron (hole) density in the p-side (n-side), the diffusion coefficients $D_{n/p}$ (see Equation (4.7)) and $L_{p/n}$ representing the diffusion length of holes and electrons. When the diode is operated in forward direction ($V_{\mathrm{ext}} > 0$), the current increases exponentially, whereas in reverse bias mode ($V_{\mathrm{ext}} < 0$) it saturates at I_0.
The second contribution, the generation current, mainly manifests for diodes operated in reverse mode and originates from charge carrier emission through generation-recombination centers located inside the band gap. These centers are either introduced by impurities or irradiation (see Section 4.5.3). Since the generation current originates from the depleted area it scales with the applied reverse bias voltage and saturates if the structure is fully depleted

$$I_{\mathrm{gen}} \propto -\sqrt{|V_{\mathrm{ext}}|} \ \text{ for } \ V_{\mathrm{ext}} < V_{\mathrm{dep}} \ . \tag{4.14}$$

However, current saturation after reaching the depletion voltage is only an idealized assumption, since for real diodes and sensors the leakage current is also affected by additional impurity related states in the band gap, defects induced by the processing, as well as interface states at the Si-SiO_2 (Section 4.3). [Mol99]

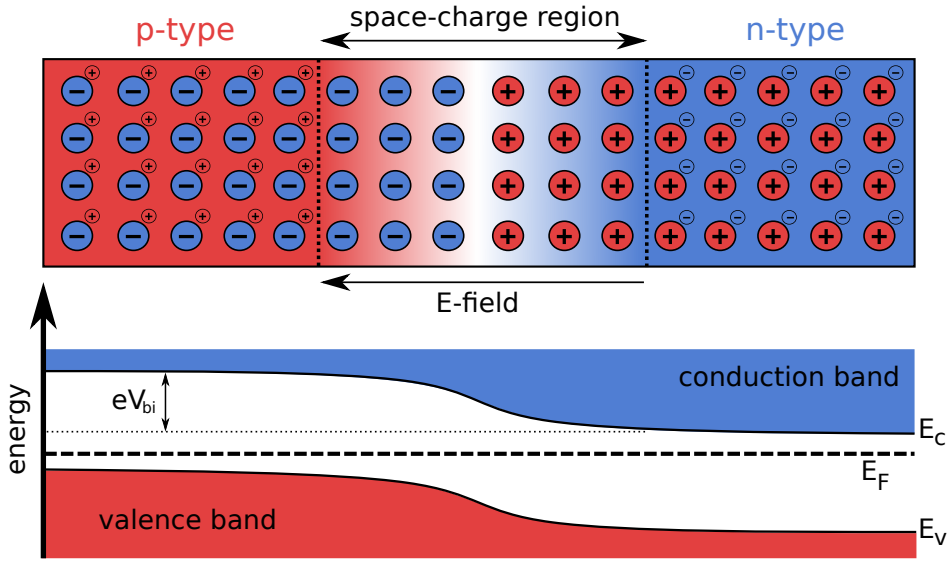

Figure 4.3.: Schematic view of a pn-junction in equilibrium. Electrons and holes recombine in the junction area due to diffusion processes caused by the different charge carrier concentrations in the p- and n-doped part. The emerging electric field originates from ionized dopant atoms and stops the diffusion processes. In the equilibrium state, a space charge region free of mobile charge carriers is established. Energy bands in the junction region are bent to achieve a constant Fermi level. Illustration following [Hin17].

As shown in [Chi13], the temperature dependence of the diode current in reverse bias mode is given by

$$I(T) \propto T^2 \exp\left(\frac{-1.21\text{eV}}{2k_B T}\right) . \tag{4.15}$$

The relation also holds for sensors, and operating them at low temperatures is a common procedure to reduce the leakage current, especially after irradiation.
If voltages far above the depletion voltage are applied, the diode shows a drastic current increase, called *breakdown*. Two different mechanisms have to be distinguished. Firstly, electrons can be lifted to the conduction band by the strong electric field (Zener breakdown). Secondly, charge carriers generated in the semiconductor in the presence of a strong electric field may gain sufficient energy in between collisions to create an additional electron hole pair. The initial charge carrier together with the additionally created charge carriers are accelerated again dissolving further charge carriers resulting in an avalanche breakdown. [Lut07]

4.2. Particle Interaction with Matter

The interaction of particles with matter strongly depends on the particle type and energy but also on the absorber medium. Designing detector devices, such as silicon sensors for position sensitive particle detection, requires a good understanding of the underlying processes to ensure an efficient performance. This section briefly discusses the interaction of heavy charged particles as well as electrons and positrons with matter. A much more detailed description of this topic can be found in [Par20].

The Bethe formula shown in Equation (4.16) describes the average energy loss per unit length (stopping power) for heavy charged particles in matter. Particle interactions are mainly based on coulomb scattering with shell electrons of the material atoms. Several parameters regarding the particle properties and the target material have to be taken into account.

$$-\left\langle \frac{dE}{dx} \right\rangle = 4\pi N_A r_e^2 m_e c^2 z^2 \frac{Z}{A} \frac{1}{\beta^2} \left[\frac{1}{2} \ln \left(\frac{2 m_e c^2 \beta^2 \gamma^2 T_{\max}}{I^2} \right) - \beta^2 - \frac{\delta(\gamma)}{2} \right] \tag{4.16}$$

$\mathbf{N_A}$	Avogadro constant
$\mathbf{r_e}$	classical electron radius
$\mathbf{m_e}$	electron mass
$\mathbf{c}$	speed of light
$\mathbf{z}$	charge of the incident particle (in units of e)
$\mathbf{Z}$	atomic number of the absorber
$\mathbf{A}$	atomic mass of the absorber
$\boldsymbol{\beta}$	ratio of particle velocity to the speed of light
$\boldsymbol{\gamma}$	Lorentz factor
$\mathbf{T}_{\max}$	max. kin. energy that can be transmitted to an electron per collision
$\mathbf{I}$	mean excitation energy
$\boldsymbol{\delta(\gamma)}$	density correction term

As shown in Figure 4.4, using the example of muons in copper, the mass stopping power strongly depends on the particle kinematics. In the range of $0.1 < \beta\gamma < 1000$ the energy loss is described by the Bethe formula with an accuracy of a few percent. At $\beta\gamma \approx 3 - 4$ the ionization related energy loss becomes minimal. Particles in this momentum rage are therefore called *minimum ionizing particles* (MIPs). Low noise levels of the detector systems are required for MIP detection in order to achieve a sufficient signal-to-noise ratio despite their low charge signal. Outside the momentum range described by the Bethe formula radiative losses are dominating at high energies, whereas atomic effects have to be considered in the low momentum regime. [Par20] [Har17]

The Bethe formula does not hold for light charged particles such as electrons or positrons due to their identical properties with respect to the electrons of the target medium. Thus, electron and positron interactions with matter can be described by different, partly overlapping processes, whereas for small and high energies one of these processes is dominating respectively. In the low energy regime ionization is the main energy loss contributor with small additional fractions coming from Bremsstrahlung, Møller ($e^- e^- \rightarrow e^- e^-$) and Bhabha ($e^- e^+ \rightarrow e^- e^+$) scattering. Towards higher energies ionization processes become less important while Bremsstrahlung effects takes over and dominate the high energy regime. [Par20]
In the scope of this thesis a beam of electrons with energies in the order of 5 GeV to 6 GeV has been used to characterize prototype silicon sensors and 2S modules. In [Kop22] it has been shown that at these energies the energy deposition of electrons in the sensor is similar to the energy deposition of minimum ionizing particles with a signal of about 22 ke^- in 290 µm silicon.

The interaction of particles with a finite medium is subject to statistical fluctuations, because the number of collisions as well as the amount of deposited energy varies within the individual scattering processes. Thus, physical models such as the Bethe formula can only give predictions of the average energy loss. The underlying probability distribution describing the energy loss of charged particles in detectors of moderate thickness is given by the Landau distribution [Par20]. Figure 4.5 illustrates distributions of the energy deposition of 500 MeV pions traversing silicon

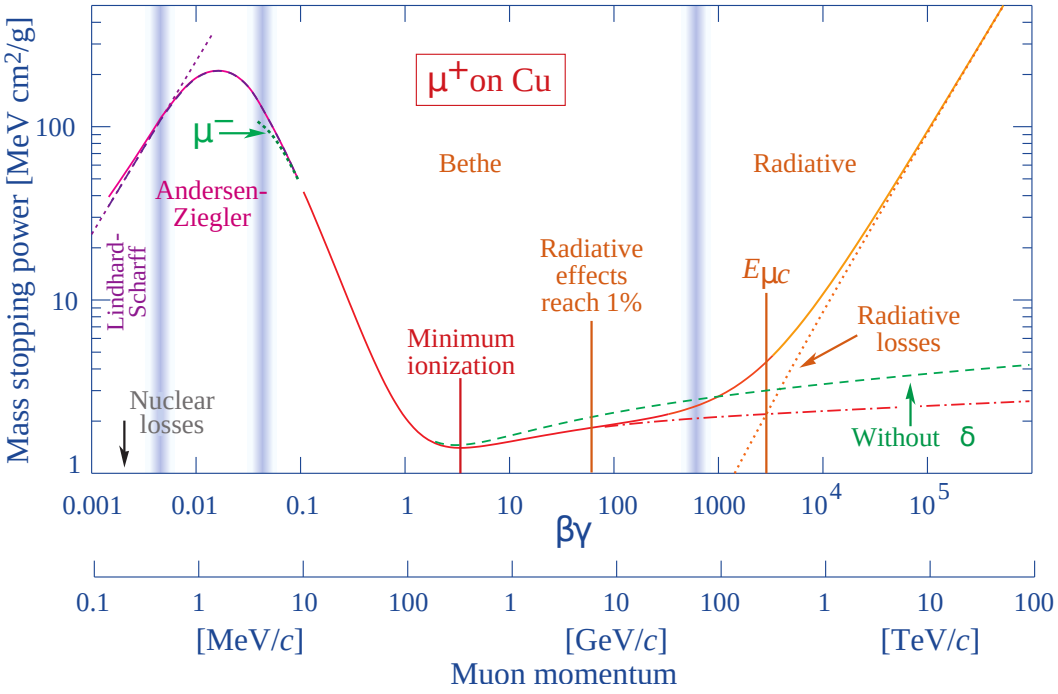

Figure 4.4.: Mass stopping power for positively charged muons in copper. In the range of $0.1 < \beta\gamma < 1000$ the sopping power is described by the Bethe equation with a distinct minimum at $\beta\gamma \approx$ 3 to 4 (minimum ionization). [Par20]

layers of different thicknesses. All distributions show a long asymmetric tail towards high energy losses that originates from rare particle interactions with high energy transfer, creating δ-electrons. As a result, the mean energy deposition is about 40 % larger than the most probable value (MPV). Furthermore, it can be seen that the MPV is shifting towards higher depositions with increasing layer thicknesses, which can be explained with the increasing probability for larger energy losses in thicker layers. Regarding the description of layers comparable to the thickness of typical silicon sensors (300 µm) the Landau distribution is not valid anymore [Par20] as the actual distributions become significantly wider than the Landau width. However, the MPV can still be used as an estimate for the energy deposition.
The most probable number of electron-hole pairs generated by a MIP traversing 300 µm of silicon is 76 μm^{-1}, whereas the average number of 108 e^-/e^+ pairs per µm is much higher [Har17].

4.3. Strip Sensor Design and Working Principle

After discussing the basic properties of silicon, the particle interaction with matter, as well as the working principle of a pn-junction, all fundamentals are in place to introduce the concept of position sensitive silicon sensors. In principle, charged particles can be detected with a simple diode. Assuming an undepleted diode volume of $1 \times 1 \times 0.3\,mm^3$, the number of free change carriers at room temperature is roughly $4.5 \cdot 10^8$, whereas a traversing MIP only creates about $2.3 \cdot 10^4$ electron-hole pairs inside the diode volume [Har17]. Thus, charge sensitive silicon detectors should always be operated in full depletion mode in order to suppress free charge carriers and to be sensitive to charge signals generated by particles. However, the position resolution of the diode is given by its size and further segmentation is needed to improve the resolution. For strip sensors the segmentation is implemented by parallelly arranged highly

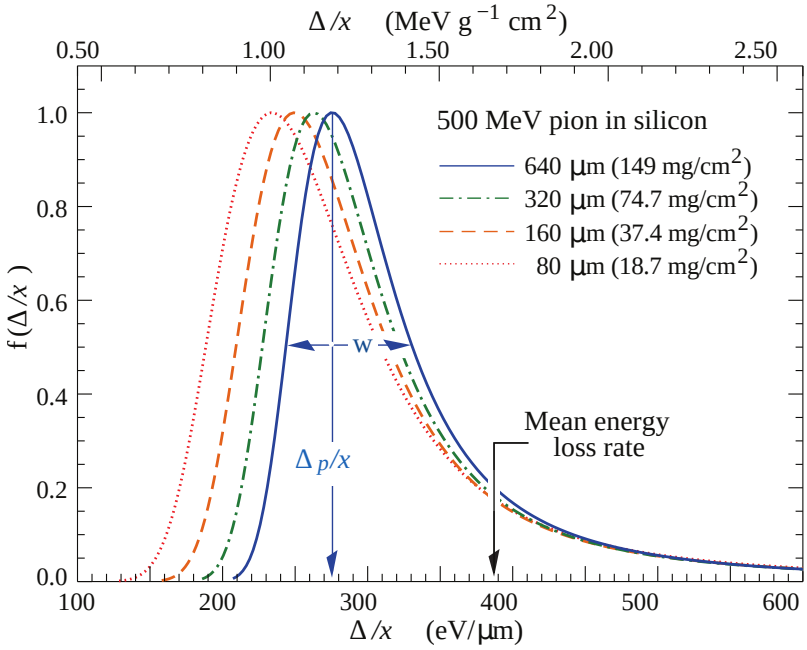

Figure 4.5.: Energy deposition distributions of 500 MeV pions traversing silicon layers with different thicknesses. The most probable value (MPV) is about 30 % smaller than the mean energy loss. [Par20]

n-doped (n^+) strip implants that are embedded in a p-doped bulk, comparable to many parallel pn-junctions. Since the main part of the sensor, the sensor bulk, is p-doped, it is called *p-type* sensor with n^+ implants (n-in-p). Accordingly, sensors with n-doped bulk are called *n-type* sensors with n^+ or p^+ implants (n-in-n or p-in-n). Figure 4.6a shows the cross-section of a fully depleted p-type sensor that is penetrated by an ionizing particle. Electron-hole pairs generated along the particle trajectory are separated by the electric field. Holes are attracted by the sensor backside, whereas electrons drift towards the strip implants. While drifting across the sensor the electrons and holes induce a charge signal (see Section 4.3.1). Since the signal is only induced into the strips located close to the particle interaction point, the particle position can be allocated to these strips. However, the strip length is rather large compared to the strip distance (pitch) and the spatial resolution is therefore mainly limited to one dimension. Pixel sensors on the other hand, feature additional segmentations along the implants, resulting in a 2D spatial resolution. For sensors with binary readout, where the readout electronics only checks if the charge signal exceed a defined threshold (1) or stays below the threshold (0), the resolution can be estimated based on the standard deviation from the true coordinate

$$\sigma^2 = \left\langle \Delta x^2 \right\rangle = \frac{1}{p}\int_{-p/2}^{p/2} x^2 \mathrm{dx} = \frac{p^2}{12} \rightarrow \sigma = \frac{p}{\sqrt{12}} \ , \tag{4.17}$$

with p describing the pitch, which is typically of the order of 100 µm [Lut07]. Nevertheless, the theoretical resolution is improved by charge sharing between neighboring strips.

A fully functional strip sensor requires additional components besides the strip implants and the sensor bulk. Figure 4.6b shows a detailed sketch of a sensor corner, similar to the design of the CMS Phase-2 Outer Tracker strip sensors. As discussed above, the sensor needs to be fully depleted to be sensitive to charge signals generated by traversing particles. Thus, high voltage is applied to the sensor backside while each strip is set to ground potential. To ensure good ohmic

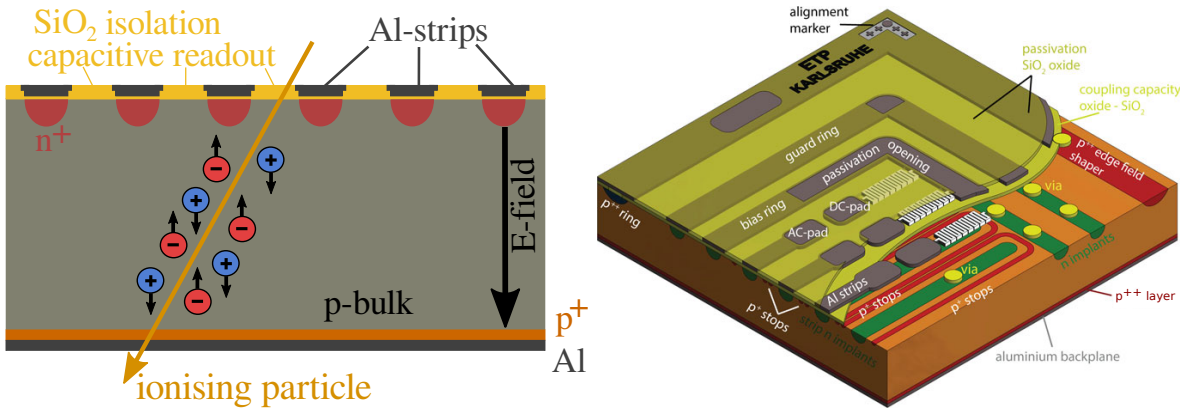

(a) (b)

Figure 4.6.: (a): Ionizing particle traversing a sensor cross-section. Charge carriers generated inside the depleted volume are separated by the electric field. The readout signal is induced by the drifting charge carriers. (b): Corner of a strip sensor with all components. See text for detailed description. Figure (b) reproduced with permission from Springer Nature based on [Har09].

connection between the sensors bulk and the aluminum backside, a highly p-doped (p^{++}) layer is added in between, avoiding a Schottky barrier. The bias potential for the strips is provided by the bias ring, which encloses the active sensor area and is connected with the individual strips via polysilicon resistors. Usually, the resistors are arranged in a meandering shape to achieve a length that correspond to resistances of the order of MΩ. All strip implants are covered by an additional aluminum layer with a layer of coupling oxide in between for the capacitive readout. For each strip, the aluminum layer can be divided into a DC and AC part. The DC part only consists of a small pad (DC-pad) that is directly connected with the strip implant by vias[2] and is only used for the electrical sensor characterization (see Section 5.3.2). In contrast, the AC part extends over the entire strip and is purely capacitively coupled to the strip implant. AC-pads located at the ends of the strips serve as interface area to connect the aluminum strips with the readout electronics via wire bonds. Each strip is additionally surrounded by p-stop implants that isolate the individual strips from each other. Electrons from the bulk that are attracted by the positively charged Si-SiO_2 interface (see Section 4.5.2) are repelled by the negative space charge of the highly p-doped implants, preventing short-circuiting electron accumulation layers between neighboring strips. When cutting the sensor from the wafer, the silicon lattice at the sensor edge is stressed and a large number of defects is introduced. Thus, protective structures are needed to preserve the active sensor area from high leakage currents by avoiding strong electric fields in the edge region. Introducing a broad edge implant with the same doping concentration as the sensor backside (p^{++}) prevents the depletion zone from reaching the highly disordered sensor edge. An additional guard ring surrounds the bias ring, which further compensates for edge effects by shaping the electric field and, thus, ensures a homogeneous potential within the active sensor area, especially for the edge strips. The whole sensor is covered with a silicon oxide passivation layer to protect it from environmental influences. However, to keep structures accessible that are needed for the sensor operation and testing, such as the AC- and DC-pads, the sensor features passivation openings at the corresponding positions. [Har17]

[2]Vertical Interconnect Accesses: commonly used to connect two conductive layers in semiconductor devices separated by an insulating layer

4.3.1. Shockley-Ramo Theorem and Weighting Field

The sensor working principle illustrated in Figure 4.6a might imply that the charge signal seen by the individual strip electrodes is only measurable with the arrival of the charge carriers. However, this is not the case as the signal is induced immediately when charge carriers start to drift in the presence of the electric field. The underlying mechanism is described by the Shockley-Ramo theorem, which states that the current induced in a readout electrode is given by

$$I_{\mathrm{i}} = -q\overrightarrow{E_{\mathrm{w}}} \cdot \vec{v} \ , \tag{4.18}$$

where q denotes the carrier charge, $\vec{v}$ the carrier drift velocity, which in turn depends on the electric field (see Equation (4.4)) and $\overrightarrow{E_{\mathrm{w}}}$ describes the weighting field. $\overrightarrow{E_{\mathrm{w}}}$ is a solely geometry-dependent quantity that defines how a drifting charge carrier couples to the individual electrodes and is derived by solving the Poisson equation for the configuration where the potential of the measurement electrode is set to one while it is set to zero for all other electrodes [Har17]. Signal induction stops when the charge carrier reaches the electrode, provided that it is not trapped by defects beforehand, as it might be the case after irradiation (see Section 4.5.3). Furthermore, it can be seen that the current induced by electrons and holes has the same sign as they drift in opposite directions but are differently charged.
As with any field, there is an associated potential V_{w} that allows to determine the total induced charge

$$Q_{\mathrm{tot}} = \int_{s_1}^{s_2} I_{\mathrm{i}} dt = q \int_{s_1}^{s_2} \mathbf{E}_{\mathrm{w}} d\mathbf{s} = q\left[V_{\mathrm{w}}\right]_{s_1}^{s_2} \ . \tag{4.19}$$

Thus, the total charge signal Q_{tot} is independent of the carrier path and velocity and only depends on the difference of the weighting potential between two given points. [Har17]

4.3.2. Sources of Noise in Silicon Sensors

The origin of noise contributions related to sensor parameters is briefly discussed in the following based on [Har17]. Charged particles traversing the sensor can only be efficiently detected if the charge signal is clearly distinguishable from the omnipresent noise. Thus, the signal-to-noise ratio (SNR) is a crucial parameter to quantify the performance of a detector system. Here, the term noise refers to statistical charge fluctuations and is commonly quantified by the Equivalent Noise Charge (ENC) given in electrons. Four main contributors can be identified, which are assumed to be independent and sum up quadratically

$$ENC = \sqrt{ENC_{I_L}^2 + ENC_{R_P}^2 + ENC_C^2 + ENC_{R_S}^2} \ . \tag{4.20}$$

The individual terms are listed below. Sensor and readout specific quantities are highlighted in bold. Other natural constants contributing to the terms are the electron charge q_e, the Boltzmann constant k_B and the Euler number e.
The shot noise term is driven by the sensor leakage current $\mathbf{I_L}$ and the integration time of the readout electronics $\mathbf{t_i}$

$$ENC_{I_L} = \frac{e}{2}\sqrt{\frac{\mathbf{I_L} \cdot \mathbf{t_i}}{q_e}} \ . \tag{4.21}$$

The parallel thermal noise term is given by

$$ENC_{R_P} = \frac{e}{q_e}\sqrt{\frac{k_B T \cdot \mathbf{t_i}}{2\mathbf{R_p}}} \ , \tag{4.22}$$

where $\mathbf{R_p}$ denotes the parallel resistance (bias resistance) and T corresponds to the operation temperature.
The impact of the sensor load capacitance $\mathbf{C_d}$, which mainly consists of the strip to backplane capacitance and the interstrip capacitance, is given by

$$ENC_C = a + b \cdot \mathbf{C_d} \ , \tag{4.23}$$

with a and b describing pre-amplifier-specific parameters. Another contribution comes from the serial thermal noise

$$ENC_{R_S} = \mathbf{C_d} \cdot \frac{e}{q_e}\sqrt{\frac{k_B T \cdot \mathbf{R_s}}{6\mathbf{t_i}}} \ , \tag{4.24}$$

where $\mathbf{R_s}$ describes the series resistance, given by the strip resistance.
Especially the thermal noise terms, but also the shot noise can be reduced by cooling the detector system, as they directly or indirectly (leakage current) scale with the sensor temperature. For detectors operated at the LHC, the dominating contribution comes from $\mathbf{C_d}$, since the integration time $\mathbf{t_i}$ is relatively small due to the high bunch crossing frequency of 40 MHz.

4.4. Manufacturing Silicon Sensors

The processes used for the fabrication of silicon sensors are based on standard technologies widely established within the semiconductor industry. Nonetheless, the number of companies that are capable of producing high quality sensors in large numbers and at acceptable costs is rather small. A main part of this thesis is dedicated to the quality control of the silicon sensors for the CMS Outer Tracker during the sensor mass production. Having a basic understanding of the sensor manufacturing process helps to better interpret results and observation made in the scope of the quality control measurements. Thus, the main processing steps towards a functional sensor, starting from the bare silicon are briefly described in the following based on [Har17] and [Hil19].

The basic raw material, quartz sand (SiO_2), is available in almost unlimited quantities. However, several processing steps are required to derive silicon of high purity usable for semiconductor fabrication. As initial step, elemental silicon is created by the reduction of SiO_2 with carbon. Thus, the silicon dioxide together with coal is heated up above the silicon melting point (1413 °C), causing the oxygen to split off and form carbon monoxide.

$$SiO_2 + 2\,C \xrightarrow{1650\,°C} Si + 2\,CO \tag{4.25}$$

The *Metallurgical Grade Silicon* (MGS) obtained from this process still contains about 4 % of impurity atoms such as iron, boron and phosphorus. Further purification is achieved by using hydrogen chloride to convert the silicon into trichlorosilane ($SiHCl_3$).

$$Si + 3\,HCl \xrightarrow{300\,°C} SiHCl_3 + H_2 \tag{4.26}$$

Due to its unique boiling point of 31.8 °C, trichlorosilane can be separated from the other impurity chlorine compounds within distillation processes. The *Electronic Grade Silicon* (EGS) with an impurity concentration $< 1/100$ parts per billion is finally obtained in the reverse process of Equation (4.26) and usually comes in the form of poly-crystalline silicon rods.

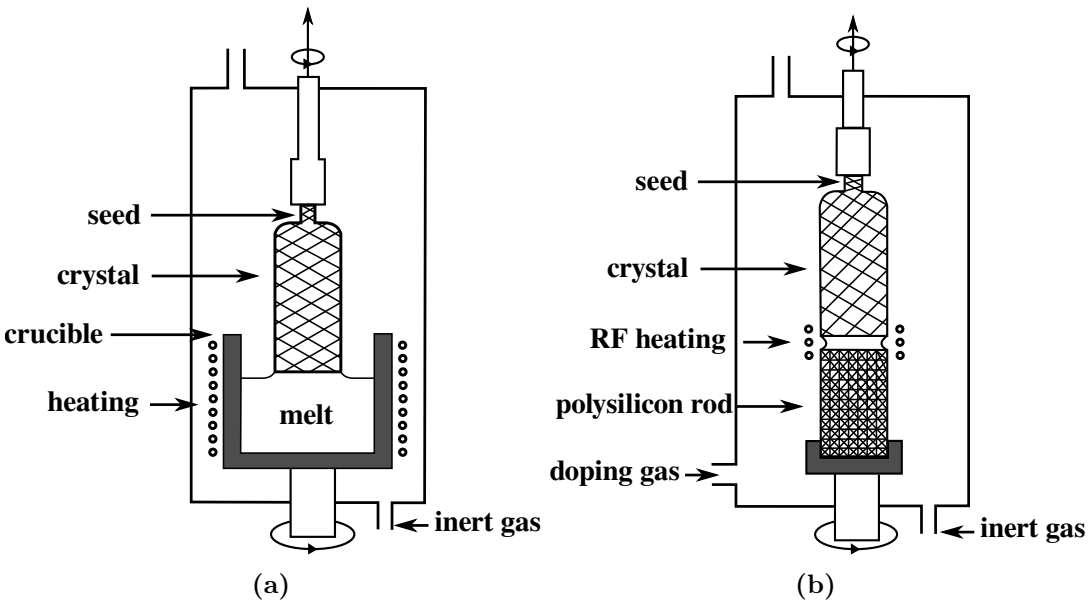

Figure 4.7.: Czochralski method (a): A seed crystal is brought into contact with the silicon melt and is slowly lifted in a rotating fashion, growing a single crystal. Float Zone (FZ) method (b): The radio frequency heater is moved along the poly-crystalline silicon rod and locally melts the silicon. A seed crystal located at the top of the rod initiates the single crystal growth process. Both figures based on [Phi23].

$$\mathrm{SiHCl_3} + \mathrm{H_2} \xrightarrow{1100\,^\circ\mathrm{C}} \mathrm{Si} + 3\,\mathrm{HCl} \tag{4.27}$$

Single crystal ingots are fabricated from the silicon rods. The two most common fabrication procedures are depicted in Figure 4.7.
The *Czochralski* method uses a crucible to melt the silicon rods and to keep the temperature just above the silicon melting point. Additional dopant atoms can be added to the silicon melt depending on the desired ingot type. The growing process is initiated by a small seed crystal that is dipped into the melt and slowly retracted afterwards. Different parameters such as the pull rate, the crystal rotation as well as the melt temperature have to be attuned to each other to ensure perfect single crystal growth. To increase the homogeneity of the dopant atoms within the crystal, the Czochralski method can be improved by performing the growing process in the presence of a magnetic field (*magnetic Czochralski* method). To prevent oxidation of the silicon the whole procedure is performed within an inert gas environment. However, the inert gas contains a fraction of impurity atoms such as oxygen and boron, which are released from the crucible walls and contaminate the silicon, reducing its purity.
The ingots used for the CMS Phase-2 Outer Tracker sensor fabrication are based on the *Float Zone* (FZ) technique. A radio frequency (RF) heater locally melts the polysilicon rod, which is brought into contact with a seed crystal to initiate the single crystal growth. The rod is then slowly moved along the RF heater to grow the single crystal, while the dopant atoms are added via gas diffusion. During the growing process impurities tend to stay within the liquid phase due to their different diffusion coefficients. Again, the main parameters to control the growing process are the temperature of the locally melted area, as well as the movement and rotation speed of the rod.

All structures investigated in this thesis are based on the FZ method. Before cutting the 1 m to 2 m long ingots into wafers, they are brought into a cylindrical shape by grinding. The bare wafers undergo further processing steps such as lapping, etching and polishing before they can be used for sensor production. In order to implement the individual sensor structures, which have been described in Section 4.3, several consecutive photolithography and etching processes are required and are exemplarily introduced in the following based on Figure 4.8. In a first step, the outer layers of the raw silicon wafer are transformed to SiO_2 by exposing them to an oxygen or water atmosphere at temperatures up to 1200 °C. Within the oxygen method (dry process) the oxide layer grows very uniform and has a high purity, whereas the growth rate is relatively slow. In contrast, the oxide layer grows faster with the water method (wet process) while the additional hydrogen atoms can deteriorate the oxide quality. Thus, the dry process is mostly used for the high quality coupling oxide, whereas the wet process is mainly applied to grow thicker field oxide or passivation layers. After growing the oxide layer, the upper side of the wafer is coated with ultraviolet light sensitive photoresist. Highly precise photo masks are used to transfer the strip pattern to the wafer by illumination with ultraviolet light. After developing the photoresist, the wafer undergoes several etching processes in which the pattern given by the mask is etched into the oxide and photoresist residues are removed. The strip implants are introduced by ion implanting where a beam of dopant ions with adjustable energy is shot on the wafer surface. Only the bulk region underneath oxide openings is doped while the remaining bulk is protected by the silicon oxide. In contrast, the wafer backside is usually doped via diffusion from gas, heavily doped amorphous silicon or dopant enriched glasses. Especially after the ion implanting process, high temperature treatments are required to anneal lattice defects introduced by the irradiation (see Section 4.5.4) and to drive the dopants further into the bulk by thermal stimulated diffusion. As a next step high quality coupling oxide is grown during several high temperature treatments within an oxygen atmosphere. Unwanted oxide at the wafer backside is removed within an additional etching process, while the wafer front is protected by a layer of photoresist. The wafer front and back is then metalized by covering it with aluminum using Chemical Vapor Deposition (CVD) or sputtering methods. Since only the strips and ring structures are intended to be covered with the aluminum at the sensor front side, another etching process is needed to remove the aluminum access at the wafer top. However, the steps described above are not quite complete, as further processing steps are required to implement additional structures such as p-stop implants or polysilicon resistors, which in turn require additional masks. Generally, the more different implantations and metal layers that have to be implemented for a sensor, the more steps and masks are needed and the more expensive the manufacturing becomes. More details about the sensor processing, including the processing steps for the p-stop structures and the polysilicon resistors, can be found in [Har17].

4.5. Radiation induced Damage in Silicon

Understanding the effects of radiation induced damage in silicon is crucial in order to develop sensors for detectors with high radiation exposure such as the CMS tracker. Hadron irradiated silicon sensors assembled in prototype modules were tested in the scope of this thesis to study the impact of radiation damage on the sensor performance. A brief overview of different irradiation-related defects and how they affect the electrical properties of the sensors is given in the following to have a qualitative explanation for the observed effects discussed in Chapter 7 and 8.

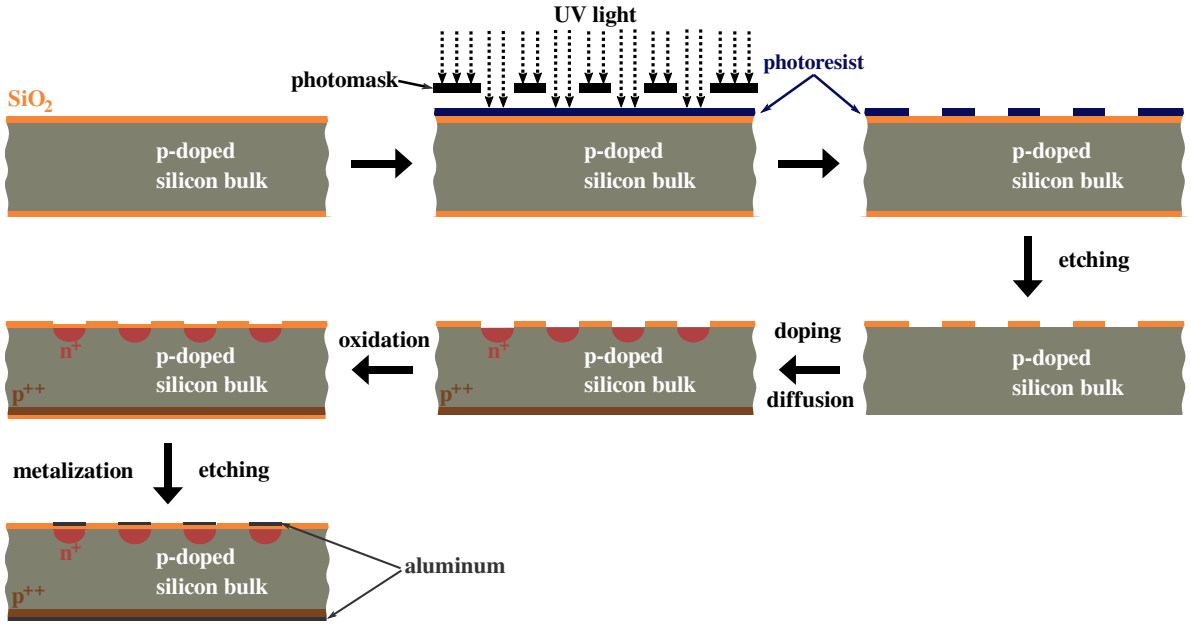

Figure 4.8.: Selected processing steps during the sensor production. See text for more details.

4.5.1. Bulk Damage and NIEL Hypothesis

Bulk damage is created by particles interacting with the silicon atoms, resulting in irregularities in the lattice structure. The type of interaction as well as the impact on the lattice strongly depend on the particle properties. A minimum energy transfer of $E_d \approx 25\,\text{eV}$ is needed to create a lattice defect in silicon by displacing an atom from its initial position. Smaller energy transfers mainly cause lattice vibrations. If the energy transfer is only slightly above E_d, the *Primary Knock on Atom* (PKA) is stopped close to the remaining vacancy forming an interstitial. The combination of a vacancy and a nearby interstitial is called *Frenkel pair*. Higher energy transfer in the order of keV is needed to create a cluster of defects. The initial PKA then further interacts with other lattice atoms initiating a cascade process while moving through the lattice. Cluster defects are mainly caused by neutrons as they are electrically neutral and can only interact via elastic scattering. In contrast, charged particles such as protons or pions, mostly interact via the Coulomb force with a smaller average energy transfer, resulting in short distance defects such as Frenkel pairs. Additionally, the particle energy is a crucial parameter since the ratio of point and cluster defects can change for different energies. Simulations of vacancies crated by protons and neutrons with different energies are shown in Figure 4.9. Vacancies introduced by low energy protons (10 MeV) are homogeneously distributed, while they become clustered and more discrete for higher energetic protons (10 GeV). [Lut07][Har17]

The *Non Ionizing Energy Loss* (NIEL) hypothesis states that the change in the material induced by any displacement damage linearly scales with the amount of energy that is transmitted within the displacing collision [Mol99]. By using the energy dependent displacement damage cross-section $D(E)$, which is a particle specific quantity, the hardness factor κ is introduced. Thus, the NIEL damage caused by any particle type can be scaled to the damage of 1 MeV neutrons (defined as 95 MeV mb), which leads to

$$\kappa = \frac{\int D(E) \cdot \Phi(E)\, dE}{D_\text{n}(1\,\text{MeV}) \cdot \int \Phi(E)\, dE}\,, \tag{4.28}$$

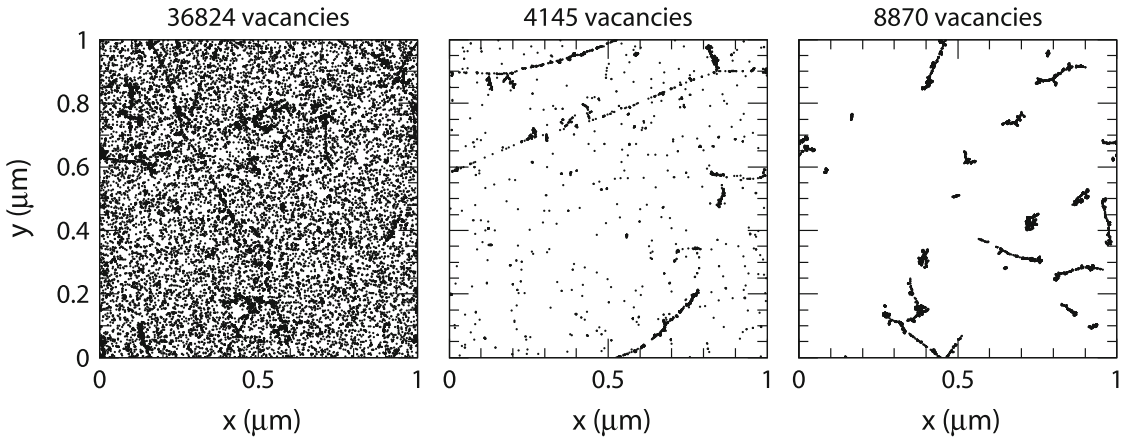

Figure 4.9.: Simulated vacancy distribution after irradiation with proton and neutrons. Each plot shows a projection for 1 µm^3 of silicon irradiated with a neutron equivalent fluence of $1 \cdot 10^{14}\,\mathrm{cm}^{-2}$. From the left to the right: 10 MeV protons, 24 GeV protons and 1 MeV neutrons. [Huh02]

where $\Phi(E)$ refers to the energy dependent particle flux (particles per cm^{-2}) and D_n denotes the displacement damage cross-section of neutrons. The 1 MeV equivalent fluence Φ_eq is therefore given by

$$\Phi_\mathrm{eq} = \kappa\,\Phi = \kappa \int \Phi(E)\,dE\ . \tag{4.29}$$

The hardness factor of the 23 MeV protons used for the irradiation of samples that are investigated within this thesis is $\kappa = 2$. All particle fluences shown in the following are normalized to the 1 MeV neutron equivalent fluence Φ_eq given in units of cm^{-2}.

4.5.2. Surface Damage

Surface damage refers to radiation damage that is generated in the SiO_2 layer as well as the Si-SiO_2 interface. Compared to the nearly perfect lattice structure of the silicon bulk, the SiO_2 lattice is highly irregular. Therefore, radiation damage affecting the lattice can be neglected. More important is the effect of ionizing particles that create electron-hole pairs. The recombination probability strongly depends on the silicon oxide quality and ranges from a few percent up to nearly 100 % [Har17]. However, some electron-hole pairs are separated, where the electron mobility is several orders of magnitude larger compared to the mobility of the holes. While the electrons drift towards the metal electrodes, the holes move in the direction of the Si-SiO_2 interface. On their way through the oxide they can get trapped by already existing defects. Due to the large silicon oxide band gap of 8.8 eV, the emission of captured charge carriers is strongly suppressed. The highest density of trapped holes, however, is located at the Si-SiO_2 interface, since the trap density is significantly increased by the lattice mismatch at the interface. As a consequence of the trapped holes, the oxide is positively charged and attracts electrons from the silicon bulk, resulting in an electron accumulation layer at the oxide interface. This layer negatively affects the resistance of neighboring strips, requiring additional isolating structures such as p-stop implants (see Section 4.3). Additionally, the accumulation layer increases the interstrip capacitance, which in turn affects the noise, as described in Section 4.3.2. [Har17] [Lut07]

4.5.3. Effects of Radiation Damage on the Sensor Properties

Defects introduced into the lattice appear as additional energy levels within the band gap. Depending on their position relative to the valence and conduction band they affect the electrical sensor properties differently by trapping and releasing charge carriers. In general, the trapping-related generation and recombination of electrons and holes in semiconductors is described by Shockley-Read-Hall statistics [SR52]. Figure 4.10 gives an overview of the three most common defects. Their impact on the sensor properties is briefly discussed in the following.

Depletion Voltage: The *effective doping concentration* N_{eff} and, thus, the depletion voltage ($V_{\text{dep}} \propto |N_{\text{eff}}|$) is mainly affected by defects causing "shallow" acceptor and donor levels. Only acceptors near the valence band (called shallow acceptors) and donors close to the conduction band (called shallow donors) are relevant for N_{eff}, as they can be easily ionized at room temperature and contribute to the effective space charge. The amount of donor and acceptor levels introduced by irradiation depends on the irradiated material as well as the particle type. Another aspect regarding the change of N_{eff} is the interaction of radiation induced defects with dopants. They can combine to more complex defects while the dopants become inactivate as space charge contributors. This effect is called donor and acceptor removal. Regarding the sensor performance, an irradiation-related increase of the depletion voltage can, depending on the sensor operation voltage, reduce the depleted sensor volume and, thus, reduce the overall charge signal.

Charge Signal: The charge signal can be further reduced due to charge carriers that get trapped by energy levels located in the mid-gap region. Since the trapping duration is of the order of µs, which is significantly longer than the usual sensor readout time (several ns), they do not contribute to the readout signal. Thus, the *Charge Collection Efficiency* (CCE), given by the ratio of the collected charge compared to the total amount of generated charge, decreases.

Leakage Current: The leakage current is mainly affected by energy levels located close to the center of the band gap. They serve as generation and recombination centers for charge carriers. Thermally exited electrons overcome the band gap more easily as they can be gradually lifted to the mid-gap level and from there to the conduction band. It has been shown in [Mol99] that the radiation induced current increase ΔI per volume V scales linearly with the fluence Φ_{eq}

$$\frac{\Delta I}{V} = \alpha \cdot \Phi_{\text{eq}} \ , \tag{4.30}$$

where α denotes the current related damage rate, which is independent of the sensor material. According to Equation (4.15) the leakage current originating from the sensor bulk is strongly temperature dependent. Cooling the sensors is the common procedure in most detectors to counteract the irradiation-related current increase. By cooling the sensor from 21 °C room temperature to −25 °C, the leakage current is reduced by a factor of about 120.
More details about radiation-induced defects and their impact on the macroscopic sensor parameters can be found in [Jun11] and [Mol99].

4.5.4. Annealing

The defect distribution in the crystal lattice introduced by irradiation is not fixed. Defects have a temperature dependent mobility allowing them to migrate through the lattice and interact with other defects. This process is called *annealing* and can be subdivided into beneficial and reverse annealing. Beneficial annealing refers to processes in which the overall effective number of defects that negatively affect the sensor properties is reduced by recombination. In contrast,

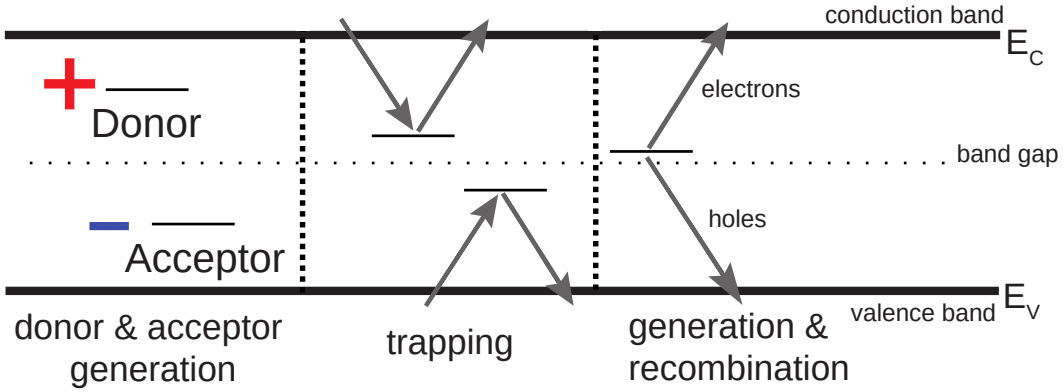

Figure 4.10.: Additional energy levels in the band gap are introduced by irradiation-related lattice defects. Left side: Ionized shallow acceptor and donor levels contribute to the space charge and affect the effective doping concentration N_{eff}. Middle: Charge carriers can get temporarily trapped by defects close to the band gap center and do therefore not contribute to the readout signal. Right side: Defects located at the band gap center serve as charge carrier generation and recombination centers increasing the leakage current. Modified from [Jun11].

reverse annealing attributes processes in which defects are combined and form more stable and complex defects that in turn deteriorate the macroscopic sensor properties. The impact of annealing on global sensor parameters such as the effective doping concentration and the leakage current has been investigated and can be described by the Hamburg Model [Mol99]. Figure 4.11a shows the annealing behavior of the radiation induced change of the effective doping concentration ΔN_{eff}. Following the Hamburg Model, the annealing behavior of N_{eff} is parameterized by three contributions: a stable annealing term, a beneficial annealing term and a reverse annealing term. In Figure 4.11a, these terms are indicated by N_C, N_A and N_γ. The annealing-independent stable part addresses the irradiation-related increase of N_{eff} due to the introduced defects and therefore scales with the fluence. Within the beneficial annealing period, a decrease in N_{eff} is observed due to the healing of defects. However, at some point reverse annealing dominates, leading to a resurgence of N_{eff} with a saturation behavior at long annealing durations. Annealing durations exceeding the beneficial annealing will increase the depletion voltage, which might even overcome the maximum possible sensor operation voltage, resulting in a reduced readout signal. Unwanted annealing can be avoided by storing and operating the sensors at temperatures smaller than 0 °C, where the mobility of defects is significantly reduced.
Figure 4.11b shows the current-related damage rate α in dependence of the annealing time for different temperatures. It can be seen that, in contrast to N_{eff}, annealing has a purely beneficial effect on the leakage current since α continuously decreases. Saturation effects can only be observed at the highest temperatures and long annealing durations. Within the Hamburg Model, the annealing-dependent damage rate is parameterized by an exponential and logarithmic term, indicating towards a combination of different underlying defects with varying decay constants. Moreover, the parameterization allows to translate an arbitrary combination of annealing temperature and duration into a room temperature (21 °C) equivalent annealing, making different annealing procedures comparable. Thus, long term annealing can be emulated by short annealing periods at high temperatures, which is also done within this thesis in order to achieve annealings equivalent to several months at room temperature. [Har17][Mol99]

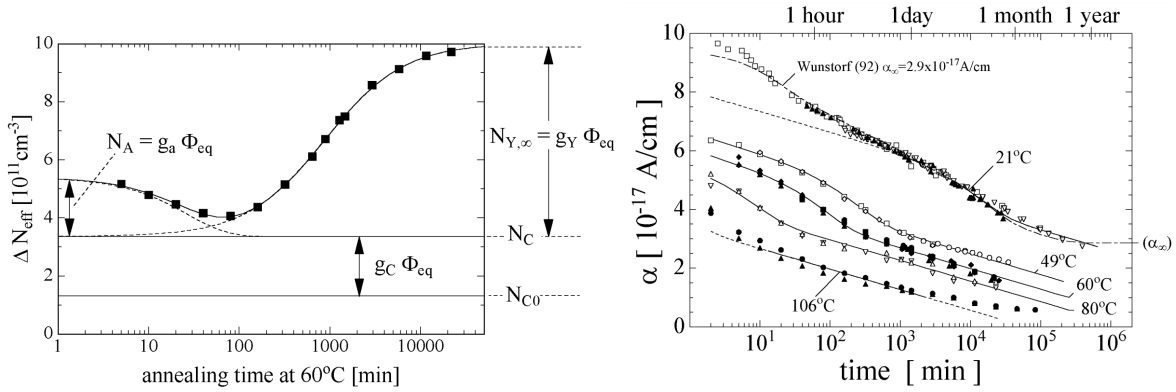

Figure 4.11.: (a): Annealing behavior of N_{eff} measured at 60 °C with a sample irradiated to $1.4 \cdot 10^{13}\,\text{cm}^{-2}$. The radiation-induced change in the effective doping concentration ΔN_{eff} decreases within the beneficial annealing period. Reverse annealing dominates after about 1 h, leading to a significant increase of N_{eff} with a saturating behavior. (b): Current related damage rate α in dependence of the annealing time measured at different temperatures. Both figures are taken from [Mol99].

Part II.

CMS Outer Tracker Sensor Production and Quality Control

5

CMS Outer Tracker Sensor Quality Control

In contrast to the Outer Tracker module production, which will start in 2023, the Outer Tracker sensor production has already started in mid 2020 and is expected to be completed by the end of 2024 with a total production goal of roughly 28 000 sensors. At the end of 2022, about one half of the required number of sensors has already been produced by *Hamamatsu Photonics K. K.* (HPK) and was delivered to CERN. Close monitoring of the sensor quality during the entire production period is essential in order to detect possible deviations from the required quality at an early stage and to take appropriate corrective measures if needed. In order to cope with the large number of sensors there are several institutes within the CMS Outer Tracker community that work together on the overall quality assurance. One main part of this thesis is dedicated to the Sensor Quality Control (SQC) at the *Karlsruhe Institute of Technology* (KIT), which is one of six SQC centers and is strongly involved in the quality assurance during the mass production. This chapter gives an overview of the Outer Tracker sensor production, introduces the quality assurance strategy and summarizes the SQC measurements at KIT.

5.1. The CMS Outer Tracker Sensors

In the past years the CMS Outer Tracker sensor community has conducted various campaigns investigating different sensor materials to find the most suitable material that meets the requirements of the CMS Outer Tracker during the high luminosity LHC phase, especially with regard to radiation hardness. These irradiation and test campaigns showed that float-zone (FZ) silicon (see Section 4.4) with n-doped strip implants in a p-doped sensor bulk is the best choice for the CMS Phase-2 Outer Tracker [Ada+17][Ada+20]. The last decision that had to be made was related to the sensor thickness. There were two options offered by HPK to chose from. A thicker version (FZ290) with an active thickness of 290 µm (physical thickness 320 µm) and a thinned version with a thickness of 240 µm (thFZ240). It has been demonstrated in [Ada+21a] that in principle both sensor versions could be used for the CMS Phase-2 Outer Tracker as none of them shows a significant drawback regarding the charge signal after irradiation. In the end, the CMS Collaboration has chosen the FZ290 sensor material, as the thinned sensors were more prone to mechanical damage on the sensor backside, which is an important aspect during the module assembly. Furthermore, the thFZ240 material would have been more expensive due to the additional processing steps to thin the sensor wafers and the overall benefit of having less material was little.

As already mentioned in Section 3.2.1 two different types of modules will be installed in the CMS Phase-2 Outer Tracker: 2S modules consisting of two strip sensors and PS modules consisting of a strip and a macro-pixel sensor. Following the module names, the strip sensors of the 2S module are called 2S sensors, while the strip and macro-pixel sensors of the PS module are named PSs and PSp sensor respectively, with the last letter indicating the sensor type (strip or pixel). Each of the sensors is processed on an individual 6-inch (150 mm) wafer, as shown in Figure 5.1. In the center of each wafer the main sensors are located. In contrast to the 2S

Table 5.1.: Geometry of the Outer Tracker sensors. The outer sensor dimensions refer to the physical sensor size while the active sensor dimensions are defined by the distances measured from the inner edges of the bias ring metallization. Strip and Pixel dimensions refer to the size of the implant.

Sensor type	Outer dimension (µm)		Active dimension (µm)		Strip/Pixel (µm)		
	width	length	width	length	pitch	width	length
2S	94 183	102 700	91 488	100 703	90	22	50 260
PSs	98 140	49 160	96 055	47 163	100	25	23 479
PSp	98 740	49 160	96 055	47 163	100	25	1 476

wafer, the PSp and PSs wafers house two full-size sensors as these sensors only have about half the size of a 2S sensor. Table 5.1 gives an overview of the exact sensor dimensions. The sensors on each wafer are surrounded by additional test structures and miniature sensors. Most of the test structures are used for the quality control described in Section 5.2 and are separated from the main sensors when the wafer is diced, resulting in so-called *cut-offs* or *half-moons*. The dicing lines on each wafer are indicated by the red lines in Figure 5.1. For the PSs and PSp wafers an additional cutting line through the wafer center is needed to separate the left and right main sensors from each other. The wafer dicing is performed by the vendor HPK and is based on the stealth dicing technology [Mas+07].

5.1.1. Outer Tracker Sensor Designs

The individual sensor and wafer layouts have been implemented by the CMS collaboration under consideration of different requirements regarding the tracking performance, the module designs and assembly techniques as well as optimal coverage of the wafer area. Layouts are passed to HPK for final revision in order to adapt the layouts to the processing at the vendor site. This ensures that the manufactured wafers meet the specifications defined by the CMS collaboration.
Both, the 2S and PSs sensor are AC coupled strip senors and share the same overall design that is shown in Figure 5.2a and Figure 5.2b on the example of a 2S sensor. In Section 4.3 the general design and working principle of AC coupled sensors has already been discussed in detail. Each strip has an AC- and a DC-pad that are located close to the sensor edge making the strips easily accessible during the electrical sensor characterization and to connect the readout electronics to the sensor via wire bonds. Meander-shaped polysilicon resistors connect the individual strips with the bias ring, which is surrounded by the floating guard ring. At the sensor corners and edges various alignment markers as well as strip numbers are processed on the edge ring metallization that define the sensor orientation during the sensor testing and the module assembly. The main difference between the 2S and PSs sensor is the sensor size and consequently the length of the strips. With a strip length of about 2.5 cm the strips of the PSs sensor are half as long as the strips of the 2S sensor. For both sensors the strips are arranged in two parallel rows that are separated at the sensor center, as shown in Figure 5.2b. While the 2S sensor is segmented into 2032 strips with 1016 strips in each row and a pitch of 90 µm, the PSs sensor features a total of 1920 strips distributed among two rows with 960 strips each and 100 µm pitch. Furthermore, all strips feature additional AC- and DC-pads at the sensors middle that are exclusively used for sensor testing, especially during the vendor quality control by HPK (see Section 5.2). Passivation openings are indicated in blue in all figures. More information about the respective sensor geometries can be found in Table 5.1.

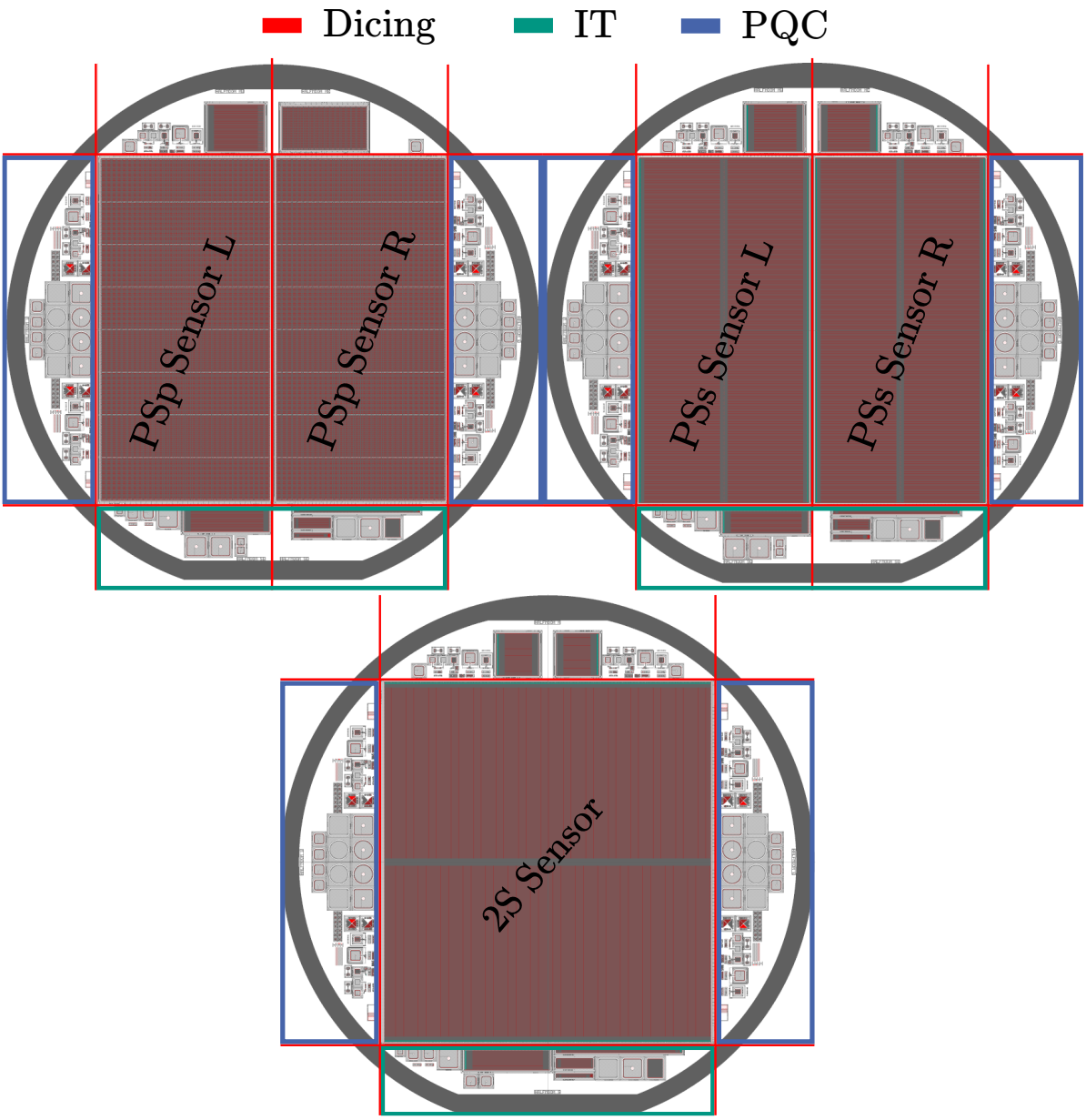

Figure 5.1.: Wafer layouts of the CMS Outer Tracker sensors.

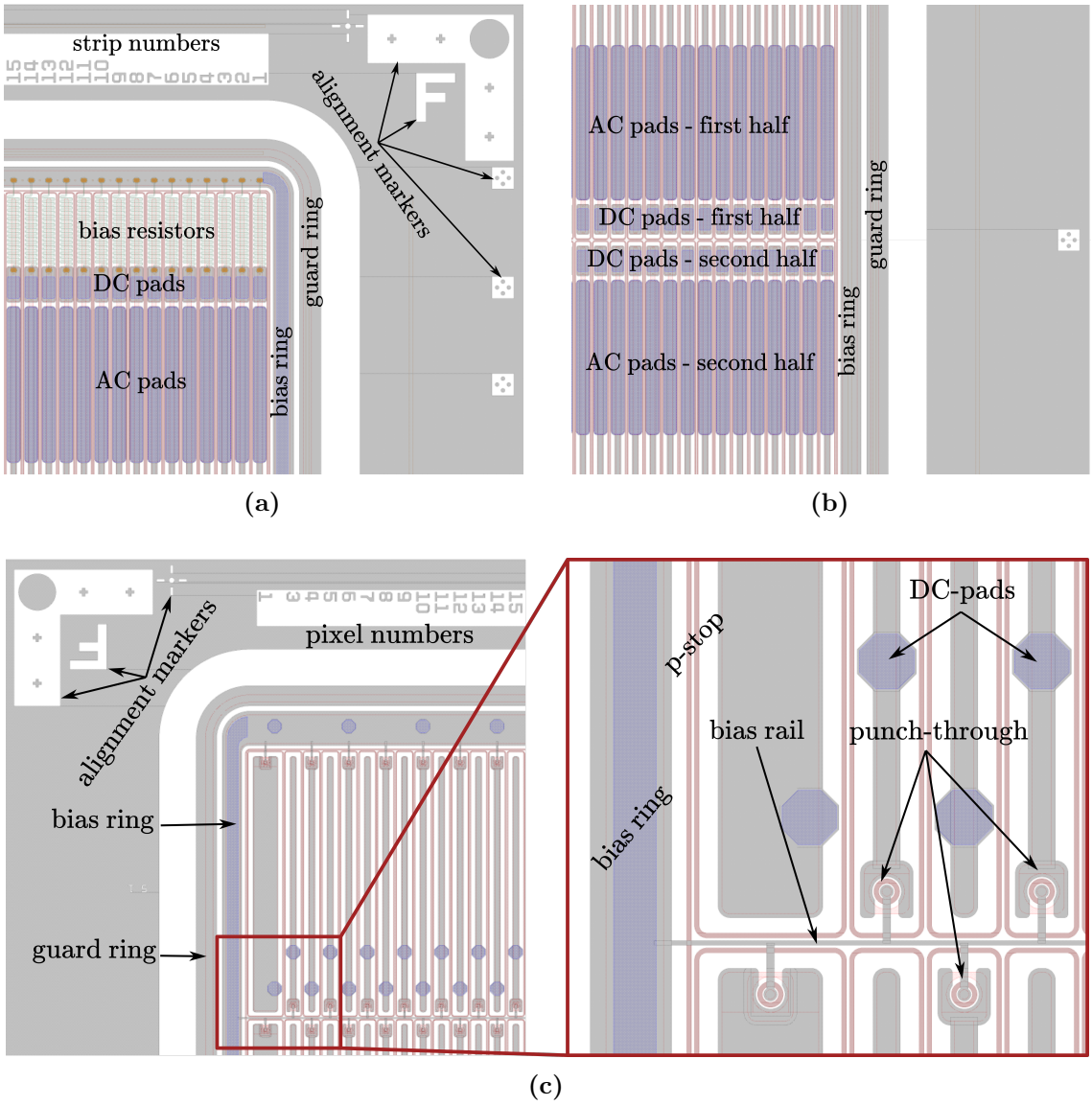

Figure 5.2.: Layouts of the CMS Outer Tracker sensors. The general design of the 2S and PSs strip sensors is shown in (a) and (b) on the example of a 2S sensor. Strips with AC- and DC-pads are implemented on the active sensor area and are connected to the bias ring via bias resistors. The sensors are additionally segmented at the sensor middle resulting in two rows of parallel strips with an extra set of AC- and DC-pads on each strip. The DC coupled PSp sensor is shown in (c). It is segmented into macro-pixels whereby each pixel possesses a DC-pad and is connected to the bias rail via a punch-through structure. Passivation openings in all figures are indicated in blue.

The PSp sensor has nearly the same size as the PSs sensor and is segmented into 30 208 macro-pixels that are arranged in a matrix configuration of 32 rows and 944 columns. The pixels have a length of about 1.5 mm and a pitch of 100 µm. Besides the significantly larger number of readout channels, another difference compared to the strip sensors is that the PSp sensor is DC coupled and, therefore, not processed with a high-quality coupling oxide. Figure 5.2c shows the sensor design with a more detailed view of the pixel configuration on the right-hand side. As with the strip sensors, the corner and edge region of the sensor features different alignment markers and pixel numbering. The active pixel area is surrounded by a bias ring and a floating guard ring. Each pixel has a punch-through structure that connects the pixel to a bias rail, which runs across the sensor, and in turn is connected to the global sensor bias ring. Thus, the bare sensor can be electrically characterized before assembling it with the readout chips (MPAs), allowing to identify non-functional sensors at an early stage. This reduces the number of wasted components, especially in the hypothetical case of a low sensor production yield. After assembly, the sensor is connected to the MPAs, which then provide the ground potential. Punch-through structures still have the functionality to allow large currents to be drained by the bias ring and not through the readout chip. Hexagonal shaped DC-pads implemented on each pixel serve as bump bond pads on the sensor side. Pads of adjacent pixels are slightly shifted with respect to each other to match the pattern provided by the MPA. In total, 16 MPA readout chips are needed to read out a complete PSp sensor. The MPAs are flip-chipped onto the sensor following a pattern of two rows with eight chips each, while one MPA reads out a pixel matrix of 16 times 118 pixels. Sensor pixels at the edge of each MPA chip have twice the size of a normal pixel cell to avoid inefficient sensor areas at the inactive MPA edges. An example of such an edge pixel can be seen in Figure 5.2c next to the bias ring. When the MPAs are flip-chipped onto the sensor small solder bumps are used to connect the sensor pads with the matching pads of the chip. However, in order to achieve a stable connection between the sensor and the bumps, all sensor passivation openings have to be processed with an under-bump metallization (UBM) consisting of electroless nickel immersion gold (ENIG). The UBM acts as bond pad for the bump bonds and allows to establish a reliable mechanical and electrical connection between sensor and chip. Contacting the sensor with probe needles (see Section 5.4.5) for electrical characterization is still possible after the UBM processing, but it can be more difficult to achieve reliable contact. A more detailed overview of the PSp sensor design can be found in [Sch19].

5.2. Sensor Production and Quality Assurance

Before giving an overview of the sensor production progress to date and the general quality assurance strategy during the mass production some general information about the sensor production at HPK is introduced.
During the sensor production all sensors are manufactured batch wise by HPK. The term batch refers to a group of wafers that are processed consecutively under identical conditions and should therefore have similar electrical properties. A batch can contain wafers from different ingots (see Section 4.4), but there should be no more than two different ingots used per batch. Each batch only contains wafers of a specific type (2S, PSs or PSp) and is labeled by a unique five digit batch number. The total number of sensors in each batch should not be smaller than 30 sensors for a 2S batch and 60 sensors for a PSs or PSp batch. After dicing the wafers, the main sensors of each wafer are packaged individually in a dedicated envelope. The remaining half-moons are packed in a separate envelope, so that they can be distributed independently of the sensors in the course of the quality assurance process. All envelopes are labeled with a unique human-readable string and a corresponding barcode that contains all

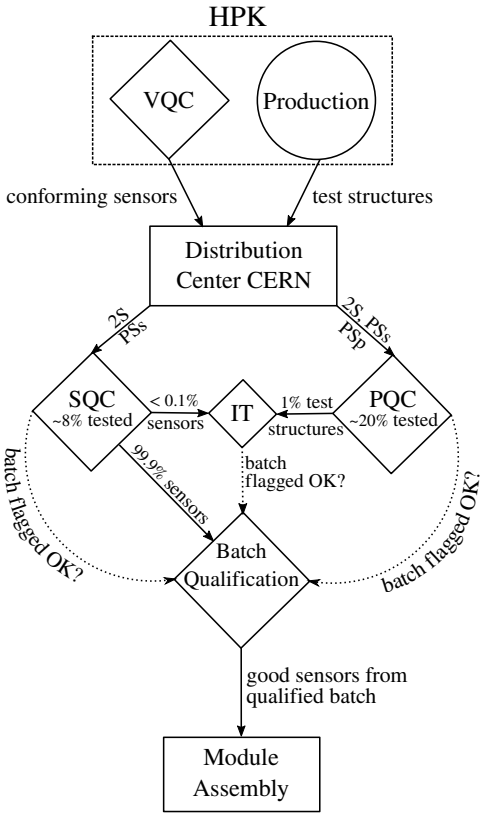

Figure 5.3.: Quality assurance strategy during the CMS Outer Tracker sensor production. Modified from [CMS17d].

relevant information such as the batch and the wafer number as well as the structure type. Thus, the contents of each envelope are clearly defined. Furthermore, the sensors feature scratch mark pads that are used by HPK to assign individual IDs for each sensor to be able to identify the sensor at any time, also without its envelope. Structures are shipped in plastic boxes that are sealed in light tight vacuum bags to protect the structures from environmental influences.

5.2.1. Quality Assurance Strategy

All sensors that will be used for the module assembly and later integration into the tracker must meet a quality standard defined by the CMS Collaboration. Thus, a quality assurance strategy for the Outer Tracker sensor production has been elaborated to closely monitor the sensor quality during mass production and to reliably detect potential quality fluctuations. Figure 5.3 gives an overview of the overall quality assurance concept.

As a first step, all full-size sensors are tested by HPK, which is referred to as the *Vendor Quality Control* (VQC). For each full-size sensor of a batch HPK performs dedicated tests to identify sensors that do not fulfill predefined specifications and to exclude these sensors from the shipment. Besides measuring the global sensor leakage current and the depletion voltage, the individual strips of the 2S and PSs sensors are tested to identify potential strip defects (see Figure 5.7) that are related to the wafer processing. However, for the PSp sensors only the sensor leakage current and the depletion voltage are measured since the electrical characterization of all 30 000 macro-pixels would be too time-consuming. Each sensor passing the VQC comes with a dedicated data file generated by HPK that summarizes the measurement

results and contains general information about the individual sensor such as its scratch pad ID or the number of the ingot from which the sensor wafer has been processed. Conforming sensors together with the corresponding wafer half-moons are shipped to the distribution center CERN. From there, the structures are redistributed among the institutes that participate in the sensor quality assurance, taking into account the expected sensor quantity required for the module assembly in the respective world regions. These institutes have specialized infrastructures and equipment to perform dedicated test on the sensors and test structures in order to evaluate the quality of each batch. In total, there are three different types of quality control procedures that are covered by the institutes: *Sensor Quality Control* (SQC), *Process Quality Control* (PQC) and *Irradiation Tests* (IT). Table 5.2 gives an overview of the institutes involved in the quality control and their specialization. The SQC centers receive all 2S and PSs sensor batches and electrically characterize a fraction of sensors from each batch in order to validate the overall sensor quality and to confirm the results from the VQC. However, the PSp sensors are not tested in the scope of the SQC, as they are directly forwarded to an external company that takes care of the MaPSA assembly by flip-chipping the MPA readout chips onto the sensors (see Section 3.4). A detailed overview of the SQC testing procedure, together with the corresponding specifications is given in Section 5.3.
The wafer half-moons of all batches are distributed among the PQC centers. PQC measurements monitor the wafer processing quality by measuring dedicated test structures on the PQC half-moons (see Figure 5.1). Since the structures are processed on the same wafer as the full-size sensors and with the same processing steps, the measurement results can be transferred to the full-size sensors to evaluate their quality. In addition, the PQC structures allow for the monitoring of parameters that are not directly measurable on the full-size sensors, but are relevant for assessing the overall quality of a batch like the oxide thickness and breakdown voltage or the bulk resistivity, just to mention a few. In general, the measurements on the sensor half-moons are not as time-consuming as the electrical characterization of the full-size sensors and a larger fraction of wafers can be tested from each batch. Furthermore, the PQC covers all three types of wafers and is therefore an important indicator of the quality of the PSp sensors in addition to the VQC performed by HPK. A detailed description of the PQC structures can be found in [Hin17].
Monitoring the radiation hardness of the sensor material is the goal of the irradiation tests that are performed at the IT centers. The main goal is to ensure that the radiation-induced effects on the sensor parameters (see Section 4.5) do not significantly change over the production period. As with the process quality control, irradiation tests are performed for 2S, PSs and PSp wafers. Different types of structures are used for the tests, all of them are located on the IT half-moon (see Figure 5.1). Miniature strip sensors with a design similar to the full-size strip sensors are irradiated with protons and/or neutrons to fluences expected at the end of CMS runtime (see Section 3.2.3) to investigate the impact of bulk damage on the charge signals in dependence of different annealing scenarios. Additional structures undergo X-ray irradiation procedures to specifically introduce surface damage in the oxide layer and, thus, to monitor the oxide quality. Usually, all structures are tested before and after irradiation to ensure that potential deviations are not related to defective structures. Batches and wafers intended for the irradiation tests are selected based on the results from the PQC measurements, whereby wafers with fluctuation in the process quality (in case there are any) are prioritized. More details about the IT structures and procedures can be found in [Mül21].
With the beginning of the sensor production an *Outer Tracker Sensor Expert Production Panel* (OTSEPP) has been formed. Results from SQC, PQC and IT are presented and discussed in regular OTSEPP meetings. Additionally, the institutes are requested to upload their measurement data to a global construction database that is hosted at CERN and accessible by the whole CMS Tracker collaboration. The decision whether a specific batch of sensors can

Table 5.2.: Institutes participating in the sensor quality control during the CMS Outer Tracker sensor production.

Institution	Country	SQC	PQC	IT
Brown University	US	✓	✓	✓
Istituto Nazionale di Fisica Nucleare (INFN)	Italy	✗	✓	✗
Institute of High Energy Physics (HEPHY)	Austria	✓	✓	✗
Karlsruhe Institute of Technology (KIT)	Germany	✓	✗	✓
National Center for Physics (NCP)	Pakistan	✓	✗	✗
National Center of Scientific Research (NCSR)	Greece	✗	✓	✗
University of Delhi	India	✓	✗	✗
University of Rochester	US	✓	✗	✗

be accepted and, thus, used for the module assembly, is made by the OTSEPP based on the combination of results from the SQC and PQC centers. As the irradiation tests are by far the most time-consuming, they are not performed on each batch and are therefore not mandatory for the batch acceptance. Furthermore, on average it takes more than four months, which is the time window for the acceptance of a batch, to irradiate and measure the structures at the IT centers so that the results are often not available when a batch has to be accepted. However, if after accepting a batch, results from the irradiation tests indicate a problem concerning the radiation hardness of the sensors, affected batches can be retroactively rejected.
As shown in Table 5.2, KIT contributes to the sensor quality assurance as a SQC and IT center and a main part of this thesis is devoted to the SQC measurements performed at KIT for the first half of the sensor production (see Section 5.2.2). More information about KIT as an IT center together with a summary of measurements from the early production stage (pre-production) can be found in [Mül21].

5.2.2. Production Schedule and Progress

The Outer Tracker sensor production has started in mid 2020 and is expected to end after a duration of about four years by the end of 2024. Within this time period a total number of about 28 000 sensors will be manufactured by HPK. The overall production schedule can be divided into three stages, the first two of which have already been completed. The first stage, the *pre-series*, only included a delivery of 40 PSs wafers (80 full-size sensors) together with the corresponding test structures. The main objective of the pre-series was to reassure the sensor design and quality and to validate the unrestricted functionality of the sensors and test structures before entering the actual production. According to the quality assurance strategy introduced above, the pre-series sensors and test structures have been distributed among the individual test centers for validation. During the sensor qualification there have been observations hinting towards a potential weakness of the bias resistor design implemented on the strip sensors and as a consequence a small design adaptation has been requested by the OTSEPP. More details regarding the design weakness and the adaptation can be found in Section 5.5.1. Besides the bias resistance issue, the combined results from all centers have shown that the pre-series quality meets the requirements. During the subsequent *pre-production* phase HPK has set up their production lines towards mass production and manufactured several 2S and PSs batches ($\sim 5\,\%$ of the total requested number of sensors) in order to prove the concept of mass production. Furthermore, the pre-production phase was used to gather more measurement statistics to once again evaluate the overall sensor quality in order to decide

whether the subsequent third stage, the *production*, can be initiated. Due to the consistently good quality of the 2S and PSs sensors delivered up to this point, in October 2020 HPK was given the green light to enter the production phase, which started at the beginning of 2021 after a four-month lead time. Figure 5.4 gives an overview of the monthly delivered quantity of 2S, PSs and PSp wafers during the pre-production and production phase including all shipments up to October 2022. For the 2S and PSs wafers the transition between the pre-production and production is clearly visible by the gap in the deliveries during the last quarter of 2020. In contrast, the PSp pre-production has been postponed due to the delayed finalization of the wafer design and, therefore, first PSp sensors have only been delivered at the beginning of 2021. Although SQC measurements are not planned for the PSp sensors, a small fraction of pre-production PSp sensors has been characterized at KIT (see Section 5.4.5) to validate the quality before entering the production phase. However, the start of the PSp production has been postponed to the third quarter of 2022 as the external company taking care of the MaPSA assembly had not yet been determined and HPK did not want to take over the long-term storage of the sensors.
At the beginning of 2022, HPK was suffering from quality problems with the wafers delivered by their supplier, which in turn resulted in a lower production yield and reduced delivery quantities of 2S and PSs wafers. The impact is clearly visible by the discrepancy between the requested and delivered number of wafers at that time. This, in combination with an, on average, slightly smaller 2S wafer delivery rate resulted in a total discrepancy of currently 1 800 2S wafers compared to the requested number. In contrast, the PSs wafer deliveries are in accordance with the requested quantity, while there is only a small discrepancy of about 80 wafers for the PSp sensors. In general, small discrepancies from the delivery schedule are not a problem anymore since the module production is delayed compared to the sensor production and a sufficient stock of sensors, that is ready for the distribution among the assembly centers, has already been built up. By the time of October 2022, a fraction of 41 %, 61 % and 24 % of the total number of requested 2S, PSs and PSp wafers, respectively, have been delivered by HPK. Thus, in summary, the overall sensor production so far has been without any major issues that would have an impact on the CMS Phase-2 Tracker upgrade schedule.

5.3. Sensor Quality Control Setups and Measurement Procedures

During the Outer Tracker sensor production, KIT as an SQC center pledged to qualify 22.5 % and 27.5 % of all delivered 2S and PSs batches, respectively. The qualification of the full-size sensors according to the standards defined within the quality assurance strategy requires dedicated setups to perform various tests on the sensors. This section introduces the measurement setups at KIT that are used in the scope of the SQC and describes the individual measurements that can be performed with these setups.

5.3.1. The KIT Probe Station

The sensor probing lab at KIT provides two custom-made probe stations that are both used in the scope of the Outer Tracker sensor quality assurance. While one of the stations is exclusively used for the electrical characterization of the full-size sensors as part of the SQC, the other station is mainly used to characterize different structures in the context of the irradiation tests but also serves as a backup for SQC. The basic design of both stations is identical and in Figure 5.5 the inner parts of the SQC probe station are shown. The sensor is placed onto a polished aluminum chuck that has several vacuum holes to fixate sensors of different geometries (2S, PSs) during the measurement. Four Peltier elements located underneath the chuck are used to precisely tune the chuck temperature that is continuously monitored during

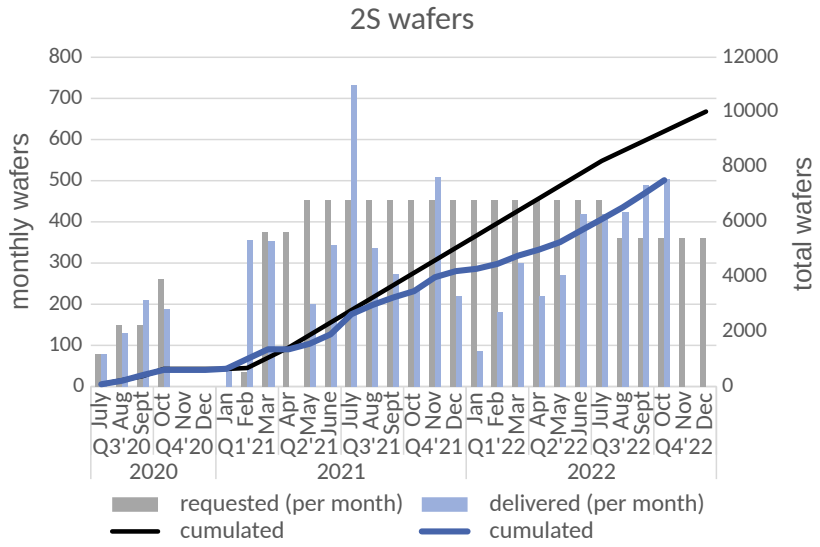

(a)

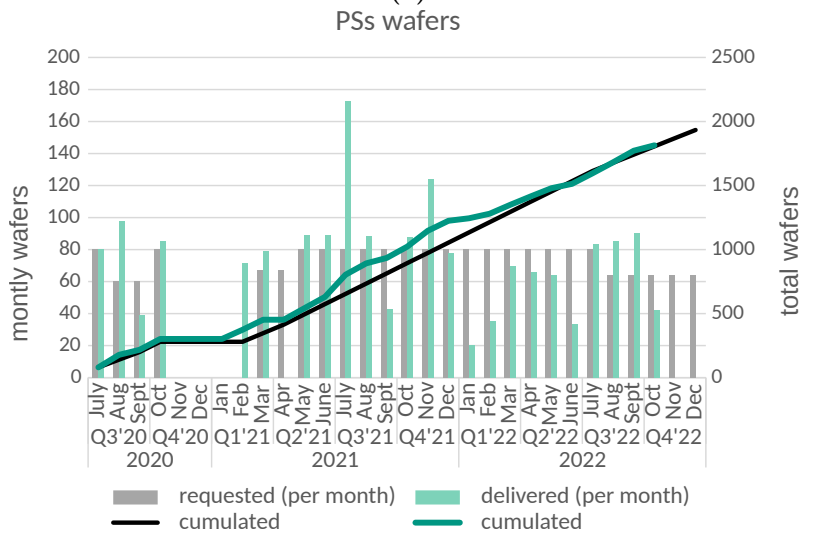

(b)

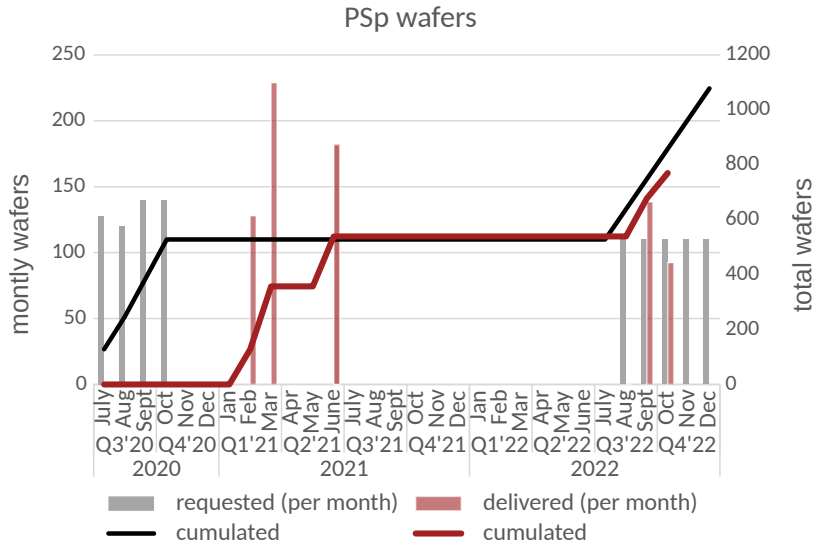

(c)

Figure 5.4.: Overview of the delivered Outer Tracker wafer quantities during the pre-production and production, divided in 2S wafers (a), PSs wafers (b) and PSp wafers (c). The histograms include all deliveries up to October 2022.

the measurement. Additionally, the chuck is connected to a precooling system that dissipates excess heat from the Peltier elements in order to protect them from overheating. Three high precision linear movement stages allow to move the chuck in all three spatial directions and to perform automated sensor tests. In order to apply a global bias potential to the sensor, the chuck and thus, the sensor backside, is set on high voltage while ground potential is provided by the bias needle which is connected to the sensor bias ring. The bias needle positioner is placed on a ledge that is directly mounted onto the chuck so that the sensor can be moved while staying biased. Additional strip needle positioners are located on a stationary ledge on the left-hand side of the chuck and are used to contact the sensor AC- and/or DC-pads to perform dedicated measurements on the strips. Since the strip needles are stationary, the sensor can be moved relative to the needles in order to test all strips of a sensor half within one measurement run. While the radius of the strip needle tips is only 2 µm the tip of the bias needle is slightly wider and has a diameter of 7 µm. Furthermore, the station provides a freely movable microscope with sufficient magnification to precisely place the needles on the sensor. The whole setup is enclosed by a lightproof aluminum box that prevents charge carrier generation by visible light and also acts as a Faraday cage to shield against electromagnetic interference (EMI). Since the electrical behavior of the sensors can be affected by the ambient humidity (see Section 5.5.3), the whole setup is constantly flushed with dry air to ensure stable environmental conditions during the measurement. The dry air also decreases the dew point to prevent condensation if structures are measured at low temperatures. In addition, the station provides an ion blower that is sitting on a ledge next to the chuck to remove static charges from the sensor (see Section 5.5.2) before starting the electrical characterization. Next to the probe station there is a rack housing various measurement devices that are listed in Table A.1 and are used to measure different sensor parameters that are described in Section 5.3.2. The whole probe station setup is controlled by a Python [Pyt22] based custom-made software framework that has been developed at KIT. The software takes care of the communication with the individual devices, monitors the environmental parameters and automatically uploads the measurement data to the local KIT database. Depending on which sensor parameter has to be measured, the individual needles have to be connected to different measurement devices. Therefore, the probe station provides a custom-made switching matrix that is controlled by the software whereby each measurement type has a defined switching state to ensure that the needles are connected to the proper devices.

5.3.2. Probe Station Measurements

This section introduces and motivates all probe station measurements that are part of the sensor quality control. If not stated differently, the nominal measurement temperature is 20 °C while the relative humidity inside the station should be smaller than 20 %.

Global Sensor Parameters - IV and CV

There are two global sensor parameters of interest for SQC, the sensor leakage current and the depletion voltage, that can be measured with only one probe needle by applying high voltage to the sensor backside while connecting the sensor bias ring.
Measuring the leakage current through the bias needle in dependence of the bias voltage (IV measurement) gives a first indication of the global sensor performance. In general, according to Equation (4.14), the leakage current depends on the depleted sensor volume and is therefore proportional to the square root of the applied voltage. After reaching the depletion voltage the current is expected to saturate as the depleted sensor volume has reached its maximum size. However, this is only an ideal assumption as there are always process-induced impurities or

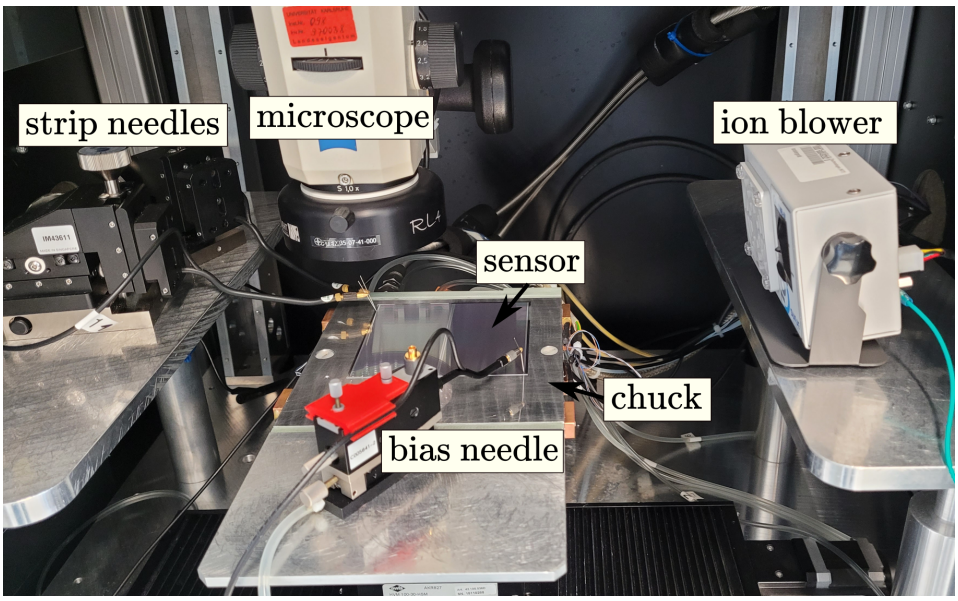

Figure 5.5.: The inside of the KIT probe station used for the SQC measurements during the Outer Tracker sensor production. The sensor is placed on a movable chuck with adjustable temperature and is contacted with different needles for the electrical characterization. A microscope enables precise positioning of the needles on the sensor.

defects in the silicon in addition to surface and edge effects that result in a slightly increasing current even after reaching full depletion. An unexpectedly high sensor leakage current or a sudden sharp current increase (breakdown) are indicators of defects of mechanical or other nature that have to be further investigated. Figure 5.6a shows example IV measurements of 2S and PSs sensors with different behavior patterns. Since the current scales with the depleted volume and thus with the sensor size, the leakage current of a 2S sensor is about twice the current of a PSs sensor. The green curve represents a 2S sensor with mechanical damage at its surface (small scratch), resulting in an overall current that is above the normal 2S level, independent of the applied voltage. Generally, the impact of mechanical sensor damage strongly depends on the type of damage (e.g. size and depth of the scratch), and it must be decided individually whether a sensor can still be used for module assembly as the damage might not only affect the leakage current, but also individual strips. An example of a 2S sensor with early breakdown at about 500 V is shown in blue. Early breakdowns can have various reasons such as point like defects on sensor structures causing high electric fields, static charges on the sensor or a high environmental humidity. In some cases the sensor can be recovered (Section 5.5.2 and Section 5.5.3). Altogether, the sensor leakage current should always be measured before any other parameter to validate that the sensor is functional and to determine its breakdown voltage in case there is a breakdown. The measurement parameters and specifications used in the scope of the sensor quality control are listed in Table 5.3.

The depletion voltage V_{dep} can be determined by measuring the sensor capacitance with an LCR meter (AC measurement at fixed frequency) while increasing the bias voltage in steps (CV measurement). Thinking of the sensor as a parallel plate capacitor, Equation (4.11) holds that the capacitance decreases proportionally to the inverse square root of the applied voltage and stays constant after being fully depleted. The common way to extract the depletion voltage is to plot $1/C^2$ in dependence of the applied voltage as it is shown in Figure 5.6b by

Table 5.3.: Overview of the sensor leakage current measurement parameters and specifications used within the sensor quality control. The specification on the current per volume at 600 V translates to 7.25 µA and 3.625 µA for 2S and PSs sensors, respectively.

Sensor bias voltage	
0 V to 400 V	5 V steps
410 V to 1000 V	10 V steps
Specifications	
current per volume at 600 V	$I_{600} < 2.5\,\mathrm{nA\,mm^{-3}}$
current ratio at 800 V over 600 V	$I_{800}/I_{600} < 2.5$
breakdown voltage	$V_{break} > 800\,V$

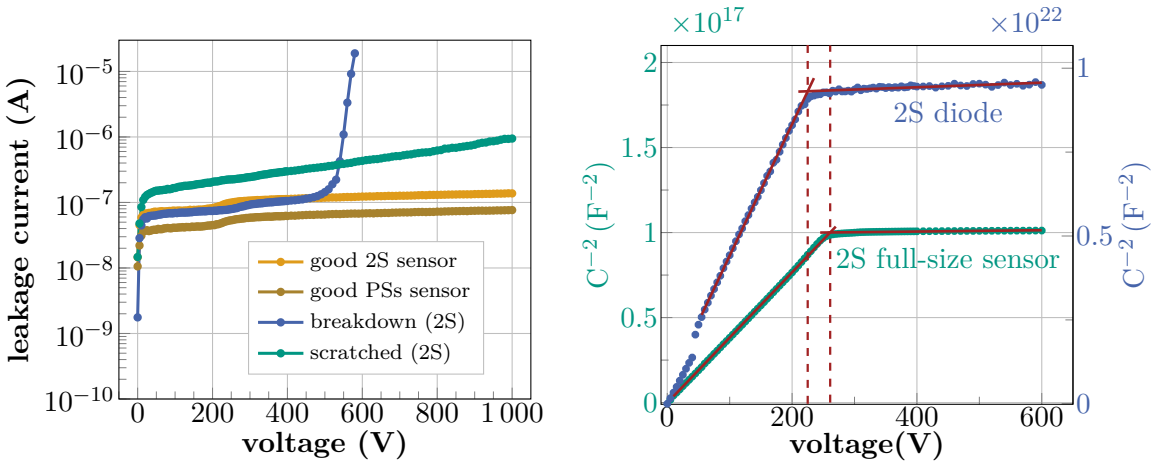

Figure 5.6.: (a): Exemplary IV measurements of 2S and PSs sensors representing different possible sensor behaviors. (b): Example CV measurements of a 2S full-size sensor and a diode of the same wafer. The depletion voltage is determined from the intersection point of two linear fits and is indicated by the vertical dashed lines. Strip sensors have slightly higher depletion voltages compared to diodes due to geometrical effects resulting from the additional segmentation.

Table 5.4.: Overview of the sensor capacitance measurement parameters used within the sensor quality control to extract the sensor depletion voltage.

Sensor capacitance/Depletion voltage (CV)	
bias voltage	0 V to 400 V in 5 V steps 410 V to 600 V in 10 V steps
AC frequency	1 kHz
AC amplitude	0.25 V
specification	$V_{dep} < 350$ V

the example of a 2S sensor and a diode. At the beginning, there is a linear increase due to the decreasing capacitance which, after reaching the depletion voltage, changes to a constant plateau as the capacitance stays constant. The depletion voltage is therefore given by the position of the kink and can be approximated by the intersection of two linear fits, indicated by the red lines. During the sensor mass production, the main objective is to monitor trends in the depletion voltage, where values measured across different batches can differ by up to 100 V. Thus, although the depletion voltage values determined with the above described method are not highly precise as the method is dominated by systematics, it still allows for detecting global trends and can be easily automated. For the automated extraction of the depletion voltage a fitting procedure based on a piece-wise defined function with two linear parts is used

$$f(x) = \begin{cases} a_1 \cdot x + b_1 & \text{for } x \leq i \\ a_2 \cdot (x - i) + a_1 \cdot i + b_1 & \text{for } x > i \ , \end{cases} \tag{5.1}$$

where i indicates the intersection point and, thus, the depletion voltage V_{dep}. The optimization of $f(x)$ to the measurement data is based on the curve_fit method provided by the Python scipy optimization package [Sci22], which implements a non-linear least-squares method. The depletion voltage together with the corresponding uncertainty is extracted from the fit parameter i.
In general, the depletion voltage measured on a strip sensor is larger than the depletion voltage extracted from a diode, even if both structures originate from the same wafer. The discrepancy is related to the additional segmentation of the sensor which changes the electric field configuration between and around the strip implants compared to a diode without any segmentation [Har17]. Therefore, the extraction of actual physical parameters from the capacitance measurement such as the doping concentration, the substrate thickness or the bulk resistivity, as it is done in the PQC, should be based on diodes instead of strip sensors to avoid unwanted effects related to the segmentation. However, monitoring the depletion voltage of the full-size sensors is nevertheless a good indicator to identify trends during the sensor production and to validate them with the PQC measurements. The measurement parameters and specifications used in the scope of the sensor quality control are listed in Table 5.4.

Strip Parameters

As exemplarily shown in Figure 5.7, sensors can have different defects related to the sensor processing or handling that might be not directly visible within the global sensor measurements but can have an impact on the electrical behavior of individual strips. Thus, measuring and monitoring of electrical strip parameters is an essential part of the overall sensor quality assurance. Furthermore, besides detecting potential defects, strip testing allows for validating the homogeneity of the electrical parameters across the sensor. There are a total of six

different strip parameters that are measured on the sensors in the context of the SQC. When using two strip needles, as it is the case for the KIT probe stations, two different needle configurations are required to cover all six parameters. The individual strip measurements and the required needle configurations are explained in the following, while a detailed overview of the measurement settings and SQC specifications of each parameter can be found in Table 5.5. All strip parameters are measured within automated sensor scans during which the sensor stays biased at 600 V. Each of the two sensor halves is measured within an independent scan.

Strip Leakage Current ($\mathbf{I_{leak}}$): For functional strips typical currents per strip length are of $\mathcal{O}(10\,\mathrm{pA\,cm^{-1}})$ and correspondingly the electrometer used for the measurement must provide an appropriate resolution. Increased leakage current on individual strips can have various reasons such as scratches on the sensor surface, faulty strip implantation (implant shorts) or inhomogeneities in the bulk, just to mention a few. In contrast, an open strip implant would result in a lower strip leakage current as the length of the strip implant connected to the DC-pad is reduced. The total sensor leakage current measured on the bias ring in the course of an IV measurement is composed of the leakage currents of the individual strips as well as contributions from the sensor periphery. Hence, in order to measure the leakage current of an individual strip, the whole sensor has to be biased while an additional needle is placed on the strip DC-pad to measure the current before entering the bias ring.

Polysilicon Resistance ($\mathbf{R_{poly}}$): The resistance of the individual polysilicon resistors should have no significant variation across the sensor to achieve a uniform distribution of the bias potential resulting in a uniform field configuration. Thus, a homogenous AC signal across the strips is ensured. Typical resistance values are in the order of 1 MΩ to 2 MΩ. The resistance of individual bias resistors is measured with the same needle configuration as the strip leakage current (contacted DC-pad). Based on Ohm's law $R = U/I$, applying a voltage to the DC-pad results in a current through the resistor that adds up to the total sensor leakage current measured on the bias ring. By driving a voltage ramp while measuring the bias current at each voltage step, the resistance is determined from the inverse slope of a linear fit. The resistance of the individual resistors can only be reliably measured if the strips are isolated from each other. Otherwise, several resistors are measured in parallel, resulting in an overall lower resistance value.

Coupling Capacitance (CC): The coupling capacitance refers to the capacitance between the strip implant and the aluminum strip and is an important sensor parameter as it is directly proportional to the signal that enters the readout electronics. Drifts in the capacitance across several strips can hint towards oxide thickness or quality deviations on the sensor. Again taking a parallel plate capacitor as a model, the coupling capacitance mainly scales with the strip length, but also depends on thickness and quality of the coupling oxide. Metal shorts connecting AC-pads of neighboring strips can be identified by an increased capacitance that is n times higher compared to the nominal capacitance value, where n is the number of strips affected by the short. In contrast, breaks in the metallization (open metal) reduce the capacitance, as only a fraction of the whole pad is connected to the AC-pad. The coupling capacitance is measured by connecting the LCR meter to the DC- and AC-pad of the same strip.

Current through Dielectric (Pinhole): In case there is a conductive connection between the DC- and AC-pad of a strip, which should not be the case for AC coupled sensors, this is referred to as a pinhole. Strips with pinholes can have an increased channel noise since the strip leakage current is not decoupled from the readout electronics. High

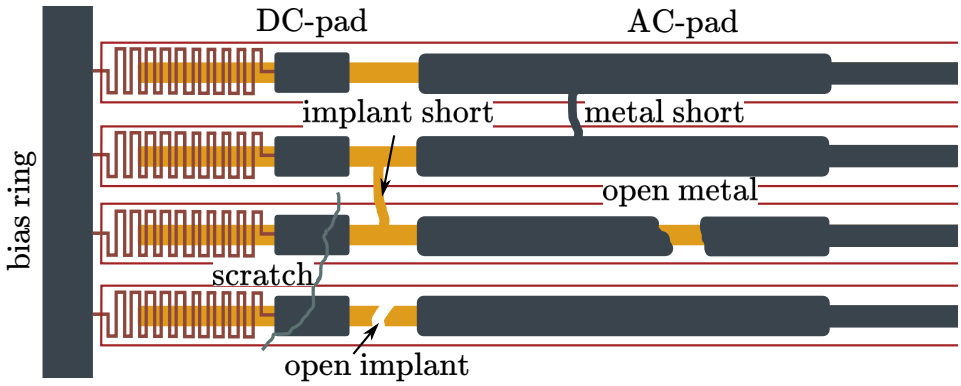

Figure 5.7.: Potential sensor defects that can be detected by the strip characterization are openings or short-circuits on the implants and the metallization, as well as scratches on the sensor surface.

strip leakage currents in combination with pinholes can not only affect the channel noise, but also damage the amplifiers of the readout chip. Pinholes can be easily identified by applying a constant low voltage to the strip DC-pad while measuring the resulting current on the AC-pad, or the other way around. For functional strips, no current is expected, and the measured currents should fluctuate around zero within the resolution of the electrometer. There are different reasons for pinholes on a sensor. Besides scratches on the sensor surface that electrically connect the AC- and DC-pad, pinholes can also be related to a gap in the coupling oxide that is filled with aluminum and thus directly connects the AC-pad with the strip implant. Furthermore, ESD events with voltage drops larger than 250 V across the coupling oxide can create permanent shorts between the aluminum strip and the strip implant.

All strip parameters described up this point are measured on single strips and either require to contact the DC-pad or the combination of DC- and AC-pad. Thus, they are referred to as *single strip parameters*. However, there are two additional *interstrip parameters* that are monitored in the scope of the SQC, which require to contact the DC-pads of two neighboring strips.

Interstrip Resistance (R_{int}): The isolation of neighboring strips is characterized by the interstrip resistance. Sufficient strip isolation is mandatory to avoid charge sharing across several strips, which would deteriorate the spatial resolution. In general, small interstrip resistances can originate from scratches and implant shorts that electrically connect neighboring strips. Furthermore, defects or processing issues on the p-stop implants can cause a reduced interstrip resistance. The interstrip resistance is measured by connecting the DC-pads of two adjacent strips and driving a low voltage ramp on one of the pads while measuring the resulting current on the other pad. Similar to the R_{poly} measurement, the resistance is determined from a linear fit. In the rare case of a leaky strip, the voltage that is modulated on the neighboring DC-pad does not significantly impact the measured current as it is already at a high level. Thus, the voltage ramp does not result in a linear behavior between voltage and current and the extracted interstrip resistance is invalid. An example of this measurement artefact compared to a normal voltage ramp is shown in Figure A.1.

Interstrip Capacitance (C_{int}): The interstrip capacitance is one of the main contributors to the total load capacitance, which is directly correlated with the noise

Table 5.5.: Overview of the strip parameters monitored in the scope of the sensor quality control. Limits for the individual sensor types are determined from the general limit by assuming a strip length of 5 cm and 2.5 cm for the 2S and PSs sensor, respectively. The general limit for the strip leakage current agreed with HPK is $2\,\mathrm{nA\,cm^{-1}}$. However, the OTSEPP decided to internally use a five times larger limit for the SQC, which still ensures a good sensor performance in the tracker and at the same time offers more leeway for the sensor acceptance and thus the sensor yield. The R_{poly} limit refers to the median resistance measured across the sensor. Furthermore, the individual strips should not fluctuate more than ±5 % around the median resistance of the sensor. The measurement configuration for R_{int} has changed from pre-production to production, whereby the configuration highlighted with an asterisk represents the pre-production configuration.

Measurement type	Pad connection	Device parameters	General limit	2S limit	PSs limit
I_{leak}	DC	—	$< 10\,\mathrm{nA\,cm^{-1}}$	50 nA	25 nA
R_{poly}	DC	[0,5] V, 5 V steps	$(1.5 \pm 0.5)\,\mathrm{M\Omega}$	—	—
CC	DC, AC	1 kHz, 1 V	$> 1.2\,\mathrm{pF\,cm^{-1}\,\mu m^{-1}}$	132 pF	75 pF
Pinhole	DC, AC	10 V	< 10 nA	—	—
R_{int}*	DC, DC	[0,5] V, 0.5 V steps	$> 10\,\mathrm{G\Omega\,cm}$	2 GΩ	4 GΩ
R_{int}	DC, DC	[0,5] V, 3 V steps	$> 10\,\mathrm{G\Omega\,cm}$	2 GΩ	4 GΩ
C_{int}	DC, DC	1 MHz, 1 V	$< 0.5\,\mathrm{pF\,cm^{-1}}$	2.5 pF	1.25 pF

(see Section 4.3.2). However, a certain interstrip capacitance is also desired to have charge sharing between the nearest strip neighbors, which in turn improves the spatial resolution of the sensor. The interstrip capacitance should be small compared to the coupling capacitance to ensure that most of the signal is coupled into the preamplifier. Typically, the ratio C_C/C_{int} should not be smaller than 50. The interstrip capacitance is measured with an LCR meter connected to the DC-pads of two adjacent strips. In general, high measurement frequencies with periods close to the chip peaking time $\mathcal{O}(20\,\mathrm{ns})$ are preferred, but are technically limited to 1 MHz to 2 MHz by the measurement device. Since the expected capacitance is of $\mathcal{O}(\mathrm{pF})$, it is essential to perform a compensation measurement with floating needles before starting the actual measurement to eliminate parasitic capacitances from the cables and the close-by needle tips.

5.3.3. Long-Term Setup and Measurement

The stability of the sensor leakage current over time is another aspect to validate the sensor quality, besides measuring the current in dependence of the bias voltage, as it is done by the IV measurement. In order to test the long-term stability of several sensors simultaneously and independent of the probe station, KIT has built a dedicated long-term setup, which is shown in Figure 5.8. The setup consist of a lightproof cabinet that houses a rack with a total of ten layers. The layers are equipped with removable copper-based long-term boards providing all necessary connections for the measurement. On the right-hand side of Figure 5.8 a long-term board equipped with a 2S sensor is shown. The board features a layer of conducting rubber on which the sensor is placed to protect it from scratches and to apply ground potential to its backside. Wire bonds providing high voltage to the sensor are placed between the sensor bias ring and a dedicated bond pad that is insulated from the rest of the board. The sensor is kept in place with a 3D printed fixation to prevent it from slipping and breaking the wire bond

connection. All long-term boards inside the rack are connected to the measurement devices via a custom-made circuit board that allows to disconnect individual sensors from the high voltage in case they show an abnormal behavior, without affecting the measurement of the other sensors. The measurement is supervised by Python-based software and runs on a dedicated readout computer. During the measurement, the housing is flushed with dry air to keep the relative humidity below 10 % and to avoid humidity-related effects on the sensors such as early breakdowns. The air temperature and humidity inside the housing is continuously monitored. However, the setup does not provide a temperature regulation and the sensor temperature therefore complies to the ambient temperature of the air-conditioned laboratory which usually fluctuates within $\pm 1.5\,°C$.
All sensors undergoing the long-term measurement are first IV tested with the setup up to 800 V to validate that the wire bonds are properly connected to the sensors and that the sensors have not been damaged when they were placed onto the long-term boards. The consecutive long-term measurement is conducted at a nominal operation voltage of 600 V and for a minimum duration of 48 h, whereby the sensor leakage currents are measured each minute. To reduce the effect of occasionally occurring larger temperature drifts (>3 °C) in the lab, the measured currents are scaled according to equation Equation (4.15) to temperature equivalent currents at 21 °C. Furthermore, the measurement data is smoothed with a Savitzky-Golay filter. The filter allows for excluding outliers related to the setup that do not represent the actual sensor behavior without distorting the overall sensor leakage current tendency. Afterwards, the sensor quality control long-term specification

$$\frac{I_{\text{max}} - I_{\text{min}}}{I_{\text{median}}} < 30\,\% \;, \tag{5.2}$$

is applied to the currents, where I_{max}, I_{min} and I_{median} correspond to the maximum, minimum and median of the measured currents. For sensors failing the specification limit it has to be decided individually whether the sensor should be assigned as bad, since leakage currents that only decrease over time would not be a problem for the sensor operation in the modules. In contrast, an unexpected strongly increasing current would represent an unwanted sensor feature.

5.3.4. SQC Procedure and Batch Acceptance

In order to ensure comparable evaluation of the sensor quality among the different SQC centers, a predefined procedure has to be followed to qualify a batch of sensors. This procedure has been developed by the CMS Outer Tracker sensor working group based on the experience from previous projects and the testing of sensor prototypes before the start of the sensor mass production. The individual steps are briefly summarized in the following.

Sensor selection: Sensors undergoing the SQC procedure are selected based on the IV measurements provided by HPK. Preference is given to sensors with the worst electrical behavior that either have an increased leakage current or show a breakdown at high bias voltages and, thus, deviate from the batch average. Additionally, in case the PQC measurements hint towards deviations in the wafer processing quality the corresponding sensors are candidates for the SQC procedure. These sensors are subject to more detailed measurement procedures including an optical inspection, single strip characterization and a long-term leakage current stability test. Additional sensors are selected randomly, uniformly distributed among the wafers of a batch, to match the required minimum number of sensors for the batch acceptance.

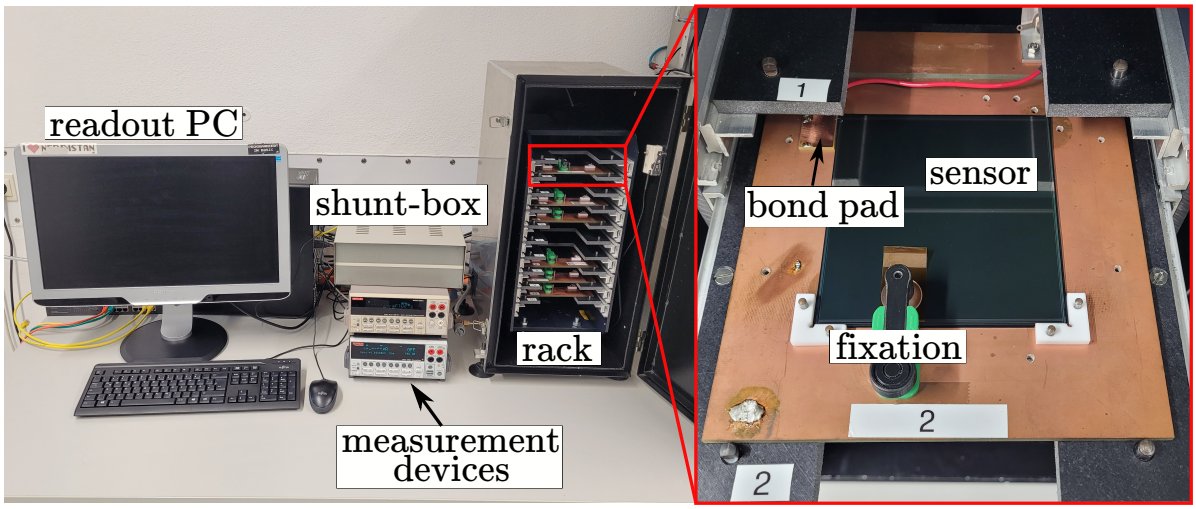

Figure 5.8.: Picture of the KIT long-term setup used in the scope of the sensor quality control. Each sensor is placed on a dedicated long-term board shown in the close-up view on the right providing all necessary connections to the measurement devices. Up to ten sensors fit into the rack and can be measured simultaneously. The measurement is supervised by Python-based software running on the readout computer.

IV/CV measurements: A minimum of five sensors from each batch is IV/CV tested according to the procedures described in Section 5.3.2. If the measurements are within the specifications and do not show any abnormalities, no further measurements are conducted on these sensors.

Optical inspection: All sensors intended for a more detailed characterization undergo an optical inspection first. The sensor front side is scanned with a high-resolution digital microscope to document its condition before it is handled in the probe station. In case sensor defects or other problems are observed during the electrical characterization the pictures can be used for further investigations. Sensors that are only IV/CV tested are not optically inspected.

Strip scans: Sensors undergoing a strip scan are first IV/CV tested to validate the overall sensor performance and to ensure that the sensor can be measured at the nominal operation voltage of 600 V. All six strip parameters introduced in Section 5.3.2 are measured on the sensor. A minimum of three (five) sensors of each 2S (PSs) batch has to be tested in order to accept a batch. The number of tested PSs sensors is larger than the number of tested 2S sensors since PSs batches contain more sensors. However, the strip tests do not cover every strip of the sensor. Single strip parameters (I_{leak}, R_{poly}, CC and Pinhole) are measured on every 4^{th} strip. This sampling rate is sufficient to detect potential cluster of strips failing specification limits and still allows to evaluate the homogeneity of strip parameters across the sensors. During the pre-production single strip parameters were tested on every strip. The procedure has been adapted to cope with the larger number of monthly delivered sensors during production phase. Furthermore, the consistently good sensor quality observed during the pre-production has shown that there is no need to stick to the higher sampling rate. In contrast, the interstrip parameters (R_{int} and C_{int}) were tested on every 50^{th} strip during the pre-production and for the production the sampling rate has been changed to every 15^{th} strip. However, at the same

time, the number of low voltage steps during the interstrip resistance measurement has been reduced (see Table 5.5), so that in the end more strips can be tested within the same measurement time. The sampling rate chosen is a trade-off between the measurement time and the sensor coverage as the interstrip measurements are overall more time consuming. In case strips violating the specifications defined in Table 5.5 are detected, the sampling rate for the region close to the affected strip is increased, to detect further potential bad strips.

Long-Term test: Long-term measurements with at least three sensors of each batch and a minimum measurement duration of 48 h are conducted to validate the leakage current stability over time. Sensors undergoing the long-term test are usually the same sensors that are intended for the sensor strip scan with the probe station.

Sensors are referred to as good if the global sensor parameters extracted from the IV and CV measurement are within the specifications defined in Table 5.3 and Table 5.4. Furthermore, the number of strips failing the specifications defined in Table 5.5 must be smaller than 1 % per sensor and there should be not more than two bad strips within a sequence of five consecutive strips. Sensors that do not meet these specifications can be rejected and in case there are three or more bad sensors within a batch, the whole batch can be rejected.

5.3.5. Measurement Systematics and Uncertainties

As introduced in the previous sections, the main goal of the SQC is to validate the sensor quality by measuring global sensor parameters but also electrical properties of the individual strips. In order to reliably detect sensors or strips that fail the specifications introduced in Section 5.3.2, the probe station setup must provide sufficient accuracy. This section briefly discusses the underlying sources of systematic effects and uncertainties of the probe station that has been used for the SQC measurements presented in Section 5.4.

Leakage Current Measurements

In general, the measurement precision is limited by the accuracy of the measurement device. All current measurements at the probe station are based on the *Keithley 6485* [Kei11], which features different measurement accuracies depending on the measurement range. The global sensor leakage current of functional 2S and PSs sensors is usually measured in the 200 nA range, whereas the strip leakage currents are measured with the 2 nA range (the smallest available range). Thus, following [Kei11] the accuracy of the measured currents I_{meas} is given by

$$\begin{aligned} \Delta I_{\text{sensor}} &= \pm\,(0.002 \cdot I_{\text{sensor}} + 10\,\text{pA}) \\ \Delta I_{\text{leak}} &= \pm\,(0.004 \cdot I_{\text{leak}} + 400\,\text{fA})\ , \end{aligned} \tag{5.3}$$

where I_{sensor} corresponds to the global sensor leakage current and I_{leak} indicates the strip leakage current. Taking a typical PSs sensor[1] measured at 600 V with $I_{\text{sensor}} \approx 65\,\text{nA}$ and $I_{\text{leak}} \approx 30\,\text{pA}$ as an example, results in an absolute (relative) measurement uncertainty of 140 pA (0.2 %) and 520 fA (1.7 %) for I_{sensor} and I_{leak}, respectively. However, there are additional setup-related influences such as temperature fluctuations that impact the measurement precision, especially for strip scans with long measurement durations $\mathcal{O}(\text{h})$. The nominal probe station measurement temperature is 20 °C, while temperature fluctuations of up to ±1 °C are allowed during the measurement. Since the sensor leakage current is temperature dependent, the fluctuations

[1] Due to its dimensions (half the size of a 2S sensor), the PSs sensor leakage currents (global and strip current) represent the smallest expected currents within the SQC measurements.

impact the measured currents. Based on Equation (4.15) and assuming the maximum allowed temperature range (19 °C to 21 °C), the measured current can be 8.5 % lower or 9.2 % higher compared to the current at 20 °C, which is significantly larger than the uncertainties related to the measurement device described above. However, this represents the maximum allowed fluctuation, while usually the measured temperature fluctuation is not larger than 0.5 °C.
To estimate the overall probe station performance with regard to the smallest currents measured in the scope of the SQC (PSs strip leakage currents), test measurements with a baby sensor[2] from an IT half-moon featuring a strip design similar to the full-size PSs sensor were performed. The strip leakage current of the same strip was measured about 8 400 times over a time period of 2.8 h resulting in a mean current of 31 pA with a standard deviation of about 1.5 pA. This gives an estimate of the overall measurement setup precision, which is about three times the uncertainty of the measurement device. Additionally, an open circuit measurement (floating needle) of the same duration was performed to estimate the measurement noise, which is about 110 fA. The corresponding histograms are shown in Figure 5.9.
In summary, the accuracy of the probe station is by far sufficient to identify bad sensors and strips failing the leakage current specifications where a measurement resolution of $\mathcal{O}(\mu A)$ and $\mathcal{O}(nA)$ is required, respectively.

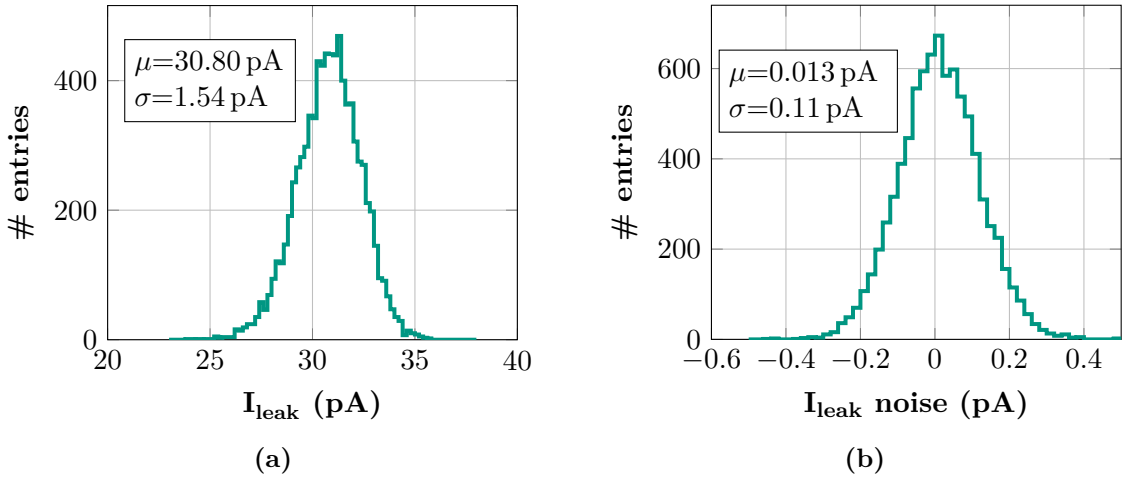

Figure 5.9.: (a): High-statistics strip leakage current measurement conducted on the same strip over a duration of about 2.8 h. The current approximately follows a Gaussian distribution with a standard deviation of 1.54 pA. (b): Leakage current noise measurement with floating strip needle. The measured current fluctuates around zero with a standard deviation of about 110 fA.

Resistance Measurements

As described in Section 5.3.2, the measurement principle to determine the polysilicon resistance or the interstrip resistance is based on measuring the increase in leakage current on the bias ring (R_{poly}) or the neighboring strip (R_{int}) while applying a sequence of different low voltages to the strip under study. Thus, resistance fluctuations are mainly related to fluctuations of the measured currents during the low voltage ramp. The typical resistance of the polysilicon resistors on the 2S and PSs strip sensors is in the order of $\mathcal{O}(M\Omega)$. Figure 5.10a shows the result of a high-statistics R_{poly} measurement conducted on the same strip over a time period of about 2.8 h, resulting in a mean resistance of 1.45 MΩ with a standard deviation of 167 Ω, which

[2] All high-statistics measurements shown in this section have been performed with this sensor.

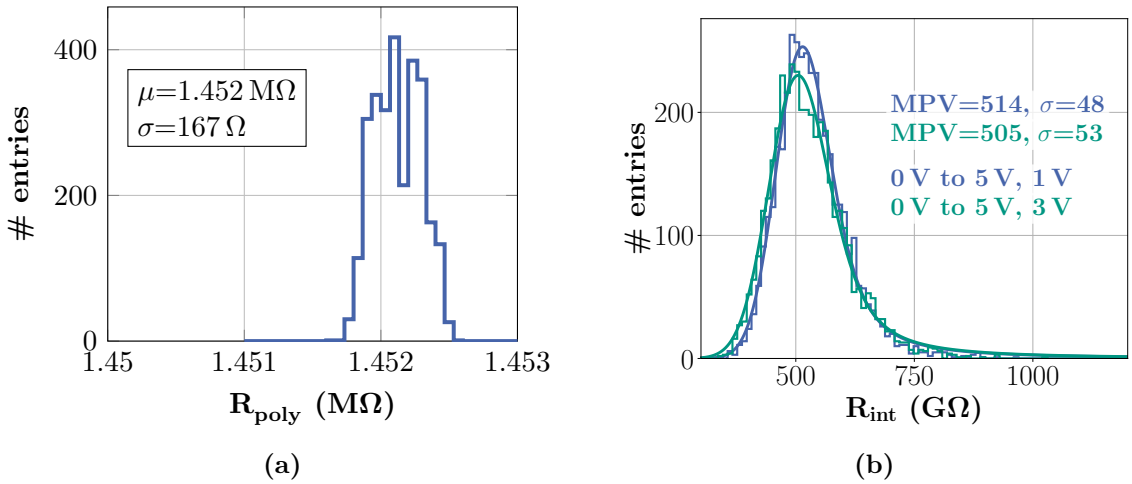

Figure 5.10.: High-statistics measurements of a polysilicon resistor (a) and the interstrip resistance (b) on a miniature sensor with a strip design equal to the PSs sensor. R_{poly} measurement fluctuations are in the sub-percent range and can be neglected. The R_{int} measurement shows larger fluctuations with a long tail towards high resistance values. The MPV and standard deviation is extracted from the measurement assuming a Landau-Gauss distribution.

is at the sub-percent level. Thus, the underlying fluctuations are not of major significance. In contrast, the interstrip resistance is several orders of magnitude larger, $\mathcal{O}(100\,\mathrm{G\Omega})$, and the measured interstrip current in dependence of the applied voltage is relatively small $\mathcal{O}(\mathrm{pA})$. Consequently, the measurement is more affected by the above mentioned leakage current fluctuations. Again, high-statistics R_{int} measurements were performed to validate the setup precision with regard to large interstrip resistance values. Figure 5.10b shows measurements conducted with two different low voltage ramps[3]. Both distribution have tails towards high resistance values and can be approximated by a Landau-Gaussian convolution.[4] These tails are related to fluctuations of the strip leakage current (see Figure 5.9a) that is measured during the low voltage ramp. Although from the statistical point of view there is a significant difference between the most probable values (MPVs), the measurements prove that both voltage ramps can be used for the SQC. In the scope of the SQC measurements, interstrip resistance fluctuations in the order of $\mathcal{O}(100\,\mathrm{G\Omega})$ are acceptable since the main objective is to detect strips with low interstrip resistance, which would feature increased interstrip currents that can be reliably detected with the probe station setup. However, based on the resistance distribution shown, the measured interstrip resistance should not be regarded a high-precision measurement.

Capacitance Measurements

The *Keysight E4980AL* LCR meter used for the capacitance measurements at the probe station provides an intrinsic accuracy of ±0.05 % [Key19]. High-statistics measurements with

[3] The R_{int} measurement procedure has been changed between the pre-production and production. During the pre-production six voltage steps (0 V to 5 V in steps of 1 V) have been used, while with the start of the production the number of steps has been decreased to three (0 V, 3 V and 5 V) to reduce the measurement duration.

[4] In general, it would be more convenient to express everything in conductance instead of the resistance, as the fit of the low voltage ramp is linear in conductance, avoiding long tails in the distribution. However, to stay consistent with the definitions and methods agreed within the OTSEPP, the resistance is considered in the following.

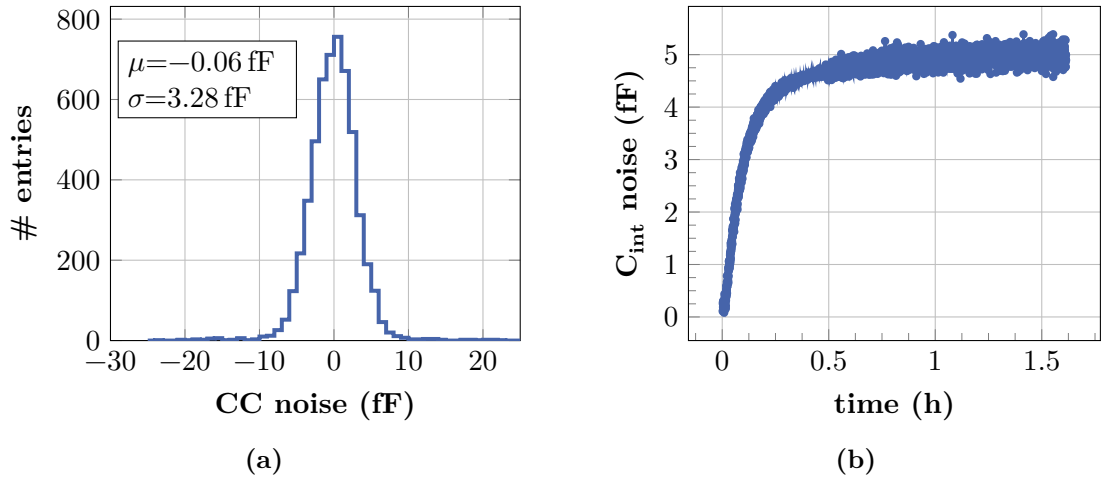

Figure 5.11.: Capacitance noise measured with the CC (a) and C_{int} (b) relay settings of the probe station. The coupling capacitance noise fluctuates around zero while the C_{int} noise shows a time-dependent behavior. However, for both relay settings the noise is in the single-digit fF order, which is significantly smaller compared to the typical strip capacitances measured in the scope of the SQC.

floating strip needles (no sensor connected) and relay settings as they are used for the coupling capacitance and the interstrip capacitance measurement are shown in Figure 5.11. For the individual measurements, the LCR meter settings defined in Table 5.5 were used. As with any capacitance measurement conducted with the probe station, offset corrections compensating for parasitic capacitances from the cables and needles were performed before the high-statistics tests. The coupling capacitance noise shown in Figure 5.11a fluctuates around zero and follows a Gaussian distribution with a standard deviation of about 3.3 fF. Compared to the typical coupling capacitance of the strip sensors that are tested in the cope of the SQC $\mathcal{O}(30\,\mathrm{pF\,cm^{-1}})$ the measurement noise is negligible. The noise measured with the C_{int} relay configuration is shown in Figure 5.11b and reveals a time-dependent behavior. At the beginning of the measurement the noise is in the sub-fF range and increases up to 5 fF where it starts to saturate. After reaching saturation, the spread across the measured capacitance noise values is much smaller compared to the noise measured with the coupling capacitance configuration, which is most likely related to the higher measurement frequency of 1 MHz. Thus, for the C_{int} measurement, the time dependent effect dominates and a minimum uncertainty of about 5 fF has to be considered, which is still significantly smaller compared to the typical interstrip capacitances $\mathcal{O}(350\,\mathrm{fF\,cm^{-1}})$ of the strip sensors. The time dependent noise behavior is in good agreement with the observations in [Met20] and seems to be related to the setup/device used for the measurement.

5.4. KIT Sensor Quality Control Results

This section summarizes the SQC results gathered during the sensor pre-production and production at KIT including all sensor deliveries up to September 2022. In total, 43 batches of 2S sensors and 10 batches of PSs sensors were qualified according to the procedure introduced in Section 5.3.4. To give a representative overview of the sensor quality provided by HPK, sensors with electrical parameters influenced by mechanical damage[5], or setup-related measure-

[5]This refers to damage such as scratches on the sensor surface that have been introduced during the sensor handling at the SQC center and is not related to HPK.

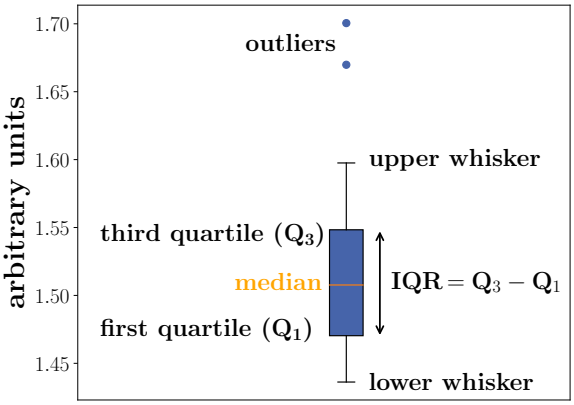

Figure 5.12.: Example of a box-whisker diagram. The size of the blue box containing the mean 50 % of all data points of a given dataset is described by the inter quartile range ($\mathrm{IQR} = Q_3 - Q_1$) while the overall median is indicated in orange. Data points outside the IQR are represented by whiskers that are placed on both ends of the box. The maximum whisker length in both directions is $n \cdot \mathrm{IQR}$ and all data points being outside this range are indicted as individual outliers. The example box-whisker diagram uses $n = 1.5$.

ment artifacts are excluded from the datasets presented in the following. In addition to the SQC measurements conducted on the strip sensors, this section also summarizes results from the electrical characterization of PSp pre-production sensors, which are not included in the standard SQC procedure and were exclusively performed at KIT.
In Section 5.3.5 it has been shown that the measurement uncertainties and systematic effects regarding the sensor parameters that are monitored within the SQC measurements are small compared to the respective specification limits. Therefore, if not stated differently, measurement uncertainties of the individual sensor parameters are not taken into account in the following. Instead, for most of the parameters box-whisker diagrams are used to summarize the measurement data collected in the scope of the sensor production in a compact and meaningful way. An example of a box-whisker diagram is shown in Figure 5.12. For a given dataset the upper and lower edge of the box is defined by the third (Q_3) and first (Q_1) quartile, which represent the median of the upper and lower half of the data, respectively. Thus, the box contains the central 50 % of all data points and its size is described by the interquartile range (IQR) with $\mathrm{IQR} = Q_3 - Q_1$. The overall data median is indicated by the horizontal orange line. Each end of the box is extended by a whisker, which has a maximum length of $n \cdot \mathrm{IQR}$, where n can be defined individually. The example plot uses $n = 1.5$. However, the upper whisker only extends to the last data point that is smaller than $Q_3 + n \cdot \mathrm{IQR}$, while the lower whisker only extends to the last data point larger than $Q_1 - n \cdot \mathrm{IQR}$. Thus, the upper and lower whisker can have different lengths. All data points exceeding the maximum whisker range are indicated as individual outliers. If not stated differently, all box-whisker diagrams summarizing SQC data are based on $n = 3$.

5.4.1. Global Sensor Parameters

Sensor Leakage Current

The main results from the sensor leakage current measurements are summarized in Figure 5.13. Leakage currents of all strip sensors tested at KIT in the scope of the SQC are depicted

in Figure 5.13a. A similar plot summarizing the currents measured by HPK can be found in Figure A.2. Each of the box-whisker diagrams summarizes the leakage currents measured at 600 V for sensors of the same batch. The sensor batch numbers are chronologically ordered and, therefore, represent the time evolution of the sensor production, starting with the pre-production on the left-hand side. Overall, the median leakage currents of the 2S sensors are about twice as large as the PSs currents, which is related to the different size of the sensors. For both sensor types, the batch median leakage current is stable over the entire production period and no significant drift towards higher or lower currents is visible. In general, the leakage currents measured among all sensor batches are significantly lower compared to the specification limits of 7.25 µA and 3.6 µA for the 2S and PSs sensors, respectively. The highest current measured is about 430 nA (2S sensor) and, therefore, none of the tested sensors fails the specification. This is expected as HPK is requested to exclude problematic sensors violating the leakage current specifications from the shipments. Furthermore, the measurements prove that there is no general problem regarding the sensor transport and handling that could cause damage to the sensors making them violate the global leakage current specification.
To validate the data provided by HPK, leakage currents of all sensors tested at KIT are correlated with the corresponding HPK currents, which is shown in Figure 5.13b. For both, the 2S and PSs sensors a linear correlation between the measured currents is visible with an underlying Pearson correlation coefficient of 0.85. The general offset between the HPK and KIT data is related to the different environment temperatures during the measurements[6]. The 2S sensor with the increased leakage current of about 430 nA (see Figure 5.13) is excluded from the plot to better resolve the correlation of the other sensors. Two clusters of data points are visible indicated by the dashed orange line that separates the clusters. Data points in the upper cluster belong to sensors from the pre-production batches while the lower cluster contains the data from the production sensors. The leakage current time evolution measured at KIT (see Figure 5.13) reveals a small offset between pre-production and production batches that is not visible in the data provided by HPK (see Figure A.2) and therefore, causes the cluster formation. Since the SQC setup used at KIT has not been knowingly modified between the sensor pre-production and production and all measurements have been performed under identical conditions, the clustering must be related to the HPK data. This conclusion is supported by the fact that some KIT measurements were performed with another probe station[7] and the measurements gathered with this station confirm the spread in the correlation. A possible explanation could be that HPK slightly adapted their measurement procedure or setup between the pre-production and production causing the offset to be not resolved in their data. However, with regard to the specification limits $\mathcal{O}(\mu A)$, the observed offset towards overall higher sensor leakage currents is negligible.
As mentioned in Section 5.3.2, besides the specification on the global sensor leakage current there is another criterion on the currents measured at 800 V and 600 V, which states that the ratio must be smaller than 2.5 to exclude sensors with breakdown voltages below 800 V. Figure 5.13c shows the correlation of the ratios calculated from KIT and HPK data for all sensors tested in the scope of the SQC. Ratios smaller than 1.5 are observed for 96 % of the tested sensors, while 99.5 % of the sensors are within the specification limit of 2.5. For most of the sensors the ratios calculated from HPK and KIT data are correlated with each other. However, there are some outliers in the ratios determined with data gathered at KIT that are located close to one, while the ratios obtained from HPK data are significantly increased

[6] HPK typically measures the sensors at about 25 °C, whereas the probe station measurements at KIT are performed at 20 °C.

[7] This station is usually used for the characterization of test structures in the scope of the irradiation test and is identical to the SQC probe station. Only IV and CV measurements, but no strip scans have been performed with this station.

and follow a vertical line up to values of about 2.8. This can be explained by the fact that these sensors are sensitive to the environmental relative humidity in a way that they show an early breakdown if they are tested at high humidities. HPK measurements are conducted at relative humidities of up to 50 %. Thus, the leakage currents of humidity sensitive sensors measured at 800 V are increased, whereas the same sensors show normal behavior when they are tested with the SQC setup, where the environmental humidity is smaller than 20 %. The humidity sensitivity of sensors is discussed in more detail in Section 5.5.3. In total there are two sensors with HPK ratios failing the specifications that were not excluded from the shipments. Similar cases were observed among other SQC centers and HPK has been requested to review their data more carefully in order to reliably exclude such sensors from the future shipments. Furthermore, there is one 2S sensor which fails the specification based on the KIT measurement but is within the specification regarding the HPK data. This is the typical behavior of sensors with breakdown voltages around 800 V, where the currents slightly fluctuate from measurement to measurement depending on the individual measurement conditions, such as temperature and humidity. Similar cases were observed among other centers, and it has to be decided for each sensor individually if it can be used for the module assembly. There is always the option to use these sensors for prototype modules that will not be installed in the CMS tracker.

Sensor Depletion Voltage

Figure 5.14 summarizes the results from all depletion voltage measurements. The time evolution is shown in Figure 5.14a starting with the pre-production on the left-hand side. Markers in the plot are grouped batch wise, with each marker representing the depletion voltage of a sensor that has been determined from the CV measurement conducted at KIT according to the extraction method described in Section 5.3.2. The specification holds that for all sensors the depletion voltage should be smaller than 350 V, indicated by the red dashed line. Despite a small group of outliers, the depletion voltage of the pre-production sensors is stable between 280 V and 300 V. Shortly after the beginning of the sensor production a trend towards higher depletion voltages occurs peaking slightly above the specification limit. The depletion voltage is inversely proportional to the bulk resistivity and, thus, to the effective doping concentration of the wafer bulk material. Since HPK purchases wafers from an external company where the bulk is already doped, they cannot tune the depletion voltage themselves. Thus, HPK has been requested to consult with their wafer supplier to receive wafers with sufficient bulk resistivity in order to meet the requirements with regard to the depletion voltage. As a consequence, a clear trend towards lower depletion voltages for the subsequent sensor batches is visible in the time evolution with a stabilization in the range of about 230 V and 250 V at the current production stage. The sensors found to be out of specification will still be used for the module assembly as their depletion voltage only slightly exceeds the upper limit which will not impact the sensor performance in the tracker. Depletion voltage variations within a batch are mainly related to wafers originating from different ingots (see Section 4.4) that have production related spreads in the bulk resistivity.
To cross-check the data provided by HPK, depletion voltages determined at KIT are correlated with the HPK values, which is shown in Figure 5.14b. The plot demonstrates a linear correlation of the data with an underlying Pearson correlation coefficient of about 0.98, confirming an overall good agreement between the KIT and HPK measurements. The quantization of values on the y-axis can be explained by the fact that the HPK depletion voltages are given with a 10 V resolution. Looking at the highest depletion voltages it can be seen that HPK did not resolve the violation of the specification. This is probably related to the larger voltage step size, which is 10 V compared to the 5 V at the SQC centers, resulting in a worse resolved kink

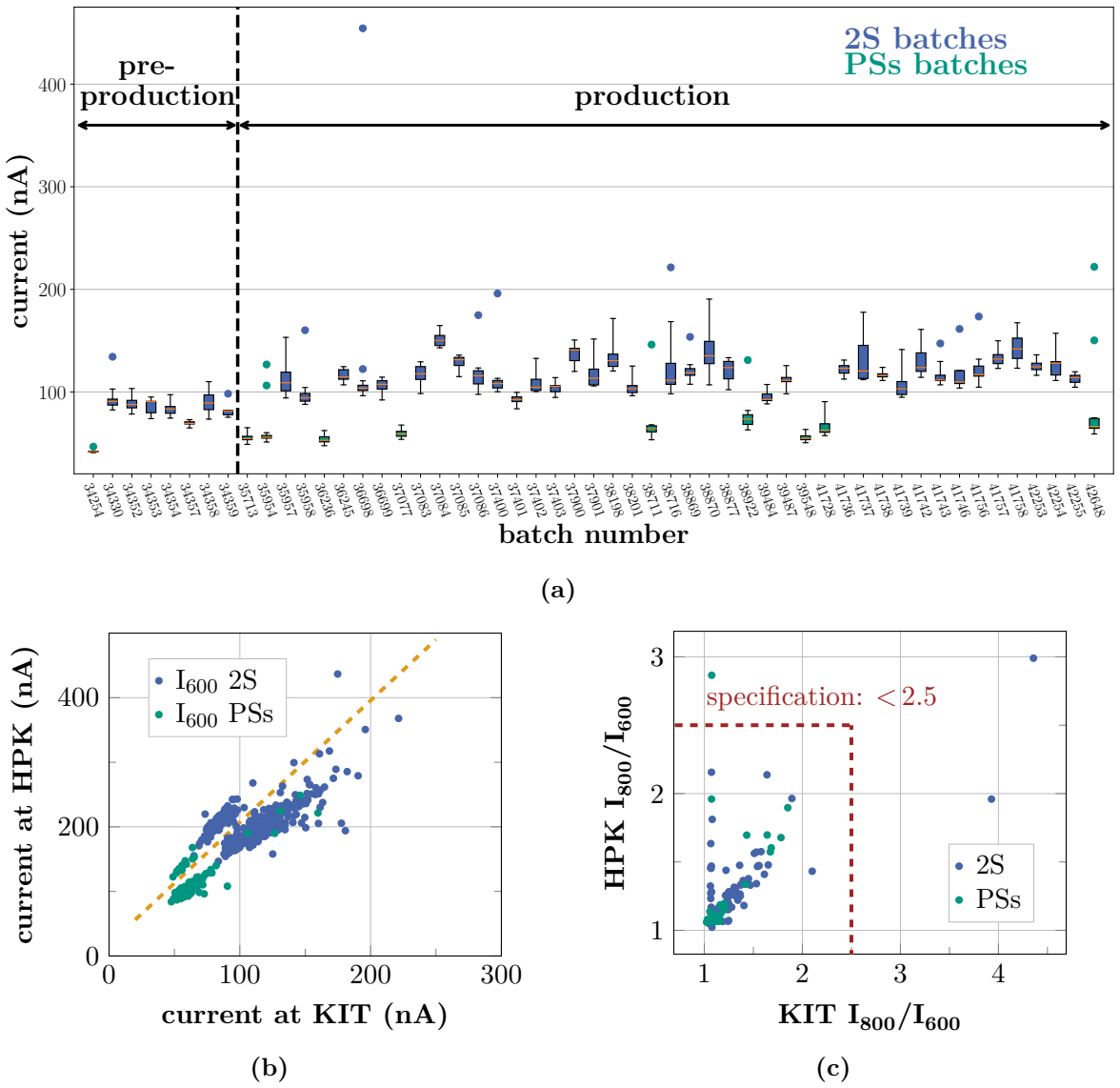

Figure 5.13.: (a) Box-whisker diagrams summarizing the sensor leakage currents measured at 600 V for all strip sensors tested at KIT batch wise. PSs sensors have about half the leakage current of the 2S sensors as they have half the size of a 2S sensor. (b): Leakage currents measured by KIT at 600 V correlated with the currents measured by HPK. The dashed line highlights the separation of the data points into two clusters corresponding to the pre-production batches (upper cluster) and production batches (lower cluster). (c): Correlation plot showing the ratios of the sensor leakage currents measured at 800 V and 600 V calculated from HPK and KIT measurements. Each of the plots includes results from 470 2S and 126 PSs sensors, respectively.

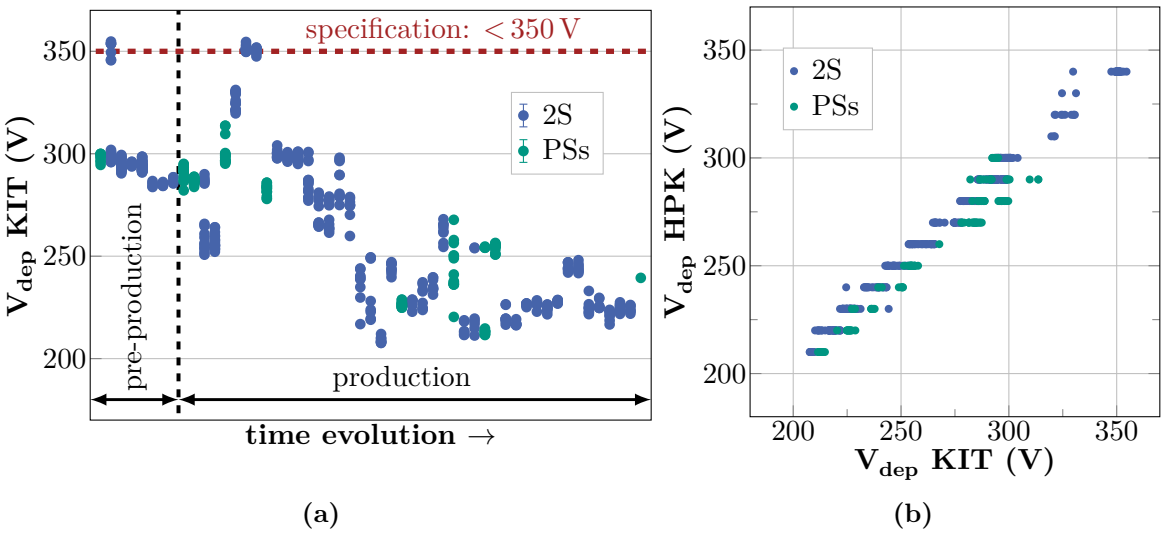

Figure 5.14.: (a): Time evolution of the sensor depletion voltage over the course of the sensor production extracted from all CV measurements conducted at KIT in the scope of the sensor quality control. (b): Depletion voltages provided by HPK correlated with the depletion voltages determined at KIT.

in the $1/C^2$ representation that indicates the depletion voltage.

In summary, one can say that the global sensor parameters measured on the sensors reveal excellent sensor quality and no major problems affecting the overall sensor performance in the tracker have been found so far. Furthermore, measurements of the sensor leakage current and the depletion voltage conducted by HPK are in good agreement with the measurements gathered at KIT in the scope of the SQC. This is of major importance as it proves that one can rely on the HPK data that is provided for each sensor, while the SQC measurements only cover a fraction of sensors in each batch.

5.4.2. Sensor Strip Parameters

Results from the sensor strip scans are summarized in the following. All strip parameters tested in the scope of the SQC were introduced in Section 5.3.2 and the corresponding measurements have been conducted according to the measurement settings summarized in Table 5.5.

Bias Resistor – R_{poly}

The polysilicon bias resistor measurements of all sensors tested at KIT in the course of the sensor production are summarized in Figure 5.15a. Resistance values measured on the individual strips of sensors belonging to the same batch are summarized batch wise in the box-whisker diagrams, while the batch numbers are sorted chronologically representing the resistance time evolution during the production. All pre-production batches have a median resistance larger than 1.8 MΩ with some outliers reaching the upper specification limit of 2 MΩ and, therefore, systematically deviate from the target design value of 1.5 MΩ. This deviation has been observed among all SQC centers and HPK has been requested by the OTSEPP to adapt their polysilicon resistor processing method in order to approximate the target value. Thus, the subsequent production batches show an overall decreased resistance compared to the pre-production with batch medians fluctuating around 1.5 MΩ. Besides the adaptation of the resistance value there has also been a modification of the resistor design due to a potential design weakness that has

been detected and investigated at the beginning of the pre-production. More information about the design change is given in Section 5.5.1. However, all pre-production sensors are still within the specification that holds $(1.5 \pm 0.5)\,\mathrm{M\Omega}$ and refers to the median resistance measured on the individual sensors. Thus, also the sensors with a small fraction of strips reaching the upper limit are within the specification since the median resistance of the corresponding sensors is smaller than the upper limit of $2\,\mathrm{M\Omega}$. In any case, sensors with bias resistor resistances close to, or slightly above the specification are not problematic with regard to the sensor performance in the tracker. The upper limit is defined to ensure that the sensor interstrip resistance is always several orders of magnitude larger compared to the resistance of the polysilicon resistors. This is of particular relevance after irradiation, where the interstrip resistance is significantly reduced due to surface damage caused by ionization (see Section 4.5.2) and values of $\mathcal{O}(\mathrm{G\Omega})$ are expected [Mül21]. Furthermore, after irradiation, the bulk resistivity decreases causing larger voltage drops across the bias resistors. $\mathrm{R_{poly}}$ values significantly larger than the specification would result in undesired high voltage drops across the resistors and consequently high voltage over the coupling oxide.
Compared to the 2S batches the PSs production batches tend to have slightly higher resistances and show an overall larger spread across the batch. Since the general design of the resistors is identical for PSs and 2S sensors this must be related to the wafer processing. However, the spread within a batch of sensors is not as relevant as the spread within the individual sensors. Large resistance deviations cause a nonuniform field configuration inside the sensor that affects the signals induced by particles crossing the sensor. Figure 5.15b shows histograms summarizing the resistance deviations of all tested 2S and PSs sensors at KIT. The deviation calculation is based on the maximum and minimum resistances measured across each sensor that are divided by the median sensor resistance resulting in two deviation values. Only the larger deviation is shown in the histograms. For 75 % of the tested sensors the resistance deviations are smaller than 5 %, while 99 % of the sensors have deviations smaller than 7 %. The largest deviation has been found to be about 8 %. Furthermore, no general trend on the PSs sensors towards higher or lower resistance values for strips located in the wafer middle (see Figure 5.1) is observed among the tested sensors. Although the specifications defined in Table 5.5 hold that the deviation around the sensor median should not exceed ±5 %, all tested sensors are regarded as good. This is motivated by the fact that the slightly larger resistance spread observed on some sensors will not severely affect the AC signal uniformity across the sensor and a strict application of the specification limit would only lead to an unnecessary reduction in sensor yield.[8]

As part of the vendor quality control HPK is requested to monitor the polysilicon resistance on each wafer and to provide the corresponding data. However, these tests are not conducted on the strips of the full-size sensors, but on test structures on the wafer half-moons. Since the whole wafer undergoes the same processing steps, results from the test structures are applicable to the full size sensors. This is validated by correlating the HPK mean resistance with the mean resistance measured on the full size sensors at KIT, which is shown in Figure 5.15c. The Pearson correlation coefficient calculated from the dataset is about 0.98 and confirms the correlation between KIT and HPK data. Resistances measured at KIT tend to be slightly larger ($50\,\mathrm{k\Omega}$ on average), which is mostly related to the different measurement temperature.[9] Furthermore, there might be setup-related offsets between KIT and HPK as well as effects related to different sample sizes from which the respective mean values are calculated. Overall,

[8] Having tight specifications agreed with HPK is beneficial from the CMS Collaboration point of view, as it allows for rejecting sensors already based on small deviations. However, it should always be evaluated by the OTSEPP whether enforcing the rejection is necessary in view of the required quality.

[9] The resistance measured on the polysilicon resistors is temperature dependent and decreases with about $10\,\mathrm{k\Omega}$ if the sensor temperature is increased by 1 °C [Fis20].

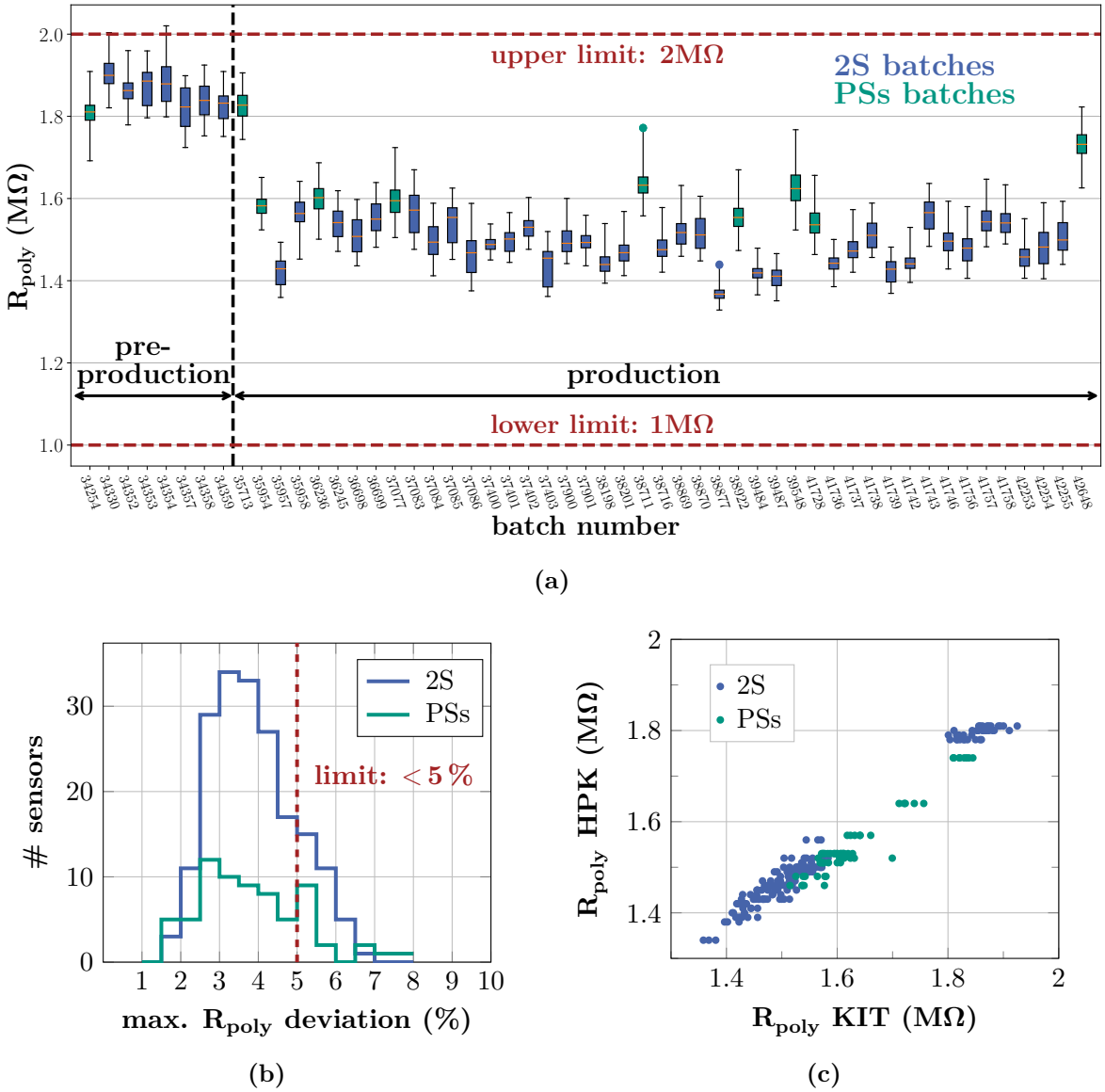

Figure 5.15.: (a): Box-whisker diagrams summarizing the polysilicon resistor measurements at KIT batch wise performed in the course of the sensor production. Batch numbers are chronologically sorted representing the R_{poly} time evolution, starting with the pre-production on the left-hand side. (b): Maximum measured R_{poly} deviation across each tested sensor. The maximum deviation refers to the largest resistance difference measured on individual strips with respect to the overall sensor median. (c): Mean polysilicon resistance measured by HPK on half-moon test structures correlated with the mean resistance measured on the full-size sensors of the same wafer at KIT.

the correlation demonstrates that data provided by HPK can be used as a reliable reference for R_{poly} on the wafer in addition to the results gathered in the course of the overall quality assurance conducted by the OTSEPP.

Current Through Dielectric – Pinhole

In the scope of the SQC measurements conducted at KIT, more than 230 000 strips have been tested so far with regard to the single strip parameters. Among all tested strips only one pinhole was found. For this particular sensor, HPK has not detected any bad strips during the vendor quality control. The small number of pinholes on the sensors tested at KIT is in good agreement with the observations across the other SQC centers and confirms the excellent sensor quality with regard to isolation between strip implant and aluminum readout strip. PQC has measured the breakdown voltage of the coupling oxide to be above 200 V. In any case, sensors with pinholes assembled to 2S modules do not pose a problem regarding the module functionality in terms of noise and signal reconstruction. Measurements with prototype modules presented in [Dro21] have demonstrated that the CBC (Section 3.3.2) is not sensitive to pinholes.

Strip Leakage Current – I_{leak}

The strip leakage current time evolution is summarized in the box-whisker diagrams shown in Figure 5.16 following the same overall representation as the plots shown previously. As for the global sensor leakage current, the median strip current of the 2S sensors is about twice the current of the PSs sensors and all batches show an overall stable behavior for the entire production period. This is expected as there was no indication of a clear trend in the global sensor leakage currents shown in Figure 5.13a, which are mainly composed of the sum of the individual strip currents of the sensors. For a large proportion of batches there are single outliers towards higher currents corresponding to strips with increased leakage current (leaky strips). The position of these strips on the sensor is randomly distributed (see Figure A.3) and can therefore not be assigned to a systematic defect related to the lithographic mask used for the wafer processing. Comparing the current of the leaky strips with the specifications indicated by the red dashed lines, the number of bad strips is negligible for both sensor types. In addition to the single outliers, some batches such as 36698 or 37401 have many strips that are indicated as outliers in the respective box-whisker diagram. These outliers belong to sensors with a group of consecutive strips with leakage currents above the sensor average. These are most likely related to contamination or handling issues during the sensor processing. An example of a 2S sensor from batch 36698 showing this kind of behavior can be found in Figure A.4. Similar observations have been made across other SQC centers. However, the fraction of tested sensors showing this behavior is in the sub percent level and all observed deviations are still within the specification limits. No impact on the overall sensor performance in the tracker is expected as the other strip parameters of these sensors do not show any significant deviation. In any case, one has to keep in mind that according to Section 4.3.2 leaky strips might show slightly higher noise levels in the module, but due to the negligible number of pinholes they do not pose any danger for the amplifiers of the readout chip. For the CBC (see Section 3.3.2) a linear relation between the strip leakage current and the channel noise has been determined in [Dro21]. Increasing the strip leakage current by 1 µA, which is twenty times the 2S sensor specification limit, would result in a channel noise increase of only about 6.5 %.

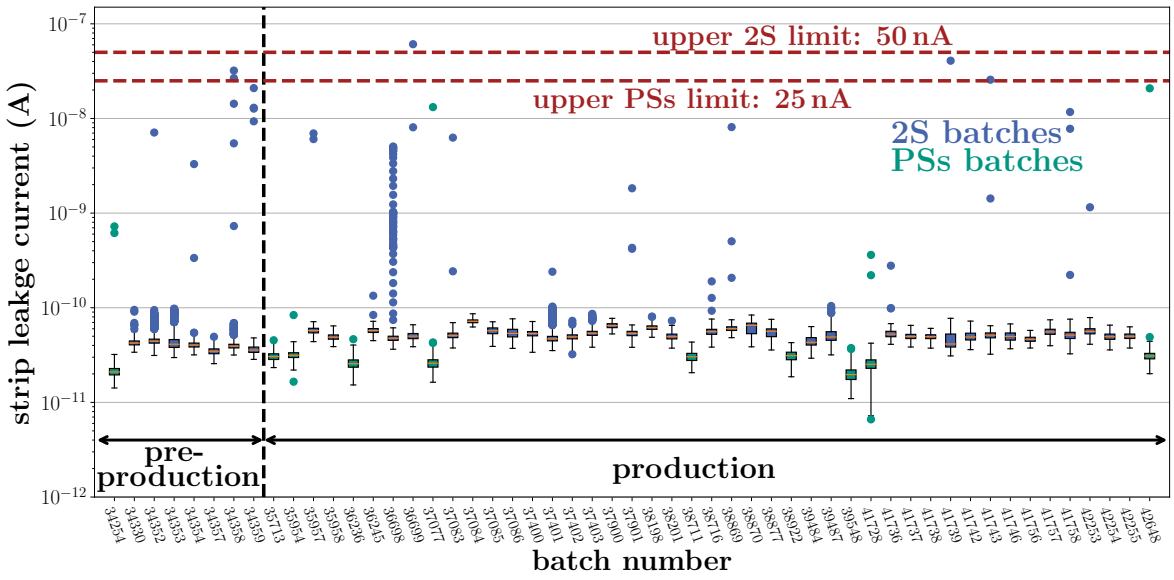

Figure 5.16.: Time evolution of the summarized batch wise strip leakage currents measured at KIT on the 2S and PSs sensors. Strips with leakage currents highlighted as outliers from the box-whisker diagram are mostly still within the specification and no sensors exceeding the allowed number of bad strips has been found.

Coupling Capacitance and Interstrip Capacitance – CC and C_{int}

Figure 5.17 summarizes the results of the strip coupling capacitance measurements batch wise. For both, the 2S and PSs sensors, no trend towards higher or lower capacitances is visible, and all tested strips are well above the respective lower specification limit. The absence of outliers towards higher or lower capacitance values proves that there are no metal shorts or breaks among the tested strips. Combining the capacitances of all tested strips on 2S and PSs sensors and normalizing them to the corresponding strip implant length and width given in Table 5.1 results in $(1.30 \pm 1.2\,\%)\,\mathrm{pF\,cm^{-1}\,\mu m^{-1}}$ and $(1.34 \pm 0.9\,\%)\,\mathrm{pF\,cm^{-1}\,\mu m^{-1}}$ for the 2S and PSs sensors, respectively. Relative uncertainties represent the standard deviation of all tested strips. The measured capacitance values are in good agreement with each other, which is expected as the 2S and PSs wafers undergo the same oxide processing at HPK. Another aspect is the capacitance deviation across each sensor given by the difference of the maximum and minimum measured capacitance. For the 2S sensors, the largest observed deviation is 4.5 pF, while for the PSs sensors it is 4 pF. These small deviations prove that the sensor wafers are processed homogeneously without any significant deviations in the oxide quality or thickness.

The interstrip capacitance measurements conducted on 2S and PSs sensors are shown in Figure 5.18 summarized batch wise. For all tested batches, the small size of the boxes and whiskers indicates an overall small capacitance spread. However, for each batch there are systematic outliers towards smaller capacitances, which originate from strips located close to the sensor edge. In general, the interstrip capacitance measured across the sensors is stable within the sensor middle, while it decreases in the edge region due to edge effects that mostly affect the first (last) four strips on each sensor half. This is exemplarily shown in Figure A.5 on the example of a 2S sensor. Combining the data measured among all tested batches, while excluding the edge strips, and normalizing the values to the strip implant length results in $(0.328 \pm 0.6\,\%)\,\mathrm{pF\,cm^{-1}}$ and $(0.425 \pm 0.4\,\%)\,\mathrm{pF\,cm^{-1}}$ for the 2S and PSs sensors, respectively. The corresponding

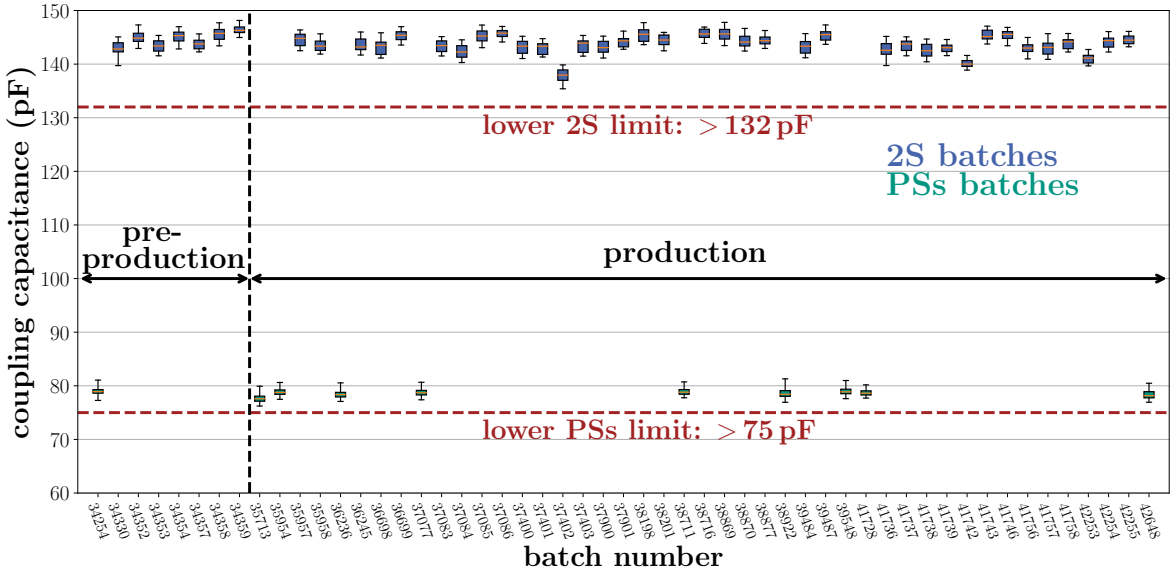

Figure 5.17.: Coupling capacitance evolution measured on 2S and PSs batches at KIT. The measured capacitances are stable across all tested batches and well above the respective lower limit, indicating a consistently high coupling oxide quality.

standard deviations are indicated as relative uncertainties. Although the pitch of adjacent strip implants is smaller for 2S sensors (90 µm) than for PSs sensors (100 µm), the normalized capacitance measured on PSs sensors is larger. Strip implants at the DC- and AC-pads of each strip are broadened, resulting in smaller distances (higher interstrip capacitances) between adjacent strips in the pad region. Pads on the 2S and PSs sensor have the same length and consequently the pad to strip ratio for PSs sensors is larger compared to 2S sensors due to the overall smaller PSs strip length. The contribution of the AC- and DC-pad region to the overall interstrip capacitance dominates, resulting in higher normalized capacitances measured on PSs sensors. As discussed in Section 4.3.2, besides the strip to backplane capacitance[10] the interstrip capacitance is the main contributor to the load capacitance, which in turn affects the noise of the readout channel. Therefore, outliers towards smaller capacitances are not problematic with regard to the sensor performance in p_T-modules. More relevant are outliers with high capacitances, which were not observed among the tested sensors as all strips show values well below the respective upper specification limits.

Interstrip Resistance – R_{int}

Results of the interstrip resistance measurements are shown Figure 5.19. Since the resistance between two strips mainly scales with the length of the strip implant, the median interstrip resistances measured for PSs batches are higher compared to those of 2S batches. Among all measured sensors, only about 2 % of the 33 000 tested strips[11] have interstrip resistances smaller than 100 GΩ and within these 2 % no strips were found to violate the specification limits that are indicated by the red dashed lines. Comparing the median resistances measured during

[10] The strip to backplane capacitance can be estimated by dividing the sensor capacitance obtained from a CV measurement by the number of strips [Har17]. This results in $(1.549 \pm 0.5\,\%)$ pF and $(0.79 \pm 0.3\,\%)$ pF for the 2S and PSs sensors measured at KIT, respectively.

[11] Note that the interstrip parameters are tested on every 50^{th} or 15^{th} strip during the pre-production or production, respectively. Thus, the overall number of tested strips is smaller compared to the single strip parameters.

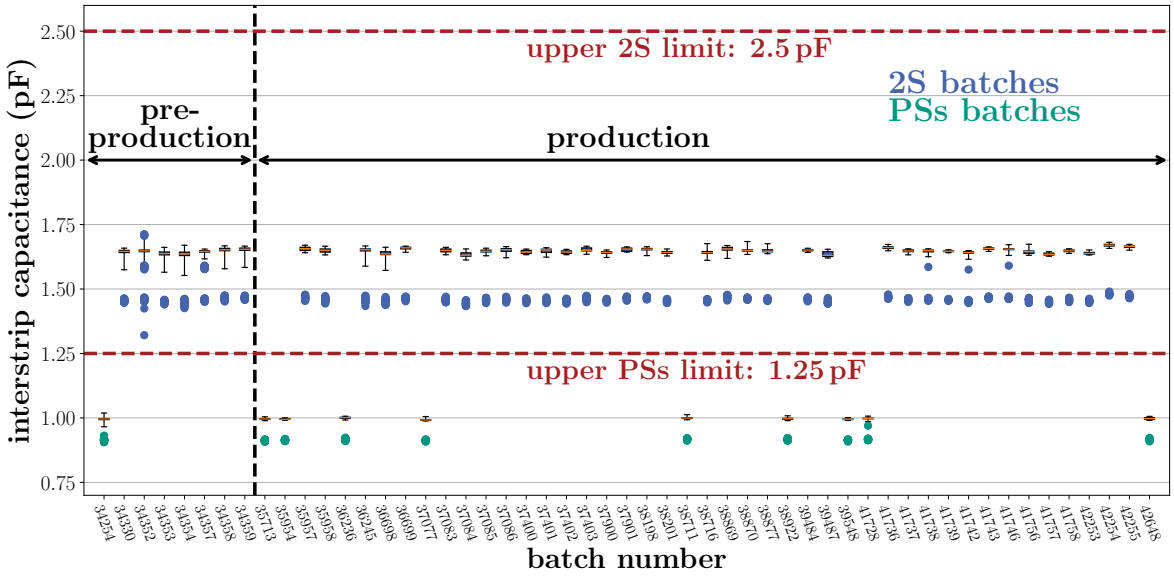

Figure 5.18.: Interstrip capacitance measured between adjacent strips on 2S and PSs sensors at KIT. The capacitance is stable over all tested batches and the overall spread across each batch is very small, indicated by the small boxes and whiskers. Systematic outliers towards smaller capacitances belong to strips close to the sensor edge, which generally show a smaller interstrip capacitance in the measurements. Overall, no strips violating the specified upper limits were found. In this plot the maximum allowed whisker length is increased to ten times the interquartile range for better visibility.

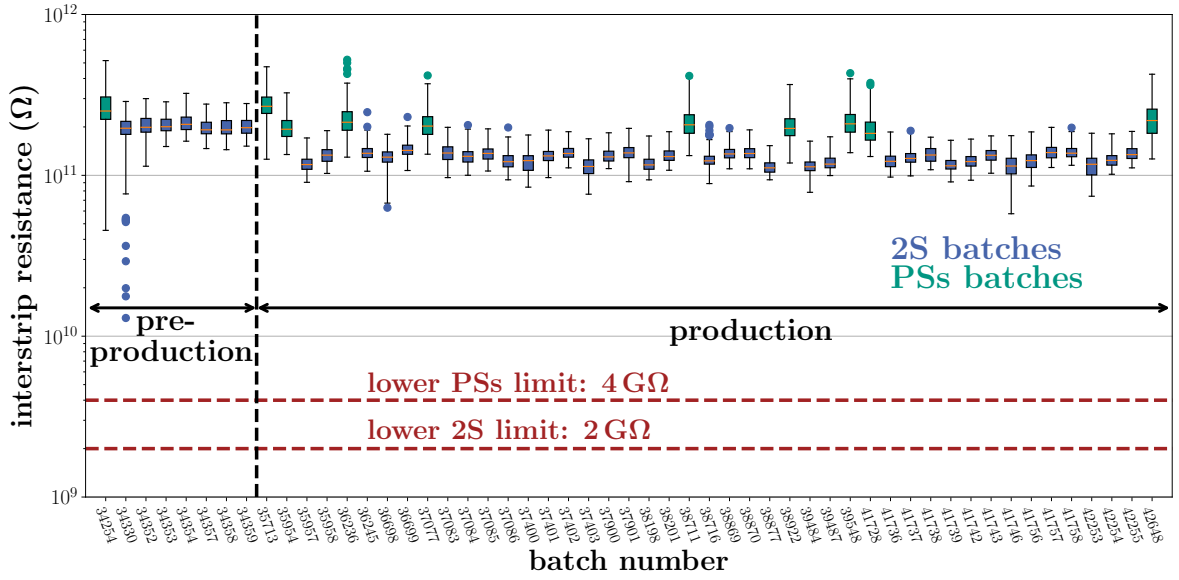

Figure 5.19.: Interstrip resistance measured at KIT on 2S and PSs sensors summarized batch wise. PSs sensors have overall higher interstrip resistances compared to the 2S sensors due to the shorter strip implants. No strips violating the respective specification limits have been detected.

the pre-production and production, there is a slight offset towards smaller resistances for the production batches that is also observed at other SQC centers. Based on the measurements conducted in the scope of the process quality control, no systematic deviations within the monitored process parameters have been found that could explain the overall resistance offset. Furthermore, the resistance distributions measured with different low voltage ramps shown in Figure 5.10b indicate that the offset is probably not related to the change of the low voltage ramp between pre-production and production, as no significant difference between the two ramps is observable. Although the origin of the offset can not be clearly identified, it does not pose a problem with regard to the specification limits. For some individual wafers distributed among different production batches, PQC measurements revealed inhomogeneities in the p-stop concentration. Based on the SQC measurements conducted at KIT no degradation compared to production wafers without inhomogeneity has been observed. Additional studies with irradiated test sensors from wafers with p-stop inhomogeneities have to be performed to prove that also after irradiation, where the interstrip resistance is significantly reduced, no significant degradation related to the inhomogeneity is expected. This, however, is subject to irradiation tests, which is a topic not covered in this work.
During the sensor production, problems were encountered related to electrostatic charges on the sensor passivation causing clusters of strips for which the interstrip resistance was significantly reduced temporarily. Since the electrostatic charges can be neutralized with ionized air, which causes the clusters to disappear, this effect is not represented in the summary plot. A more detailed overview of the observed effects together with a description of the measures taken to prevent them in the further course of the sensor production is given in Section 5.5.2.

To summarize, the results shown from the 2S and PSs sensor strip tests at KIT confirm the overall excellent sensor quality. Despite the polysilicon resistance, where an adaptation of the processing has been requested to slightly reduce the resistance value, all monitored strip parameters show stable values over the entire pre-production and production period so far.

Overall, the monitored strip parameters are well within the specifications and the number of individual strips failing the specification limit is negligible.

5.4.3. Sensor Long-Term Measurements

The main goal of the long-term measurement is to prove that the sensor leakage current is stable over time and does not show an unexpected increase during the sensor operation. In Section 5.3.3 the long-term setup and measurement procedure (current measured over 48 h at 600 V) has already been introduced in detail. The histogram shown in Figure 5.20a summarizes the relative spread of the individual sensor leakage currents during the 48 h measurement period according to Equation (5.2). No current spread exceeding the 30 % specification limit has been observed within 160 sensors tested. However, one 2S sensor is excluded from the histogram since it showed a drastic current decrease during the measurement as depicted in Figure 5.20b. This particular sensor already showed a strongly humidity-sensitive behavior during the probe-station measurements. It can be clearly seen that the long-term operation of the sensor has a positive effect on its leakage current which decreases by a factor of four during the first half of the measurement period and stabilizes at about 500 nA afterwards. This kind of sensor behavior is discussed in more detail in Section 5.5.3. Although the sensor fails the long-term specification, it should not be directly excluded from the module assembly as the leakage current is only decreasing during the measurement and is still within the leakage current specification (7.25 µA at 600 V) of a 2S sensor. In general, sensors with unstable long-term behavior are flagged in the CMS database, and it has to be decided individually whether they are suitable for the module assembly.

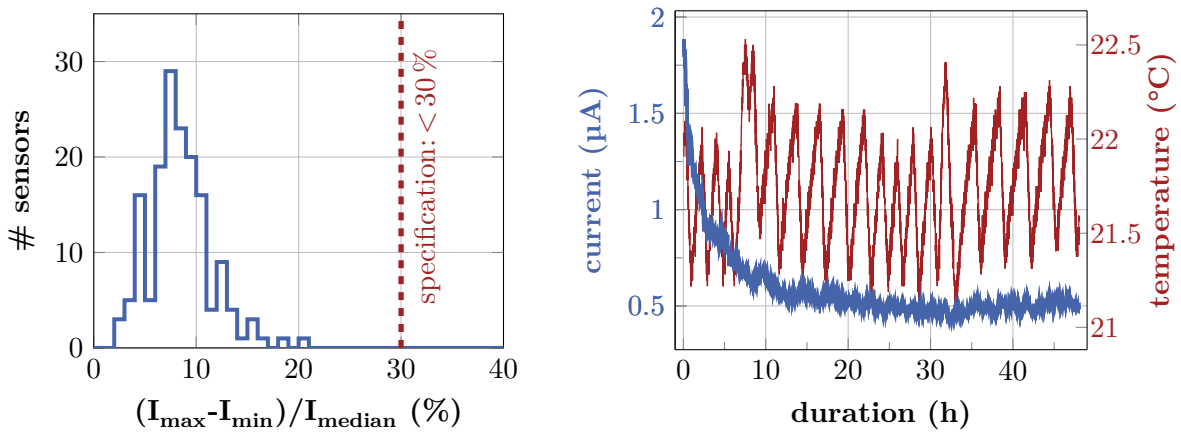

Figure 5.20.: (a): Sensor leakage current deviations during the 48 h long-term measurement, extracted from 160 sensors tested. (b): One 2S sensor with unstable leakage current that strongly decreases over time and thus violates the specification has been excluded from (a).

5.4.4. Sensor Dicing Precision

Various jigs are used for the different steps during the module assembly. Some of these jigs use alignment pins against which the sensors are carefully pushed to establish a precise sensor positioning. Therefore, the sensor alignment in the module, especially the strip-to-strip (2S module) or strip-to-pixel (PS module) alignment between the two sensor layers depends

on the precision of the sensor dicing edges. Crooked cutting lines that are not in parallel to the strip/pixel implants result in an unwanted sensor misalignment. Since the p_T-modules introduced in Section 3.2.2 require precise strip-to-strip (strip-to-pixel) alignment for efficient p_T discrimination, the cutting precision of the sensors is a crucial parameter. The specifications hold that the cutting line of each sensor edge must have a precision of $\pm 10\,\mu m$ ($20\,\mu m$ wide acceptance window) to ensure a sufficient alignment precision during the module assembly. Although the dicing precision measurement is mainly subject to the module assembly procedure (see e.g. [Mai19]), it is also monitored in the scope of the sensor quality control at KIT. This allows to detect potential problems at an early stage, as the module production starts about two years delayed compared to the sensor production.

The dicing precision measurement is based on pictures taken from the sensor corners with a high-resolution digital microscope at 200×magnification and follows the approach introduced in [Sal22]. Pictures are always recorded with the same sensor orientation as indicated in Figure 5.21a, where the unique arrow alignment marker is located at the top right sensor corner pointing towards the first strip of the sensor. At this orientation, the respective sensor edges are labeled according to the cardinal directions. For each corner, the distance d_{ref} between the dicing edges and a reference point at the sensor periphery is determined. Figure 5.21c shows the measurement principle with an example of the upper sensor edge of the top right sensor corner. To determine the position of the cutting edge, the picture is converted into a binary format resulting in a sharp transition between the dark sensor edge and the brighter background, which is exemplarily shown in the left part of Figure 5.21c. Thus, the sensor edge position given in pixel coordinates is extracted for each pixel column individually, by searching for the transition pixel where the content changes from 0 (white) to 1 (black). All edge coordinates reconstructed from the picture columns are then fitted with a linear function

$$e(x) = a_e x + b_e \ , \tag{5.4}$$

to reconstruct the course of the edge within the image, where a_e and b_e represent the slope and y-intercept of the fitted dicing line. As a next step, the midpoint coordinate (x_c, y_c) of the circular shaped alignment mark is determined via template matching. Both, the binary picture conversion and the template matching, are based on the Python package *OpenCV* [Ope22]. By defining a linear function

$$f(x) = -\frac{1}{a_e}x + y_c + \frac{1}{a_e}x + x_c \ , \tag{5.5}$$

that crosses the circle midpoint at (x_c, y_c) and runs orthogonal to the cutting edge $e(x)$, the intersection point (x_i, y_i) of the two linear functions e(x) and f(x) is described by

$$x_i = \frac{y_c - b_e + \frac{1}{a_e}x_c}{a_e + \frac{1}{a_e}} \quad \text{and} \quad y_i = \frac{y_c - b_e + \frac{1}{a_e}x_c}{1 + \frac{1}{a_e^2} + b_e} \ . \tag{5.6}$$

Finally, the distance between the circle center and the intersection point, which serves as reference measure of the cutting accuracy at each corner is derived from

$$d_{\text{ref}} = \sqrt{(x_c - x_i)^2 + (y_c - y_i)^2} \ . \tag{5.7}$$

The reference distance introduced above is determined for each edge at both sensor corners, whereby the difference Δd between the two reference distances represents the dicing precision along the respective sensor edge.

However, the contour of the aluminum mask and the sensor edge might be smeared among adjacent pixels affecting the precision of the measurement. To estimate the resulting uncertainty a toy Monte-Carlo experiment has been performed. Before the calculation of each d_{ref} value, the circle center coordinates (x_{c}, y_{c}) and the position of each edge transition pixel extracted from the binary picture are varied with an offset that is Gaussian distributed using a standard deviation of three pixels. This procedure is repeated 1000 times for the same set of pictures and the standard deviation of the resulting Δd distribution serves as uncertainty estimation on the dicing precision measurement. By following the above described procedure an uncertainty in the order of $\pm 4.5\,\mu\mathrm{m}$ has been found.
Figure 5.21b summarizes all dicing precision measurements including 112 2S and 36 PSs sensors, with the individual edges being represented by the cardinal directions following Figure 5.21a. Combining all measurements (592 edges) results in a mean precision of $-0.1\,\mu\mathrm{m}$ with a standard deviation of $\pm 1\,\mu\mathrm{m}$. The uncertainty related to the measurement method of $\pm 4.5\,\mu\mathrm{m}$ has to be added to the individual values shown in the histograms. However, even considering the uncertainty, the distributions confirm that, independent of the edge position, the dicing precision of all tested sensors is well within the specification of $\pm\,10\,\mu\mathrm{m}$.

5.4.5. PSp Sensor Pre-Production Sensor Tests

As mentioned in Section 5.2.1 the PSp full-size sensors are not included in the standard SQC procedure as they are only IV/CV tested by HPK before being forwarded to an external company that takes care of the MaPSA assembly. Besides the HPK measurements, only results from PQC and IT serve as input for the quality control of the sensors. Thus, with the start of the PSp pre-production in early 2021 the Outer Tracker sensor group decided to test a small fraction of full-size sensors from the first few batches to ensure that the full-size sensors have the desired quality. These tests were performed exclusively at KIT and the results are summarized in the following.

In total, 12 PSp pre-production sensors, each sensor from a different batch, were shipped to KIT. All sensors were IV/CV tested with the KIT probe station. Regarding the total sensor leakage current and depletion voltage, no sensors failing the specifications were found. Furthermore, the measurement results from KIT were consistent with the data provided by HPK. Five of the sensors were subject to long-term tests, which confirmed a stable sensor leakage current over time. A summary of the IV and CV measurements can be found in Figure A.6 and Figure A.7 respectively, while the long-term measurements are summarized in Figure A.8.
To not only evaluate the global sensor performance, but also the electrical behavior of individual macro-pixels, sensor pixel scans with a total of five sensors were performed. Since the PSp sensors are DC coupled there are only three different pixel parameters of interest that can be measured with the probe station: the pixel leakage current and the capacitance and resistance between two adjacent pixels. Similar to the SQC strip sensor measurements, all pixel PSp pixel parameters were measured at 600 V bias voltage, corresponding to the nominal sensor operation voltage in the tracker. In general, there are no dedicated specifications on the individual PSp sensor pixel parameters since the pixels are not tested in the scope of the SQC. However, the global specifications for the strip sensors defined in Table 5.5 multiplied with the pixel length (about 1.5 mm) are used in the following as a criterion for bad pixels to keep the measurements comparable to the strip sensor tests.

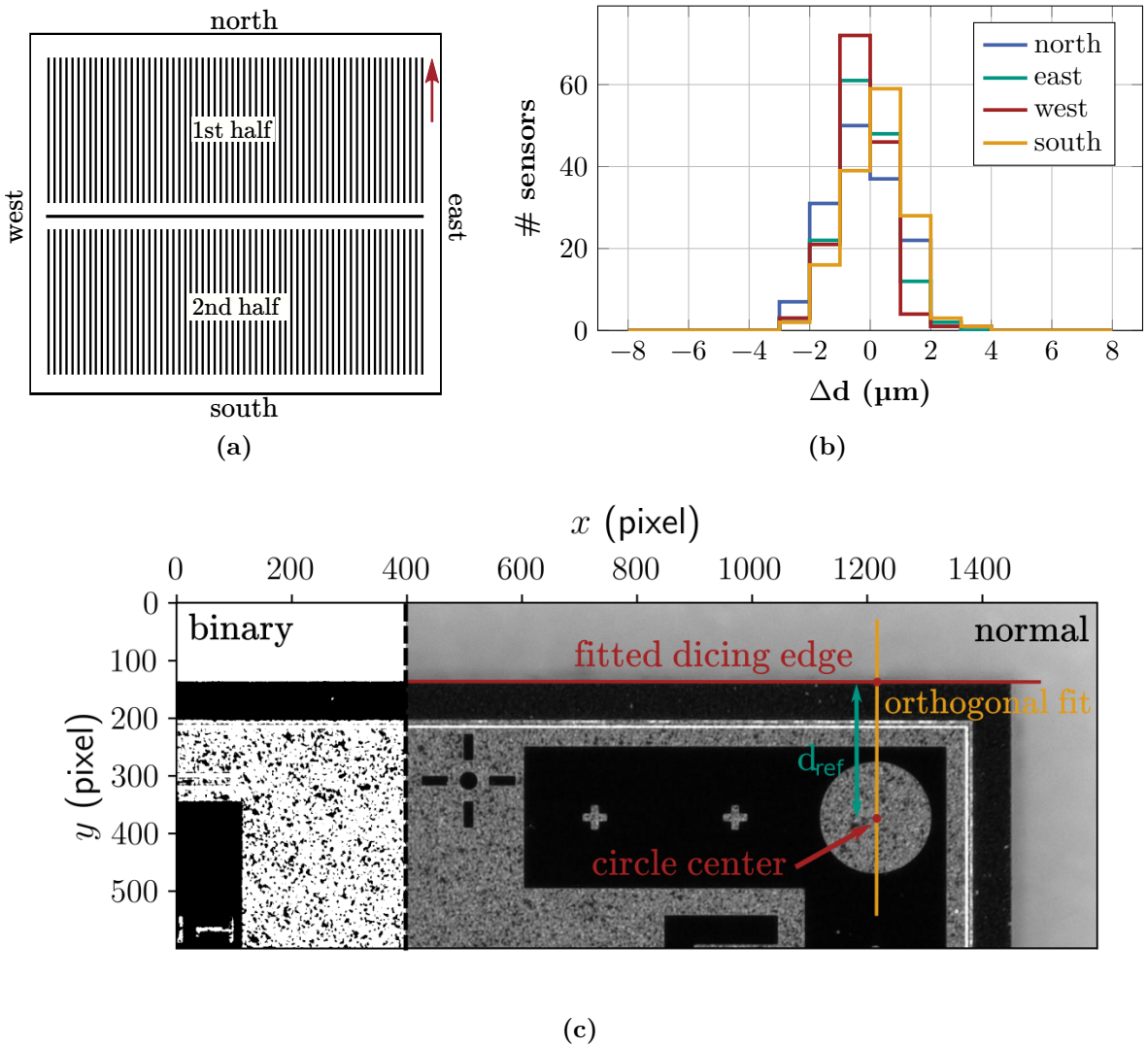

Figure 5.21.: (a): Sensor orientation and naming conventions for the dicing precision measurement. (b): Dicing precision of 159 tested sensors, subdivided into the four different edge positions. (c): Extraction of the reference distance d_{ref} between the circle center and the upper dicing edge on the example of the top right sensor corner. The left part of the picture exemplarily shows a corner fraction after conversion into a binary format to achieve a sharp transition between the sensor edge and the background for the extraction of the edge pixels. The circle center is determined via pattern recognition, while the dicing edge is extracted from a linear fit of the reconstructed edge pixels.

Pixel Leakage Current

Figure 5.22a exemplarily shows the 2D pixel current distribution across one of the tested PSp full-size sensors, while the maps of the other four sensors can be found in Figure A.9. Each sensor was tested in two independent measurement runs, with each run covering one sensor half corresponding to 16 rows of pixels. Testing all 30 208 macro-pixels per sensor would have been too time-consuming[12] and therefore, only every 10^{th} pixel of a row was measured, resulting in about 3 000 tested pixels per sensor. As mentioned in Section 5.1.1, the PSp sensors are processed with under-bump metallization, making it more difficult to achieve reliable electrical contact between the needle and the pixel DC pad. Thus, pixels with leakage currents smaller than 2 pA were remeasured during the sensor scan to ensure that the small currents do not originate from poor electrical contact with the pad. Pixel currents of all five tested sensors are summarized in Figure 5.22b. The median pixel currents vary between 4.3 pA and 6.2 pA. Multiplied with the total number of pixels per sensor the median currents are in good agreement with the overall sensor leakage currents, ranging from 135 nA to 185 nA. Each box-whisker diagram shows a fraction of outliers towards higher currents which mostly originate from pixel clusters with increased leakage current. In the example histogram shown in Figure 5.22a the cluster is located on the left sensor half. Similar clusters were observed on most of the other tested sensors, but at different locations. The clusters might originate from local process variations across the sensor, but are in any case not problematic as none of the pixels exceeds the specification limit of 1.5 nA. Furthermore, the pixel leakage current map shown in Figure 5.22a reveals a circular shaped configuration of pixels with increased leakage current in the middle of the sensor. The circle has about the same size as the rubber-based suction cup of the pickup tool that is used for the sensor handling. This points towards an effect introduced by the pickup tool that locally affects the electrical properties of the sensor. After about one month of storage inside a drying cabinet the area with the circular shaped pattern was remeasured without touching the sensor with the pickup tool beforehand. No pattern was observed anymore[13]. Thus, the effect introduced by the tool is only temporary and does not have a lasting impact on the sensors. In any case, the increase in leakage current is far below the specification and, therefore, does not pose a problem. The influence of the sensor handling on the electrical sensor parameters, especially regarding the pickup tool, is discussed in more detail in Section 5.5.2.

Interpixel Capacitance and Resistance

Results from the interpixel measurements are summarized in Figure 5.23. For all tested sensors both parameters, the interpixel capacitance and resistance, were measured within the same sensor scan. As with the pixel leakage current measurement, each sensor was tested within two independent runs covering one sensor half respectively, where only every 20^{th} pixel on the sensor was tested to compensate for the time-consuming low voltage ramp[14] of the interpixel resistance measurement. Thus, the measurements cover about 1 500 pixels per sensor. Figure 5.23a exemplarily shows the 2D interpixel capacitance histogram from one of the tested PSp sensors. The capacitance of each sensor half is homogenous across the sensor while a small difference between the upper and lower sensor half is visible. This is probably related to slightly different offset values obtained from the capacitance compensation measurement, which were performed for each sensor half individually before starting the measurement. Furthermore, in the top right

[12] Measuring I_{leak} on every 10^{th} pixel of a PSp full-size sensor takes about 7.5 hours.

[13] The effect introduced by the pickup tool might have already disappeared at an earlier stage within the gap between the initial and second measurement.

[14] Measuring C_{int} and R_{int} on every 20^{th} pixel of a PSp full-size sensor takes about 20 hours.

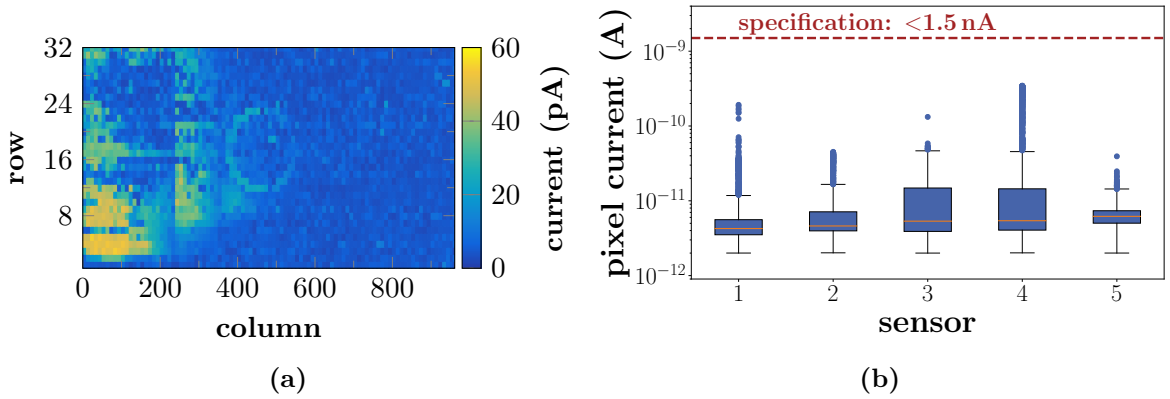

(a) (b)

Figure 5.22.: (a): 2D histogram showing the pixel leakage currents measured across one of the tested PSp full-size sensors. Each sensor row has been measured with a pixel sampling rate of 1/10 pixels. (b): Box-whisker diagrams summarizing the pixel leakage currents of all five tested sensors. No pixels exceeding the specification limit have been found. The histogram shown in (a) corresponds to sensor number two.

sensor corner, where the bias needle was placed during the measurement, there is a small region with decreased capacitance values caused by distortion effects between the strip needles used for capacitance measurement and bias needle. In Figure 5.23b this effect is visible for all tested sensors by the systematic outliers towards smaller capacitance values. During the sensor scans pixels with capacitances smaller than 50 fF were remeasured to ensure that outliers were not related to poor electrical contact between the needles and the DC pads due to the UBM. Overall, no pixels exceeding the upper limit of 75 fF were found. The median interpixel capacitances among the tested sensors range from 56 fF to 60 fF. Since the pixel pitch is identical to the PSs sensor the interpixel capacitance measured on the PSp sensors can be compared to the interstrip capacitance of the PSs sensors by taking into account the different implant length. However, this is only an estimation as each pixel has a punch-through structure that might have an additional impact on the measured capacitance. Assuming a PSs interstrip capacitance of about 1000 fF (see Figure 5.18) corresponds to a PSp interpixel capacitance estimation of about 59 fF, which, considering the measurement uncertainties discussed in Section 5.3.5, is in good agreement with the measured median values on the PSp sensors.

Results from the interpixel resistance measurements of all five tested sensors are summarized in Figure 5.23c. Since the resistance between two adjacent strip/pixel implants is inversely proportional to the implant length, the PSp sensors have significantly higher resistance values compared to the 2S and PSs strip sensors. As mentioned in Section 5.3.2 the resistance between two pixels is measured by driving a low voltage ramp on the pixel DC pad while measuring the change of the leakage current on the DC pad of the neighboring pixel. However, at this point it should be noted that due to the high interpixel resistance of the PSp sensors, the pixel leakage current does not change significantly during the low voltage ramp. Consequently, for functional pixels the extracted resistance values strongly fluctuate, indicating that the resistances are too large to be precisely measured, although the maximum applied low voltage was increased to 10 V.[15] During the sensor scans, pixels with resistance values exceeding 15 TΩ were remeasured to avoid a large spread of the values. This procedure is justified since the goal

[15] For the PSp interpixel resistance measurements the low voltage ramp has been adapted to [0 V, 5 V, 10 V] instead of [0 V, 3 V, 5 V] as it is used in the scope of the SQC for the strip sensors.

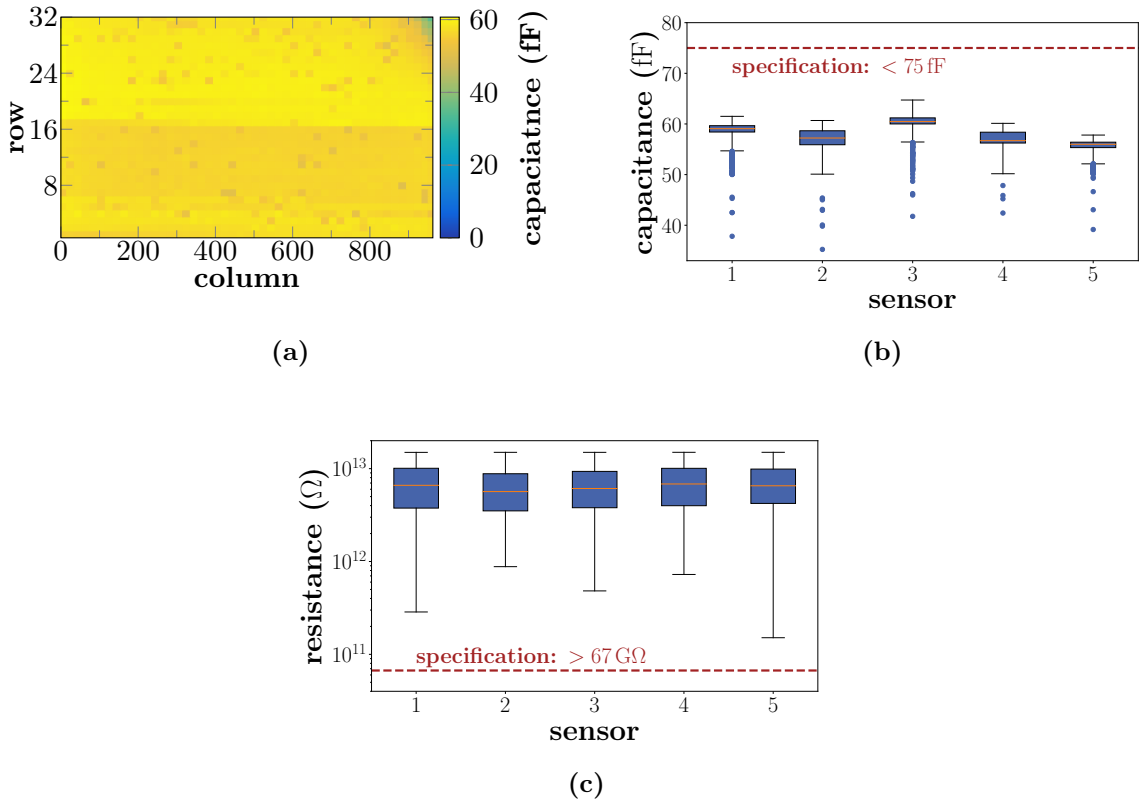

Figure 5.23.: PSp sensor interpixel measurement results. (a): 2D histogram of the interpixel capacitance across one of the tested PSp full-size sensors. Histograms of all tested PSp sensors can be found in Figure A.10. The small capacitance difference between the upper and lower sensor half is related to different offset values from the capacitance compensation measurement. (b): Summary of the interpixel capacitance measurements from all five tested sensors. None of the tested pixels exceeds the upper specification limit. The histogram shown (a) belongs to sensor number two. (c): Results from the interpixel resistance measurement. All tested pixels have resistance values well above the specification minimum. About 1 500 pixels were tested per parameter and sensor.

of the measurement is to detect pixels with low interpixel resistance, which would be noticeable by a strongly increasing interpixel current during the low voltage ramp, which can be reliably detected with the setup. Within the total of about 7 500 pixels tested, the smallest measured interpixel resistance value was 151 GΩ, which is still well above the lower specification limit of 67 GΩ for the PSp sensor.

In summary, the measurements shown in this section confirm that the quality of the tested PSp sensor meets the requirements with regard to the global sensor parameters, but also the electrical properties of the individual macro-pixels. Based on the measurements, feedback has been given to HPK to proceed with the PSp sensor production as intended.

5.5. Specific Findings and Problems during the Sensor Production

As shown in the previous sections, the sensors delivered by HPK until the end of 2022 show overall excellent quality and no severe problems have been observed so far. However, in the

course of the sensor testing at KIT there have been some specific findings and minor problems which, although they are not problematic for the operation of the sensors in the detector, may enable deeper understanding of sensor properties.

5.5.1. Bias Resistor Design Change

In the course of the sensor production, the design of the bias resistor has been adjusted between the pre-production and production phase due to a potential design weakness. The observations and measurements conducted at KIT that led to the design adaptation are briefly summarized in the following.
During the qualification of the PSs pre-series sensors of the batch 33234 a full-size sensor showed an increased leakage current during the interstrip measurements of the first sensor half. Subsequent IV measurements revealed an early breakdown at about 300 V with a sensor leakage current in the order of 40 µA at 600 V bias voltage. The origin of the increased sensor leakage current was tracked down in two steps. First, single strip measurements were repeated and four adjacent bad strips with high strip leakage currents and low bias resistances were found on the first sensor half as it is shown in Figure 5.24a. In a second step, the sensor region of the bad strips was investigated with a Charge-Coupled Device (CCD) infrared camera. The camera allows to precisely locate the origin of high current densities by recording electroluminescence radiation in the infrared spectral range coming from the recombination of charge carriers. The infrared picture was recorded while operating the sensor at 600 V inside the probe station with the light being switched off. In order to match the high current density regions with the positions of the structures on the sensor, the infrared picture is superimposed with a normal picture of the sensor that was taken with identical camera and sensor position. The resulting picture is shown in Figure 5.24b. Red areas correspond to sensor regions with high current densities and are correlated with the bad strips identified during the strip scan. It can be seen that for all four bad strips the currents originate from the edges of the strip implants. In this region the implant edge is located underneath the corner of the meander-shaped polysilicon resistor with the coupling oxide in between. To give a possible explanation for these observations one can think of the following scenario. Whenever a current flows through the resistor, there is a drop of the electrical potential across the resistor that is proportional to the current. Assuming an unexpected high current, the potential drop could cause a short circuit between the edge of the strip implant and the bias resistor, as the resulting field exceeds the dielectric strength of the oxide. The short circuit and the resulting local damage to the sensor substrate can deteriorate strip parameters such as the bias resistance and the strip leakage current as it has been observed for the above introduced sensor. The weakest point is expected to be at the region of the implant edge and the overlapping corner of the polysilicon resistor due to the field peaks occurring in the edge areas. Thus, combining the information from the strip measurements and the infrared picture suggests that the implant edge together with the overlapping polysilicon corner might be a potential weak spot of the sensor design. In order to validate this hypothesis dedicated studies with square sensors from the half-moons of the PSs pre-series sensor wafers were performed in the course of a bachelor thesis [Fis20]. Furthermore, acknowledge must be given to Andreas Nürnberg, who was involved in most of the sensor tests. The main outcome of these tests is briefly summarized in the following.

The overall test strategy was to provoke strip failures similar to the ones observed with the full-size sensor by inducing high strip currents through light shining on the sensor ("sensor stress test"). Hence, the sensors were operated at 1000 V bias voltage while the intensity of the probe station ring light was gradually increased until the desired total sensor leakage current $\mathcal{O}$(mA) was reached. This operation state was maintained for several minutes and

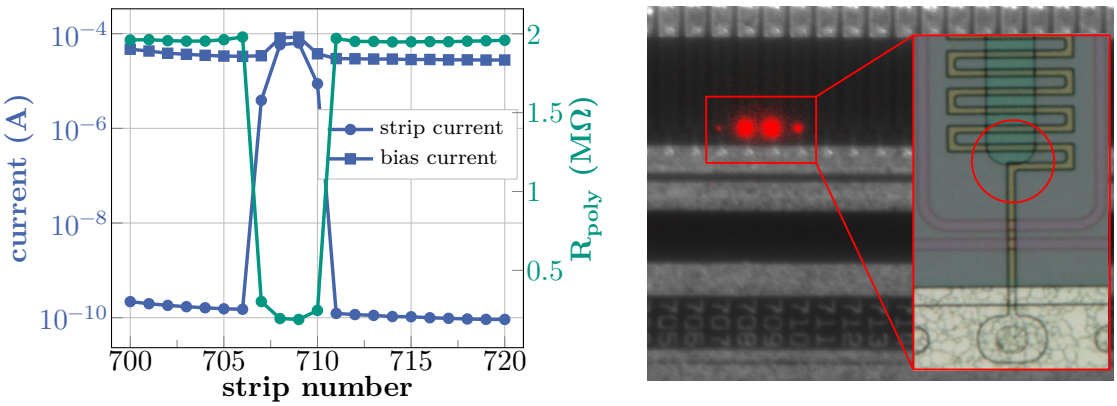

(a) **(b)**

Figure 5.24.: (a): Strip and sensor leakage current together with the bias resistance measured at 600 V on the PSs pre-series full-size sensor of batch 33234 after an early breakdown at 300 V was observed. Four subsequent strips with significantly increased strip leakage current and decreased bias resistance are visible. (b): Picture taken with an infrared camera at the location of the bad strips. The red spots indicate high current densities originating from the edges of the strip implants that are overlapping with the corners of the polysilicon resistors.

the procedure was repeated for different total sensor currents. In between the individual high current treatments strip measurements were conducted in a dark environment to monitor the strip parameters. Figure 5.25a exemplarily shows the outcome of a high current sensor stress test that was performed with a square sensor from the PSs pre-series batch 33234. During the sensor treatment the current was increased in several steps starting with 5 mA and going up to a maximum of 12 mA. Divided by the number of strips this corresponds to strip currents in the range of 39 µA and 90 µA, which is way above the expected strip leakage currents of the sensors in the CMS tracker, even for the highest expected sensor fluence. It can be clearly seen that the failure of strips can be deliberately induced by the treatment described above. During the initial two current steps, only the first 40 strips of the sensor were tested. Strips with increased leakage current appear at a sensor current of 8 mA while outliers of the bias resistance already occur at 5 mA. After operating the sensor at 12 mA almost all strips show leakage currents that are nearly two orders of magnitude larger than the initial strip currents. Some bias resistors show a deviation towards lower resistances, but also outliers with significantly increased resistances are visible. As described in Section 5.3.2, the bias resistance is measured by applying a low voltage ramp to the DC pad of the strip while measuring the resulting increase of the sensor current on the bias ring. In case of a damaged strip, the linear behavior of the current in dependence of the applied voltage from which the resistance is determined can be significantly disturbed. Thus, the resistance values measured for the defective strips should not be regarded as precise physical values. The deviations in the measurement just show that the strip/resistor is damaged and does not behave like a functional strip/resistor anymore.

In order to consolidate the assumption of a potential weakness of the bias resistor design, the same tests were repeated with sensors from previous prototype R&D sensor batches. These sensors feature a slightly different polysilicon bias resistor design, where the edge of the strip implant does not overlap with the corner of the resistor, as it is the case for the pre-series sensors. In general, the bias resistor design is adapted by the manufacturer to achieve the

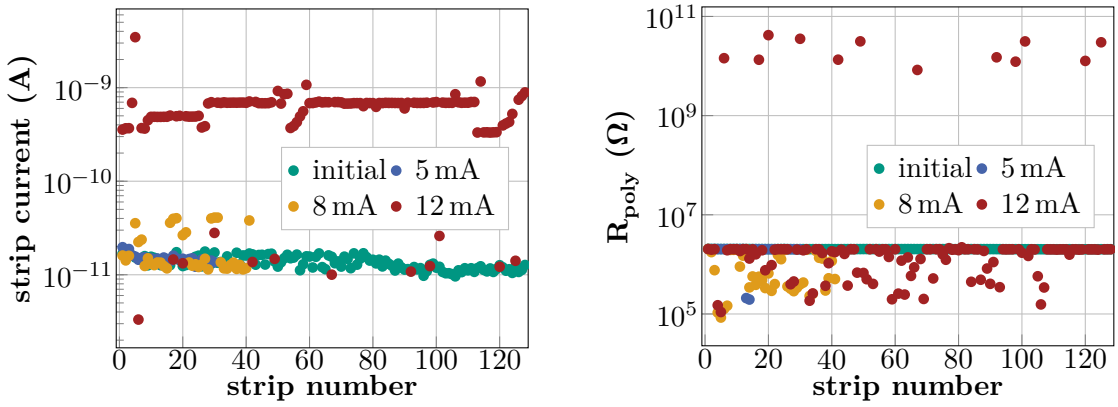

Figure 5.25.: Strip leakage current (a) and bias resistor measurements (b) of a PSs pre-series square sensor after subsequently operating the sensor at high leakage currents to provoke strip failures. Both strip parameters show a clear degradation compared to the initial state after the sensor stress tests. Data taken from [Fis20].

target resistance value based on the process implementation at their facility. Unfortunately, this resulted in the design deviation of the pre-series sensors compared to the R&D sensors. In the course of stress tests with R&D sensors, no strip failures could be provoked. This observation strengthened the presumption that the sensor bias resistor design implemented on the pre-series sensors is a potential weak spot. Therefore, the OTSEPP decided to request a design adaptation by HPK, following the design of the R&D sensors. Figure 5.26 shows a direct comparison between the old and the adapted design, where the corner of the polysilicon resistor is moved away from the edge of the strip implant. At the time the design change was requested, HPK had already started manufacturing sensors for the pre-production phase, and it was therefore only possible to implement the design change for the sensors manufactured within the subsequent production phase. Thus, all pre-production sensors feature the old bias resistor design.

When HPK had delivered the first production sensors to the Outer Tracker sensor testing centers, the sensor stress tests were repeated with several square sensors to validate the robustness of the new design. As expected, the tests confirmed that the adapted design is more robust since no strip failures could be provoked during the tests. However, at this point it must be emphasized once again that the conditions under which the strip failures occurred during the sensor tests do not correspond to the operation conditions of the sensors in the detector, also after irradiation. During the standard quality control tests of the pre-production sensors no further problems related to the bias resistor design were observed among all test centers. Furthermore, in the scope of the pre-production irradiation tests presented in [Mül21], no strip failures related to the R_{poly} design have been observed among all tested irradiated baby sensors. The only scenarios in which sufficiently high strip currents could occur are mechanically damaged sensors, or a beam loss event during the operation in the tracker causing charge signals in the sensors that are significantly larger compared to the signals expected during normal detector operation. Therefore, the pre-production sensors with the old bias resistor design can still be used for the module assembly.

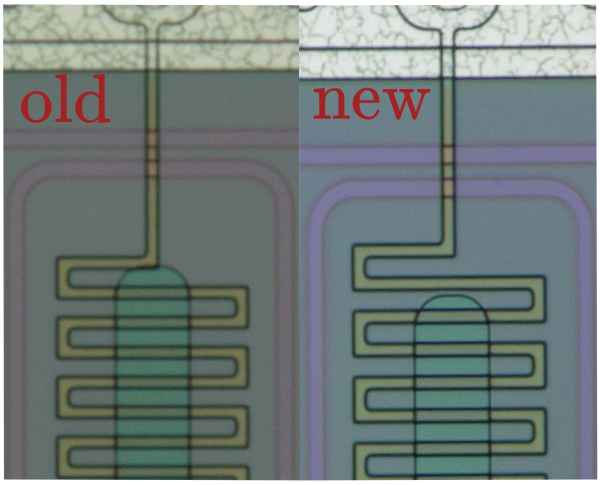

Figure 5.26.: Comparison of the old and new bias resistor design. Within the new design the corner of the meander-shaped resistor is moved away from the edge of the strip implant, making it more robust against high strip currents.

5.5.2. Electrostatically Charged Sensors

In the course of the sensor production it has been observed at various SQC centers that some sensors are electrostatically charged when they are taken out of their envelope. Figure 5.27a shows an example of a charged 2S sensor laying on a white soft plastic-based envelope inlay[16]. An electric field meter is placed above the sensor to measure the voltage that originates from the static charges sitting on the sensor. For this particular sensor, the field meter indicates a voltage of about 350 V, whereas for other sensors voltages of up to 700 V were measured at KIT. Static charges have been found to be responsible for clusters of strips with decreased interstrip isolation and early sensor breakdowns. Although the underlying physical processes causing these problems are currently not fully understood, the observations are briefly summarized in the following as they might be relevant for the upcoming module production. All measurements showing the effects related to charging were conducted at KIT, while similar effects were observed at other SQC centers.

Decreased Interstrip Isolation

In the course of the SQC measurements at KIT, sensors with clusters of strips with reduced interstrip resistance were found, as exemplarily shown in Figure 5.27b. Typically, strips in the cluster region additionally showed slightly increased interstrip capacitances and occasional outliers towards lower polysilicon resistances as depicted in Figure 5.27d and Figure 5.27e, respectively. In [Kön+16] it has been shown with p-in-n strip sensors that the interstrip resistance measured on sensors with electrostatically charged passivation layers is significantly reduced. A similar behavior is expected for n-in-p sensors, for which, due to the additional p-stop isolation, higher charge densities are required to impact the interstrip resistance. At KIT, it has been proven among different electrostatically charged sensors, that the cluster location is correlated with the position at which the sensors are touched with the vacuum pickup tool. The suction cup of the pickup tool and the tool itself are made from ESD safe materials and, therefore, follow the GND potential provided through the operator who is using

[16] Inside the sensor envelope, each sensor is placed in between two layers of soft plastic-based inlays to protect the sensor front- and backside. The inlays also allow to remove the sensor from the envelope without touching it directly.

the tool and stands on a grounded ESD mat. Handling charged sensors with the tool introduces charge inhomogeneities that can cause high electric fields locally, which ultimately influence the strip parameters.
The low voltage ramps performed to extract the interstrip resistance reveal that the interstrip currents measured in dependence of the voltage do not follow a linear behavior. Instead, as shown in Figure 5.27c, there is an exponential increase after exceeding a certain threshold voltage with interstrip currents of up to $\mathcal{O}(\mu A)$ at 5 V. For functional 2S sensor strips, typical interstrip currents range from 20 pA to 50 pA, depending on the applied low voltage. The currents and threshold voltages vary for the individual strips, indicating that strips within the cluster are affected to different degrees by the static charges. Thus, by measuring the interstrip resistance based on a low voltage ramp with a smaller maximum voltage (2 V instead of 5 V), only a few outliers are detected while most of the strips behave normal as indicated by the green markers in Figure 5.27b. In general, due to the exponentially increasing interstrip current that clearly differs from the expected linear ohmic behavior, the interstrip resistances measured for the outliers[17] should not be regarded as meaningful values, they just indicate that the interstrip isolation is reduced. Additional measurements (not shown in the plot) revealed that the interstrip current does not necessarily behave symmetrical for low voltage ramps with negative and positive polarity.
At the present time, the exact physical background to explain the observed measurement artifacts is not yet fully understood by the OTSEPP and only an assumption can be given at this point. The electrostatic potential of the charges on the sensor passivation could attract electrons from the bulk and increase the electron density at the Si-SiO_2 interface and thus deteriorate the interstrip isolation. Furthermore, an enlarged electron accumulation density would increase the polarizability, resulting in a larger interstrip capacitance [Har17], like observed for the affected sensors. As can be seen from Figure 5.27e and Figure 5.27b, R_{poly} outliers are correlated with the strips that show low interstrip resistances even when using the smaller low voltage ramp, indicating that the interstrip isolation in this particular region is most affected by the static charges. Thus, the R_{poly} outliers originate from measurement artifacts related to insufficient strip isolation impacting the measurement. If the individual strips are not properly isolated, the measured resistance does not correspond to a single bias resistor, but a configuration of different resistances in parallel composed of the interstrip resistance and the bias resistance of the adjacent strips. Measuring R_{poly} at smaller voltages, e.g. 1 V instead of 5 V, would result in resistance values in the expected range as the exponential interstrip current indicating the reduced interstrip resistance only occurs at higher voltages (see Figure 5.27c).

Early Sensor Breakdown

Besides the strip clusters with reduced interstrip isolation, charged sensors with early breakdowns at bias voltages significantly smaller than the specification limit of 800 V were found at KIT and other SQC centers. The frequency of sensors with early breakdowns related to static charges is however significantly smaller compared to the occurrence of sensors with clusters of temporary bad strips. As shown in Figure 5.28 using the example of an affected 2S sensor, the breakdown voltage can be increased by operating the sensor slightly above its breakdown voltage for several minutes. This procedure is also referred to as *sensor training* and by repeating the training at different voltages the sensor can be recovered. From the leakage current measured over time during each training step, which is shown in Figure 5.28b, a beneficial effect is clearly visible as the sensor leakage current continuously decreases. Correspondingly, the breakdown

[17] The measurement software automatically performs a linear fit to determine a resistance value, independent of the interstrip current behavior.

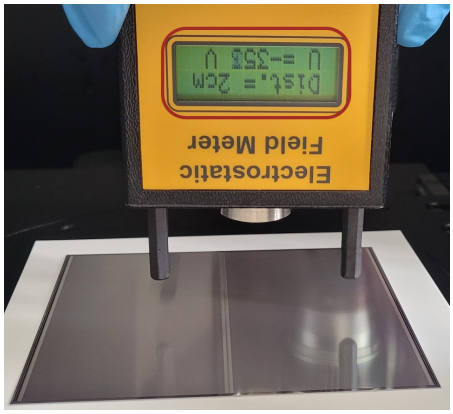

(a)

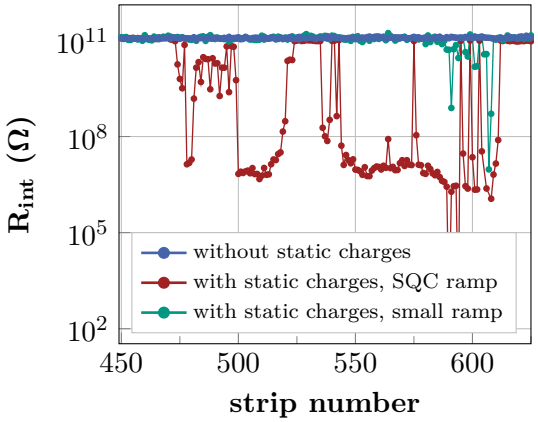

(b)

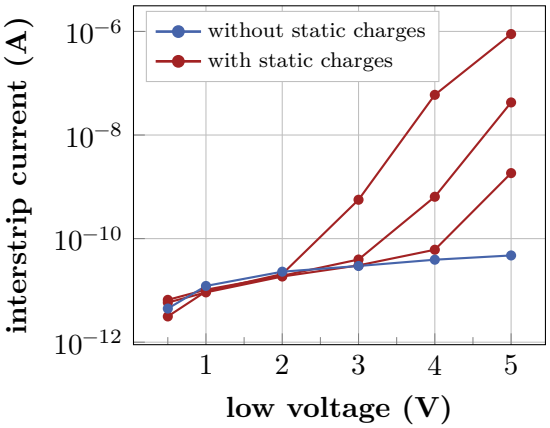

(c)

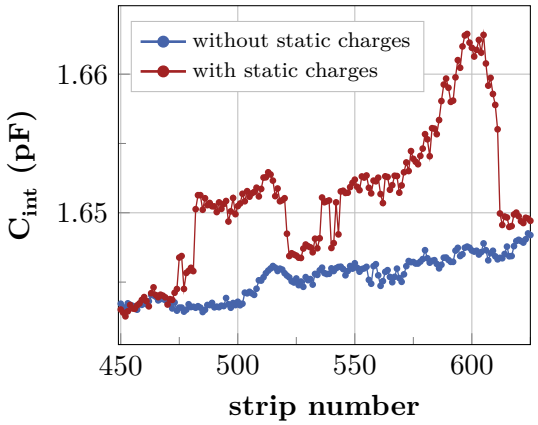

(d)

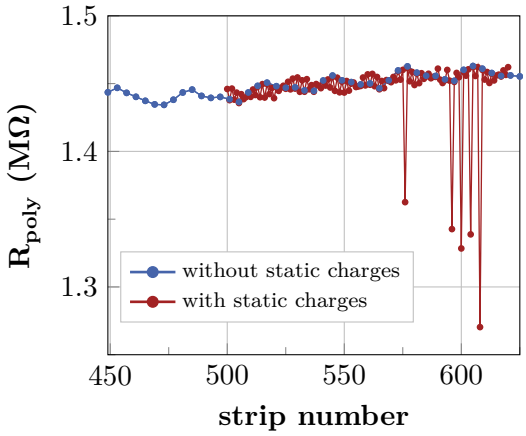

(e)

Figure 5.27.: (a): Electrostatic field meter measuring a voltage of 353 V, indicating static charges on the 2S sensor. Typical strip measurement artifacts related to static charges are summarized in (b), (c), (d) and (e). Affected sensors have clusters of strips with reduced interstrip isolation (b). The interstrip current measured during the low voltage ramp increases exponentially while individual strips show different interstrip currents. Additionally, the interstrip capacitance in the cluster region is increased (c) and there are individual strips with reduced R_{poly} (e). The clustering effect is related to the sensor handling. The pickup tool attracts charges from the overall charged sensor surface and causes high charge densities locally.

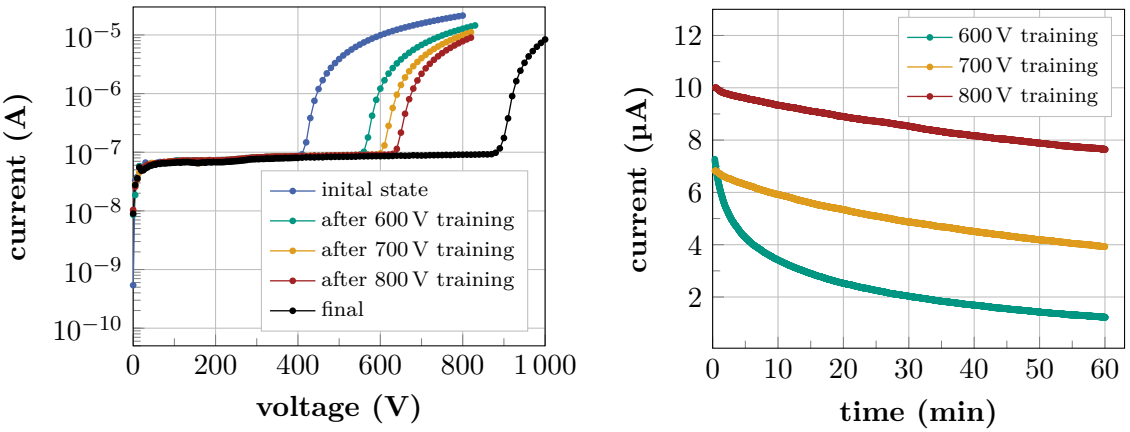

(a) (b)

Figure 5.28.: (a): 2S sensor with initial early breakdown at about 400 V. The breakdown voltage can be increased by keeping the sensor biased for several minutes at a voltage slightly above its breakdown voltage (sensor training) as shown in (b).

voltage increases after each training step, with the training effect being most pronounced after the first step. Only after exceeding a breakdown voltage of 600 V sensor strip tests can be performed with the probe station. The final IV shown in black is within the IV measurement specifications again and was measured after additional training steps at higher voltages and a storage time of about one month inside the drying cabinet.[18]

In any case, static charges on the sensors pose a serious issue with regard to the progress of the sensor quality control, as affected sensors clearly violate the specifications. Strip clusters can remain for several days or even weeks, due to the slow charge dissipation on the sensor. In principle, the charge dissipation could be improved by increasing the environmental humidity during the sensor storage. However, this is not a feasible option as the sensors are also affected by humidity as shown in Section 5.5.3. Furthermore, the recovery of charged sensors with early breakdowns is time-consuming and slows down the sensor qualification progress. The root cause of the sensor charge-up is related to the envelope inlays as they turned out to be not ESD safe.[19] Thus, HPK has been requested by the OTSEPP to make appropriate adjustments to the packaging material to avoid future problems. Negotiations with their packaging material supplier are ongoing. In the meantime, it has been found that all sensors with clusters of strips showing low interstrip resistances can be recovered by using a commercial ion blower [Wol22]. Similar observations for the p-in-n sensors are described in [Kön+16]. The same applies to sensors with a charge-up related early breakdown. They can be recovered much faster with the ion blower than with the above described sensor training. Ion blowers create large amounts of negative and positive ions based on the corona discharge effect and the resulting ionized air is distributed towards the sensor by a fan. Charges located on the sensor surface attract ions of opposite polarity and get neutralized. The ion blower installed inside the KIT probe station (see Figure 5.5) that is used for the full-size sensor treatment, is positioned about 30 cm apart from the sensor chuck to achieve a uniform distribution of the ionized air across the sensor. Usually, application times of about 20 min are sufficient to recover the strips of affected sensors, whereas the recovery of sensors with early breakdowns can take up to an hour. In order to prevent the occurrence of strip clusters with reduced interstrip

[18] Long-term storage of the sensor can also have a beneficial effect, as the static charges dissipates over time.
[19] ESD safe sensor packaging is contractually agreed with HPK.

resistance in the further course of the production, the sensor handling procedure at KIT has been adjusted. Each sensor intended for a strip scan is first treated with the ion blower before touching it with the pickup tool. During the treatment the sensor remains on the envelope inlay, similar to the configuration shown in Figure 5.27a. Thus, static charges on the sensors that would get attracted by the pickup tool are neutralized beforehand. A treatment duration between five and ten minutes inside the closed probe station was found to be sufficient to reliably avoid the formation of strip clusters with reduced interstrip resistance. The additional expenditure of time due to the precautionary treatment is significantly smaller compared to the time needed to recover and remeasure sensors with cluster of strips affected by static charges. However, the ion blower treatment before strip scans should not be performed just once, but every time the sensor is unpacked from the envelope as sensors can get recharged by repackaging.

In summary, the problems related to static charges that were found in the course of the sensor production so far are only of temporary nature and do not pose a general risk for the sensor performance in the CMS tracker. However, especially during the module production, where a much larger number of sensors is handled, the effects discussed above are expected to occur more often. At the current time it is not known whether and how strip clusters with reduced interstrip isolation caused by static charges would affect the module performance. As shown above, for most of the strips an interstrip potential of more than 2 V is necessary to provoke an exponential increase of the interstrip current, while for smaller interstrip potentials the sensor behaves normal. In any case, commercially available ion blowers [Wol22] have proven to be a useful tool to quickly and efficiently recover sensors affected by static charges. Each module assembly center should have an ion blower available and one should think about including the default sensor ion blower treatment into the overall assembly procedure. Since sensors can get charged at any time they are handled, the observed effects underline the importance of ESD compliant workplaces.
Furthermore, it should be noted that the ATLAS collaboration, which currently also purchases silicon strip sensors from HPK for the upgrade of the ATLAS inner tracker [ATL17], has informed HPK about similar charge-up related sensor problems. As for the strip sensors investigated in this work, the packaging material was found to be the root cause for the sensor charge-up. The ATLAS collaboration also makes use of ion blowers to recover affected sensors.

5.5.3. Humidity related Sensor Breakdowns

In the course of the sensor quality control measurements it was observed at several SQC centers that some full-size sensors are sensitive to environmental humidity. Affected sensors show early breakdowns during the IV measurement, whereby the breakdown voltage is humidity dependent. Relative and absolute air humidity must be distinguished. The absolute humidity describes the mass of water vapor in the air and is given in units of $\mathrm{g\,m^{-3}}$. In contrast, the relative humidity is defined by the ratio of the measured absolute humidity and the maximum amount of water vapor that can be absorbed by the air at a given temperature. If not stated differently, all humidity values shown in the following refer to the relative humidity. Figure 5.29 shows the impact of different humidity levels on the sensor leakage current on the example of four different randomly selected 2S sensors from the same batch. For the measurements, the sensors were mounted onto long-term boards (see Section 5.3.3) that were placed inside a climatic chamber [CiK23] allowing to test the sensors under controlled environmental conditions. A picture of the measurement setup can be found in Figure A.12. The sensors were stepwise exposed to different humidities up to 50 % while the ambient air temperature was kept at 20 °C. In general, a humidity related deterioration of the sensor IV can already occur after only a few minutes of exposure time.

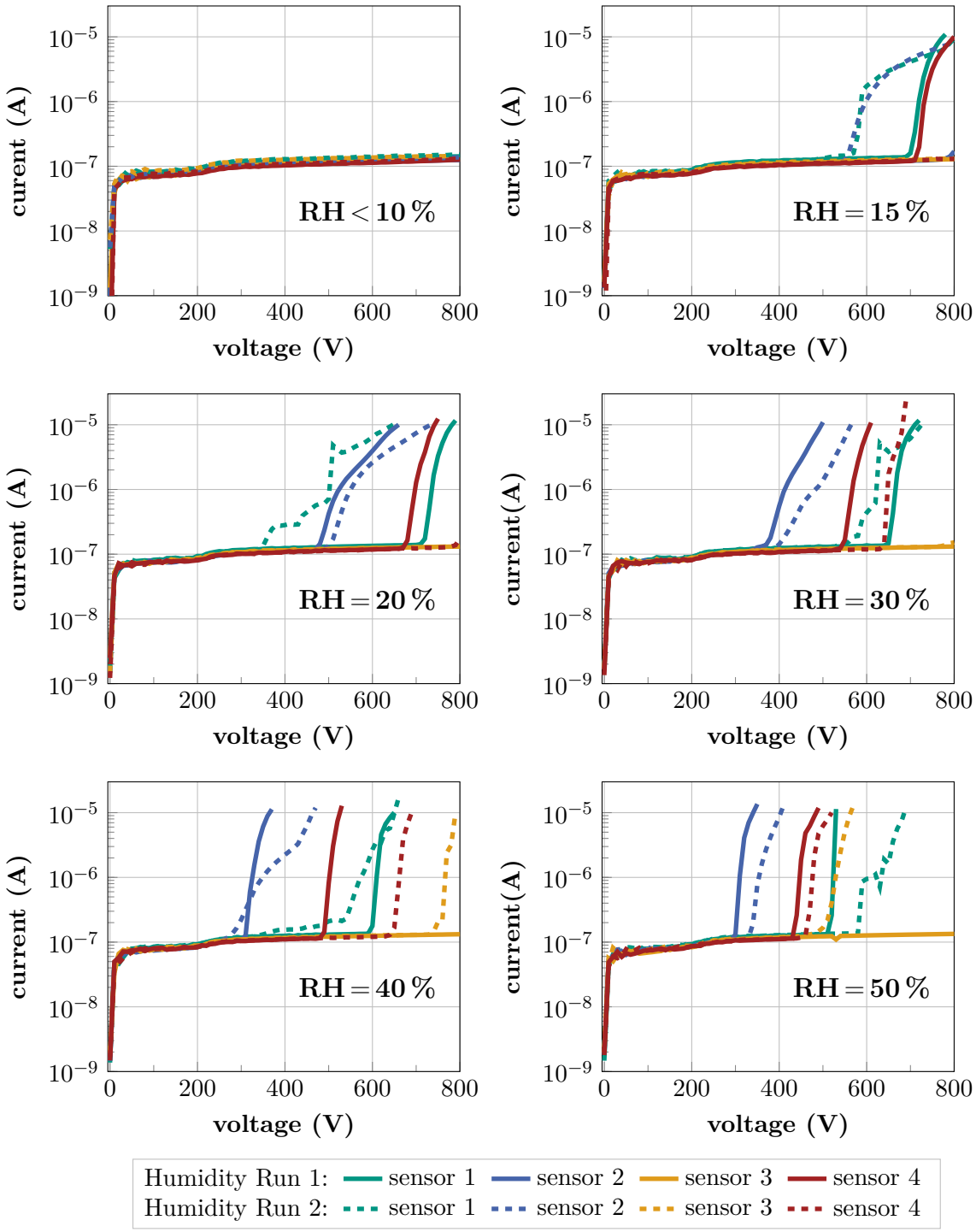

Figure 5.29.: IV measurements with four different 2S sensors at different relative humidities. Measurements were performed using a climatic chamber at a constant air temperature of 20 °C. The IV curves were measured after exposing the sensors for about four hours to the respective humidity. A general trend towards lower breakdown voltages with increasing humidity is observed for almost all sensors.

The IV curves shown in the plots represent the sensor performance after being exposed to a given humidity for about four hours to address for longer exposure times (e.g. during the module assembly). In total, two independent humidity scans with the same sensors were performed one after the other. At relative humidities smaller than 10 % all sensors show a stable leakage current up to 800 V. Increasing the humidity to 15 % already leads to a reduction of the breakdown voltage for some of the sensors. Within the subsequent humidity steps more and more sensors show early breakdowns, while there is a general trend towards lower breakdown voltages at higher humidities. Comparing the behavior of the individual sensors at the same humidity level reveals that they behave differently with regard to the breakdown voltage. Furthermore, the breakdown behavior observed on identical sensors within the two independent humidity scans is not fully consistent, especially at the lower humidity levels. It was observed for all four tested sensors that the reduced breakdown voltage introduced by high humidity exposure can last for a certain period of time ranging from hours up to days, even if the environmental humidity is reduced below 10 % again. However, it was found that the sensor recovery can be accelerated by either operating the sensor slightly above its breakdown voltage (sensor training, see Figure 5.28), or by treating it with the ion blower, similar to the early breakdowns caused by static charges. The exact physical reason responsible for the observed humidity effects is not yet understood by the OTSEPP. Regarding the sensor quality control measurements, the humidity sensibility does not pose a problem as the sensors are always tested in a sufficiently dry environment. In contrast, during the module assembly sensors might be exposed to high humidity levels for several hours, depending on the environmental conditions in the clean rooms. Thus, it is expected that assembly centers will encounter sensors/modules with early breakdowns at a certain frequency. All assembly centers must be made aware of the humidity susceptibility and the methods found to recover the sensors should be communicated accordingly by the OTSEPP. In any case, the measurements demonstrate the importance of adequate sensor/module storage in a dry environment whenever it is possible.

The sensor temperature in the CMS Phase-2 Outer Tracker is expected to be about −20 °C. Thus, evaluating the humidity sensitivity at low temperatures is of special interest. Unfortunately, the climatic chamber available at KIT does not allow for detailed humidity studies at low temperatures due to technical limitations [CiK23]. However, based on low temperature laboratory tests and beam test measurements with different 2S module prototypes (see [Kop22] and Chapter 8), where the sensor temperature was about −20 °C, no limitations regarding early sensor breakdowns were observed. During these tests the dew point of the ambient air was kept at about −50 °C by flushing the setups with dry air. The dew point in the current CMS tracker is in the range of −50 °C to −60 °C [Shv23] and similar values can be expected for the Phase-2 Tracker. As it is not clear whether the absolute or relative humidity level is the critical parameter causing early breakdowns, both parameters should be considered. The humidity tests shown above demonstrate that at 20 °C and relative humidities smaller than 10 %, which correspond to an absolute humidity smaller than $1.73\,\mathrm{g\,m^{-3}}$, the sensors do not show early breakdowns. Assuming a dew point of −50 °C in the tracker and an ambient temperature of −20 °C in close proximity to the sensors results in a relative humidity of about 5 % and an absolute humidity of $0.054\,\mathrm{g\,m^{-3}}$. Even at a sensor temperature of −25 °C the relative humidity would stay below 10 % at −50 °C dew point.[20] Thus, the humidity sensitivity of the sensors is not expected to pose a problem regarding the module operation at low temperatures in the Phase-2 Tracker. It should be considered to perform humidity tests at low temperatures with sensors/modules at institutes with proper infrastructure to further deepen the understanding of the humidity effects.

[20] For the estimation of the respective humidities the online tools [Pam23] and [Sin23] were used.

Part III.

CMS Outer Tracker Sensor and Module Beam Tests

6
Beam Test at DESY

Beam test measurements are a common method to characterize detectors with regard on parameters that cannot be tested in the laboratory due to lack of infrastructure. The *Device Under Test* (DUT) is illuminated with a high-energy particle beam, while the individual particle tracks are reconstructed with a beam telescope consisting of six individual planes, each equipped with a highly granular pixel sensor. Thus, important parameters characterizing the DUT performance such as the particle detection efficiency or the spatial resolution can be precisely measured. In the scope of this thesis, several beam tests with different DUTs have been performed. All of them took place at the *Deutsches Elektronen-Synchrotron* (DESY) test beam facility in Hamburg, Germany. This chapter gives a general overview of the DESY test beam setup and the frameworks that have been used for data acquisition and analysis. Detailed introductions of the DUTs investigated in this work, together with the measurement results, are presented in Chapter 7 and Chapter 8.

6.1. DESY Test Beam Facility and Beam Area

In total, the DESY test beam facility provides three beam lines that can be operated independently. The beam lines are located next to the electron synchrotron *DESY-II*, which serves as injector for the *PETRA-III* storage ring [Wec+04]. Particle beams for the beam lines are indirectly generated from the *DESY-II* synchrotron beam. As shown in Figure 6.1, carbon fiber targets are placed into the beam orbit to generate bremsstrahlung photons that leave the beam pipe tangentially towards the beam line. Secondary targets are used to convert the photons into electrons and positrons via pair production. The generated particles pass a dipole magnet and a subsequent collimator. Based on the strength and polarity of the dipole field, which can be adjusted by the beam test user, beams of different energy and particle charge are picked up by the collimator and are supplied to the beam line. Beam energies in the range of 1 GeV to 6 GeV are available, whereby two main aspects have to be taken into account when choosing the beam energy. On the one hand, high beam energies are always beneficial for the measurement precision in terms of track resolution as less multiple scattering takes place. On the other hand, the measurement precision also depends on the underlying statistics and datasets with many events are preferred. Since the particle rate strongly depends on the selected beam energy, a few hundred Hz at 5 GeV and only a few Hz at 6 GeV, it takes more time to accumulate a certain number of events at higher energies. Thus, the measurements presented in this thesis have been performed at different beam energies ranging from 4 GeV to 5.4 GeV to fulfill the planned measurement program within the given beam time and to have a better precision for specific measurements where needed. Even for the smallest chosen beam energy, electrons behave as minimum ionizing particles (see Section 4.2). More information about the DESY test beam facility and the beam lines can be found in [Die+19] and [Beh+17].

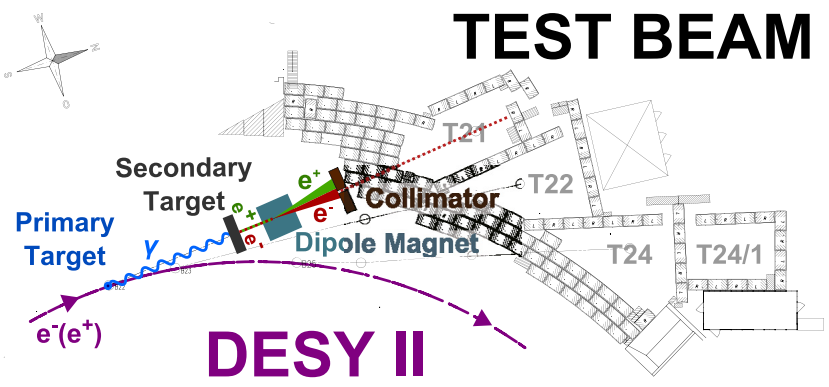

Figure 6.1.: Principle of beam generation at the DESY test beam facility. High-energy bremsstrahlung photons created via a primary target that is placed in the DESY II beam orbit are converted to electron-positron pairs by a secondary target. By passing a dipole magnet the beam is fanned out, and the following collimator only picks up particles of defined energy and charge. [Die+19]

The beam line used for the measurements presented in this thesis provides the DATURA[1] beam telescope shown in Figure 6.2a. It is designed to fulfill most of the user demands regarding integrability of different DUTs, good spatial resolution and appropriate trigger rates. The telescope consists of six aluminum frames, that are split between two independent telescope arms. Each aluminum frame is equipped with a highly granular MIMOSA26 pixel sensor [Hu-+10]. Within an active sensor area of $21.2 \times 10.6\,\mathrm{mm}^2$, the pixels are grouped in 1152 columns and 576 rows with a pixel pitch of 18.4 µm. The binary resolution of 5.3 µm is further improved by charge sharing and has been measured to be (3.24 ± 0.09) µm. Thus, telescope track resolutions down to 3 µm can be achieved, whereby the resolution depends on the spacing between the individual telescope planes and the overall material budget in the beam. Detailed information regarding the telescope tracking performance can be found in [Hen+16].
As schematically shown in Figure 6.2b, the DUT is placed in the telescope center, surrounded by the up- and downstream telescope arms. Since the telescope arms can be moved independently, gaps between the arms and the DUT are minimized to achieve the best possible tracking performance. The right-handed coordinate system used to describe the setup is defined by the z-axis, which runs in parallel to the beam and enters the telescope from the right-hand side. In order to precisely position the DUT with respect to the beam, it is mounted onto an x-y-movement stage and an additional rotation stage.
With $\mathcal{O}(100\,\mu\mathrm{s})$, the integration time of the MIMOSA26 sensors is much longer than the 25 ns readout time of the DUTs investigated in this thesis. Consequently, the telescope data contain many more tracks compared to the DUT and a timing reference is needed to determine the track matching to the one triggered by the scintillators. Thus, an additional detector with an integration time identical to the DUT is installed within the telescope. Different reference planes have been used within the beam tests, a CMS Phase-1 pixel barrel module [Ada+21c] and a single ATLAS FE-I4 pixel assembly [Bar10].
Besides the DATURA telescope, the beam line provides a *Trigger Logic Unit* (TLU) [Cus09] that distributes trigger signals to all Data Acquisition Systems (DAQ) including the telescope, the reference plane and the DUT. The trigger signals come from scintillators, placed at both telescope ends, with a geometrical acceptance similar to the MIMOSA26 active area. By

[1] DESY Advanced Telescope Using Readout Acceleration

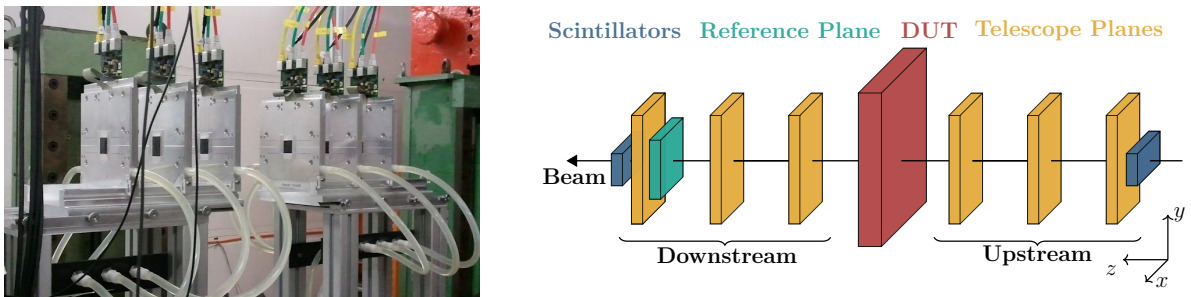

(a) (b)

Figure 6.2.: (a): DATURA beam telescope without additional components. The telescope planes are equipped with high granular MIMOSA 26 pixel sensors. Three of the six pixel planes are installed on each of the two telescope arms, which can be moved independently. As schematically depicted in (b), the DUT is placed in the telescope middle, surrounded by the up- and downstream arms. Particles passing the entire telescope generate signals in both scintillators whose coincidence triggers the event readout. The reference plane compensates the different readout durations of the telescope and the DUT.

coinciding the scintillator signals, the readout of events with particles crossing the entire telescope is triggered.

6.2. Data Acquisition and Analysis

6.2.1. The EUDAQ Data Acquisition Framework

The C++-based EUDAQ framework has been used for data acquisition during the beam tests. It is split into different modules, each of them specialized for a dedicated task. The *Run Control* is the key module and interacts with all other modules using TCP/IP sockets for communication. All detector systems such as the DUT, the telescope or the reference plane have an individual *EUDAQ producer* that connects the systems to the *Run Control*. The producers receive commands to initialize and configure their respective system and to start and stop the data acquisition. Configuration files provide the settings that have to be applied within the initialization and configuration steps to prepare the system for data taking. Furthermore, the producers forward the data collected by their detector to the *Data Collector*, which merges the individual data streams and saves the combined data on hard drive. During data acquisition, the *Monitor* module reads the data files and provides live information such as detector hit maps and correlation plots to the user. Log messages of all modules are displayed and stored by the *LogCollector* for debugging. Once started, the data acquisition continues until a user-defined number of events is reached or the data collection is stopped manually. All events recorded within one data acquisition sequence are summarized to a run, whereby individual runs are always recorded under fixed DUT settings. More information about the EUDAQ framework can be found in [EUD16] and [Liu+19].

6.2.2. The EUTelescope Analysis Framework

For the analysis of the beam test data presented in this thesis, the modular EUTelescope framework has been used. EUTelescope is embedded in the ILCSoft framework [Apl+09], which provides several useful software tools such as the event-based Linear Collider I/O

(LCIO) [Gae+05] data format, the event processor Marlin [Gae+07] and the Geometry API for Reconstruction (GEAR) [Deu07] language. Within the analysis flow shown in Figure 6.3, different processors are subsequently executed by Marlin. Each processor fulfills a dedicated task and has its own set of configurable parameters that are stored in a eXtensible Markup Language (XML) file. The analysis flow with its individual steps is briefly described in the following based on [Bis+20], where a more detailed description can be found.

The detector raw data recorded by EUDAQ is *converted* into the event-based LCIO data format. Some detectors might have noisy channels with hits that do not belong to an actual particle passage. These channels have to be identified and ignored within the further analysis as they would degrade impact the track reconstruction. Thus, after data conversion, the *NoisyPixelFinder* iterates through the data of each detector and searches for channels with hit occupancies[2] exceeding a user defined threshold. All noisy channels are stored in a dedicated database, which can be accessed during the further analysis steps. Within the subsequent *Clustering* process hits of adjacent channels are summarized to clusters for each detector layer. All channels contributing to a cluster are compared with the previously created noisy channel database and in case of a match the corresponding cluster is discarded. Up to this step, the position of channels belonging to a cluster is only given in the local coordinate system of the respective detector, described by row and column indices. For the reconstruction of tracks the hit positions have to be translated into the global coordinate system of the telescope. The *HitMaker* takes the cluster information and determines the local hit position given by the charge-weighted center of gravity for both spatial directions. In case of binary detector data, the individual channels cannot be weighted with their charge signal and the center of gravity equals the geometrical cluster center. The local hit positions of each layer are then transformed into the global coordinate system using the GEAR file, which contains all geometrical information that is need for the transformation. However, the position information provided by the user written GEAR file is rather imprecise, and a software-based *Alignment* is required to optimize the positions of the individual planes with respect to each other. EUTelescope provides different track-based alignment processors with different complexity. Overall, the alignment procedure is split in two steps, the pre-alignment and the more precise iterative alignment. The pre-alignment already takes place within the *HitMaker* process after the coordinate transformation and provides a first rough correction of the telescope geometry. Particle tracks are reconstructed by propagating the hit position of the first plane to all other planes of the setup, excluding the DUT. By repeating this procedure for a subset of events while sampling the deviations between the extrapolated track and the actual hit position (residuals) for each plane, pre-alignment parameters can be extracted that are used to update the detector positions given in the GEAR file. In order to further improve the alignment precision, the following iterative alignment steps are based on the more advanced General Broken Line (GBL) [Kle12] tracking algorithm, which takes into account multiple scattering of beam particles. The GBL track information is provided to the Millepede II framework to solve the linear least-squares-problem with a simultaneous fit of all parameters [Blo07]. Alignment corrections obtained after each iteration are applied to the GEAR file. The whole alignment procedure only includes the telescope layers and the reference plane while the DUT is treated as a passive scattering layer. Furthermore, the alignment does not include position corrections along the beam axis, as the tracking precision is barely sensitive to small variations along the z-axis. All z-positions provided to the GEAR file have been measured during the beam test using a measuring tape and have an accuracy of a few millimeters. After the setup is fully aligned, the *Track Fitter* reconstructs the final tracks

[2] Hit occupancy: number of hits divided by the number of triggers.

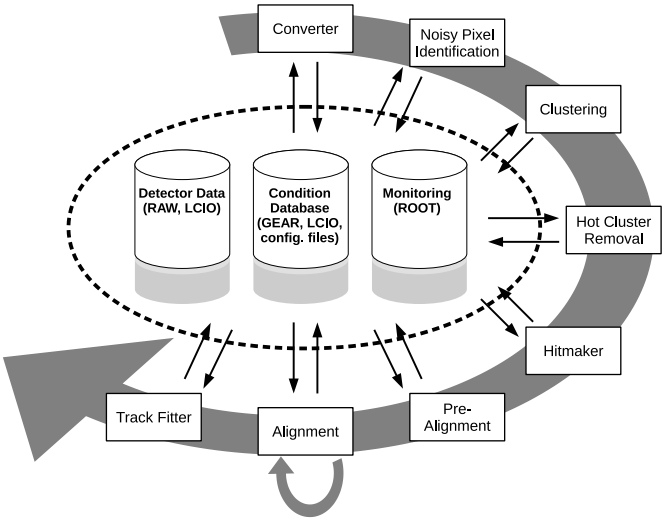

Figure 6.3.: Analysis chain of the EUTelescope framework for the reconstruction of tracks measured with a beam telescope. The different processors used during the analysis are indicated by the white rectangles, each of them fulfills a dedicated task. Within the analysis flow, the processors assimilate input data and provide an updated data version or a new data output to the subsequent processor. Monitoring plots give insight in the analysis progress. [Bis+20]

and saves the corresponding information to a ROOT [Bru+97] file, which serves as input for the DUT analysis.

6.2.3. DUT Analysis

All relevant information needed for the DUT analysis is provided within the ROOT output files generated by EUTelescope after completing the final tracking process of a run. The main objective of the analysis is to characterize the DUT performance regarding central parameters such as the particle detection efficiency by processing the track information of each run. In general, the parameters of interest that can be extracted depend on the type of DUT and the measurement program. Beam test measurements presented in this thesis include efficiency studies with PSp prototype sensors, shown in Chapter 7, and measurements with fully functional 2S modules, shown in Chapter 8. Similar analyses were used in the scope of previous beam tests, which can be found in [Sch19],[Dro21] and [Kop22]. The general workflow of the DUT analysis and all relevant definitions needed for the understanding and interpretation of the results shown in this thesis are introduced in the following. More details can be found in references mentioned above.

Reference Tracks: Not all telescope tracks reconstructed by EUTelescope are suitable for the analysis. Due to the significant longer integration time of the telescope compared to the DUT, each triggered event contains several tracks that do not match the timing of the DUT readout. Thus, cluster information from the reference plane is used to extract tracks with proper timing. Only tracks passing the reference plane within a defined spatial window that is placed around

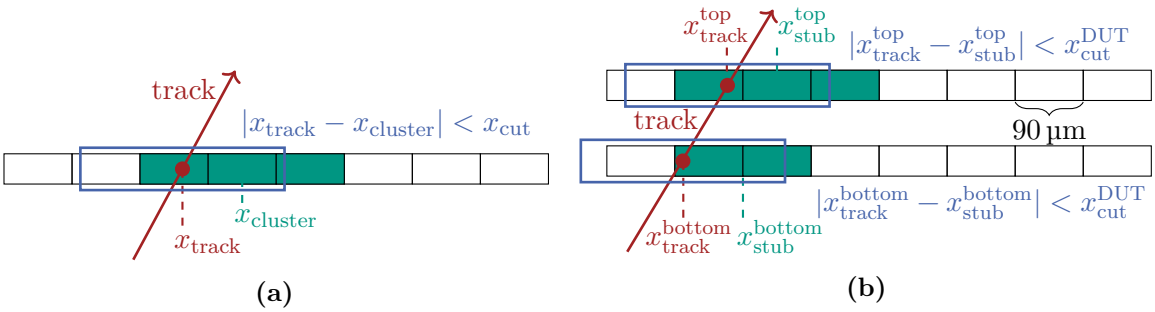

Figure 6.4.: (a): Illustration of the cluster matching for the x-coordinate. Tracks are matched to clusters of the sensor, if the distance between the cluster center and the track is smaller than the applied matching cut x_{cut}. (b): Illustration of the stub matching. Reference tracks only match the stub signal, if the track distance to the cluster center in the seed and correlation layer is smaller than the residual cut $y^{\text{DUT}}_{\text{cut}}$. Modified from [Kop22].

the center of reference plane clusters are assigned as *reference tracks* and serve as input for the further analysis steps. The corresponding residual cuts in x and y direction are defined by

$$\underbrace{|x^{\text{ref}}_{\text{cluster}} - x_{\text{track}}|}_{x\text{-residual}} < x^{\text{ref}}_{\text{cut}} \quad \text{and} \quad \underbrace{|y^{\text{ref}}_{\text{cluster}} - y_{\text{track}}|}_{y\text{-residual}} < y^{\text{ref}}_{\text{cut}} \ , \tag{6.1}$$

with x/y_{track} representing the coordinates of the interpolated track intersection with the reference plane and $x/y^{\text{ref}}_{\text{cluster}}$ describing the position of the reference cluster center. Figure 6.4a depicts the matching of a track and a cluster for the x-coordinate. The acceptance window size given by $x^{\text{ref}}_{\text{cut}}$ and $y^{\text{ref}}_{\text{cut}}$ depends on the geometry of the reference plane. Two different reference planes were used for the beam test measurements presented in Chapter 7 and Chapter 8. An ATLAS FE-I4 single chip detector [Bar10] with a pixel dimension of 250 µm×50 µm, and a CMS BPIX module [Ada+21c] with a pixel size of 150 µm×100 µm. The reference plane residual cuts applied within the analysis correspond to the pixel dimensions of the respective reference plane sensor that was used for the measurement.

Cluster Efficiency: The capability of the DUT to detect the passage of charged particles is quantified by the *cluster efficiency*. As the name indicates, it is determined by matching reference tracks to DUT clusters. The track matching procedure is again based on residual cuts (see Equation (6.2)) by defining an acceptance window for the interpolated tracks around the DUT cluster center.

$$\underbrace{|x^{\text{DUT}}_{\text{cluster}} - x_{\text{track}}|}_{x\text{-residual}} < x^{\text{DUT}}_{\text{cut}} \quad \text{and} \quad \underbrace{|y^{\text{DUT}}_{\text{cluster}} - y_{\text{track}}|}_{y\text{-residual}} < y^{\text{DUT}}_{\text{cut}} \tag{6.2}$$

Tracks fulfilling the matching criteria are referred as *matched cluster tracks*, whereby the individual cuts have to be adapted to the segmentation of the DUT.
After iterating through all reference tracks of a run and applying the residual cuts, the cluster efficiency ϵ_{cl} is given by the ratio of matched reference tracks according to Figure 6.4a and the total number of reference tracks

$$\epsilon_{\text{cl}} = \frac{n_{\text{matched cluster tracks}}}{n_{\text{ref tracks}}} \ . \tag{6.3}$$

Stub Efficiency: In case of having a 2S module (see Section 3.3) as DUT, in addition to the cluster efficiency of the individual sensors, the module *stub efficiency* can be extracted. Stub information provided by the module contains the stub position and the stub bend. The stub position defines the location of the cluster center in the seed layer. In contrast, the stub bend only describes the offset between the stub position and the cluster center in the correlation layer. Therefore, the actual cluster position in the correlation layer has to be calculated from the stub position and the stub bend. As shown in Figure 6.4b, reference tracks are matched simultaneously to the clusters in both sensors layers by applying the same x-residual cut as for the cluster efficiency. Only if the matching criteria in both sensor layers are met, the reference track is assigned as a *matched stub track*. After iterating through all events of a run, the stub efficiency ϵ_{stub} is given by the ratio of matched stub tracks and the total number of reference tracks

$$\epsilon_{\text{stub}} = \frac{n_{\text{matched stub tracks}}}{n_{\text{ref tracks}}} \ . \tag{6.4}$$

Efficiency Uncertainties: Since the efficiency measurements equal a counting experiment, the statistical uncertainty on the extracted efficiency value is given by the standard error of the mean value of a binomial distribution

$$\sigma_\epsilon = \sqrt{\frac{\epsilon(1-\epsilon)}{n_{\text{ref tracks}}}} \ . \tag{6.5}$$

The uncertainties of all stub and cluster efficiencies shown in this thesis have been calculated based on the above equation. However, for $\epsilon = 1$ and $\epsilon = 0$ the above equation does not provide a reasonable uncertainty value. For those two cases, the uncertainties are calculated as a Clopper-Pearson interval using a confidence level of 68.3 %.

Spatial Cuts and Channel Masking: Depending on the DUT dimensions, data may contain valid reference tracks of particles that did not pass the DUT within its active area. According to Equation (6.3) this would reduce the overall cluster efficiency. Therefore, *spatial cuts* on the interpolated track intersection at the DUT position are required to discard reference tracks pointing outside the active DUT area.
Channels with missing or broken bond connections are not able to detect particles as the charge signals from the sensor cannot be forwarded to the respective channel of the readout ASIC. Affected channels appear as inefficient in the analysis and would negatively affect the overall DUT efficiencies. Since the reason for their inefficiency is known and is not related to the general DUT property, these channels are masked. Additionally, the DUT might have noisy channels that imply particle hits not belonging to an actual particle passage. Already within the EUTelescope analysis chain, clusters containing channels with hit occupancies exceeding a defined threshold are removed from data. Thus, reference tracks pointing to a region with noisy channels cannot be matched to a cluster, resulting in local inefficiencies that have to be accounted for. All reference tracks pointing to masked channels are discarded and do not contribute to the efficiency calculation.
Figure 6.5 shows exemplary global cluster efficiency maps of a pixel sensor before and after applying spatial cuts and masking of channels.

DUT post Alignment: All DUT positions given in the initial GEAR file are estimations based on measurements with a tapeline and do therefore not match the accuracy needed for the analysis. Since EUTelescope only includes alignment procedures for the telescope and the reference plane, the DUT has to be aligned based on the output of the analysis. Thus, after selecting valid reference tracks and masking inefficient DUT areas, the remaining tracks are used

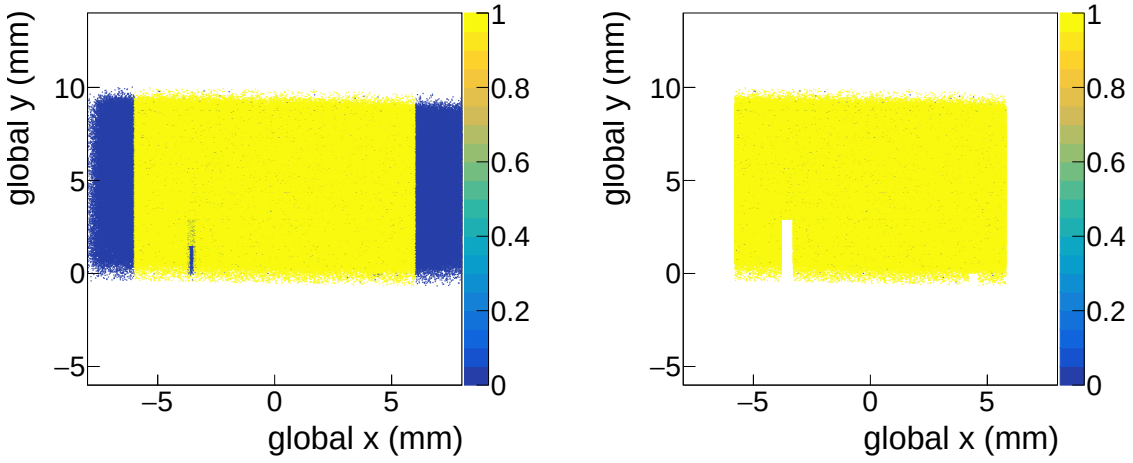

Figure 6.5.: (a): Example of a two-dimensional DUT cluster efficiency map of a pixel sensor without any spatial cuts and channel masking. Inefficient regions (blue) on the left and right side originate from reference tracks passing the DUT outside its active area. Small inefficient regions within the active area are related to noisy channels or broken bond connections. (b): Same efficiency map after applying spatial cuts on the reference tracks and masking inefficient channels.

to calculate x and y residuals, which serve as input for the extraction of alignment corrections. Different degrees of freedom can be corrected depending on the residual type and axis. The individual corrections are applied subsequently to the GEAR file, whereby after each correction step the final tracking process with EUTelescope and the DUT analysis have to be repeated to accommodate the updated DUT position. Overall, the DUT post alignment includes position corrections for all three spatial direction as well as rotations around the y and z axis. A more detailed description of the alignment can be found in [Kop22].

TDC Distribution and Cuts: During the beam test measurements there is no synchronization between the particle beam and the signal sampling of the DUT readout ASIC, as it will be the case for the operation in the CMS tracker. In order to measure realistic efficiencies, representing the best possible DUT performance, charge signals generated by particles traversing the DUT have to be sampled at their maximum. In CMS, detector latencies would be found for maximum signal. The arrival of trigger signals is super sampled by a 320 MHz clock, splitting the 25 ns DUT readout frame into eight time-to-digital converter (TDC) phases. Each TDC phase is evaluated independently, resulting in efficiency distributions as they are shown in Figure 6.6. Different DUT parameters influence the shape of the distribution. On the one hand, the time the signal stays above the threshold decreases with increasing threshold. On the other hand, the overall charge signal decreases with irradiation as a fraction of charge carriers get trapped by irradiation induced defects. Both aspects reduce the overall cluster efficiency, but also the number of efficient TDC phases. Thus, only the most efficient phase is used for the extraction of final DUT parameters in order to get representative results reflecting the most realistic DUT performance with regard on the operation in the CMS tracker. For the distributions shown in Figure 6.6 the most efficient TDC phases are coloured.

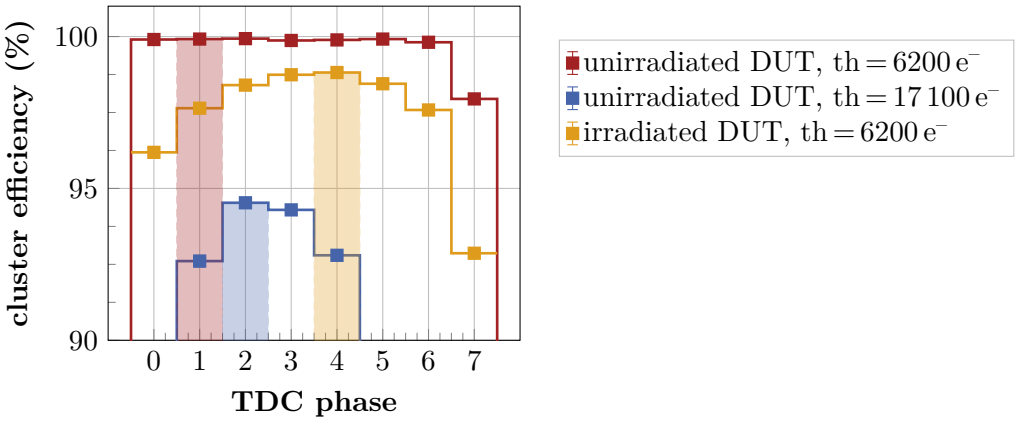

Figure 6.6.: The TDC phase binned cluster efficiency depends on different DUT parameters. High readout thresholds (th) and irradiation reduce the overall cluster efficiency but also the number of efficient bins. DUT parameters are extracted from the most efficient bin only, highlighted by the background color.

7

Irradiated Single MaPSA Beam Test with FZ290 Sensors

In order to find the most suitable sensor material and design for the CMS Outer Tracker PSp sensors, studies with prototype sensors processed on thFZ200 wafers have been presented in [Sch19]. Besides a general electrical characterization of the sensors, the studies included beam test measurements with unirradiated and irradiated prototype sensors. The impact of different sensor irradiation levels on the particle detection efficiency was studied, as well as the influence of different sensor design approaches. Similar studies with unirradiated prototype sensors based on the thicker FZ290 wafer base material were performed in [Wit20]. To complete the overall picture with regard to the performance of differently irradiated FZ290 prototype sensors, which was decided to be the final sensor material for the CMS Outer Tracker (Section 5.1), another series of beam test measurements was conducted in mid 2020 at DESY in the scope of this thesis. In addition to efficiency studies at perpendicular beam incidence, the impact of inclined particle passage on the global sensor detection efficiency was studied. This is of particular interest, as the biasing structures that are implemented on the sensor to connect the individual pixels to the global sensor bias ring have been found to cause inefficient regions on the sensor at perpendicular beam incidence. The main outcome of the beam test measurements is summarized in the following after an introduction of the samples investigated and the infrastructure used for the measurements.

7.1. The Single Macro-Pixel Sub-Assembly (MaPSA) and the MaPSA Test Setup

As introduced in Section 3.4, the PSp full-size sensor in the PS module is read out by 16 MPA chips (see Section 3.4.2) that are connected by bump bonds on top of the sensor forming a *Macro-Pixel Sub-Assembly* (MaPSA). With a size of one sixteenth of a full-size MaPSA, the single MaPSA shown in Figure 7.1a forms the smallest possible MaPSA version comprising one MPA chip and a matching PSp single sensor. Single MaPSAs allow for testing of the combination of sensor and readout chip during the prototype phase without having to equip a complete full-size sensor and are therefore commonly used by the sensor designers and chip developers. In Figure 7.1a, the single MaPSA is mounted on a dedicated carrier PCB with the sensor backside facing upwards. Besides a HV-filter for the sensor high voltage the board features a PCI-ex16 connector to access all 118 MPA pins that are wire bonded to electrical traces implemented on the board. As shown in Figure 7.1b, the single MaPSA carrier board is plugged into a custom-made interface board that has been designed and developed by Rutgers University in the USA. All voltage levels required by the MPA are provided through the interface board, while the sensor high voltage has to be applied from an external device. The board together with the single MaPSA is embedded into a housing made of aluminum that has been designed at KIT. In order to test irradiated samples, the mount provides a closable housing for the single MaPSA with a copper cooling block inside. During operation, the housing

is flushed with dry air to avoid the formation of ice at low temperatures. An FC7 evaluation board [Pes12] serves as interface between the data acquisition software and the MaPSA interface board. The FC7 is designed around the Xilinx Kintex-7 FPGA and offers two FPGA Mezzanine Card (FMC) slots, one of which is used for the connection to the MaPSA interface board via a high-density 68-pin VHDCI cable and a matching FMC card adapter. More details about the single MaPSA assembly and the corresponding test setup can be found in [Sch19].

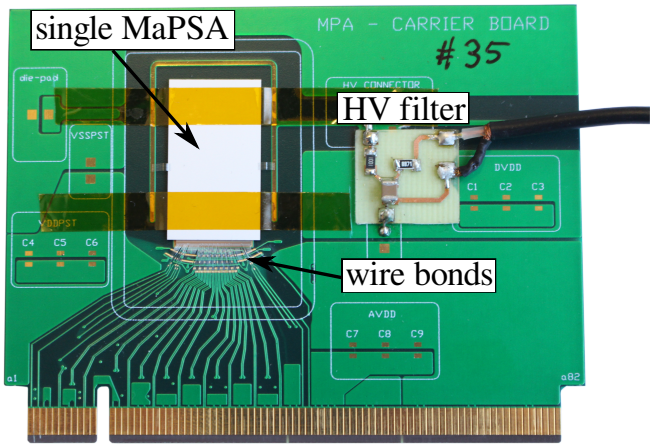

(a)

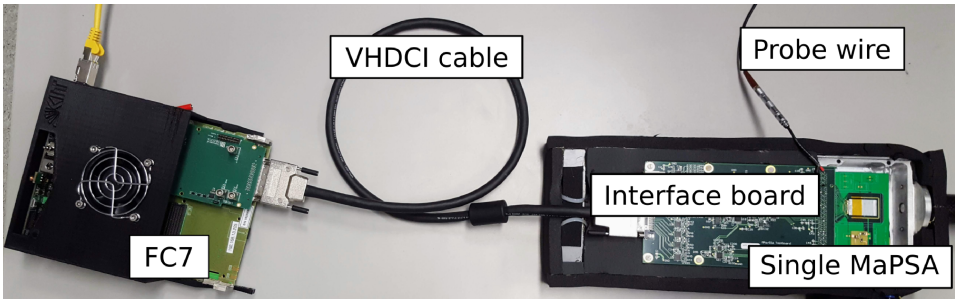

(b)

Figure 7.1.: (a): Single MaPSA assembly mounted and wire bonded onto a dedicated PCB carrier board. The sensor bias voltage is provided via an external cable connected to an HV filter sitting on the PCB. Wire bonds connect the MPA with the routing lines on the PCB. The assembly is read out with the MaPSA setup shown in (b), consisting of a dedicated interface board that is connected to the FC7 data acquisition board via a VHDCI cable. Figure (b) is taken from [Sch19].

7.1.1. Single MaPSA Readout and Calibration

In preparation for data taking the single MaPSA must be calibrated first. To configure and read out the MPA a dedicated firmware version is uploaded to the FC7, while the Python-based acquisition and control software runs on an external readout computer and communicates with the FC7 through the local network. The software provides different routines for the assembly calibration. Besides calibrating the MPA bias blocks for a correct power distribution across the chip, the thresholds of the analogue pixel frontends need to be equalized, which is referred to

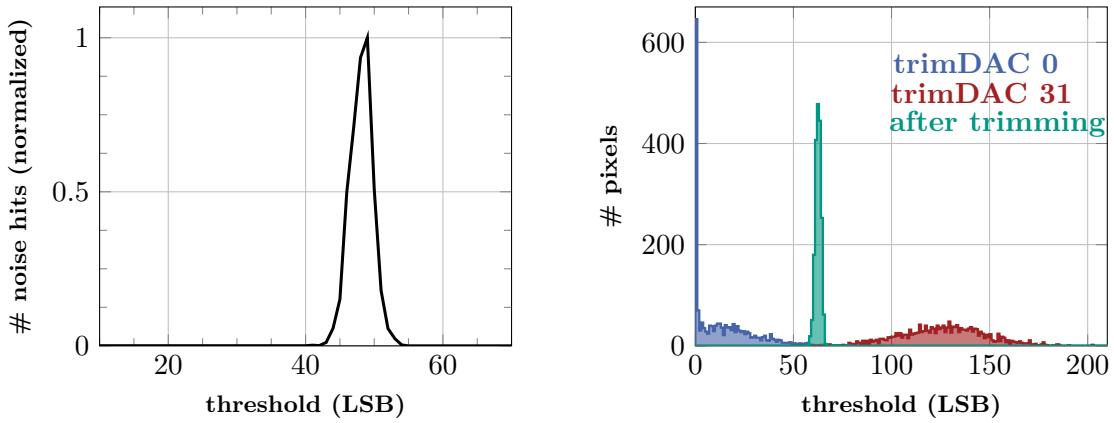

Figure 7.2.: (a): Number of noise hits in dependence of the threshold measured with one pixel frontend in the edge-sensitive readout mode. In the histogram the number of noise hits measured for each threshold is normed to the noise hit maximum measured at the peak. The baseline distributions of the untrimmed pixel matrix for the minimum (blue) and maximum (red) trimDAC setting is shown in (b). Before trimming the frontends, the baseline distributions show a wide spread, whereas after trimming a narrow distribution is obtained (green). Data taken from [Wit20].

as trimming. The trimming ensures uniform response of all readout channels across the chip. Within the trimming procedure, the number of noise hits is measured in dependence of the applied threshold, which is given in units of the *least significant bits* (LSB). The resulting noise peak is exemplarily shown in Figure 7.2a for one pixel frontend. As mentioned in Section 3.4.2, the MPA trimming is based on the asynchronous readout mode, where the ripple counter simply counts how often the signal exceeds the threshold (edge sensitive). Thus, at low thresholds, only one rising edge is detected as the noise signal constantly stays above the threshold keeping the comparator output high. With increasing threshold, the number of recorded hits increases as the noise signal stays above the threshold less frequently resulting in a characteristic noise peak. If the threshold is increased even further, fewer and fewer noise signals exceed the threshold and the number of recorded noise hits drops down to zero. The threshold value at which most of the noise hits are detected (noise maximum) serves as baseline for the trimming procedure. The overall trimming goal is to shift the baseline of each pixel frontend to a common threshold (trimming target) by adjusting the individual frontend thresholds with the 5-bit trimDAC.

Figure 7.2b shows the baseline distribution of an untrimmed assembly with the highest (red) and lowest (blue) trimDAC setting. Applying the lowest trimDAC value shifts the baselines towards low thresholds, while the highest trimDAC setting results in a baseline shift towards high thresholds. A wide spread of the individual baseline positions can be seen for both distributions. The common trimming target for the baselines of each pixel is chosen to be close to the midpoint between the two distributions to ensure that each pixel frontend can reach the target with the given 5-bit trimDAC. For each frontend channel, the trimming procedure determines the trimDAC value that has to be set in order to shift the channel baseline to the overall trimming target. The baseline distribution after the assembly trimming is shown in green, demonstrating a narrow peak and therefore uniform response throughout the whole pixel matrix. For the beam test measurements shown in this chapter, the threshold is always applied

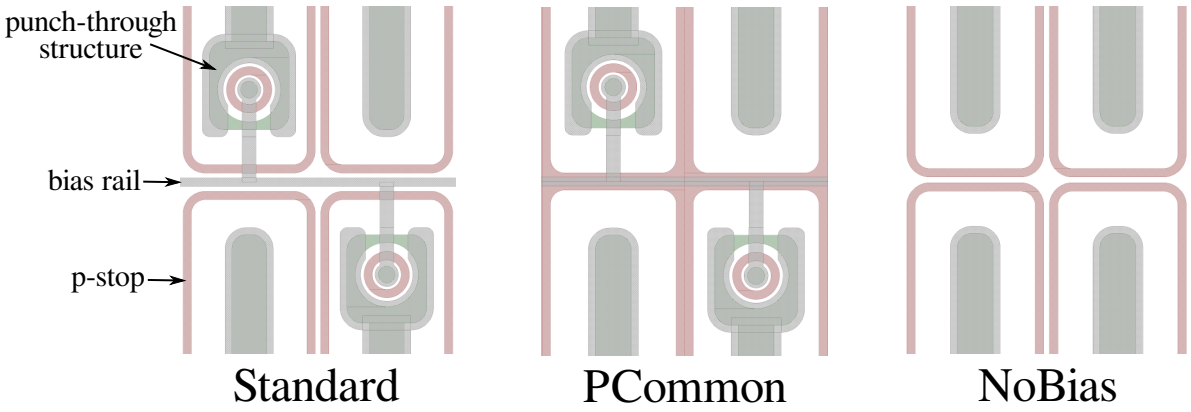

Figure 7.3.: Comparison of the three different PSp sensor designs investigated in the scope of this work. The Standard and PCommon design both feature biasing structures for each pixel implant, whereby the p-stop structures of the PCommon design are merged to a common p-stop structure that effectively shields the bias rail from the sensor bulk. In contrast, the NoBias design does not provide any biasing structures.

relative to the mean of the baseline distribution that is determined after the trimming. More information about the trimming procedure can be found in [Wit20].

7.2. Single Sensor Designs

In [SD19], it has been observed that the bias rail, which connects the individual macro-pixels with the global bias ring, negatively affects the charge collection efficiency resulting in a reduced particle detection efficiency at the rail region for perpendicular particle incidence. Thus, single sensors with different sensor designs were implemented on a dedicated PSp prototype wafer (see [Sch19]) to study the impact of different bias and interpixel isolation schemes on the global sensor detection efficiency. The three different design approaches that were tested in the scope of this work are shown in Figure 7.3. The Standard design, which is the most conservative design choice, is shown on the left-hand side. It comprises punch-through structures for each pixel as well as individual atoll p-stop implants that surround each n-doped pixel implant. The punch-through structures are connected to the global bias-grid by short aluminum routing lines, whereby the bias grid runs on top of the oxide layer. Hence, the rail is electrically isolated from the p-doped bulk substrate. In the PCommon design, each pixel is still biased via an individual punch-through structure, but the p-stop implants are merged to a common p-stop configuration that is shared by adjacent pixels. Thus, the bias rail is routed above the p-stop implant, which acts as an additional shielding layer between the grounded rail and the sensor bulk. Simulations showed that the p-stop shielding has a beneficial effect on the charge collection efficiency at the bias rail region [SD19]. For the last design approach, called NoBias design, no biasing structures are implemented at all, while the atoll p-stop configuration is similar to the Standard design. In order to deplete the sensor, ground potential has to be provided through the readout chip. Applying high voltage to the bare sensor without readout chip would result in a depletion zone that does not extend to the full active sensor volume. Consequently, the main drawback of the NoBias design is that the sensor can only be fully characterized after equipping it with the readout chip. However, with regard to the charge collection efficiency the NoBias design is expected to be the most efficient design due to the missing bias structures that deteriorate the overall charge collection efficiency.

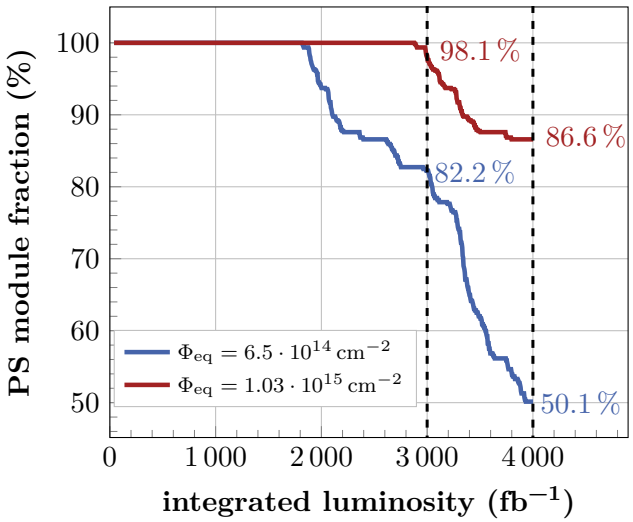

Figure 7.4.: Fraction of PS modules that will receive a maximum fluence of $6.5 \cdot 10^{14}\,\mathrm{cm}^{-2}$ (blue) and $1.03 \cdot 10^{15}\,\mathrm{cm}^{-2}$ (red) in the CMS tracker as a function of the total integrated luminosity. The fluence values correspond to the single MaPSA assembly fluences investigated in this work. PS module fractions at the nominal ($3000\,\mathrm{fb}^{-1}$) and ultimate ($4000\,\mathrm{fb}^{-1}$) CMS run time scenario are highlighted by the colored numbers. Data based on [CMS23a].

7.3. Single MaPSA Samples

All assemblies investigated in this work comprise PSp single sensors from prototype wafers processed by HPK. The n-in-p sensors are based on float-zone silicon wafers with a physical and active thickness of 320 µm and 290 µm, respectively. Thus, the wafer base material is similar to the final material that will be used for the CMS Outer Tracker. For each of the above introduced sensor designs at least three functional assemblies were built for beam test studies. To investigate the impact of radiation damage on the sensor performance with regard to the particle detection efficiency, two assemblies of each design were irradiated with 23 MeV protons at the *Karlsruhe Compact Cyclotron* (KAZ) [ZAG22]. A medium 1 MeV neutron equivalent fluence of $6.5 \cdot 10^{14}\,\mathrm{cm}^{-2}$ and a maximum fluence of $1.03 \cdot 10^{15}\,\mathrm{cm}^{-2}$ were chosen to probe different sensor irradiation states during the CMS tracker operation. Figure 7.4 shows the fraction of PS modules whose expected maximum fluence in the CMS tracker is equal to or lower than the respective irradiation fluence as a function of the total integrated luminosity. For the nominal scenario ($3000\,\mathrm{fb}^{-1}$) it can be seen that the maximum assembly fluence nearly meets the maximum expected PS module fluence in the CMS tracker with less than 2 % of the modules accumulating slightly higher fluences. However, for the ultimate runtime scenario ($4000\,\mathrm{fb}^{-1}$) about 14 % of the PS modules will receive fluences higher (max. $1.43 \cdot 10^{15}\,\mathrm{cm}^{-2}$) than the maximum irradiation fluence, which therefore does not represent the worst-case scenario.

Annealing of radiation damage (see Section 4.5.4) is another aspect that impacts the sensor performance with regard to the charge signal and leakage current. During LHC operation, the sensors in the tracker will be kept at about −20 °C and will therefore not accumulate any annealing. However, during the maintenance periods with a yearly duration of about two weeks, the sensors could be intentionally annealed by heating up the tracker to room temperature to reduce the sensor leakage current, which in turn decreases the overall module power consumption. While annealing always has a beneficial impact on the leakage current, the charge signal generated in the sensor decreases after exceeding room temperature annealing

durations of several weeks (see Figure B.2). Assuming twelve years of detector operation an annealing time of about 24 weeks (168 days) would result. In case of unforeseen repair phases additional annealing might be accumulated. Thus, to cover the worst-case scenario, assemblies irradiated to the maximum fluence were annealed to a room temperature equivalent annealing time of 200 days. According to the lower sensor fluence, the medium irradiated assemblies received a shorter annealing of 42 days, to cover the sensor performance at an earlier stage of the tracker operation. One should take note that the procedure of irradiation and subsequent annealing does not fully represent the sensor operation in the detector, where irradiation and annealing takes place iteratively. However, iterative irradiation and annealing of structures is not feasible at the available hadron irradiation facilities. Therefore, the subsequent procedure represents the best possible approximation and is commonly used in the field of irradiation studies with silicon structures.

7.4. Beam Test Measurement Results

Part of the beam test measurements with the unirradiated assemblies was conducted in the scope of my master thesis [Wit20] and the corresponding results are briefly summarized to have a reference for the irradiated assemblies. Pictures of the MaPSA setup integrated into the DATURA beam telescope can be found in Figure B.1. The DESY beam test facility and the general analysis workflow are introduced in Chapter 6 and are not further discussed here. The objective of the beam test measurements presented in the following was the evaluation of the sensor performance with focus on the different design approaches and irradiation effects.

7.4.1. Cuts and Definitions

As introduced in Equation (6.2), x- and y-residual cuts are applied within the analysis to match reconstructed particle tracks with clusters of hits on the DUT. The respective cuts have to be adapted to the DUT geometry to get meaningful results for the cluster efficiency. The pixel cell size of the PSp macro-pixel sensors investigated in this chapter is $100\,\mu\text{m} \times 1467\,\mu\text{m}$. Figure 7.5a shows the cluster efficiency in dependence of different DUT residual cuts based on data measured with an unirradiated single MaPSA based on the Standard sensor design. First of all, it can be seen that for cuts smaller than the pixel cell size there is a distinct drop in the cluster efficiency as only a small fraction of tracks matches the acceptance window. By enlarging the cut windows, more and more tracks are matched with DUT clusters resulting in an efficiency increase with a saturation at large cuts. Figure 7.5b shows the cluster efficiency projection along the blue and green dashed lines in the histogram. The residual cuts applied within the data analysis presented in this chapter are indicated by the black dashed lines. For the x-residuals a cut of $200\,\mu\text{m}$ is chosen, which corresponds to twice the pixel pitch. On the one hand, the cut ensures that only clusters with a center that is located within two pixels around the extrapolated track intersection point are accepted. Thus, events with δ-electrons causing large asymmetric clusters are excluded. On the other hand, the cut is sufficiently large to achieve a high efficiency, which starts to saturate at the chosen cut setting (see Figure 7.5b). For the y-residual cut $900\,\mu\text{m}$ is chosen, which is about 60 % the pixel size. Thus, the acceptance window (two times the residual cut) to match reconstructed tracks with DUT clusters along the y coordinate is slightly larger than the pixel cell. In general, as can be seen in Figure 7.5b, the cluster efficiency is less sensitive to the y-residual cut and further increasing the cut size would not significantly increase the cluster efficiency.
As mentioned in Section 7.1.1, the position of the characteristic noise peak serves as baseline for the threshold equalization. For the beam test measurements presented in the following, all thresholds are applied relative to the mean of the baseline distribution after equalization.

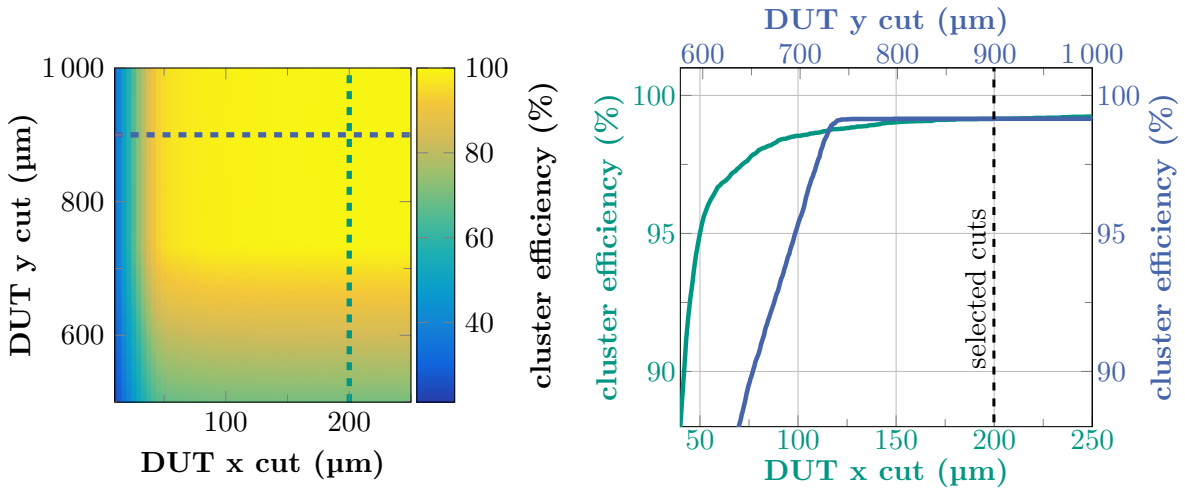

Figure 7.5.: (a): Cluster efficiency measured with an unirradiated single MaPSA in dependence of different DUT residual cuts. The x- and y-cut define the size of the acceptance window to match reconstructed tracks with clusters of hits on the DUT. Increasing the cut windows results in an overall larger efficiency. (b): Cluster efficiency projections along the blue and green dashed lines shown in (a). The residual cuts used for the analysis are indicated by the black dashed line. For the variation of the DUT x cut, the y cut was set to 900 µm, while for the variation of the y cut the x cut was set to 200 µm.

To convert relative thresholds given in units of LSB into an electron equivalent threshold, a conversion factor of $110\,\mathrm{e}^{-}\,LSB^{-1}$ is used [Wit20].

7.4.2. Unirradiated Assemblies at Perpendicular Beam Incidence

The main findings from the beam test measurements with the unirradiated assemblies are summarized in Figure 7.6. Most of the data shown in the plots are based on [Wit20].

Threshold Dependency

From the data gathered during threshold scans shown in Figure 7.6a it can be seen that, independent of the threshold, the Standard design shows the overall smallest cluster efficiency. Only for threshold settings smaller than $3\,\mathrm{ke}^{-}$ cluster efficiencies above 99 % can be reached. In contrast, assemblies equipped with sensors featuring the PCommon and NoBias design reach cluster efficiencies well above 99 %, even for thresholds larger than $5\,\mathrm{ke}^{-}$. Thus, the PCommon and NoBias design provide a larger operation window with regard to the applied threshold as the decline in efficiency is less significant. Among all three tested design versions, the NoBias design yields the overall highest efficiency. However, when searching for the optimal threshold settings, not only the efficiency but also the noise occupancy needs to be considered. The latter is defined as the number of noise hits per channel and readout sequence and should be several orders of magnitude smaller compared to the channel occupancy, which will be about 1 % during the HL-LHC phase. Thus, a noise occupancy of $1 \cdot 10^{-4}$ is taken as an upper limit in the following. The noise occupancy shown in Figure 7.6a corresponds to the Standard assembly and can be regarded as a reference for the unirradiated assemblies. It was determined by counting the number of noise hits in all pixel frontends for a defined readout duration $\mathcal{O}$(ms).

The total number of recorded hits is then divided by the number of readout channels and is normalized to a readout duration of 25 ns, which corresponds to the LHC bunch crossing frequency. Repeating this procedure at different threshold settings yields the presented noise occupancy. At a relative threshold of about 1.2 ke^- (orange dashed line) the noise occupancy falls below $1 \cdot 10^{-4}$, and, therefore, indicates the minimum threshold that should be applied. Thus, at reasonable thresholds cluster efficiencies above 99 % can be reached with all tested assemblies. However, the shown noise occupancy should only be regarded as an estimation for the PS module, since the single MaPSA does not represent the final electrical configuration as it will be in the PS module. Dedicated tests with PS module prototypes are required to get an assessment regarding the module noise.

Efficiency Maps

Particle tracks reconstructed from hits in the telescope layers have a spatial resolution of less than 10 µm. Thus, it is possible to measure the position-dependent cluster efficiency in order to track down potential inefficient sensor regions. Pixels on the PSp sensor are periodically arranged, and for the localization of inefficiencies related to the sensor design it is sufficient to focus on a pixel matrix consisting of 2×2 pixels. To increase the statistics, the illuminated sensor area is divided into smaller subareas of 2×2 pixels that are then superimposed. The corresponding efficiency maps of all three tested sensor designs are shown in Figure 7.6b. Layouts of the individual pixel designs are depicted above the respective efficiency map. The corresponding measurements were performed at a sensor bias voltage of 400 V and a threshold of about 1.3 ke^-.
Starting with the Standard design, shown at the top, circular shaped inefficient areas are located at the positions of the punch-through structure of each pixel. Electrons generated by particles traversing the sensor close to the punch-through structures are mainly attracted by the ground potential of the structure and do, therefore, not contribute to the readout signal. Additionally, the ground potential of the bias rail attracts electrons from charge signals generated close to the rail. The electrons accumulate at the silicon dioxide interface between the p-stop implants of adjacent pixels. Since the time the electrons need to overcome the p-stop barrier is much longer compared to the sampling time of the readout chip, they do not contribute to the signal [Sch19]. As a consequence, an additional inefficient band along the bias rail can be clearly seen in the efficiency map of the Standard design. A closer look at the bias rail region reveals that the inefficiencies are more pronounced at the interpixel region, where four pixels border each other. This is related to charge sharing effects that additionally reduce the charge signal seen by the individual pixels.
The efficiency map measured with the PCommon design, which is shown in the middle of Figure 7.6b, proofs a beneficial effect of the optimized p-stop configuration implemented in this design approach. In contrast to the Standard design, no inefficiencies are observed at the bias rail region due to the shielding effect of p-stop implants that directly run underneath the rail. However, the inefficiencies related to the punch-through structures remain as the PCommon design does not differ from the Standard design in this respect.
As expected due to the missing biasing structures, the NoBias design shown at the bottom of Figure 7.6b is fully efficient across the whole pixel matrix. Thus, the NoBias design can be regarded as baseline for the maximum achievable PSp sensor cluster efficiency.

The efficiency maps of the individual sensor designs confirm the overall efficiency differences observed in the threshold scan. More details concerning the beam test measurements with the unirradiated single MaPSAs as well as a direct comparison of the performance of the FZ290 and the thFZ200 sensors prior to irradiation can be found in [Wit20].

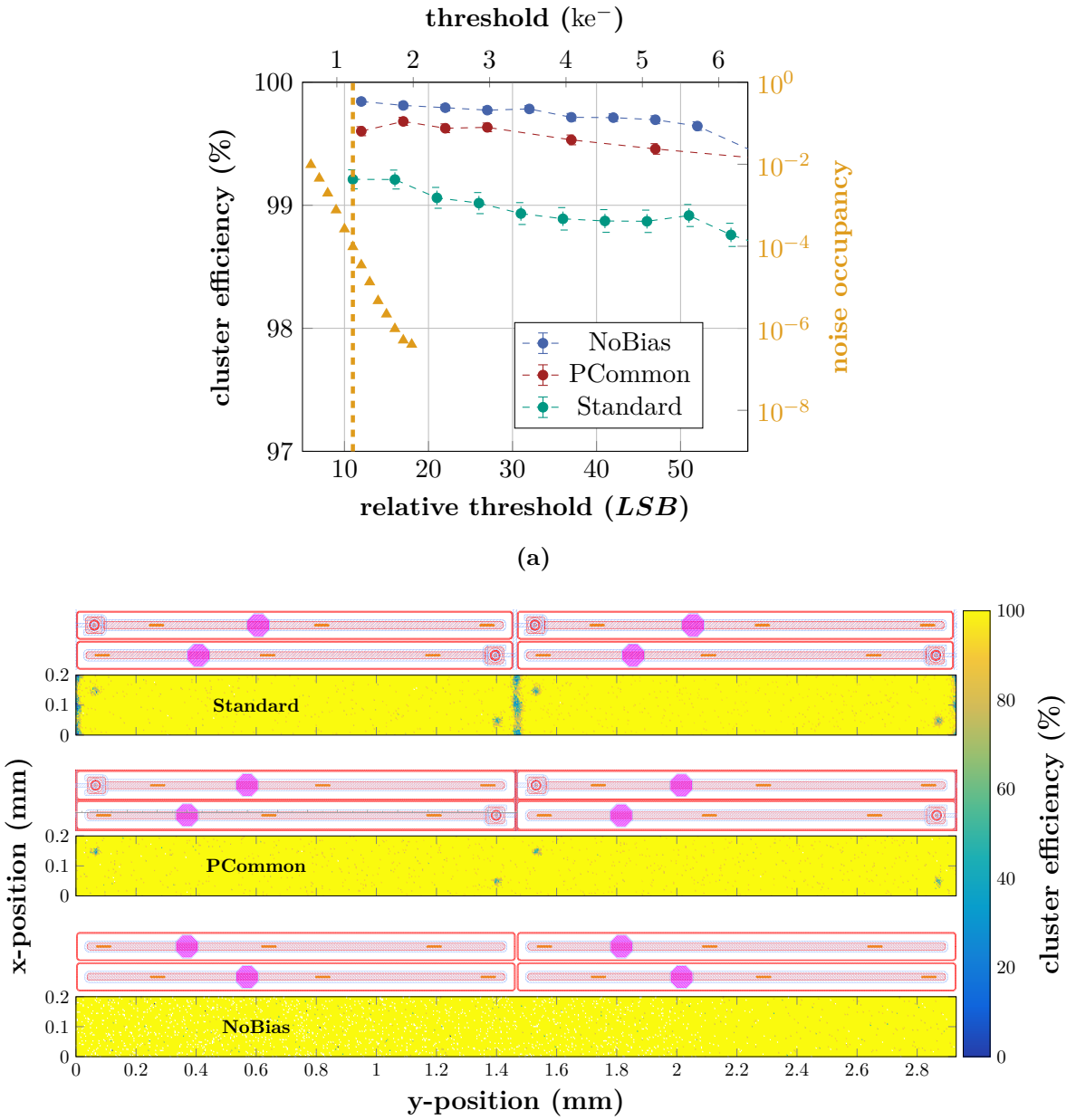

Figure 7.6.: (a): Cluster efficiency in dependence of the threshold setting measured with unirradiated single MaPSAs comprising the Standard, PCommon and NoBias sensor design. The expected noise occupancy for an unirradiated single MaPSA in dependence of the threshold is indicated by the orange markers, with the orange dashed line representing the threshold setting at which a noise occupancy smaller than $1 \cdot 10^{-4}$ is reached. (b): 2D histogram showing the position dependent cluster efficiency measured across a 2×2 pixel area for the three different sensor designs at a threshold of about 1.3 ke$^-$. The corresponding pixel layout is shown above each efficiency map. Both, the threshold scan and the efficiency maps were measured at a sensor bias voltage of 400 V.

7.4.3. Irradiated Assemblies at Perpendicular Beam Incidence

As mentioned in Section 7.1, the MaPSA setup features a copper-based cooling bridge that can be connected to a chiller. During the beam test measurements all irradiated assemblies were cooled down to about −20 °C sensor temperature to reduce the sensor leakage current and to prevent thermal runaway during the operation. If not stated differently, all irradiated assemblies were tested at 600 V sensor bias voltage, which corresponds to the nominal module operation voltage in the CMS Outer Tracker.

Threshold Dependency

The cluster efficiency at perpendicular beam incidence in dependence of the relative threshold measured with differently irradiated assemblies is summarized in Figure 7.7. The plot on the left-hand side shows the general course of the efficiency including high threshold settings, while the plot on the right-hand side focuses on the region relevant for the detector operation. For reference, the results discussed above from the unirradiated assemblies are added to the plots. The noise occupancy shown in orange corresponds to the maximum irradiated Standard assembly and serves as a reference for the other assemblies. In order to reach noise occupancies smaller than $1 \cdot 10^{-4}$, a minimum threshold of about 1.4 ke$^-$ is required (orange dashed line), which is slightly higher than for the unirradiated assembly (1.2 ke$^-$). Again, the noise occupancy only reflects the single MaPSA performance and additional measurements with irradiated PS module prototypes are required to get a more precise estimate of the module noise occupancy in the tracker. In general, efficiencies measured with irradiated assemblies decrease significantly stronger with increasing threshold compared to unirradiated assemblies. This is related to the reduced charge collection efficiency of the sensor after irradiation. Similar to the observations before irradiation, assemblies equipped with NoBias sensors yield the highest cluster efficiency among all tested irradiated assemblies. With efficiencies of about 99.7 % measured at low threshold settings the irradiated NoBias assemblies perform as good as the unirradiated assembly, independent of the fluence. Even for thresholds up to 3 ke$^-$ the efficiency remains above 99 %. In contrast, the PCommon design, which is only slightly less efficient than the NoBias design before irradiation, shows a clearly reduced efficiency for both assembly fluences. At reasonable threshold settings efficiencies slightly below 99 % can be reached, corresponding to an efficiency decrease of about 0.7 % compared to the unirradiated assembly. The most conservative design approach, the Standard design, shows the overall lowest cluster efficiency. At 1.4 ke$^-$, the performance of the medium irradiated Standard assembly is comparable to the PCommon assemblies with efficiencies close to 99 %. However, the maximum irradiated assembly only reaches efficiencies close to 98.5 % and shows the overall strongest dependency on the applied threshold.

Bias Voltage Dependency

Although the target sensor operation voltage in the CMS Outer Tracker is 600 V there is the option to increase the voltage up to 800 V. This is of particular interest for sensors that have accumulated irradiation damage. Firstly, the full depletion voltage is shifted towards higher voltages due to the change of the effective doping concentration (see Section 4.5.3), and secondly, an overall higher electric field in the sensor reduces the probability of charge trapping related to irradiation induced defects. In order to estimate the gain in efficiency that could be obtained by increasing the PSp sensor bias voltage, the cluster efficiency was measured at different voltages up to 800 V. The results are shown in Figure 7.8. Regarding

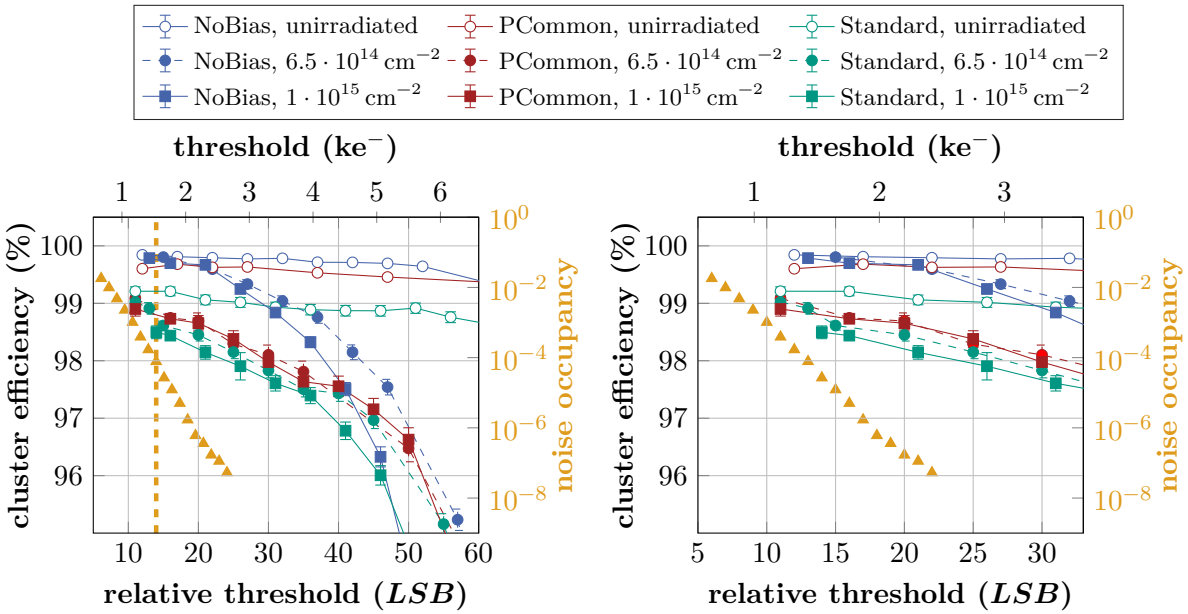

Figure 7.7.: Cluster efficiency in dependence of different threshold settings. For each sensor design, two different fluences, a medium 1 MeV neutron equivalent fluence ($6.5 \cdot 10^{14}\,\mathrm{cm}^{-2}$) and maximum fluence ($1 \cdot 10^{15}\,\mathrm{cm}^{-2}$) were tested. The upper x-axis represents the threshold in electron equivalent. All assemblies were operated at a sensor bias voltage of 600 V. The noise occupancy shown in orange belongs to the maximum irradiated Standard assembly and serves as a general reference for the irradiated assemblies. At about 1.4 ke$^-$ the noise occupancy falls below $1 \cdot 10^{-4}$, indicated by the dashed orange line. The right plot shows a zoomed version of the left plot with regard to the threshold range.

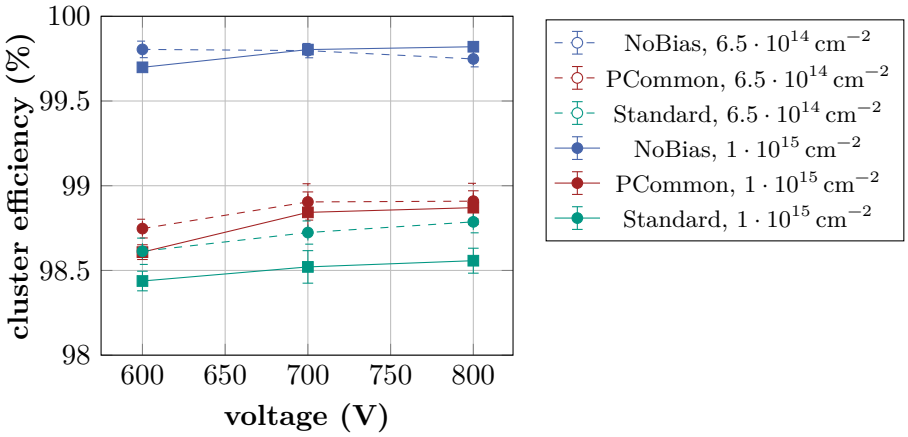

Figure 7.8.: Cluster efficiency in dependence of the sensor bias voltage measured with the differently irradiated assemblies. The efficiency gain obtained from increasing the nominal bias voltage (600 V) by 200 V is relatively small and ranges between 0.1 % and 0.25 %. A relative threshold of about 1.7 ke^- was applied to all assemblies.

the NoBias design, only the higher irradiated assembly shows a slightly increased efficiency at higher voltages. In contrast, assemblies based on the Standard and PCommon design reveal increasing efficiencies for both investigated fluences. However, the overall efficiency gain is in the sub-percent level ranging from 0.1 % to 0.25 %. In general, increasing the sensor bias voltage always comes with the drawback of higher sensor leakage currents, which, in turn, increases the module heating power due to the overall higher power consumption. In the end, it has to be evaluated whether the slight gain in cluster efficiency is worth the additional thermal power, which has to be dissipated by the cooling system. However, the bias voltage dependency of the stub detection efficiency, which can only be tested with a fully assembled PS module, should also be considered in the bias voltage decision. The stub efficiency can be approximated by the product of the single sensor efficiencies and is, therefore, more affected by the bias voltage. Additional beam test measurements with an irradiated PS module are needed to precisely evaluate the effect of higher bias voltages on the stub efficiency.

7.4.4. Efficiency Maps and Interpixel Efficiency

The origin of the efficiency decrease observed on the irradiated PCommon assemblies becomes obvious by looking at the efficiency maps shown in Figure 7.9a. Both irradiated PCommon assemblies show inefficiencies at the bias rail region similar to the Standard design. Thus, the shielding effect of the p-stop implants located underneath the bias rail (see Figure 7.3) is strongly reduced after irradiation. This observation is in good agreement with the results obtained from beam test measurements with irradiated thinner thFZ200 PCommon sensors investigated in [Sch19]. The NoBias sensors are the only sensors that remain efficient across the whole active pixel area, even at the highest tested fluence.

While the efficiency maps allow for tracking down the origin of inefficiencies, a more detailed comparison of the individual designs is rather difficult. Therefore, Figures 7.9b to 7.9d show projections of the cluster efficiency along the y-axis, in the sensor region where the biasing structures are implemented. The individual plots are grouped by the different assembly fluences. In general, the efficiency values shown in the projections should not be regarded as absolute values as they depend on the binning, especially at the areas of local inefficiencies. However,

applying the same binning to all data sets still allows to directly compare the individual designs. Regarding the efficiency dips related to the punch-through structures, no differences between the PCommon and Standard design are observed among all tested assembly fluences. This is expected as the two designs do not differ in this regard. As already seen in the efficiency histograms prior to irradiation (Figure 7.6b), the main efficiency loss of the Standard design is related to the bias rail, where the efficiency decreases slightly below 60 %. In contrast, the NoBias design is fully efficient, while the PCommon design only shows an efficiency decrease by less than 1 % that is not resolved in the projection plot. After irradiation the efficiency further decreases to a minimum of about 25 % at the medium fluence, whereas at the maximum fluence it drops slightly below 20 %. The bias rail inefficiencies of the PCommon design after irradiation are almost similar to the Standard design with efficiency dips down to 30 % and 28 % at the medium and maximum fluence, respectively. In each of the shown projection plots the width of interpixel region where the efficiency is affected by the bias rail is about (55 ± 4) µm and is indicated by the red background. The inefficiencies caused by the punch-through structures have a diameter of about (36 ± 4) µm. Considering the given uncertainties due to the limited telescope resolution, which is estimated to be about 4 µm [Hen+16], the widths of the inefficiencies do not change significantly with increasing fluence. Looking closer at the interpixel region of the maximum irradiated NoBias design reveals a small efficiency decrease by about 2 % that is barely visible in the projection plot. This decrease is related to charge sharing effects between the four bordering pixels, which reduces the charge signal seen by the individual pixels to 1/4 of the generated charge in addition to the overall deteriorated charge collection efficiency after irradiation.

7.4.5. Efficiency at Inclined Particle Incidence

In the previous sections it has been shown that the bias structures implemented in the Standard and PCommon design cause inefficient regions within the active sensor area. While inefficiencies related to punch-through structures only slightly reduce the overall cluster efficiency (see PCommon design prior to irradiation), the bias rail has a more significant impact. As shown in Figure 7.9, the bias rail related inefficiencies are most pronounced for the Standard design, whereby the difference compared to the PCommon design becomes less significant after hadron irradiation. However, all measurements presented so far only represent the situation at perpendicular beam incidence. Testing the sensor performance at inclined particle incidence is of particular interest as a large fraction of PS modules will be hit at an angle by the particles traversing the CMS tracker.[1] The deposited charge signal of these particles is consequently spread across a broader sensor area. Thus, as exemplarily indicated by the green arrow in Figure 7.10, at sufficiently large angles a fraction of charge carriers will always be deposited outside the inefficient sensor regions, which in turn improves the overall cluster efficiency. In general, the incidence angle that is needed to overcome the inefficient area depends on the position where the particle hits the sensor. The worst-case scenarios are indicated by the red arrows. Assuming the above mentioned widths and an active sensor thickness of 290 µm, incidence angles lager than 10.9° and 7.1° are required to overcome the bias rail and punch-through inefficiency, respectively. In contrast, particles hitting the sensor in the middle of the inefficient regions (blue arrows) can pass them already at smaller angles. To study the impact of different angles of particle incidence, the MaPSA setup was tilted with respect to the beam. Dedicated 3D printed mounts were used to achieve different tilting angles ranging from

[1] About 75 % of all PS modules in the tracker will be hit at an angle of at least 5°. This estimation is based on the model presented in [Sch19], which calculates the particle incidence angle on the individual PS modules by considering the module tilt angle and assuming that particles created at the interaction point penetrate the tracker along a straight line in the rz-plane.

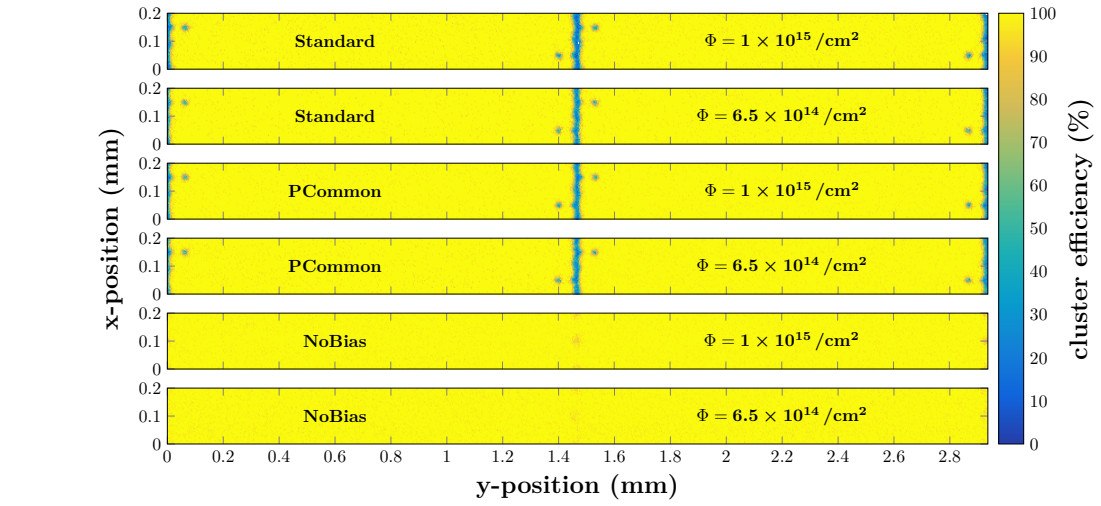

(a)

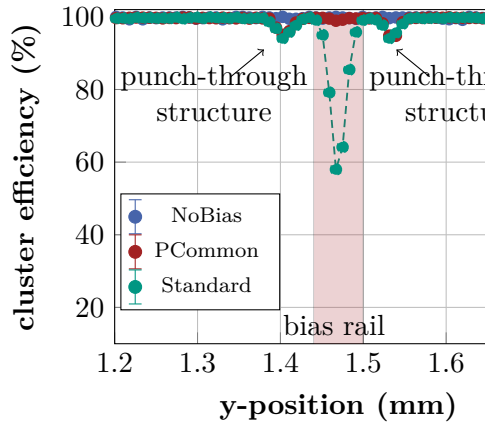

(b) fluence: unirradiated

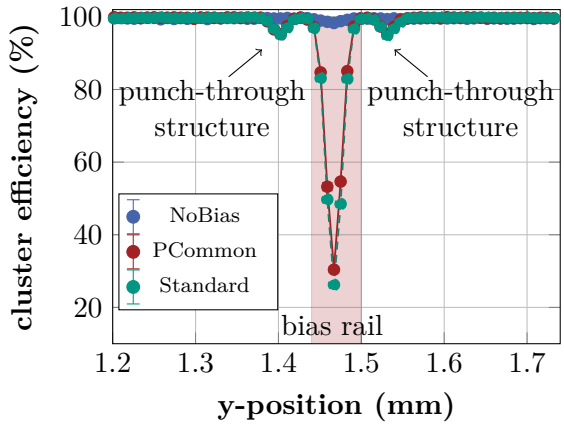

(c) fluence: $6.5 \cdot 10^{14}\,\mathrm{cm}^{-2}$

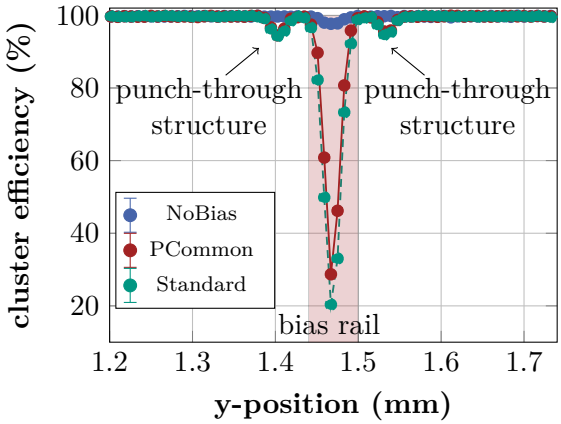

(d) fluence: $1 \cdot 10^{15}\,\mathrm{cm}^{-2}$

Figure 7.9.: (a): 2D histograms showing the position dependent cluster efficiency measured across a 2×2 pixel area for differently irradiated assemblies. Projections along the y-axis at the interpixel region measured with unirradiated and irradiated assemblies are shown in (b), (c) and (d). Prior to irradiation (b) inefficiencies related to the bias rail are only visible for the Standard design. After irradiation with hadrons to different fluences, (c) and (d), the PCommon design exhibits inefficiencies at the bias rail, similar to the Standard design. Only the NoBias design remains fully efficient. All unirradiated assemblies were tested at 400 V and a threshold of about 1.3 keV, whereas for the irradiated assemblies the voltage and threshold were increased to 600 V and about 1.7 ke^{-}, respectively.

5° to 30°, with an uncertainty of about ± 2.5°. A picture of the tilted MaPSA setup integrated into the beam telescope can be found in Figure B.1b. All measurements shown in the following were exclusively performed with the Standard design as it is most affected by the bias rail inefficiencies. Two assemblies, the unirradiated and the maximum irradiated, were tested.

Figure 7.11a shows results from threshold scans at 400 V sensor bias voltage measured with the unirradiated assembly at different tilting angles. The largest increase in efficiency is observed in the step from 0° to 5°, where the cluster efficiency already rises slightly above 99.5 %. By further increasing the tilt angle, efficiencies up to 99.8 % can be reached, which is comparable to the performance measured with the NoBias design. However, at about 10° a saturation effect sets in and no significant difference to the subsequent tilt angles is observed with regard to the efficiency at low thresholds. This is in good agreement with the maximum angle of 10.9° in the worst-case scenario mentioned above. Inclined particle incidence also affects the charge signal as the particles cover a longer distance in the active sensor area. Assuming 76 electron-hole pairs per µm [Har17] and 290 µm active sensor thickness, the charge signal ranges from 22.12 ke^- to 25.45 ke^- for tilting angles of 5° and 30°, respectively. The increased charge signal is clearly visible in the measurements as for tilt angles larger than 5° the cluster efficiency does not significantly change with increasing threshold, forming a stable plateau.
Threshold scans measured with the maximum irradiated Standard assembly at different tilt angles are shown in Figure 7.11b. In contrast to the unirradiated assembly, tilting the assembly by 5° does barely affect the cluster efficiency. Instead, the first noticeable efficiency increase is observed at 10° with a subsequent strong increase at 15°. This is related to the reduced charge collection efficiency after irradiation, that in combination with charge sharing effects between pixels at the bias rail region, results in an overall smaller charge signal seen by individual pixels. Thus, larger tilt angles are required to achieve similar efficiencies as for the unirradiated tilted assembly. Increasing the tilt angle above 15° does not lead to a significant increase in efficiency at low thresholds, but allows for applying higher thresholds without significant efficiency loss as a larger amount of charge is generated that partly compensates for the overall smaller charge signal after irradiation.

7.4.6. Conclusion and Outlook

Beam test measurements with proton irradiated single MaPSAs based on FZ290 PSp prototype sensors featuring three different design approaches were performed. For each of the sensor designs, two different fluences were tested, a medium 1 MeV neutron equivalent fluence of $6.5 \cdot 10^{14}\,\mathrm{cm}^{-2}$ and a higher fluence of $1 \cdot 10^{15}\,\mathrm{cm}^{-2}$. In addition to the irradiation, the medium irradiated assemblies received an annealing equivalent to 40 d at room temperature, whereas the higher irradiated assemblies were annealed to 200 d. Thus, different states during the CMS tracker operation could be tested, while the higher fluence can be regarded as worst-case scenario after $3000\,\mathrm{fb}^{-1}$. Only about 2 % of the PS modules will face higher fluences.
Among all three design approaches, the NoBias design performed best with cluster efficiencies up to 99.7 %, even at the highest fluence and annealing. However, the NoBias design comes with the drawback that sensors cannot be fully electrically characterized before equipping them with readout chips due to the missing biasing structures. In contrast, the Standard and PCommon sensor design both comprise biasing structures, allowing to characterize the bare sensor before equipping it with the readout chips. These biasing structures, namely the punch-through structures and the bias rails, were found to introduce inefficient regions within the active sensor area. Prior to irradiation the inefficiencies related to the grounded bias rail can be mitigated by shielding the bulk with p-stop structures that are merged to a common p-stop configuration, which directly runs underneath the bias rail. This approach is implemented in

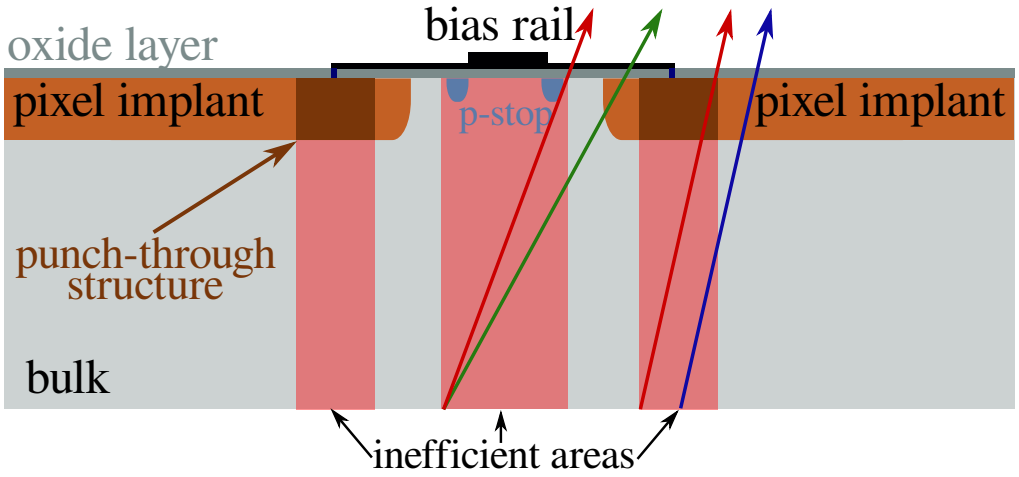

Figure 7.10.: Simplified schematic of the sensor cross-section at the bias rail region. Inefficient sensor areas underneath the bias rail and the punch-through structures are highlighted in red. Particles crossing the sensor at sufficiently large angles (green and blue arrow) can overcome the inefficient regions. The angles of incidence to overcome the inefficient regions depend on the position at which particles hit the sensor (red vs. blue arrow).

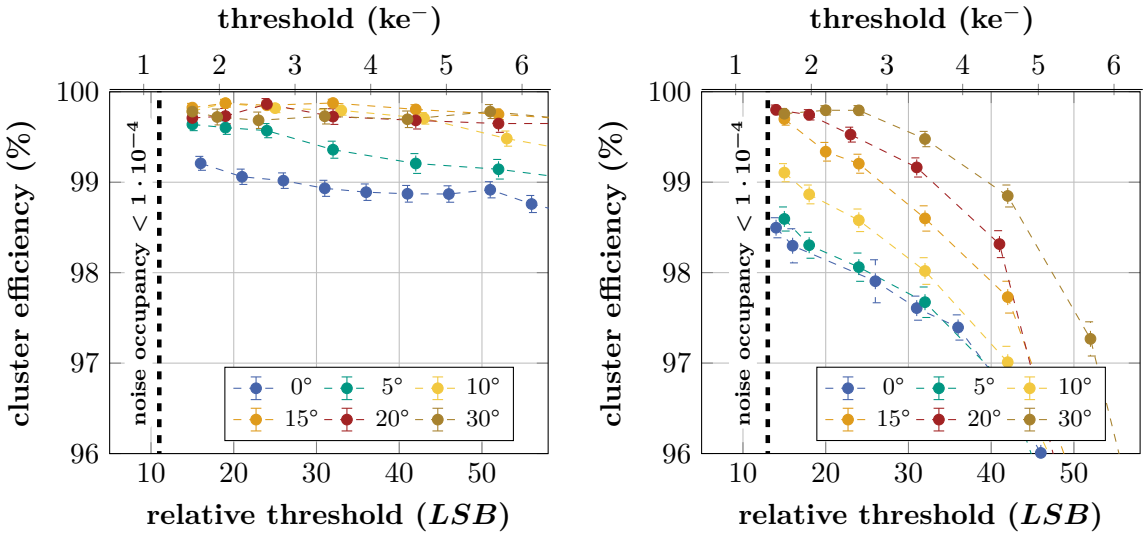

(a) fluence: unirradiated

(b) fluence: $1 \cdot 10^{15}\,\mathrm{cm}^{-2}$

Figure 7.11.: Cluster efficiency in dependence of the relative threshold measured with assemblies featuring the Standard sensor design. The assemblies were differently tilted with respect to the particle beam to emulate inclined particle incidence on the sensor. Measurements with the unirradiated assembly at 400 V sensor bias voltage are shown in (a), whereas the efficiencies measured with the maximum irradiated assembly ($1 \cdot 10^{15}\,\mathrm{cm}^{-2}$) are depicted in (b). The irradiated assembly was operated at 600 V. Cluster efficiencies over 99.5 % can be reached with both assemblies, although larger tilt angles are required for the irradiated assembly. The minimum threshold settings that need to be applied to reach noise occupancies smaller than $1 \cdot 10^{-4}$ are indicated by the black dashed lines.

the PCommon design and yields an efficiency gain of about 0.5 % prior to irradiation compared to the more conventional Standard design with atoll p-stop structures. However, after hadron irradiation and at low thresholds the beneficial effect decreases to about 0.15 % and 0.3 % at the medium and highest tested fluence, respectively.
In the end, the CMS Collaboration decided to use the more conservative Standard design for all PSp sensors in the Phase-2 Outer Tracker for various reasons. Firstly, the NoBias design, which would have provided the highest particle detection efficiency, was discarded due to the lack of possibility to test the bare sensors. None-functional sensors could only be detected after equipping them with a full set of readout chips, entailing the risk of high additional costs in case of a low sensor yield during sensor production. Secondly, the advantage of the PCommon design that is mainly present prior to irradiation is put into perspective by the fact that the Standard sensor shows a noticeable efficiency increase at inclined particle incidence. Prior to irradiation the efficiency increases by about 0.4 % for particle incidence angles larger than 5°. Even at the highest tested fluence the global efficiency increases by over 1 % if particles cross the sensor at angles larger than 15°. Additionally, at the time the design decision had to be made, only the more conservative Standard design has been tested on FZ290 PSp full-size sensors without showing any severe problems [Wit20]. Taking the risk of using the PCommon design without having it tested on full-size sensors was not commensurate with the marginal gain in efficiency that could be expected.
Results from beam test measurements presented in this chapter were shared with the CMS tracker simulation group. Simulations based on the CMS software framework CMSSW were implemented by the group to estimate the impact of the inefficient sensor bias rail regions on the tracking performance. Figure 7.12a and Figure 7.12b show the simulated tracking efficiency in dependence of the pseudoprapidity η and the particles' transverse momentum, respectively. The simulations are based on 9 000 top quark-antiquark pair production ($t\bar{t}$) events at a center-of-mass energy of 14 TeV with an average of 200 superimposed pileup collisions. Both plots compare the scenario with and without the bias rail inefficiency, while the punch-through structures are not taken into account. Within the simulations, the inefficient bias rail area is assumed to have a width of 37.5 µm. Hits in the PSp sensors are discarded as soon as a small part of a simulated particle track is inside the inefficient sensor region. This represents the most pessimistic scenario, as it does not take into account the beneficial effect of inclined particle incidence. From the simulations, it can be seen that the bias rails do not have a significant impact on the tracking efficiency, which shows an overall decrease in the range of 1 % to 3 %.
The CMS Tracker simulation group is currently working on a more realistic implementation that takes into account the beneficial effect of inclined particle incidence, which was demonstrated in Section 7.4.5. A slight improvement of the tracking performance based on the more realistic model can be expected.

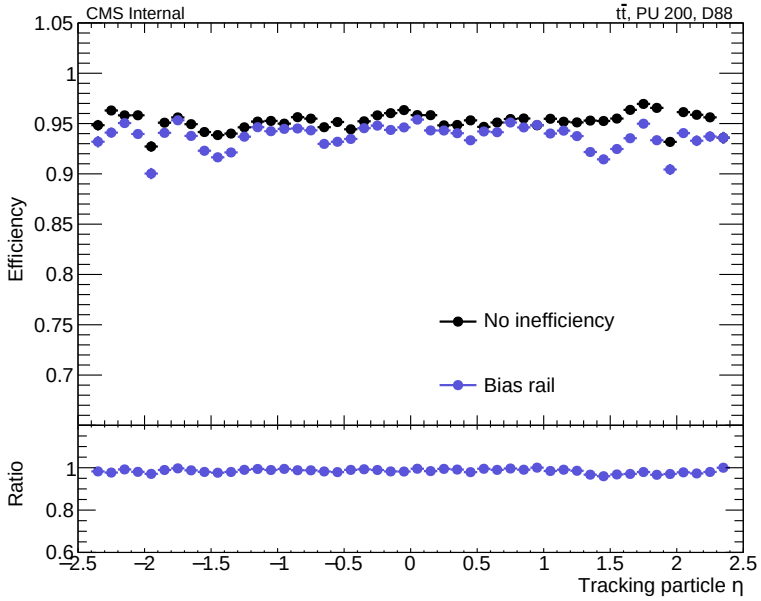

(a)

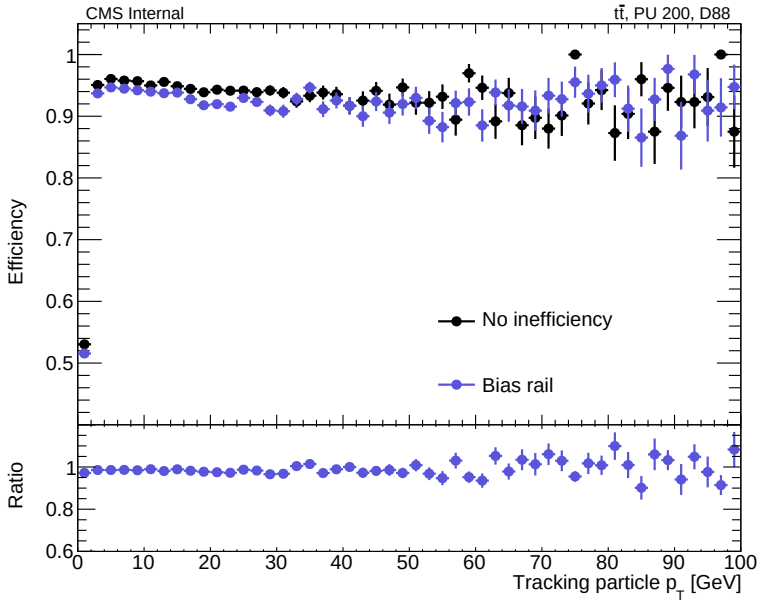

(b)

Figure 7.12.: Tracking efficiency as a function of the pseudoprapidity (a) and the particles' traverse momentum (b) determined based on 9 000 $t\bar{t}$ events with 200 superimposed pileup collisions, simulated with CMSSW. Overall, efficiency reduction related to the PSp sensor bias rail is in the order of 1 % to 3 %. [CMS23c]

8
2S Module Beam Tests

KIT as a 2S module assembly center is strongly involved in the qualification of 2S module prototypes. Extensively testing each module iteration is essential to identify potential weaknesses and to eliminate them in the next iteration. In the past, KIT has contributed to several beam tests at DESY in order to evaluate the prototypes' functionality with regard to the cluster and stub detection efficiency. A selection of results collected in the course of these beam tests can be found in [Kop22] and [Dro21]. Since mid 2021, a new 2S module prototype iteration is available that is based on the design and components introduced in Section 3.3. KIT was one of the first assembly centers that received the new module components to build and test the latest module iteration. A summary of lab tests including noise investigations and thermal cycling can be found in [Kop22]. To complete the characterization of the latest prototypes, additional beam tests were performed in June and November 2021 at the DESY beam test facility. Figure 8.1 shows a fully assembled 2S module of the latest version mounted on an aluminum module carrier.
In addition to a module with unirradiated components, a second module with radiated sensors and frontend hybrids was built to study the impact of radiation damage on the overall module performance. The combination of irradiated sensors and frontend hybrids had never been tested before on module level. Results gathered during these beam tests are summarized in this chapter after introducing the module prototypes in more detail.

8.1. Module Readout and Calibration

The 2S module readout is based on the *Phase 2 Acquisition and Control Framework* (Ph2_ACF) [CMS23b], a C++-based software framework developed and maintained by the CMS community to communicate with all Phase-2 modules of the Inner and Outer Tracker. As with the MaPSA setup (see Section 7.1), an *FC7 evaluation board* [Pes12] serves as interface between software and module. The FC7 runs a dedicated firmware, developed for data acquisition and communication with the 2S module prototypes. Operating the module with external trigger, as it is the case during beam test operation, requires to use both FMC slots on the FC7. One slot serves as interface for the trigger signals while the second slot is equipped with a dedicated adapter card featuring optical transceivers to connect the module via its optical fibers. The Ph2_ACF provides several routines to perform functional tests and to prepare the system for data acquisition. Routines, relevant for this chapter, are briefly introduced in the following.

Noise Measurement: Efficient module operation requires a high signal-to-noise ratio. Therefore, the noise of the CBC readout chips is an important quantity to characterize the module performance. Due to the binary processing of hits in the CBC, the noise of each channel is determined by measuring the noise hit occupancy. At a given threshold the noise hit occupancy is obtained from the number of recorded noise hits divided by the number readout triggers and is measured in the absence of external signals. Measuring the noise hit occupancy at different thresholds results in the integrated noise spectrum, which is referred to as *s-curve* because

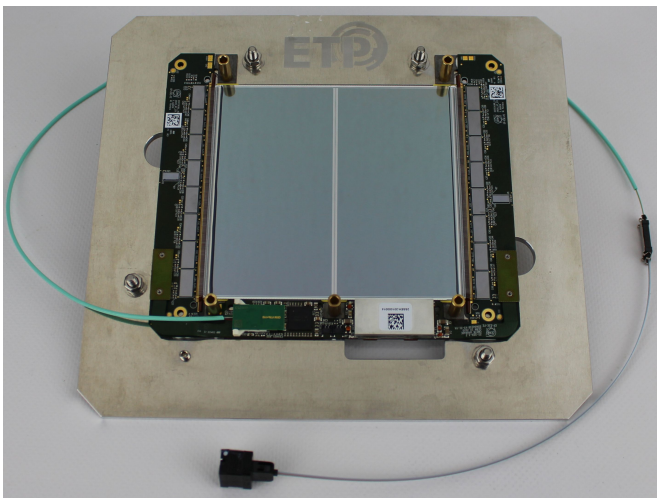

Figure 8.1.: Picture of the latest 2S module prototype version mounted onto an aluminum module carrier that allows for safe and easy handling of the module. The optical fiber used for connecting the module to the off-module electronics is wrapped around the module carrier. Picture taken from [Kop22].

of its characteristic shape. An example of an s-curve measured with one frontend channel is shown in Figure 8.2a. For the CBC, high comparator thresholds correspond to low threshold configurations, which are given in units of V_{cth}. Thus, starting at high comparator thresholds the detection of noise hits is suppressed, and consequently the noise hit occupancy is almost zero. By reducing the threshold, more and more noise hits are detected, and the noise hit occupancy starts to increase until it saturates at one. Assuming the noise to be Gaussian distributed, the obtained s-curve follows an error function

$$f(x) = \frac{1}{2}\mathrm{erf}\left(\frac{x-\mu}{\sqrt{2}\sigma}\right) + c \ , \tag{8.1}$$

whereby two main parameters can be extracted from a fit:

- The *pedestal* represents the threshold value for which the occupancy reaches 50 % and is given by the parameter μ.
- The *channel noise* is quantified by the standard deviation σ.

The Gaussian noise spectrum reconstructed from the fit parameters is shown in Figure 8.2a.

Offset Calibration and Relative Threshold: As mentioned in Section 3.3.2, the response of individual frontend channels is not uniform due to process variations. Thus, the channels need to be trimmed to compensate for this mismatch. The trimming routine performs threshold scans with each channel and determines its pedestal. By individually adjusting the 8-bit offset registers, the pedestal positions of all channels are shifted to a global target value. Figure 8.2b shows a 2D histogram of the noise hit occupancy measured with one CBC after performing the trimming routine. The CBC shows a uniform pedestal distribution across all channels. In preparation for data taking, a global threshold is applied to all channels. The difference between the global threshold and the pedestal position is defined as relative threshold. For the conversion of relative thresholds given in units of V_{cth} into electron charge equivalent values a conversion factor $1\ V_{\mathrm{cth}} = 156\,\mathrm{e}^-$ is used [Mai19]. If not stated differently, all threshold values shown in the following refer to relative thresholds.

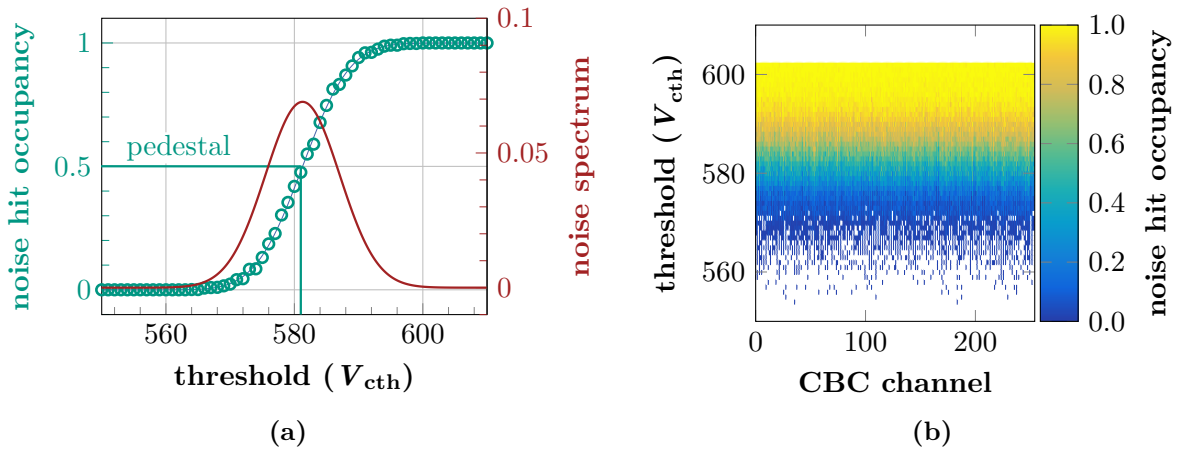

Figure 8.2.: (a): Noise hit occupancy of one CBC channel in dependence of the threshold. The s-curve follows an error function and its derivative, a Gaussian distribution, describes the underlying noise spectrum. (b): Noise hit occupancy of one CBC after offset calibration. The s-curves of all channels show a uniform distribution.

8.2. Characterization of Irradiated Module Components

The main goal of the module prototype characterization is to proof that the modules are fully functional and stay operable over the entire CMS runtime. In this regard, besides testing the general module functionality other aspects such as radiation damage and its impact on the module performance must be taken into account. Thus, a 2S module with irradiated sensors and frontend hybrids was built in addition to a normal prototype module. Although not all module components were irradiated, the module is named *irradiated module* in the following, while the other module is called *unirradiated module*.
An overview of all irradiated components is given in Table 8.1. The irradiation was performed with 23 MeV protons at the Karlsruhe compact cyclotron (KAZ) [ZAG22] with an underlying fluence uncertainty of about 15 %. As indicated in Table 8.1, the fluences of the bottom and top sensor are about 10 % lower compared to the maximum expected fluences in the respective CMS runtime scenarios. Figure 8.3 sets this deviation into perspective by showing the integrated 2S module fraction that will be exposed to a certain fluence considering the two different scenarios. It can be seen that the sensor fluences chosen to probe the different CMS scenarios can be regarded as worst-case approximation for nearly all modules. In the nominal scenario only 2.7 % of all 2S modules exceed the bottom sensor fluence, while in the ultimate scenario the fraction of modules facing fluences higher than the top sensor fluence is only 1.4 %. To account for the effect of annealing that might be accumulated during the yearly scheduled two weeks of maintenance, the 2S sensors were annealed after irradiation. A room temperature equivalent annealing of 140 days was chosen for both sensors assuming that the tracker is warmed up to room temperature during each maintenance period within 10 years of operation.
In contrast to the sensors, the fluence of the frontend hybrids is significantly lower. This results from the fact that the maximum expected ionizing dose for 2S modules in the Outer Tracker (about 150 kGy [CMS23a]), which is the relevant parameter for the chips, was already reached after an irradiation corresponding to a fluence of $1 \cdot 10^{14}\,\mathrm{cm}^{-2}$. Reaching high ionizing doses at low fluences is a feature of the low energy proton irradiation facility.

Table 8.1.: Fluence and dose overview of the components assembled in the irradiated 2S prototype module. For the frontend hybrids the nominal and ultimate fraction refers to the maximum expected dose in the respective CMS operation scenario, while for the sensors the fractions refer to the maximum expected fluences. Fluence and dose values of the scenarios are based on [CMS23a].

Component	Fluence (cm^{-2})	Dose (kGy)	Nominal fraction (%)	Ultimate fraction (%)	Annealing (days at 21 °C)
frontend hybrids	$1 \cdot 10^{14}$	150	132	99	—
bottom sensor	$3.7 \cdot 10^{14}$	555	88	66	140
top sensor	$5.2 \cdot 10^{14}$	780	123	92	140

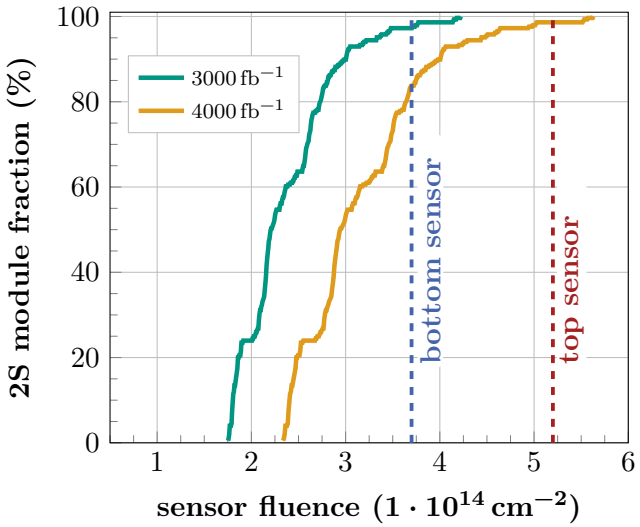

Figure 8.3.: Fraction of 2S modules that are exposed to a certain maximum fluence (or less) for the nominal (green) and ultimate (orange) CMS run time scenario. The fluences of the bottom ($3.7 \cdot 10^{14}\,\mathrm{cm}^{-2}$) and top ($5.3 \cdot 10^{14}\,\mathrm{cm}^{-2}$) sensor of the irradiated 2S module investigated in this chapter are indicated by the blue and red dashed lines. Fluence values taken from [CMS23a].

Sensor Characterization

In preparation for the module assembly all sensors were fully characterized with the probe station following the SQC procedure described in Section 5.3 and no bad strips were detected. Since the measurement results are similar to the standard SQC results of 2S sensors, they are not shown in detail here. However, the irradiated sensors were additionally tested after irradiation to validate their functionality and to quantify the irradiation impact on the sensor leakage current and depletion voltage. Due to time constraints, only IV and CV measurements were performed. The corresponding results are shown in Figure 8.4. The sensor leakage current after irradiation is significantly increased compared to an unirradiated 2S sensor ($\mathcal{O}(150\,\mathrm{nA})$ at 20 °C) and scales with fluence. IV measurements taken after annealing clearly show the beneficial effect on the leakage current. Taking 600 V as reference, the current of both sensors is halved by the annealing. At the time the sensors were measured, the annealing duration was only 130 days instead of the targeted 140 days to account for additional annealing during module assembly. The CV measurements taken after irradiation and annealing reveal a shift of the depletion voltage from 350 V towards voltages above 600 V, where the measured capacitance starts to saturate. Extracting precise depletion voltages from CV measurements of the irradiated sensors is not possible as the kink in the curve is less pronounced. The curves can only be used to get a rough estimate. However, based on the CV measurements it can be expected that increasing the module bias voltage above the nominal voltage of 600 V will have a positive effect on the cluster efficiency measured on the sensors.
After sensor characterization the module was assembled following the assembly steps described in [Mai19]. To validate the module operability with regard to the leakage current, the module was measured with a dedicated station [Kop18] that provides cooling infrastructure for the module. The measurement (yellow curve in Figure 8.4a) proves that the module is operable up to 800 V without thermal runaway, provided that it is sufficiently cooled. In contrast to the probe station, the sensor temperatures during the module IV measurement are not precisely known as they are only cooled indirectly. The module sitting on its carrier was placed on the copper cooling bridges of the test station, which were set to −35 °C during the measurement. This corresponds to the nominal operation temperature of cooling system in the tracker [Apo+17].

Skeleton Tests

The 2S module frontend hybrids (FEH) and service hybrid (SEH) usually undergo a reception test at the module assembly sites before being assembled into the module to make sure that they are fully functional. Thus, the service hybrid is connected to the frontend hybrids forming an u-shaped *module skeleton*, which can be calibrated and tested by using the module readout software and methods introduced in Section 8.1. To study the impact of irradiation on the bare frontend hybrids dedicated skeleton tests were performed using the identical set of hybrids before and after irradiation.
Regarding the noise measured on the skeleton, no irradiation-related increase was observed. The mean noise remained at a constant level of about 2.3 V_{cth} with a standard deviation of less than 0.2 V_{cth}, which is consistent with the typical noise level of a skeleton. The corresponding noise distributions can be found in Figure C.1.
Besides the skeleton noise the response of individual frontend channels to a defined charge signal is another parameter that should remain unaffected by irradiation. Although the CBC is a binary readout chip, it is possible to reconstruct the shape of injected test signals by measuring the hit occupancy in dependence of the threshold (s-curve scan) for different delays between signal readout and pulse injection. This is shown in Figure 8.5 for one CBC channel

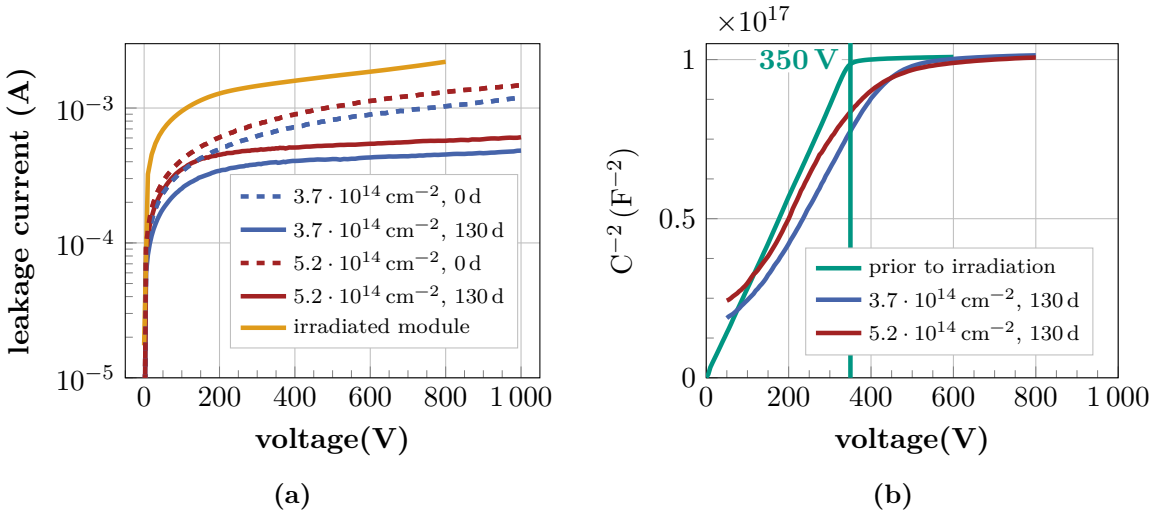

Figure 8.4.: (a): Leakage current of the irradiated 2S sensors measured at −20 °C before and after annealing. The current scales with the sensor fluence. After receiving annealing of 130 days, the sensor leakage current at 600 V is decreased by a factor of two. The module IV proves that the module can be operated up to 800 V without thermal runaway. (b): CV measurements of the irradiated 2S sensors after annealing compared to the unirradiated state.

where the trigger delay is gradually increased in steps of 5 ns. Starting at delays smaller than 4900 ns, where no test pulse is injected yet, the pedestal extracted from the hit occupancy stays at a constant threshold of about 589 V_{cth} defining the channel baseline. With further increasing delays the pedestal is shifted towards higher thresholds due to the injected charge signal and reaches its maximum after about 25 ns. The maximum pedestal shift with respect to the channel baseline defines the signal amplitude. For signal injection, the CBC internal test pulse generator circuit was used. The amount of injected charge can be adapted with an 8-bit DAC that defines the voltage amplitude to charge the 20 fF capacitors[1] in the generator circuit. Figure 8.6 shows amplitude distributions measured with the same set of channels before and after irradiating the frontend hybrids. Charge signals ranging from 8.6 ke^- to 30 ke^- were injected to test different signal strengths. Comparing the distribution mean values, there is a slight trend towards larger signal amplitudes after irradiation. However, for each set of amplitude distributions the relative deviation of the mean value is smaller than 2 % and is therefore not of practical relevance. Moreover, the amplitude spread indicated by the standard deviation also remains unchanged. The fact that the amplitude spread increases with the amount of injected charge originates from the 25 % tolerance of the capacitors in the test pulse generator circuit. The larger the injected charge signal, the larger the absolute signal spread measured among the individual frontend channels. Overall, the test pulse measurements prove that the signal detection is not negatively affected by irradiation and the frontend hybrids remain fully functional.

8.3. Module Noise Measurements

The noise level measured on the fully assembled module is a crucial parameter that impacts the overall module operability. The higher the average channel noise the larger the threshold that needs to be applied to sufficiently suppress noise hits during data taking. High thresholds on

[1] Each CBC frontend channel has its individual capacitor.

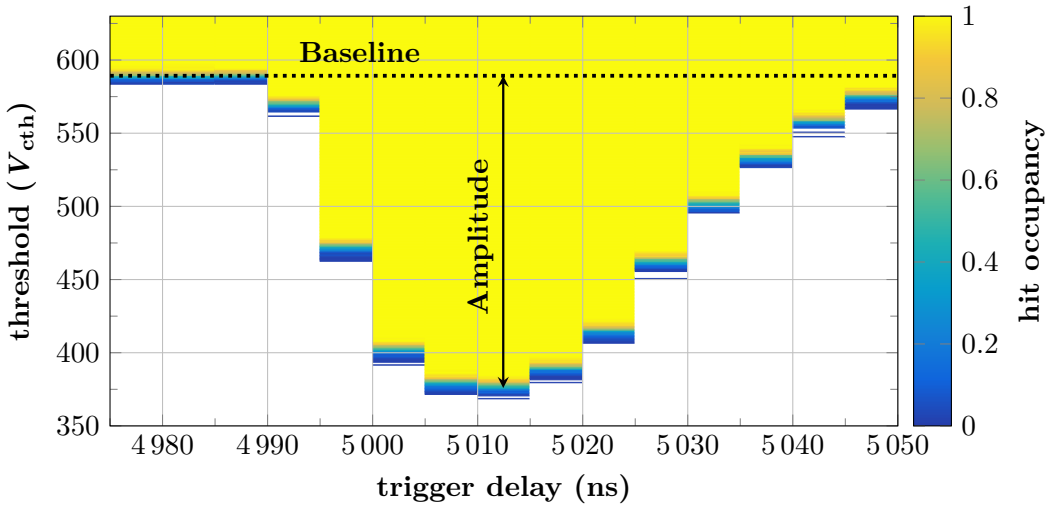

Figure 8.5.: Pulse reconstruction of a 30 ke$^-$ test signal injected with the CBC internal pulse generator circuit. The hit occupancy in dependence of the threshold is measured for different trigger delays. Depending on the delay between charge injection and signal readout, the pulse is sampled at different phases. The charge pulse amplitude is defined as the threshold difference between the baseline and the maximum pedestal shift.

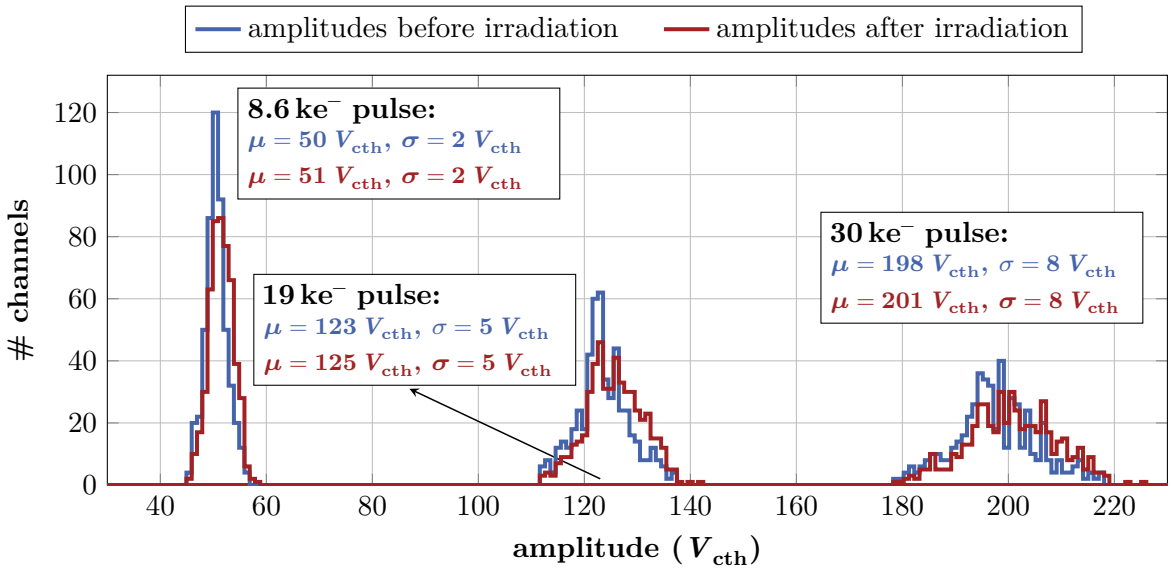

Figure 8.6.: Reconstructed signal amplitudes after injecting varying charge pulses into the CBC frontend channels by using the internal pulse generator circuit. Amplitudes were measured on a total of 512 channels with the module skeleton before and after irradiating the frontend hybrids. The hybrids were irradiated to a fluence of $1 \cdot 10^{14}$ cm^{-2} corresponding to an ionizing does of 150 kGy. Overall, no significant irradiation related change in the amplitude distribution is observed among the different charge injections.

the other hand can impact the particle detection efficiency. This becomes especially relevant for irradiated sensors where the overall charge signal is reduced due to the radiation-induced defects. In general, the module noise depends on environmental influences such as stray electromagnetic fields and grounding levels on the module hybrids. Thus, intensive noise studies with the latest 2S module prototype version were performed in [Kop22]. The main outcome relevant for this chapter is briefly summarized in the following.

1. The noise measured on the module is increased in the presence of different electrical ground levels between the module and its supporting structure, e.g. the module carrier. Thus, the service hybrid offers a dedicated grounding pad that is extended to one of the module fixation points on the left-hand side Al-CF bridge. When mounting the module on its supporting structure the screw used for module fixation also serves as ground connection between the SEH grounding pad and the supporting structure. This configuration corresponds to the grounding scheme as it will be used for the 2S module installation in the CMS Outer Tracker. However, it has been found that the lowest noise level is obtained by using two additional grounding points that are located on the left and right frontend hybrid, respectively. A picture showing this grounding configuration can be found in Figure C.2. If not stated differently, all module measurements presented in the following were conducted using the optimized configuration to minimize the noise as much as possible.

2. Despite the additional grounding connections on the hybrids, the noise levels measured on the latest prototypes are still higher compared to the older prototype 8CBC3 modules with a discrepancy of about $+0.8\,V_{\mathrm{cth}}$. Especially on the bottom sensor, the latest prototypes show an excess noise contribution deviating from the Gaussian expectation shown in Figure 8.2a. As introduced in Section 3.3, sensor high voltage is provided from the service hybrid via two flexible tails that are connected to the sensor backside. With the current bias circuit configuration the sensor backplanes are directly connected to each other through the tails. It has been found that the sensors together with the tails form a resonant circuit, with the two closely spaced sensors acting as capacitor and the tails forming the inductor. As the DC-DC converter stage on the service hybrid is located directly above the HV tails, oscillating currents between the two sensors can be induced through the tails, which in turn deteriorates the module noise. Adding $100\,\Omega$ resistors to each of the tails changes the impedance of the circuit and significantly mitigates the module noise as the current oscillation between the sensors is reduced. For the next module iteration, resistors will be added to all tails for noise mitigation.

At the time the DESY beam test measurements took place, the noise optimization by installing resistors on the HV tails was not yet known. Therefore, the noise measurements do not represent the final configuration as it will be in the Outer Tracker, but can be regarded as worst-case estimation. Figure 8.7 shows the channel noise distributions measured with the prototype modules investigated in this chapter. All measurements were either performed at room temperature or at a sensor temperature of about $-20\,°\mathrm{C}$ using the cooled module test box. Compared to the $2.3\,V_{\mathrm{cth}}$ noise level measured on the module skeleton (see Section 8.2), the mean noise of the fully assembled unirradiated module measured at room temperature is increased by a factor of three. The higher noise is mainly related to the additional load capacitance (see Section 4.3.2) coming from the silicon sensors that are attached to the frontend channels. Based on the noise measured with the unirradiated module at about $-20\,°\mathrm{C}$ sensor temperature, which is similar to the temperature the modules will have in the tracker, a noise reduction of about $0.8\,V_{\mathrm{cth}}$ is observed compared to the room temperature measurement. This is in good agreement with the noise temperature scaling studies shown in [Kop22]. Comparing

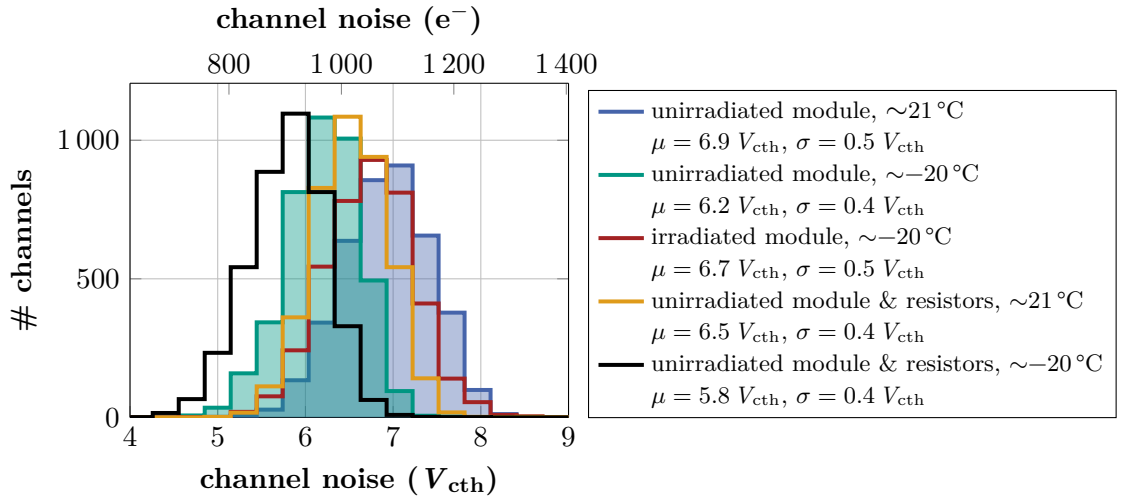

Figure 8.7.: Channel noise distributions of the modules investigated in this chapter measured at different temperatures and 600 V sensor bias voltage. Most of the measurements were conducted with the optimized ground configuration using the grounding pads on the service and frontend hybrids. The unirradiated module with resistors integrated to the HV tails (orange and black) was tested only using the service hybrid ground and yields a noise reduction of 0.4 V_{cth}.

the mean noise measured with the unirradiated and irradiated module at low temperature reveals a difference of about 0.5 V_{cth}. Different aspects have to be taken into account here. In [Dro21] it has been shown that the noise scales linearly with the strip leakage current with a slope of

$$m = (0.419 \pm 0.002)\ V_{cth}\,\mu A^{-1}\ . \tag{8.2}$$

During the noise measurement the total leakage current of the irradiated module was 2.3 mA, yielding an average noise increases of about 0.2 V_{cth}. Due to the significantly lower sensor leakage current prior to irradiation the leakage current impact on the noise of the unirradiated module can be neglected. Another aspect is the general noise deviation among different modules that can be estimated to about 0.3 V_{cth} [Kop22]. In combination with the given temperature uncertainty related to the module test setup, this yields an overall uncertainty that matches the deviation observed between the unirradiated and irradiated module.
After the beneficial effect of adding resistors to the sensor bias circuity on the module noise has been discovered, the unirradiated module was retested with resistors added to the HV tails. The corresponding noise distributions measured at room temperature and −20 °C are shown in orange and black, respectively. Although only the service hybrid ground was used for the measurements, the mean noise is decreased by 0.4 V_{cth} compared to the module configuration without resistors but with optimized grounding configuration.

8.4. Beam Test Measurements

The DESY beam test facility and the analysis workflow have been introduced in Chapter 6. During the beam test measurement, the 2S module was installed inside a light-tight DUT box that was mounted onto movement and rotation stages. For the irradiated module an additional copper cooling bridge connected to an external chiller was integrated into the box to provide sufficient cooling to the module allowing for operation without thermal runaway. With this setup configuration sensor temperatures in the range of −15 °C to −20 °C were reached,

similar to the module test box used in the laboratory. In contrast, the unirradiated module was not actively cooled and operated at room temperature. Pictures of the setup can be found in Figure C.3. For all measurements presented in the following the DUT box was positioned in the beam so that the sensor center, where the strips are arranged in two parallel rows (see Section 5.1.1), was illuminated. This configuration was chosen to maximize the number of tested strips.
In order to obtain meaningful results from the analysis discussed in Section 6.2, the residual cuts that are used to match reconstructed particle tracks with clusters of hits on the DUT have to be adapted to the 2S sensor geometry. The impact of different cuts on the cluster efficiency has already been discussed in Section 7.4.1 for a macro-pixel sensor. Following the same argumentation, the x residual cut used for the 2S analysis is chosen to be twice the strip pitch, which corresponds to 180 µm for a 2S sensor. Since the 2S sensor strip length of about 5 cm is significantly larger than the sensor area illuminated with the beam, no y residual cut is applied.

8.4.1. Single Sensor Characterization

Before evaluating the module functionality with regard to stub detection (see Section 8.4.2), the single sensor performance is studied. All results shown in the following are based on measurements at perpendicular beam incidence. If not stated differently, all sensors were operated at 600 V bias voltage.

Threshold Dependency

Figure 8.8 summarizes the cluster efficiency and noise occupancy measured with the unirradiated and irradiated 2S module as a function of different threshold settings. For reference, the electron equivalent threshold is indicated on the upper x axis. Looking at the overall course of the efficiency curves reveals cluster efficiencies of 99.8 % with all sensors at the lowest tested threshold setting of 3.9 ke^-. However, increasing the threshold by only 0.8 ke^- already leads to a slight efficiency decrease on the irradiated sensors that becomes more pronounced as the threshold further increases. The efficiency drop of the higher irradiated sensor is pronounced more strongly, which is to be expected as the deterioration of the sensor charge collection efficiency scales with fluence. In contrast, the unirradiated sensors show consistent behavior, forming a stable plateau at 99.9 % cluster efficiency up to thresholds of about 9.3 ke^-.
For module operation in the tracker not only the cluster efficiency, but also the noise occupancy needs to be taken into account. Noise occupancies shown in the plot were measured for each sensor individually and represent the probability to detect a noise hit per channel and triggered readout. As already mentioned in Chapter 7, the noise occupancy should be significantly smaller compared to the hit occupancy. In the following $1 \cdot 10^{-4}$ is taken as an upper limit for the noise occupancy, which is two orders of magnitude smaller compared to the expected hit occupancy in the tracker [CMS17d]. In Figure 8.8, the limit is indicated by the black dashed lines. For both modules the bottom sensor noise occupancy is significantly higher compared to the top sensor. This is related to the above mentioned noise contribution induced from the DC-DC converter stage through the sensor HV tails that mainly affects the bottom sensor. In order to fall below the occupancy limit of $1 \cdot 10^{-4}$, thresholds of at least 4.7 ke^- have to be applied, where the efficiency of the irradiated sensors already starts to decrease. However, the minimum cluster efficiency of 99.5 % targeted by the CMS Collaboration [Ada+21a] is still reached at this threshold setting. For the module top sensors there is no limitation regarding the threshold settings as the noise occupancy is sufficiently low, already at the smallest tested threshold. The discrepancy in the top sensor noise occupancy between the irradiated and

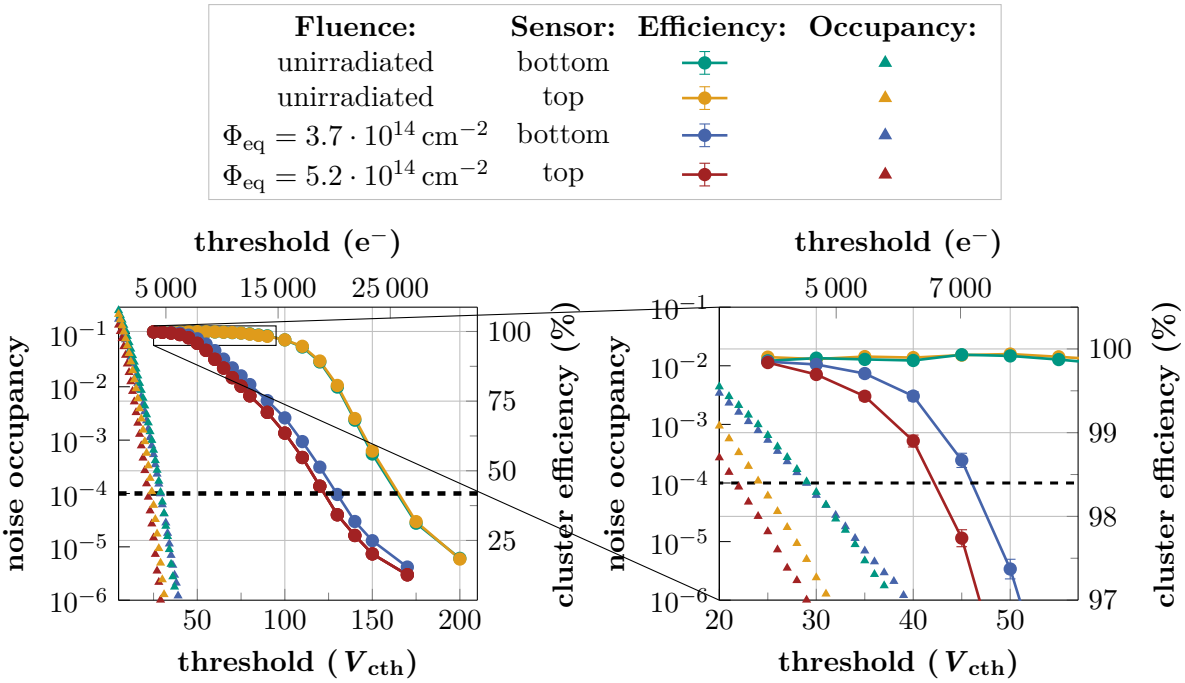

Figure 8.8.: Sensor cluster efficiency (left y axis) and noise occupancy (right y axis) in dependence of the applied threshold. The right plot shows a zoomed section in the threshold range relevant for module operation in the tracker. All sensors were tested at 600 V bias voltage and at perpendicular beam incidence. A minimum threshold of 4.7 ke$^-$ must be applied to reach bottom sensor noise occupancies smaller than $1 \cdot 10^{-4}$. Prior to irradiation, the module provides a larger operation window with cluster efficiencies above 99.8 % up to thresholds of 9.3 ke$^-$. Efficiencies of the irradiated sensors scale with the fluence. Only at the lowest threshold setting (3.9 ke$^-$), cluster efficiencies of 99.8 % are reached.

unirradiated sensor is mainly related to the temperature difference. Lower sensor and chip temperatures yield an overall reduced noise.

Bias Voltage Dependency

To evaluate the impact of different bias voltages on the sensor cluster efficiencies, voltage scans with both modules were performed. Results are shown in Figure 8.9. Since the cluster efficiency of irradiated sensors is more sensitive to the threshold (see Figure 8.8), scans at two different threshold settings were performed with the irradiated module. Efficiencies measured at the lower threshold setting (4.7 ke$^-$) are shown in the upper plots, while the voltage scans at the higher threshold (7 ke$^-$) are summarized in the bottom plots. The lower threshold corresponds to the minimum that must be applied in order to reach noise occupancies smaller than $1 \cdot 10^{-4}$ with the module bottom sensors. Since the efficiency measured with the sensors assembled in the unirradiated module behave similar and are less affected by the threshold setting, only the top sensor at 7 ke$^-$ is shown in the plots.
Prior to irradiation, cluster efficiencies exceeding 99.8 % are already reached at 175 V. This is about 85 V less than the sensor depletion voltage that has been determined by performing a CV measurement with the sensor before assembling it into the module. Thus, the charge signal generated by particles crossing the only partly depleted sensor is already sufficient to overcome the threshold. Further increasing the sensor bias voltage does not improve the

efficiency, resulting in a stable plateau.
As indicated in Figure 8.4, the sensors used to assemble the irradiated module had a depletion voltage of about 350 V prior to irradiation. Regarding the specification limit that is applied in the scope of the sensor quality control, this corresponds to the upper limit for the sensor acceptance (see Table 5.3). Sensors with depletion voltages close to the specification limit were specifically chosen for the irradiated module as they represent the worst-case scenario that can be expected during the sensor production. As discussed in Section 7.4.3, the charge collection efficiency of irradiated sensors is influenced by two main aspects: charge trapping related to radiation-induced defects and the increase of the sensor depletion voltage (see Figure 8.4) due to the changing effective doping concentration. Both effects can be mitigated by increasing the sensor bias voltage. First looking at the overall course of the efficiency measured with the irradiated sensors shows that the efficiency increase is less steep compared to the unirradiated sensor, indicating a slower growth of the depletion zone inside the sensor. Consequently, higher voltages must be applied to reach maximum efficiency. Concentrating on the voltage range relevant for module operation (600 V to 800 V) the gain in efficiency at 800 V, which is the maximum sensor voltage that could be applied in the tracker, is almost negligible considering the underlying uncertainties. However, at the higher threshold setting of 7 ke^-, the beneficial effect of increasing the bias voltage is clearly visible as the cluster efficiency continuously increases without saturation until 800 V. Increasing the sensor bias voltage always comes with the drawback of overall larger module power consumption and, consequently, a larger amount of heat that must be dissipated by the cooling system. Thus, regarding the module operation in the tracker, increasing the sensor bias voltage should only be considered if the modules need to be operated at threshold settings larger than 4.7 ke^-, as for smaller thresholds the gain in efficiency is negligible.

Sensor Inefficiencies

In contrast to the macro-pixel sensors investigated in Chapter 7, the strip sensors assembled in 2S modules do not feature any biasing structures within the active sensor area that reduce the sensor efficiency. Inefficiencies, especially after irradiation, are solely related to charge sharing effects between neighboring strips. Depending on the overall number of charge carriers generated in the sensor and the threshold setting, the signal fraction seen by the individual strips might be too small to be registered by the binary readout. By looking at the cluster efficiency in dependence of the interpolated track intersection point on the sensors, inefficiencies related to charge sharing can be studied on the sensors irradiated to different fluences. The upper plots in Figure 8.10 summarize the position dependent cluster efficiency measured across two neighboring strips (x coordinate). The plots are obtained by dividing the illuminated sensor area into smaller subregions, each containing a pair of adjacent strips. These subregions are then superimposed to increase the statistics. Irradiated sensors were tested at low and high threshold settings with the results shown in the left and right plot, respectively. Independent of the sensor fluence and the readout threshold, the highest efficiency is measured close to the center of the strip implants at $x = 45\,\mu\mathrm{m}$ and $x = 135\,\mu\mathrm{m}$. Here the charge signals generated by particles crossing the sensor are barely affected by charge sharing as most of the charge is collected by the directly overlying strip implant. However, looking at the gap region between two neighboring strip implants ($x = 90\,\mu\mathrm{m}$) the decreasing efficiency related to charge sharing becomes clearly visible. As expected, the inefficiencies scale with the sensor fluence and the irradiated sensors are more sensitive to the threshold settings. The width of the region affected by the inefficiency is about 50 µm and is indicated by the red background.
Additional inefficiencies related to charge sharing are present at the sensor middle, where the sensor is segmented into two parallel rows of strips (see Section 5.1.1). The plots at the

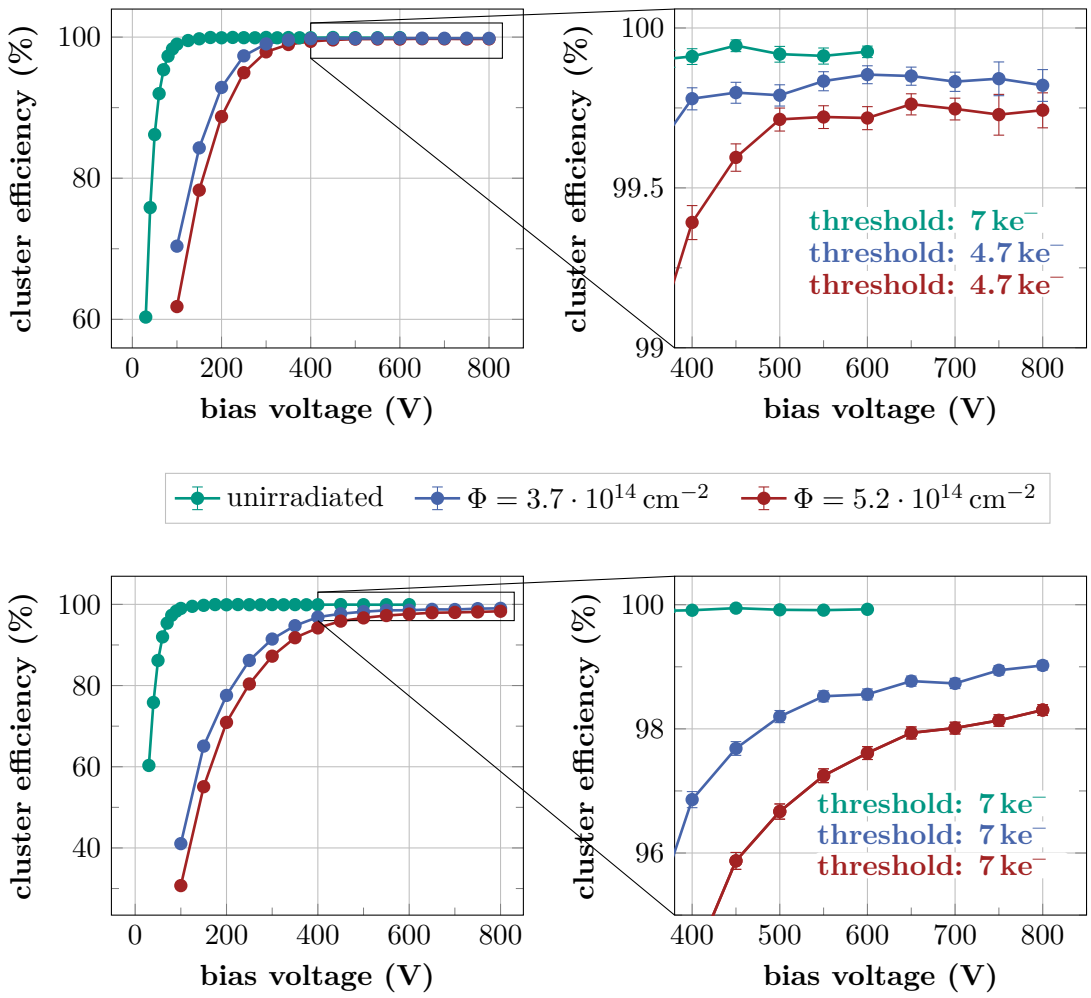

Figure 8.9.: Cluster efficiency measured in dependence of the sensor bias voltage. Irradiated sensors were tested at a threshold of 4.7 ke$^-$ and 7 ke$^-$ with the results shown in the upper and lower plots, respectively. The unirradiated sensor was only tested at 7 ke$^-$ and is added in all plots for reference. The threshold of 4.7 ke$^-$ corresponds to the minimum threshold that must be applied in order to reach noise occupancies smaller than $1 \cdot 10^{-4}$ for the module bottom sensors. Overall, the irradiated sensors must be operated at higher voltages compared to the unirradiated sensor in order to reach maximum cluster efficiency. At the lower threshold setting of 4.7 ke$^-$ no efficiency boost is observed by increasing the voltage from 600 V to 800 V, while at the 7 ke$^-$ threshold setting, the cluster efficiency continuously increases for both sensor fluences without saturation up to 800 V.

bottom of Figure 8.10 show efficiency projections parallel to the strips (y coordinate) with the sensor middle being at $y = 0\,\text{mm}$. Again, all strips illuminated by the beam are superimposed in one plot to increase the statistics. First looking at the efficiencies measured at the lower threshold settings (left plot) reveals that the inefficiencies at the sensor middle are more distinct compared to the inefficiencies along the x axis discussed above. Furthermore, with a width of about 70 µm the affected area is slightly wider. This can be explained by the fact that at the sensor middle more than two strips adjoin each other and consequently the charge signal is shared among a larger number of strips. As expected, at higher threshold settings (right plot) the inefficiencies at the sensor middle of the irradiated sensors become larger. Moreover, the impact of charge sharing between adjacent strips within the same row is visible in the projection as the efficiency measured along the strips is shifted towards smaller values for the irradiated sensors. Only small areas close to the sensor middle remain nearly as efficient as the unirradiated sensor. These areas are correlated with the position of the strip DC- and AC-pads at the sensor middle. The width of the strip implant is 22 µm, but at the DC- and AC-pad position it is extended to 55 µm and 60 µm, respectively. Due to the wider implants, charge sharing effects at the pad region are reduced as the interstrip region is smaller, which results in a higher efficiency. Overall, the observed inefficiencies are in good agreement with the performance of the individual sensors observed in the threshold and bias scans.

8.4.2. Module Stub Performance

Providing stub information to the CMS Level-1 track finder is a central functionality of the CMS Outer Tracker modules. Thus, the stub identification was tested with the unirradiated and irradiated 2S module during the DESY beam tests. Before discussing the results, two aspects concerning the stub efficiency measurement should be taken into account:

1. The sensors assembled in the irradiated module have been exposed to different fluences (see Table 8.1). This configuration does not represent a realistic scenario as the sensors of individual modules in the CMS tracker will be exposed to similar fluences. Since for the detection of stubs clusters in both sensor layers are correlated with each other, the different sensor fluences affect the overall stub efficiency. Results obtained from the irradiated module can be regarded as the worst-case approximation for the nominal CMS runtime scenario.

2. Modules are only capable of detecting stubs from particles that generate hits in the same half of the bottom and top sensor layer as they are read out by the same frontend hybrid. Cluster information is not shared between the two hybrids. Therefore, particles crossing the module at the sensor middle might not create a stub signal, although the individual sensors might have seen a hit, but at different sensor halves. In [Kop22] it has been shown that the sensor mid-region that is insensitive to stubs signals extends over an area of about ±40 µm. During the beam test measurements the sensor middle was illuminated to maximize the number of strips hit by the beam. However, this configuration comes with the drawback that the stub efficiency measured with the modules is underestimated. The ratio between the inefficient area in the sensor middle and the area illuminated by the beam is about 0.9 %, whereas the ratio between the inefficient area and the whole active sensor is only about 0.08 %. A measurement-based assessment of the impact of the inefficient area on the stub efficiency is given in the next section.

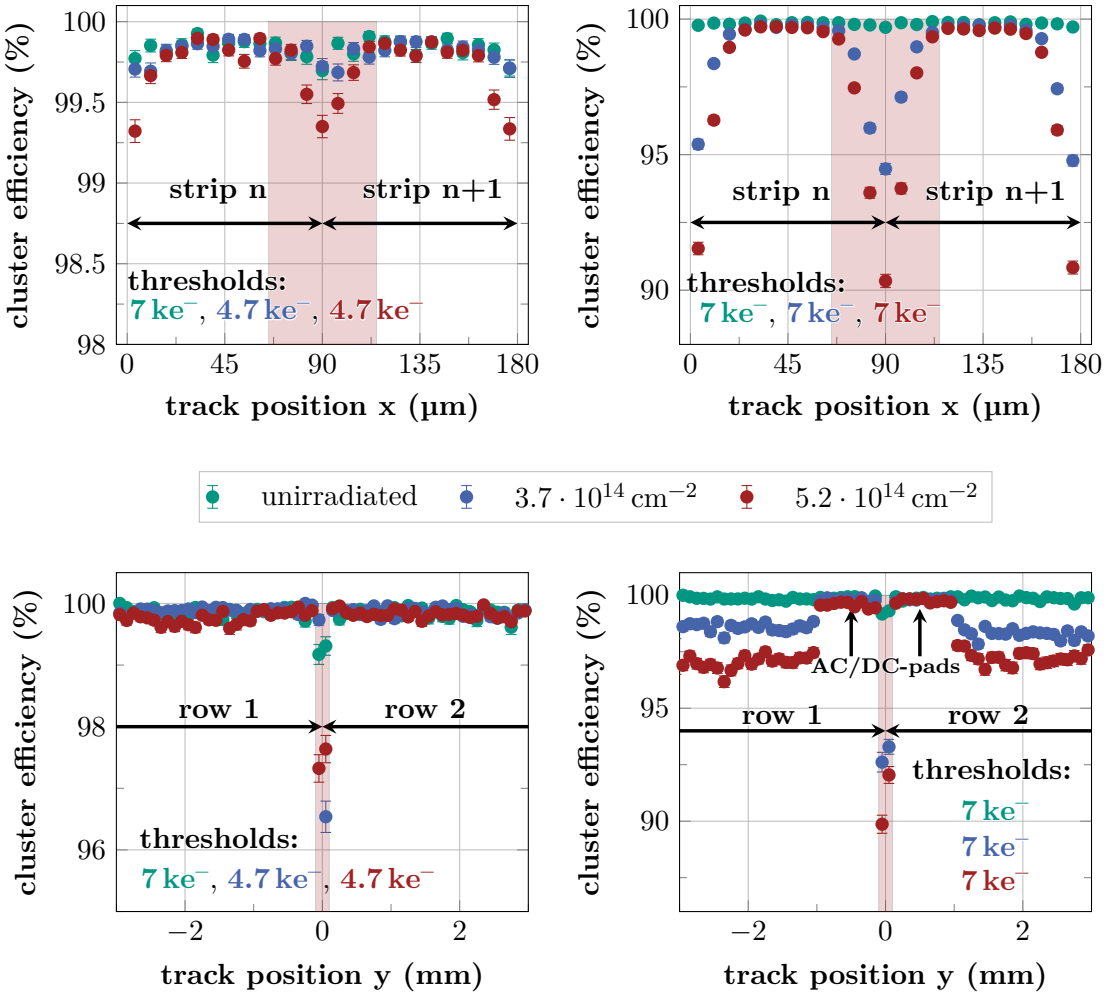

Figure 8.10.: Position dependent cluster efficiency measured along the sensors' x and y direction at 600 V sensor bias voltage. Irradiated sensors were tested at two different thresholds. Results obtained at the lower and higher threshold setting are shown in the left and right plots, respectively. Inefficiencies related to charge sharing occur at the interstrip region (upper plots) and at the sensor middle (bottom plots), where the sensor is segmented into two rows of strips. Irradiated sensors are affected more strongly by the inefficiencies due to the smaller charge collection efficiency and are more sensitive to the threshold setting.

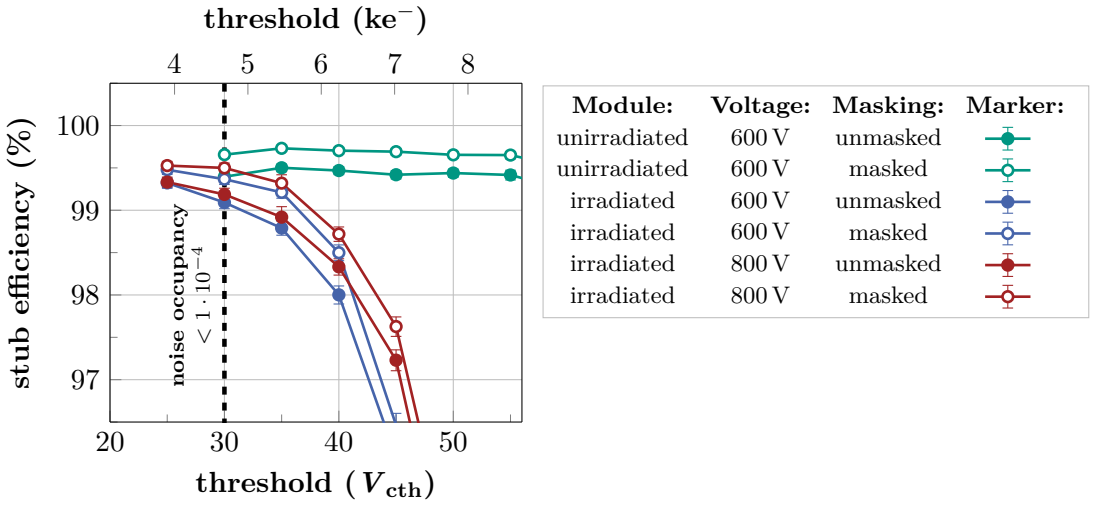

Figure 8.11.: Stub efficiency measured wit the unirradiated and irradiated module at different threshold settings and perpendicular beam incidence. The irradiated module was tested at 600 V and 800 V. Unfilled marker indicate the stub efficiency where an area of ±40 µm was masked in the analysis to study the impact of the inefficient sensor middle. Even with the irradiated module, stub efficiencies above 99 % can be reached at 600 V and without masking. Increasing the bias voltage to 800 V has a beneficial effect on the stub efficiency.

Stub Efficiency at Perpendicular Perticle Incidence

To quantify the impact of the threshold setting and the sensor bias voltage on the module stub detection efficiency, threshold scans at different voltages were performed. Results are shown in Figure 8.11. Similar to the single sensor cluster efficiencies shown in Figure 8.8, the stub efficiency of the unirradiated module remains stable up to thresholds exceeding 8 ke⁻. In contrast, the stub efficiency measured with the irradiated module slightly decreases with each threshold step. However, taking 4.7 ke⁻ as reference threshold, where the bottom sensor noise occupancies fall below $1 \cdot 10^{-4}$, stub efficiencies above 99 % are reached, even with the irradiated module. As mentioned above, the measured efficiency values are slightly underestimated due to the insensitive sensor middle that was illuminated with the beam during the measurements. Discarding particle tracks crossing the sensor within an 80 µm wide window placed around the sensor middle clearly improves the stub efficiencies. The corresponding values are indicated by the transparent markers. Taking into account the first three tested threshold settings on each module reveals an average absolute efficiency gain of about 0.25 % with the unirradiated module, while for the irradiated module the absolute gain is about 0.33 %. The larger gain obtained on the irradiated module is related to additional charge sharing effects (see Figure 8.10) that enforce the stub inefficiency at the sensor mid-region. Comparing the stub efficiencies measured at different voltages indicates that by boosting the voltage to 800 V the stub efficiency increases by 0.1 % at the target threshold of 4.7 ke⁻. Similar to the cluster efficiency measured on the single sensors (see Figure 8.9) the voltage related efficiency gain increases at larger threshold settings.

Stub Efficiency at Inclined Particle Incidence

The module's capability of transverse momentum (p_T) discrimination based on stubs was tested with both modules. In the CMS tracker, charged particle trajectories are bent differently by

the 3.8 T strong magnetic field depending on the particle's transverse momentum. To emulate bent particle tracks at the DESY beam line, the modules were stepwise rotated with respect to the beam while the stub efficiency was measured. Depending on the module rotation angle ϑ, the equivalent particle transverse momentum in the CMS tracker can be estimated by

$$p_T[\text{GeV}] \approx \frac{0.57 \cdot R[\text{m}]}{\sin(\vartheta)} \ , \tag{8.3}$$

where R indicates the radial module position in the tracker [CMS17d].
Figure 8.12 shows stub efficiencies measured with the unirradiated module for different rotation angles ranging from $-25°$ to $25°$. The plot contains angular scans performed at two different stub correlation window settings. For small module rotation angles the stub efficiency remains high forming a plateau with efficiencies above 98 %, independent on the window setting. However, looking closer at the plateau region, where the efficiency is expected to remain constant, an efficiency decrease of about 1 % is observed within the angular range of $\pm 13°$. This behavior is related to stub noise events and has already been observed in previous stub efficiency measurements presented in [Mai19] and [Zie22]. Stub noise events originate from falsely correlated clusters in the top and bottom sensor due to multiple track events, secondary particle events or fake hits in the sensor layers. In [Kop22] a detailed discussion and classification of stub noise events can be found. As mentioned in Section 3.3.2, the CBC always prioritizes stub events with small bend code, as these events correspond to particles with high $\mathrm{p_T}$. With increasing module rotation angle the bend of valid stub signals becomes larger and consequently the probability of prioritizing a stub noise event with small bend code over the valid stub signal increases. This results in a slightly decreasing stub efficiency at small rotation angles, which is in good agreement with the measured efficiencies at the plateau region.
By further rotating the module, the cluster displacement exceeds the correlation window size, resulting in a sharp efficiency drop as the number of stub signals found by the module drastically decreases. Thus, the stub efficiency in dependence of the module rotation angle follows a turn-on curve. Enlarging the size of the correlation window from ± 4.5 strips to ± 5 slightly shifts the flank towards larger rotation angles.
For symmetry reasons the stub efficiencies measured at the same rotation angle, but different rotation direction should be identical. However, the zero setting of the rotation stage might have had a small offset that can be different for the individual angular scans. Thus, before comparing stub efficiencies measured during independent scans, all rotation angles must be corrected by their offset. To obtain results comparable to previous 2S module angular scans, an alignment procedure similar to the procedure described in [Kop22] is used. For each angular scan the offset is obtained by fitting an error function (Equation (8.4)) to the left and right side of the stub efficiency turn-on curve. Error functions fitted to the right part of the turn-on curve are shown in Figure 8.13a. The error function used for the fits is given by

$$\epsilon_{\text{stub}}(\vartheta, a, b, c, d) = 100 - 50 \left(\text{erf} \left(\frac{\vartheta - a}{\text{b}} \right) \cdot c + d \right) \ , \tag{8.4}$$

with the parameter a representing the inflection point, where the stub efficiency reaches 50 % and b describing the width of the turn-on curve. The parameters c and d represent a scaling and offset factor, respectively. Taking the inflection points of both sides as reference for the offset correction, the angular offset ϑ_{off} is given by

$$\vartheta_{\text{off}} = \begin{cases} 0.5 \cdot (|a_{\text{left}}| - |a_{\text{right}}|), & \text{for } |a_{\text{left}}| > |a_{\text{right}}| \\ -0.5 \cdot (|a_{\text{left}}| - |a_{\text{right}}|), & \text{for } |a_{\text{left}}| < |a_{\text{right}}| \end{cases} \tag{8.5}$$

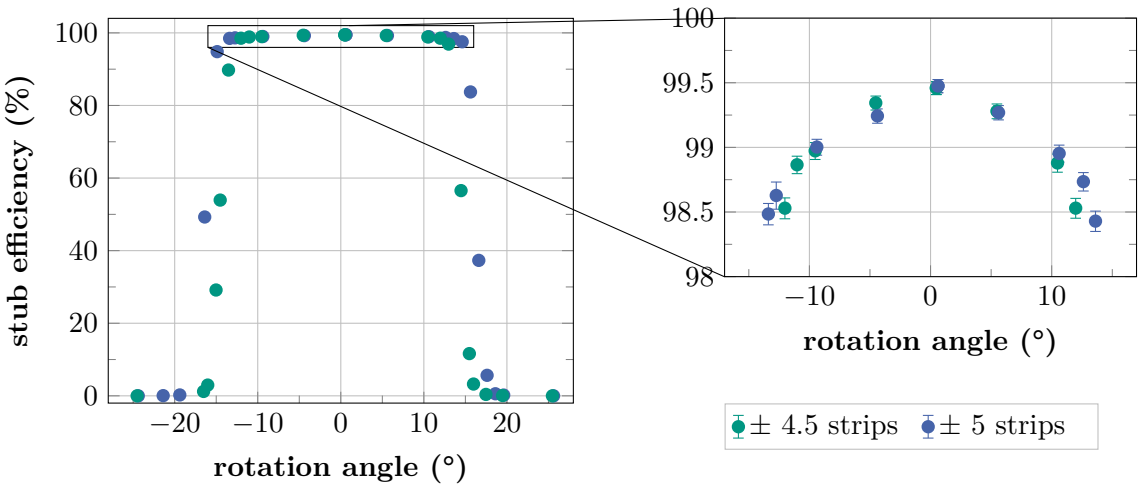

Figure 8.12.: Stub efficiencies measured in dependence of the beam incidence angle. At small angles the efficiency remains high ($> 98\,\%$) as the displacement of clusters created by particles crossing the two sensor layers is smaller than the size of the correlation window. Decreasing stub efficiencies in the angular range of $\pm 13°$ (right plot) are related to stub noise events. The measured stub efficiency shows a distinct drop at particle incidence angles exceeding the acceptance window. Larger windows shift the sharp efficiency drop towards larger angles.

Table 8.2.: Parameters obtained by fitting the error function described in Equation (8.4) to the stub efficiency measured in dependence of the particle incidence angle shown in Figure 8.13a. The geometrical expectation of the inflection point position is determined based on Equation (8.8).

module (window)	χ^2/ndf	inf. point (°)	width (°)	geo. expectation (°)
unirradiated (±4.5)	40.8	14.5±0.1	1.0±0.1	14.52 – 14.87
unirradiated (±5)	27.6	16.1±0.1	0.9±0.1	15.98 – 16.35
irradiated (±4.5)	21.5	14.6±0.1	1.1±0.1	14.52 – 14.87

After applying the offset correction ϑ_{off} to all angle values, the stub efficiencies measured for positive and negative rotation angles are combined to increase the statistics. Figure 8.13a compares all stub efficiency turn-on curves obtained after following the alignment procedure. The obtained inflection point and width, which are the main parameters characterizing the efficiency turn-on behavior, are summarized in Table 8.2.

Large χ^2/ndf values obtained from the respective fits point towards a systematic uncertainty unaccounted in the fit model, namely the precision of the module rotation stage, that dominates the overall measurement precision. The angle uncertainty introduced by the rotation stage is estimated to be $\pm 0.1°$. The impact of the angle uncertainty on the fit parameters is evaluated by the following procedure: For a given dataset each angle value is smeared by adding a uniformly distributed offset value with the offset being limited by the interval $[-0.1°, 0.1°]$. The modified dataset undergoes the above described evaluation method based on the error function fit, resulting in slightly different fit parameters. This procedure is repeated 20 000 times while storing the fit parameters. Since the resulting sample size is sufficiently large, the

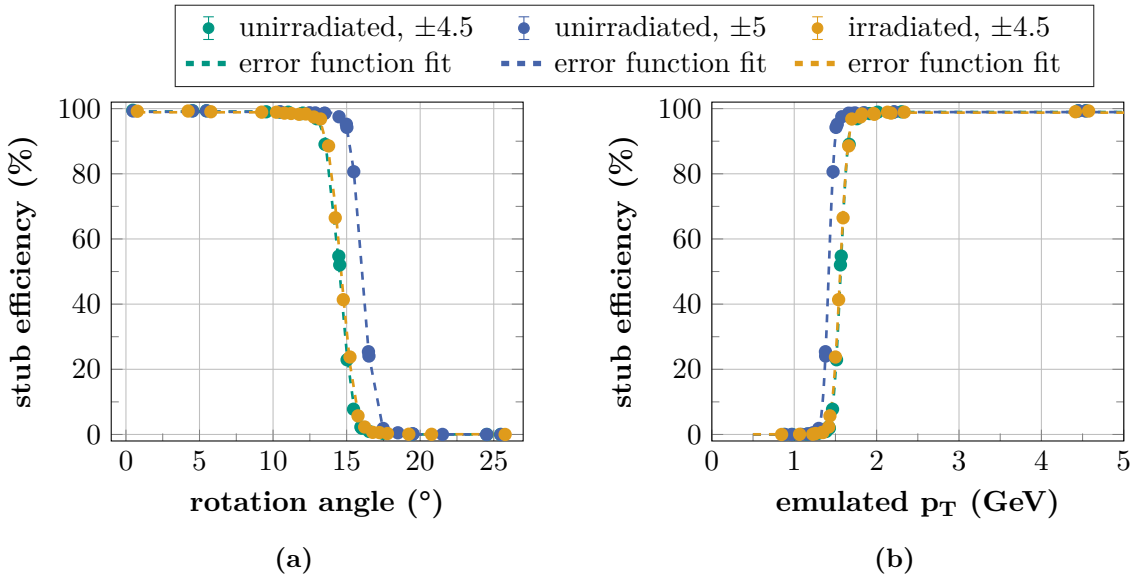

Figure 8.13.: (a): Module stub efficiency for irradiated and unirradiated sensors measured at different beam incidence angles and correlation window settings. (b): Stub efficiency as a function of the emulated particle transverse momentum (p_T), assuming a radial module distance of 67.8 cm from the interaction point in the tracker. The conversion from track incidence angles shown in (a) to the transverse momentum shown in (b) is based on Equation (8.3). All turn-on curves were fitted with an error function to extract the turn-on inflection point and width. The corresponding fit parameters are listed in Table 8.2 and Table 8.3 for (a) and (b), respectively. Turn-on curves measured with the unirradiated and irradiated module at identical window settings (±4.5 strips) are in good agreement with each other. All measurements were performed at 600 V and threshold settings of 7 ke^- and 4.7 ke^- for the unirradiated and irradiated modules, respectively.

fit parameter distributions follow Gaussian distributions (Central Limit Theorem). By using the corresponding sample variance

$$s^2(p) = \frac{1}{n-1}\sum_{j=1}^{n}(p_\mathrm{j} - \bar{p})^2 \ , \tag{8.6}$$

where n is the sample size, p_j each value in the sample and $\bar{p}$ the mean of all p_j, the confidence interval for the fit parameter p can be calculated by

$$z_{\frac{\alpha}{2}} < \frac{p - \bar{p}}{\sqrt{s^2(p)}} < z_{1-\frac{\alpha}{2}} \ , \tag{8.7}$$

with α indicating the confidence level, which is chosen to be 99.5 % ($\alpha = 0.005$) in the following. The uncertainties of the fit parameters shown in Table 8.2 correspond to the obtained confidence intervals taking into account the angle uncertainty. Directly comparing the unirradiated and irradiated module at a window setting of ±4.5 strips shows, that considering the given uncertainties, the modules deliver comparable results regarding the inflection point and width of the turn-on curve. On the one hand, this demonstrates that radiation damage introduced to the sensors does not deteriorate the cutoff resolution, but only slightly reduces the overall stub efficiency (see Figure 8.11). On the other hand, the measurements prove that independently assembled modules deliver consistent results. Furthermore, the results are in good agreement with results from previous beam test measurements with an older 2S module prototype version (8CBC3) [Kop22], where a turn-on shift of (14.49±0.04)° and a width of (1.19±0.04)° was measured with a module with irradiated sensors.
The expected inflection point position for a given correlation window setting can be geometrically estimated by

$$\vartheta_\mathrm{inflection} = \left[\arctan\left(\frac{\mathrm{window}\cdot 90\,\mu\mathrm{m}}{\text{sensor spacing [}\mu\mathrm{m]}}\right), \arctan\left(\frac{(\mathrm{window}+0.5)\cdot 90\,\mu\mathrm{m}}{\text{sensor spacing [}\mu\mathrm{m]}}\right)\right] \ . \tag{8.8}$$

The sensor spacing (center to center) of the investigated modules at the module center, which was illuminated by the beam during the measurements, was measured to be (1.63±0.02) mm using a high-resolution digital microscope. The discrepancy compared to the 1.8 mm module design value is mainly related to a different design of the Al-CF bridges that was used for the module assembly. These bridges were originally designed for sensors with different active thicknesses. Applying the tested window settings of ±4.5 and ±5 to the above relation yields inflection points in the range of (14.52 to 14.87) ° and (15.98 to 16.35) ° for the two different window sizes, respectively. This is in good agreement with the inflection points summarized in Table 8.2.

As mentioned above, the module rotation angle can be translated into a particle transverse momentum by using Equation (8.3). Figure 8.13b shows the resulting stub efficiency in dependence of the emulated $\mathrm{p_T}$ by assuming a radial module distance of 68.7 cm from the interaction point. This distance corresponds to the innermost layer of the Tracker Barrel 2S section (see Section 3.2.1), where a stub window size of ±4.5 strips is foreseen [CMS23a]. The turn-on curves were evaluated similar to the above described procedure considering the underlying angle uncertainty. Parameters obtained from the fit are summarized in Table 8.3. Regarding the window setting of ±4.5 strips, the $\mathrm{p_T}$ threshold of both modules is at about 1.55 GeV. Particles with lower $\mathrm{p_T}$ are rejected as they do not generate valid stub signals. Increasing the correlation window size to ±5 strips slightly shifts the $\mathrm{p_T}$ threshold towards smaller $\mathrm{p_T}$ values (1.42 GeV). Taking into account the uncertainties, the cutoff resolution given by the ratio of the turn-on width and inflection point is consistent for all angular scans and is found to be smaller than 8 %.

Table 8.3.: Parameters obtained by fitting error functions to the stub efficiency turn-on curves as a function of the emulated particle transverse momentum shown in Figure 8.13b.

module (window)	χ^2/ndf	inf. point (GeV)	width (MeV)	cutoff res. (%)
unirradiated (±4.5)	52.9	1.56±0.01	99±10	6.3±0.7
unirradiated (±5)	36.1	1.42±0.01	81±10	5.7±0.7
irradiated (±4.5)	21.4	1.56±0.01	107±8	6.9±0.5

8.4.3. Conclusion and Outlook

Laboratory and beam test measurements with the latest 2S module prototypes were presented in this chapter. In addition to a module with unirradiated components, a second module with proton-irradiated frontend hybrids and sensors was investigated. The frontend hybrids were irradiated to a 1 MeV neutron equivalent fluence of $1 \cdot 10^{14}\,\mathrm{cm}^{-2}$, corresponding to an ionizing dose of 150 kGy. Dedicated hybrid tests (module skeleton tests) performed prior to and after irradiation did not reveal any irradiation related degradation of the frontend hybrid properties regarding the channel noise and the reconstructed shape of injected test signals.
The fully assembled 2S modules were tested at the DESY beam test facility. Measurements with the unirradiated module demonstrate that cluster efficiencies of 99.9 % and stub efficiencies of 99.5 % can be reached for thresholds up to 9.3 ke^-. Sensors assembled in the irradiated module received different fluences of $3.7 \cdot 10^{14}\,\mathrm{cm}^{-2}$ and $5.2 \cdot 10^{14}\,\mathrm{cm}^{-2}$ to probe the nominal and ultimate CMS runtime scenario. Even with the highest irradiated sensor, cluster efficiencies well above 99.5 % are reached at a threshold setting of 4.7 ke^-, where the noise occupancy falls below $1 \cdot 10^{-4}$. At perpendicular beam incidence, stub efficiencies of 99.1 % were measured with the irradiated module. Rising the sensor bias voltage from 600 V to 800 V increases the stub efficiency by about 0.1 %. However, the cluster efficiencies measured on the single sensors is barely affected by the bias voltage increase and beneficial bias voltage effects become visible only for thresholds larger than 4.7 ke^-.
To validate the transverse momentum discrimination mechanism, modules were stepwise rotated with respect to the beam emulating particles with different transverse momenta. For identical correlation window settings the unirradiated and irradiated module delivered consistent results regarding the $\mathrm{p_T}$ threshold and the width of the characteristic stub efficiency turn-on curve. Furthermore, the results are in good agreement with previous beam test measurements, during which an older 2S module prototype iteration (8CBC3) was tested [Kop22].
A known problem of the latest 2S module prototype iteration is the overall increased noise level compared to previous prototypes. Intensive noise investigations (see [Kop22]) showed that the DC-DC converter stage sitting on the service hybrid above the sensor HV tails introduces noise to the sensor bias potential via the tails. This effect can be mitigated by adding 100 Ω resistors to each of the tails. Figure 8.14 compares noise occupancies measured at room temperature and 600 V sensor bias voltage with the same module before and after attaching resistors to the HV tails. While the top sensor noise occupancy remains nearly unchanged, the bottom sensor occupancy is clearly reduced. The threshold setting required to reach bottom sensor noise occupancies below $1 \cdot 10^{-4}$ decreases by about 470 e^-. Thus, the module operation window is enlarged towards smaller threshold settings, which is especially relevant for modules with sensors that have accumulated radiation damage, where the cluster and stub efficiency is much more sensitive to the applied threshold settings. In the final module iteration resistors will be added to all HV tails. Taking into account the expected noise reduction due to the design improvements, the measurements presented in this chapter demonstrate that the 2S module

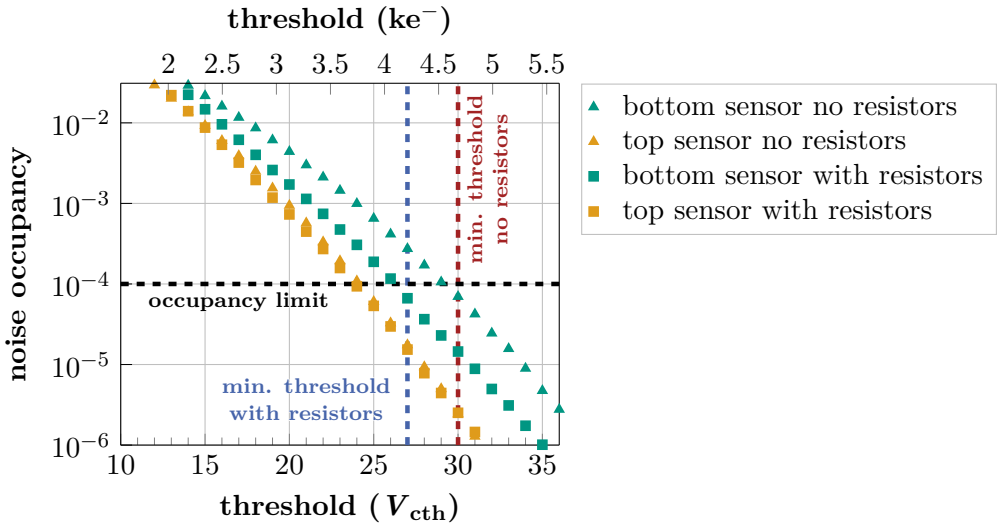

Figure 8.14.: Noise occupancy measured with the unirradiated module before and after attaching 100 Ω resistors to the HV tails. All measurements were performed at room temperature and 600 V sensor bias voltage. The noise occupancy measured on the bottom sensor is clearly reduced after attaching the resistors, whereas the top sensor noise occupancy is barely affected. Thus, the minimum threshold setting that must be applied to reach bottom sensor noise occupancies smaller than $1 \cdot 10^{-4}$ is reduced by at least 3 V_{cth}, corresponding to about 0.5 ke^-.

design meets all requirements, and efficient module operation can be expected for the entire HL-LHC runtime.

Part IV.

Summary and Outlook

9
Summary and Outlook

By 2029, the *Large Hadron Collider* (LHC) at CERN[1] will be upgraded to the *High Luminosity LHC* (HL-LHC), resulting in an instantaneous luminosity increase by a factor of five to seven. With an average of up to 200 simultaneous proton-proton collisions (pileup) the particle flux through the detectors will raise drastically. This sets new demands on the experiments regarding the radiation tolerance of detector components and efficient triggering on interesting events for physics analyses. To cope with these new requirements during the HL-LHC phase, the *Compact Muon Solenoid* (CMS) experiment will be fundamentally revised in the scope of the Phase-2 Upgrade. A major part of the upgrade is the complete replacement of the silicon tracker. The new tracker will feature improved radiation hardness, a higher density of sensitive elements (pixels and strips) and an overall lower material budget. Special modules, called p_T-modules, made of two closely spaced silicon sensors will be installed in the outer part of the tracker (Outer Tracker). These p_T-modules are capable of providing track elements (stubs) to the CMS Level-1 track finder at the bunch crossing frequency of 40 MHz, which is required to keep the CMS trigger system efficient at HL-LHC conditions. To cope with bandwidth limitations, a pre-selection of particle hits based on the particles' transverse momentum (p_T) is required on module level, giving the modules their name. The trajectory of charged particles crossing the detector is bent the stronger in the 3.8 T magnetic field of CMS the lower the p_T is. Hence, the displacement of charge signals generated by particles crossing the sensors of a p_T-module is a measure of the particles' transverse momentum. Correlating hits in the two sensor layers and defining a geometrical cut on the displacement ensures that only track information from particles exceeding a certain p_T-threshold is passed to the CMS Level-1 track finder while keeping all hits for readout at L1-trigger acceptance. This reduces the amount of track data forwarded to the trigger system by one order of magnitude without losing events of physics interest. Two different types of p_T-modules will be installed in the Outer Tracker. The region closer to the interaction point will be equipped with PS modules made of a macro-pixel sensor (PSp sensor) and a strip sensor (PSs sensor). Less granular 2S modules consisting of two identical strip sensors (2S sensors) will be placed in the outer region.

CMS Outer Tracker Sensor Quality Control

In mid 2020, the sensor mass production has started with a total production quantity of about 28 000 sensors and is expected to be completed by the end of 2024. Monitoring the sensor quality is essential to ensure that the sensors meet the requirements set by the CMS Collaboration and can be used without any restrictions for the module assembly. Thus, all manufactured sensors undergo a Vendor Quality Control (VQC) at *Hamamatsu Photonics K.K.* (HPK) first and only sensors confirming pre-defined specifications are supplied. Furthermore, the CMS Collaboration has developed a quality assurance strategy for the mass production that is based on three tasks covered by several CMS member institutes spread across different continents that work together: Sensor Quality Control (SQC), Process Quality Control (PQC) and Irradiation Tests (IT).

[1] European Organization for Nuclear Research

The *Karlsruhe Institute of Technology* (KIT) contributes to the quality assurance as an IT and SQC center and is member of the *Outer Tracker Sensor Expert Production Panel* (OTSEPP). A main part of this thesis is dedicated to the SQC measurements conducted at KIT. In total, 43 batches of 2S sensors and 10 batches of PSs sensors were characterized. The sensor quality control relies on sample based sensor tests for each batch delivered by HPK and monitors global sensor parameters such as the leakage current and depletion voltage as well as electrical parameters of individual strips.

Overall, the SQC measurements performed at KIT confirm the excellent quality of the investigated 2S and PSs batches, which complies with the results gathered at the other five SQC centers within the CMS collaboration. The average sensor leakage currents measured on both sensor types are at least one order of magnitude smaller compared to the specification limits with breakdown voltages above 800 V. Long-term tests conducted on 160 sensors prove stable sensor leakage currents over time. Corrective measures have been initiated regarding the depletion voltage. There were batches from the early stage of the production with a few sensors reaching the upper depletion voltage limit of 350 V. Corresponding feedback was given to HPK by the OTSEPP and in the further course of the production the depletion voltage was adapted and has stabilized in the range of 200 V to 250 V. Overall, the sensor leakage currents and depletion voltages measured at KIT are in good agreement with the data taken by HPK in the course of the VQC. This is essential as the SQC covers only a fraction of sensors from each batch and the conformance of data validates the reliability of the vendor quality control, which covers every sensor delivered.

Sensor strip tests conducted at KIT prove the good uniformity of the individual parameters across the sensors and thus confirm a uniform processing of the sensor wafers. The number of strips violating the specification limits of the individual monitored strip parameters is negligible. At the beginning of the production, the resistance of the polysilicon resistors was found to be close to the upper specification limit of 2 MΩ and HPK was requested by the OTSEPP to adapt the processing parameters, resulting in a resistance reduction to about 1.5 MΩ.

In the course of the SQC measurements it was observed that electrical parameters measured on the sensors can be temporarily deteriorated by static charges on the sensor surface that are introduced by the sensor packaging material. In most cases, charged sensors exhibit clusters of strips with low interstrip resistance introduced by the pickup tool used for the sensor handling, which changes the charge configuration on the sensor surface. Furthermore, in rare cases, static charges cause a significant reduction of the breakdown voltage. It is demonstrated in this thesis that both effects can be recovered by neutralizing the charges with a commercial ion-blower. The environmental humidity was found to be another parameter that can impact the sensor performance. Exposing sensors to high humidity levels for several minutes/hours can cause a temporary early sensor breakdown that lasts for hours/days. Humidity tests with sensors showed that the sensor recovery can be accelerated by operating it in the breakdown condition, or by treating it with the ion-blower. For the sensor operation in the tracker the humidity sensitivity is not expected to be a problem as the humidity level will be sufficiently low to avoid the occurrence of early sensor breakdowns. However, both, the sensitivity to static charges and the environmental humidity must be kept in mind whenever sensors are handled, especially with regard to the upcoming module production.

Accurately diced sensor edges are essential for the module assembly to achieve precise sensor alignment in the p_T-modules. The dicing precision of the sensor edges was evaluated based on pictures taken with a high-resolution digital microscope during the optical sensor inspection. Among 148 sensors tested, no sensor edge failing the dicing precision specification of ±10 µm was found.

At the beginning of the PSp sensor pre-production KIT as the only SQC center evaluated the quality of the sensors, which are not included in the standard SQC procedure. Based on the

conducted measurements covering global sensor parameters as well as dedicated pixel tests, no violation of the specifications was found. According feedback and green light for the production was given to HPK based on these sensor tests.

Beam Test Measurements with Prototype Sensors and Modules

The second part of this thesis focuses on beam test studies with prototype sensors and modules at the DESY[2] test beam facility in Hamburg, Germany. By placing the prototypes in the middle of a beam telescope and illuminating them with a highly energetic electron beam, the prototypes' particle detection efficiency can be measured based on the particle tracks reconstructed with the telescope.
Miniature versions of the PSp macro-pixel sensor based on the final sensor material, that will be used for the CMS Outer Tracker, were assembled with matching readout chips, forming single *Macro-Pixel Sub Assemblies* (single MaPSAs). Part of the assemblies were irradiated with protons to fluences as they are expected after ten years of operation in the CMS Tracker. At perpendicular particle incidence the pixel biasing structures implemented on the sensors cause inefficient regions across the active sensor area. Thus, assemblies with three different sensor design approaches for the biasing structures were built and tested. The main goal of the beam test studies was to evaluate the impact of radiation damage on the particle detection efficiency and to compare the different designs. Sensors based on the Standard and PCommon design both feature punch-through structures and bias rails, while in the PCommon design the bias rail is shielded from the sensor bulk by a common p-stop structure extending below the rail. The beneficial effect of the shielded rail on the detection efficiency prior to irradiation was validated in previous beam test studies with a global efficiency increase of about 0.5 % compared to the Standard design. However, based on measurements with the irradiated assemblies it is demonstrated in this thesis that the shielding effect is reduced after hadron irradiation. At the highest tested neutron equivalent fluence of $1 \cdot 10^{15}\,\mathrm{cm}^{-2}$, the PCommon design only yields an efficiency increase of about 0.3 % compared to the Standard design, which reaches efficiencies close to 99 %. Due to the lack of biasing structures sensors based on the NoBias design yield the overall highest efficiency, reaching 99.8 %, even at the maximum tested fluence.
Particles crossing the sensor at an angle can overcome inefficient areas resulting in an efficiency increase that scales with the angle. Thus, the influence of different angles was investigated with sensors based on the Standard design. Prior to irradiation the efficiency increases significantly by about 0.4 % already at incidence angles of roughly 5°. After irradiation, angles of at least 10° are required to obtain a comparable increase. Overall, efficiencies up to 99.8 % can be reached for incidence angles larger than 15°.
In the end, the CMS collaboration selected the more robust and conservative Standard design for the Outer Tracker PSp sensors. The NoBias design would have yielded the highest detection efficiency, but due to missing biasing structures the sensors could only be tested after equipping them with readout chips. In case of a potential low sensor yield during the production this could have caused hardly assessable additional costs due to the higher material consumption. The advantage of the PCommon design over the Standard design is mainly present prior to irradiation and is put into perspective by the positive effect of inclined particle incidence, which already manifests at small angles.

The Outer Tracker module production is expected to start mid 2023. KIT as a 2S module assembly center pledged to built up to 2000 2S modules. In the past, KIT contributed to the validation of the module design and functionality by building prototype modules and intensively testing them. Beam test measurements with the latest and almost final 2S module prototype

[2] Deutsches Elektronen-Synchrotron

iteration were performed in the scope of this thesis to prove their unrestricted functionality. In addition to an unirradiated module, a second module assembled with proton irradiated sensors and frontend hybrids was tested. Different 1 MeV neutron equivalent fluences of $3.7 \cdot 10^{14}\,\mathrm{cm}^{-2}$ and $5.2 \cdot 10^{14}\,\mathrm{cm}^{-2}$ were chosen for the two sensors of the irradiated module to probe different CMS operation scenarios. With the unirradiated module particle detection efficiencies of 99.9 % are reached at reasonable bias voltage and threshold settings. Sensors assembled in the irradiated module show only small radiation related degradations and reach efficiencies of 99.8 % and 99.7 % for the medium and maximum sensor fluence, respectively. Thus, even after more than ten years of CMS operation during the HL-LHC phase 2S modules will be capable of efficiently detecting charged particles. Increasing the bias voltage from 600 V to 800 V does barely affect the efficiency of the irradiated sensors. For both modules a minimum threshold of $4.7\,\mathrm{ke}^-$ must be applied to reach noise occupancies smaller than $1 \cdot 10^{-4}$, which is two orders of magnitude smaller than the expected hit occupancy.
The $\mathrm{p_T}$-discrimination mechanism was tested by stepwise rotating the modules with respect to the electron beam to emulate differently bent particle trajectories. Both modules show the expected turn-on behavior of the stub efficiency and at identical window settings similar results regarding the $\mathrm{p_T}$-threshold and resolution are obtained.
However, the module noise level is slightly increased compared to previous prototype iterations, which is mainly related to the DC-DC converter stage on the service hybrid that induces noise through the sensor HV tails. In the final module iteration, resistors will be added to the tails, which together with additional optimizations of the service hybrid grounding scheme, will significantly reduce the noise level. Measurements presented in this thesis prove that adding resistors to the HV tails reduces the minimum required threshold setting for efficient module operation by about $470\,\mathrm{e}^-$. Thus, the final module design will provide an additional safety margin regarding the threshold operation window.

Conclusion and Outlook

Altogether, this thesis has contributed to the CMS Phase-2 Outer Tracker upgrade project in various aspects. Results from the single MaPSA beam test served as input for the selection of the final PSp full-size sensor design. Furthermore, the results were shared with the CMS Tracker simulation group. Models simulating the expected tracking efficiency considering the bias rail inefficiency at different particle incidence angles are currently under evaluation.
In the scope of this work the sensor quality control at KIT was performed and supervised for the first half of the ongoing sensor mass production. KIT has established itself as a reliable SQC center by qualifying about one quarter of the overall delivered 2S and PSs sensor batches and will further contribute with the same throughput till the end of the production. Besides the standard SQC measurements the impact of static charges and the exposure to high environmental humidity, which both can temporarily deteriorate the sensor performance, was investigated. Based on the findings the measurement procedures at KIT regarding the sensor handling were improved to avoid the occurrence of temporary sensor failures in the future. This sets the baseline for smooth measurement progress during the rest of the sensor production period. Moreover, the experience gained is of major importance for the sensor handling during the upcoming module production.
Another contribution to the Phase-2 Upgrade project was made by validating 2S module prototypes. Based on beam test studies it is demonstrated that the latest and almost final 2S module design meets the requirements set by the CMS collaboration. Efficient module operation can be expected during the entire tracker operation time, even for 2S modules exposed to the highest expected fluence levels.

Part V.

Appendix

A

Appendix to Chapter 5

Table A.1.: Measurement devices installed at the KIT SQC probe station.

Device name	Device type
Keithley 2410	high voltage source
Keithley 6485	picoamperemeter
Keithley 2450	low voltage source
Keysight E4980AL	precision LCR meter

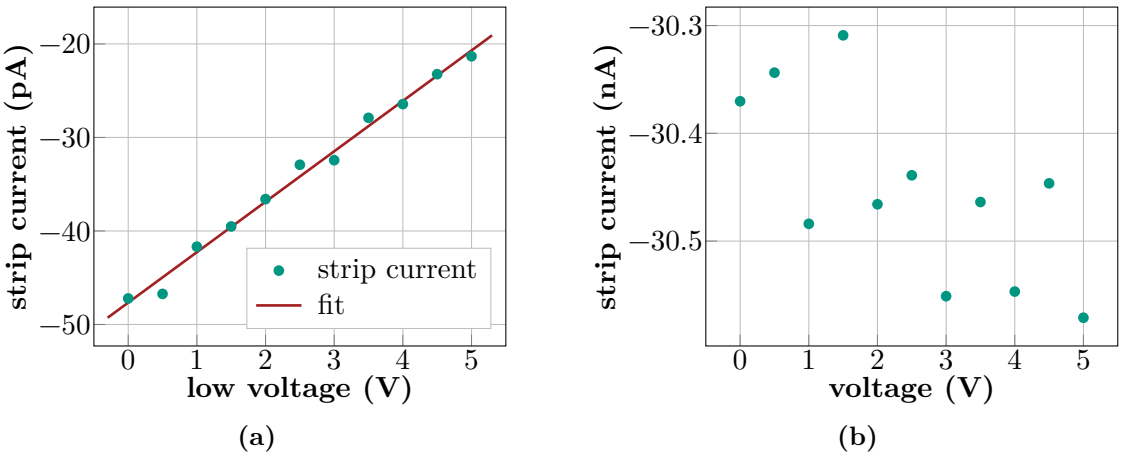

Figure A.1.: In order to measure the interstrip resistance (R_{int}), the DC pads of two neighboring strips are contacted with strip needles. A sequence of different low voltages is applied to one of the strips, while the resulting strip leakage current is measured on the adjacent strip. For a functional pair of strips the strip leakage current scales linearly with the applied voltage. This is shown in (a) on the example of a 2S sensor. The interstrip resistance is determined from the inverse slope of a linear fit, which yields $(185 \pm 10)\,\mathrm{G\Omega}$ for the example. As can be seen from (a), the measured current changes by about 5 pA if the low voltage is increased by 1 V. Thus, in case the interstrip resistance is measured on a leaky strip, which is shown in (b), the leakage current increase in dependence of low voltage applied cannot be resolved, and the measurement does not yield a meaningful resistance.

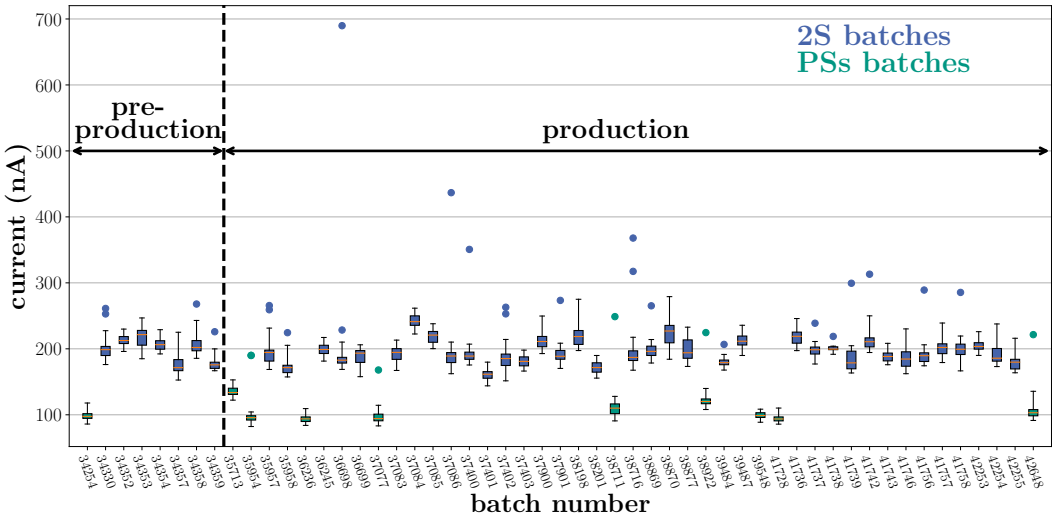

Figure A.2.: Sensor leakage currents measured by HPK at 600 V bias voltage summarized batch wise. The plot includes all 2S and PSs batches that were shipped to KIT up to September 2022 in the scope of the sensor quality control. All sensors are well within the specification limit, which is 7.25 µA and 3.625 µA for the 2S and PSs sensors, respectively.

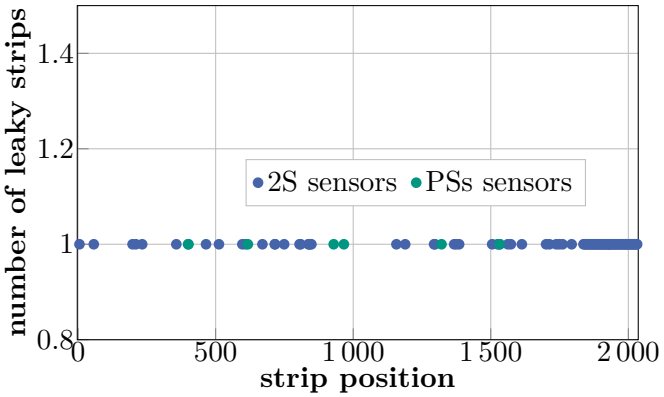

Figure A.3.: Position and frequency of leaky strips found across all sensors tested at KIT in the scope of the SQC. In this plot, strips are refereed to as leaky if the strip current exceeds 100 pA and 50 pA for 2S and PSs sensors, respectively. All strips are uniformly distributed across the sensor and there is no increased number of leaky strips in a specific sensor region, that would hint towards a systematic wafer processing problem. The higher density of leaky strips observed on 2S sensors at strip positions larger than 1 800 is related to one specific sensor that is shown in Figure A.4.

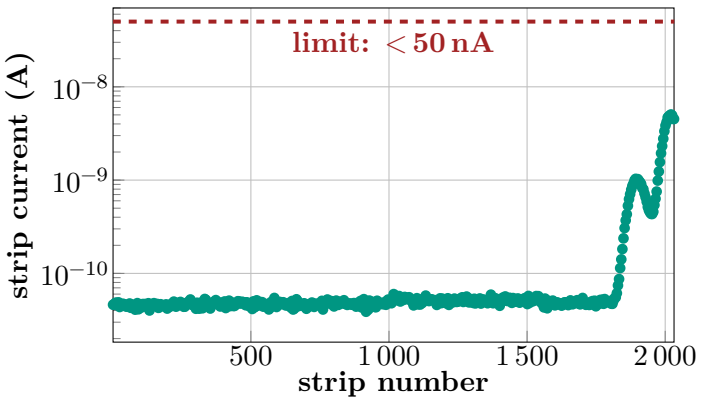

Figure A.4.: Example of a 2S sensor from batch 36698 showing a systematic strip leakage current deviation across the sensor. From strip 1800 onwards, the measured leakage current continuously increases by a factor of up to 100. The deviation is related to the wafer processing. All strips are still within the specification, which holds $< 50\,\mathrm{nA}$ for a 2S sensor.

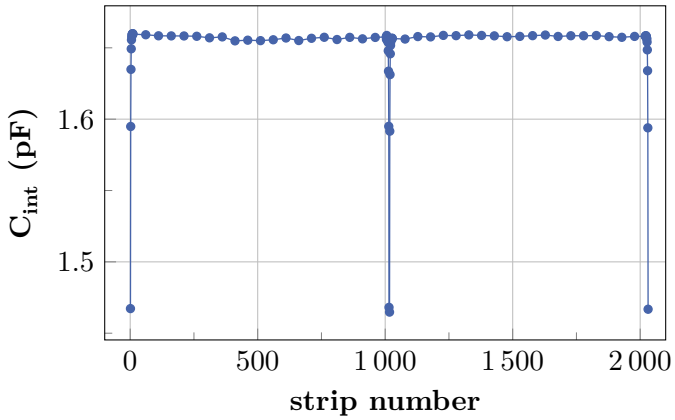

Figure A.5.: Example of an interstrip capacitance measurement conducted on a 2S sensor. Both sensor halves, each consisting of 1016 strips were tested within two independent sensor scans. For each half the measured capacitance decreases at the sensor edge due to edge effects, while it is constant for the rest of the sensor.

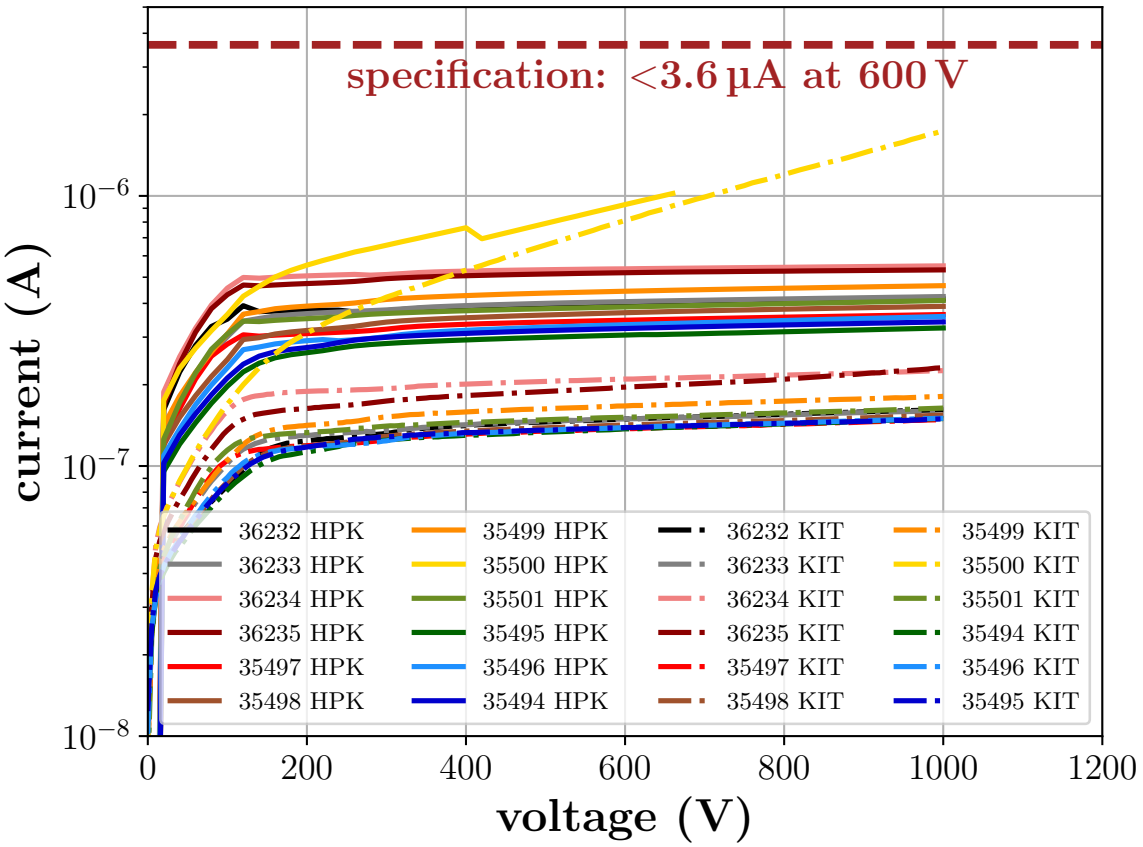

Figure A.6.: Sensor leakage current in dependence of the bias voltage measured for all pre-production PSp full size sensors that were shipped to KIT. The measurements at KIT are in good agreement with the HPK measurements, no sensor exceeds the specification limit of 3.6 µA at 600 V. The global offset between the KIT and HPK data is related to different environment temperatures during the measurement (∼20 °C at KIT and ∼24 °C at HPK).

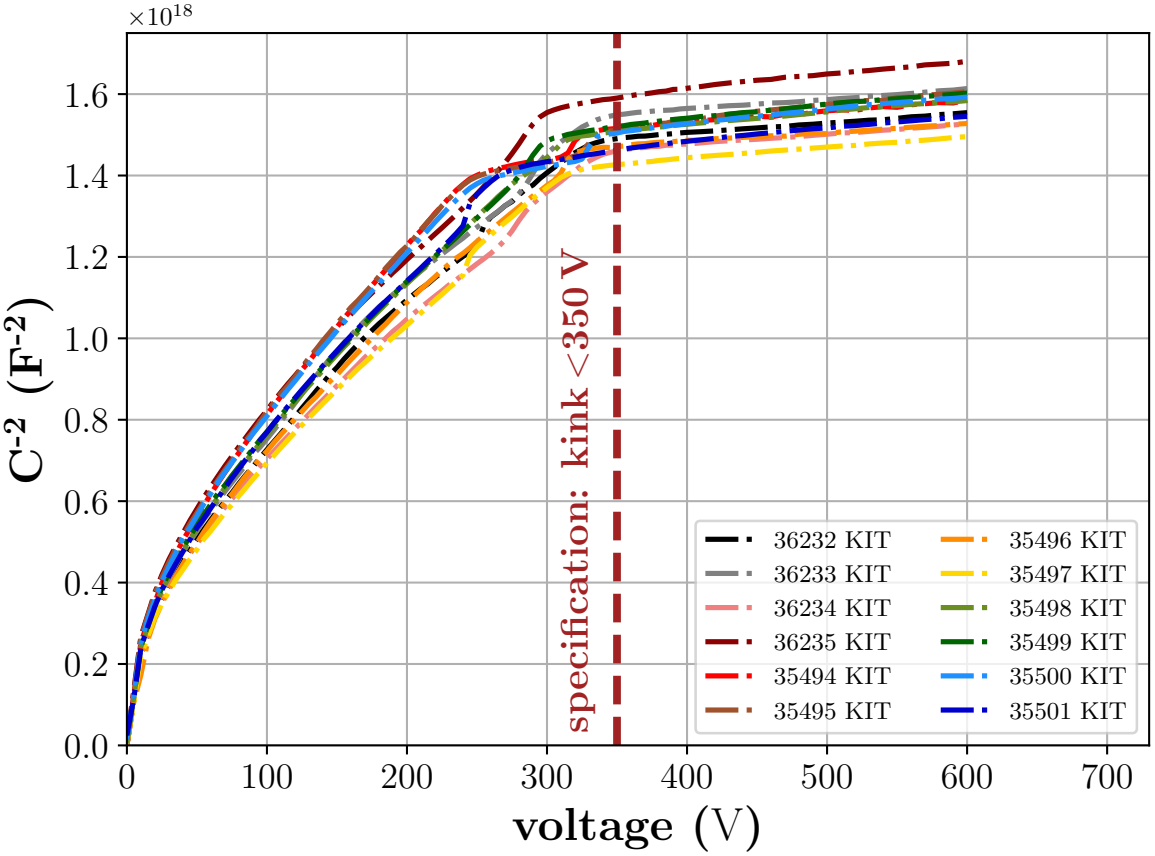

Figure A.7.: CV measurements of all pre-production PSp full-size sensors that were shipped to KIT. The sensor depletion voltage, indicated by the kink in the curve, is smaller than the upper specification limit of 350 V for all sensors. Thus, all tested sensors fulfil the specification regarding the depletion voltage.

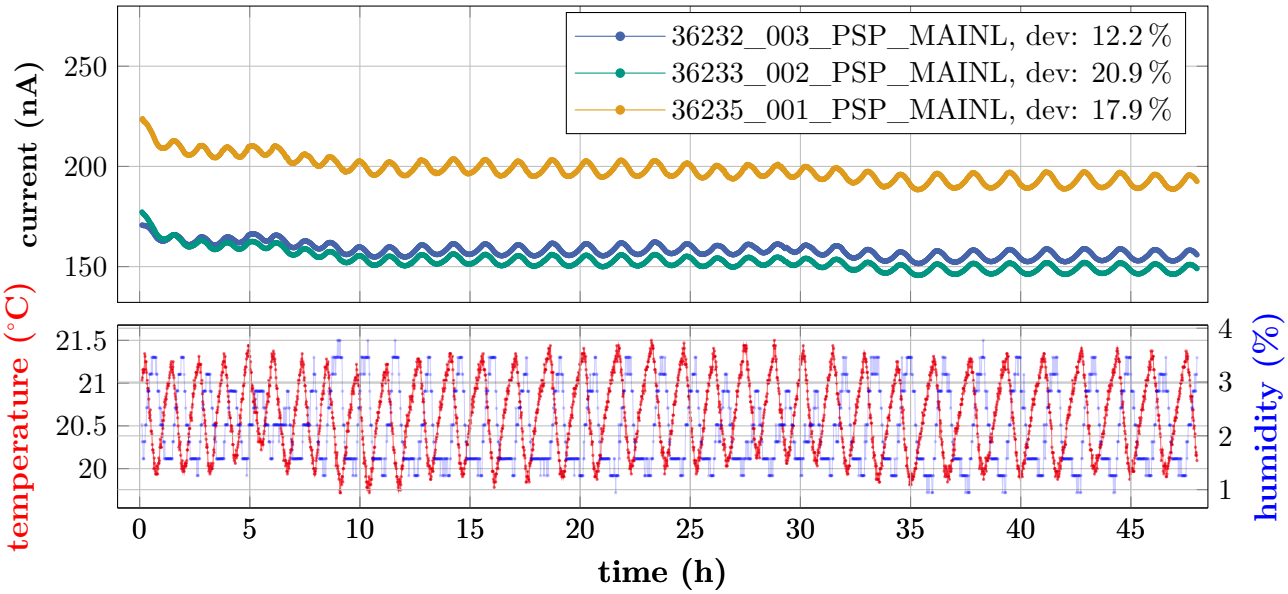

(a)

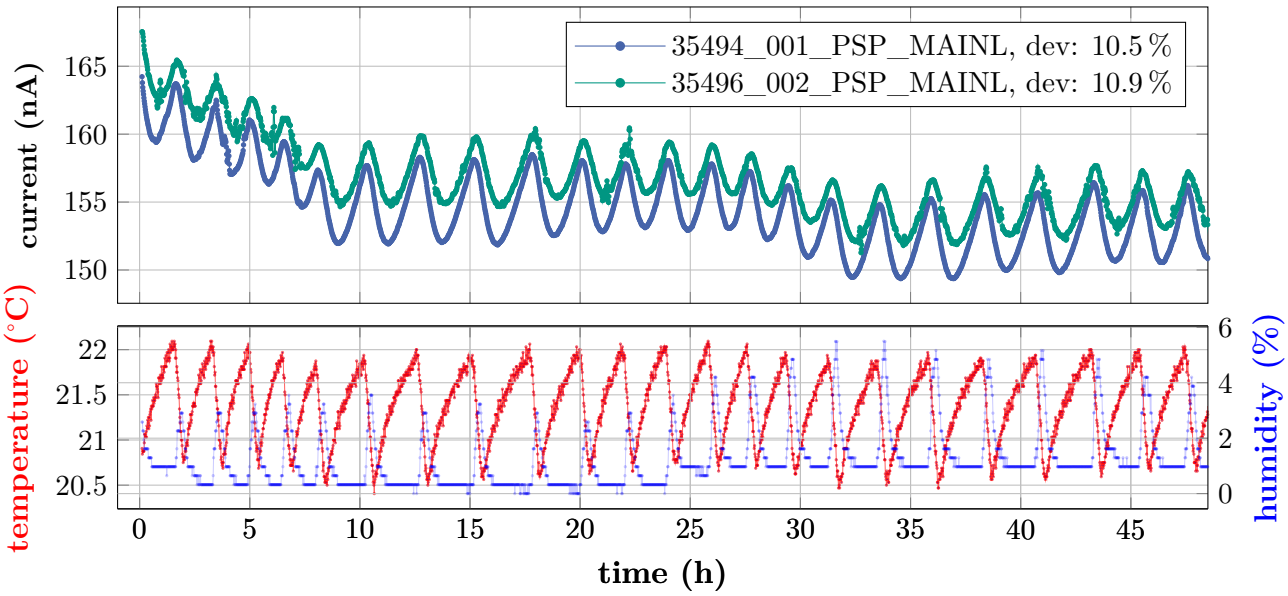

(b)

Figure A.8.: Long-term measurements with PSp pre-production sensors. The sensors were biased at 600 V for a duration of 48 h while the sensor leakage current was measured every minute. Two independent measurement runs with different sensors were performed, shown in (a) and (b). Applying the long-term specification defined in Equation (5.2), all sensors show current deviations smaller than 30 % and are therefore within the specification limit. Fluctuations in the measured leakage current are related to temperature fluctuations during the measurement since the long-term setup does not provide active temperature control.

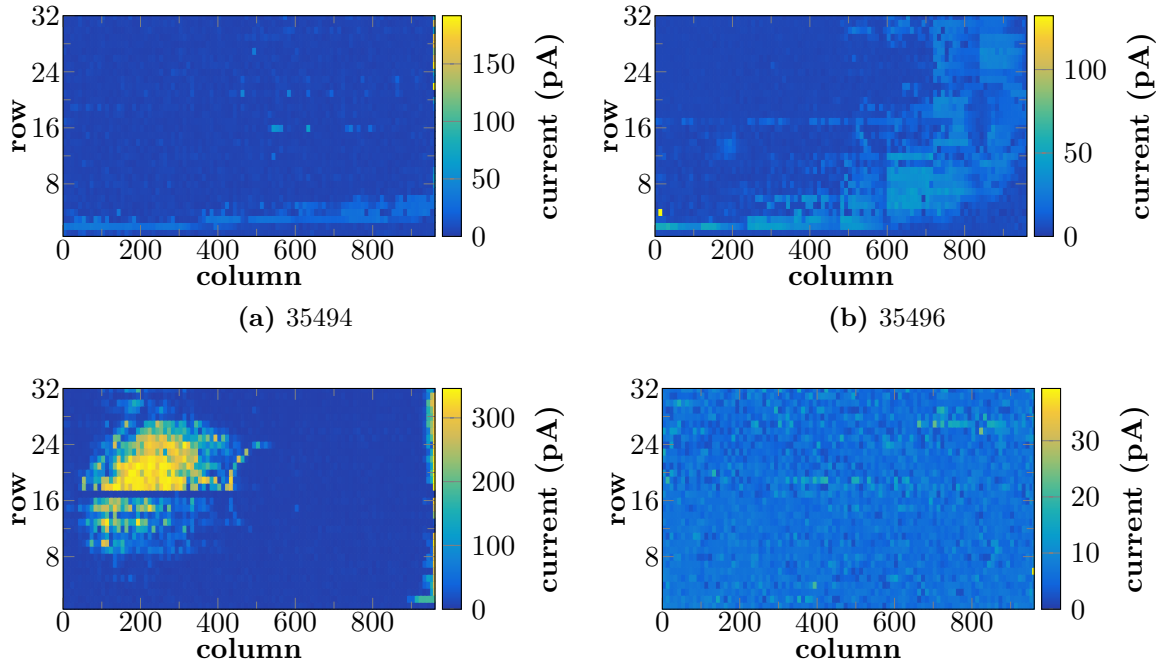

(a) 35494 **(b)** 35496

(c) 36232 **(d)** 36235

Figure A.9.: Pixel leakage current measured on four different PSp pre-production sensors labeled by the batch number. The histograms show the leakage current of individual pixels measured on every 10th pixel of different PSp pre-production sensors. Each sensor was scanned within two independent runs, whereby each run covered one sensor half, corresponding to 16 rows of pixels. Although some sensors show clusters of pixels with increased leakage current, all pixels are within the upper specification limit of 1.5 nA.

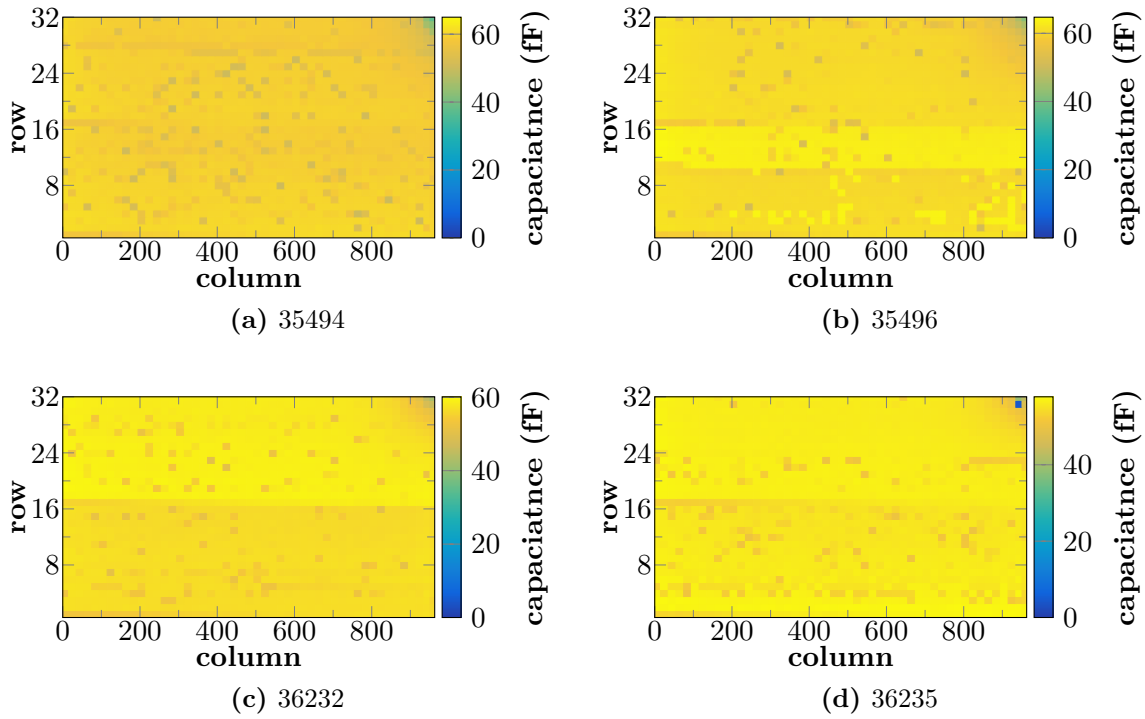

Figure A.10.: Interpixel capacitance measured on four different PSp pre-production sensors labeled by the batch number. The histograms show the capacitance measured between adjacent pixels on every 20th pixel pair, corresponding to 1 500 tested pixels per sensor. Each sensor was scanned within two independent runs, whereby each run covered 16 rows of pixels. Overall the sensors show homogenous capacitance values across the whole sensor. Small offsets between the upper and lower sensor half are related to slightly different offset calibration values. Decreased capacitances in the top right sensor corner are related to interference effects between the strip needles used for the capacitance measurement and the bias needle. All tested pixels have capacitances smaller than the upper specification limit of 75 fF.

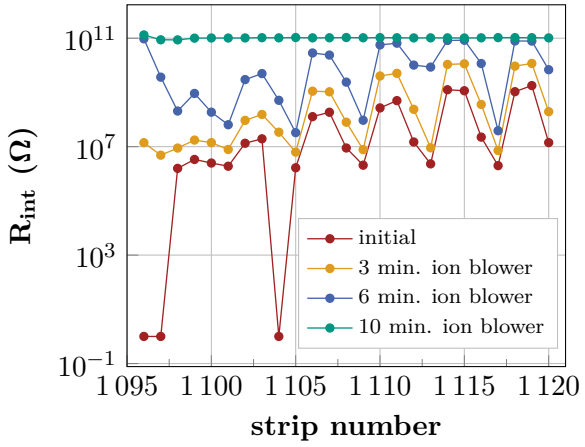

Figure A.11.: Effect of the ion blower application on a group of strips with reduced interstrip resistance related to static charges on the sensor. After each iteration step, the measured interstrip resistance increases and is fully recovered after about 10 min.

Figure A.12.: Climatic chamber setup used to study the humidity sensitivity of sensors. The sensors (four 2S sensors) are mounted on long-term boards and placed inside the chamber. Measurement devices located next to the chamber allow to measure leakage currents while the sensors are exposed to different relative humidity levels.

B

Appendix to Chapter 7

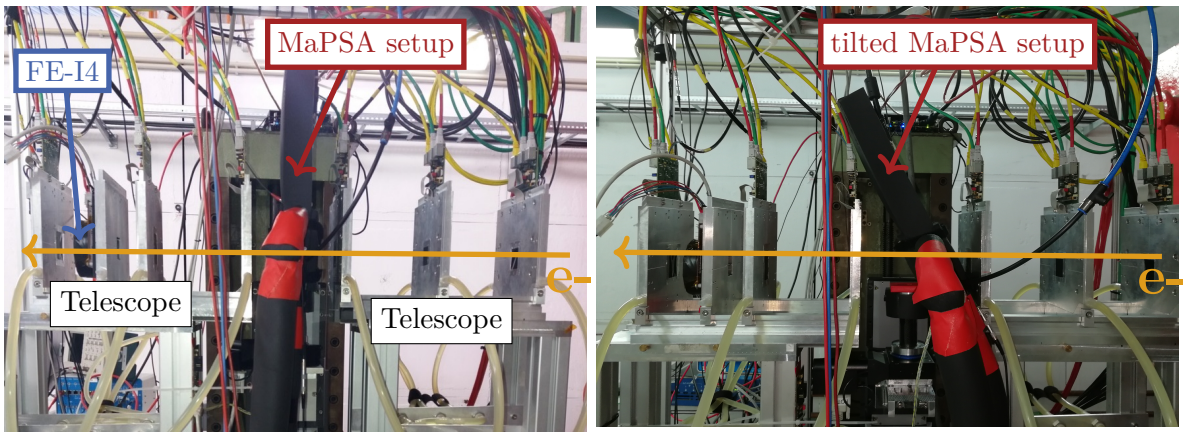

(a) **(b)**

Figure B.1.: (a): MaPSA setup integrated into the DATURA beam telescope. The electron beam enters the telescope and setup from the right-hand side. (b): In order to study the assembly performance at inclined particle incidence the setup was screwed onto dedicated 3D printed mounts with different tilting angles. The picture exemplarily shows the setup tilted by 20° with respect to the beam.

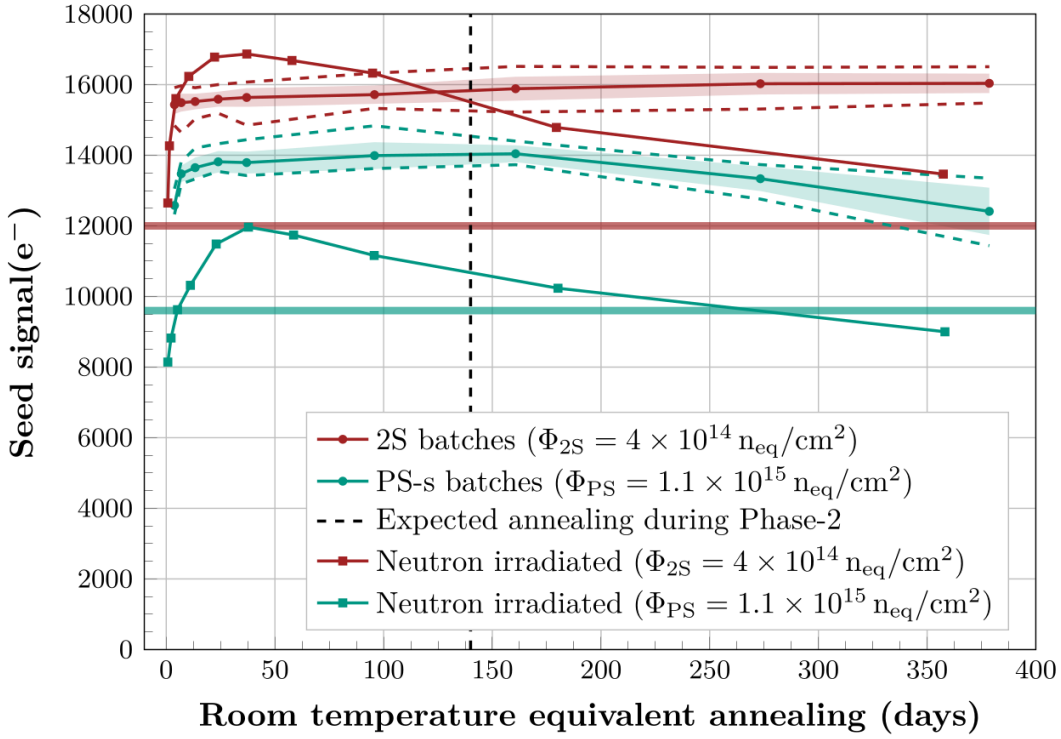

Figure B.2.: Results from irradiation tests conducted in the scope of the CMS Outer Tracker sensor pre-production. The plot shows seed signals measured for differently irradiated test sensors from 2S and PSs wafers measured in dependence of different annealing durations with a ALiBaVa system [Mar+07] at 600 V sensor bias voltage. Charge signals are generated in the sensors by electrons emitted from a Sr^{90} source that is placed above the sensor. For each electron passing the sensor, the seed signal is determined which represents the largest charge signal seen by a single strip (seed strip). Several thousand events are recorded to increase the statistics and to extract a meaningful value for the seen signal. Circular markers represent proton irradiated samples while the rectangular marks belong to neutron irradiated sensors. For the lower proton fluence (red circles) a purely beneficial annealing effect is observed, whereas reverse annealing is visible for the higher fluence (green circles) and long annealing durations. Beneficial and reverse annealing is even more pronounced for the samples irradiated with neutrons. Plot taken from [Mül21], where much more details regarding the measurements can be found.

C
Appendix to Chapter 8

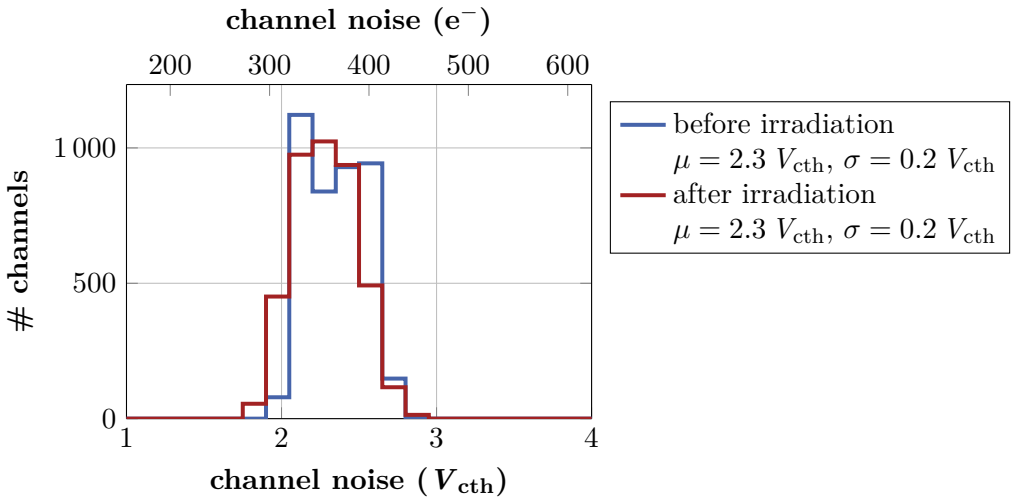

Figure C.1.: Channel noise distribution measured with the same skeleton before and after irradiation. The skeleton was irradiated to a fluence of $1 \cdot 10^{14}\,\mathrm{cm}^{-2}$ corresponding to an ionizing dose of 150 kGy. No irradiation related noise increase is observed.

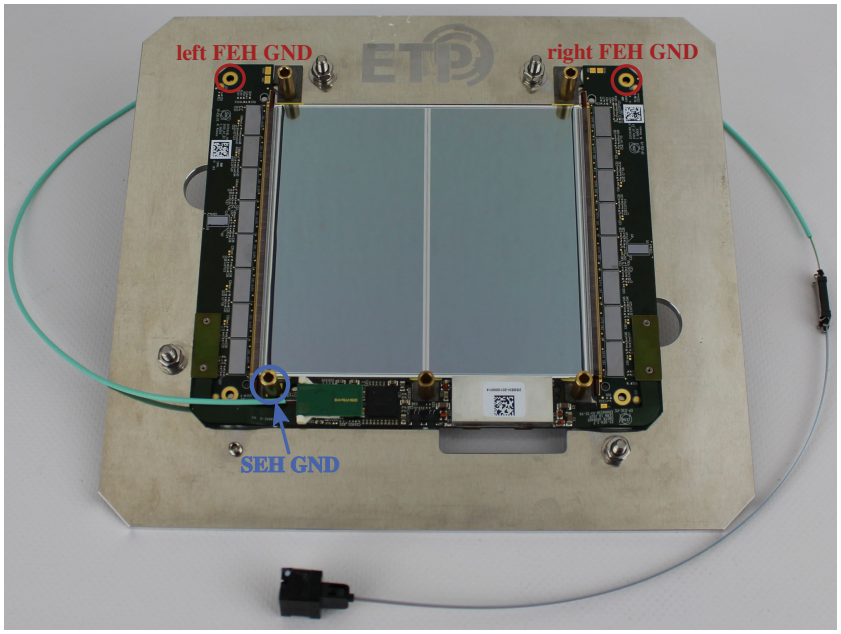

Figure C.2.: The picture shows a 2S module mounted onto an aluminum module carrier. The module frontend hybrids (FEHs) and the service hybrid (SEH) offer grounding connections to avoid different electrical ground levels between the module and the carrier that might negatively affect the module noise. For the measurements presented in this thesis, both the FEH ground pads (red) and the SEH ground pad (blue) were used to reduce the noise as much as possible. Picture modified from [Kop22].

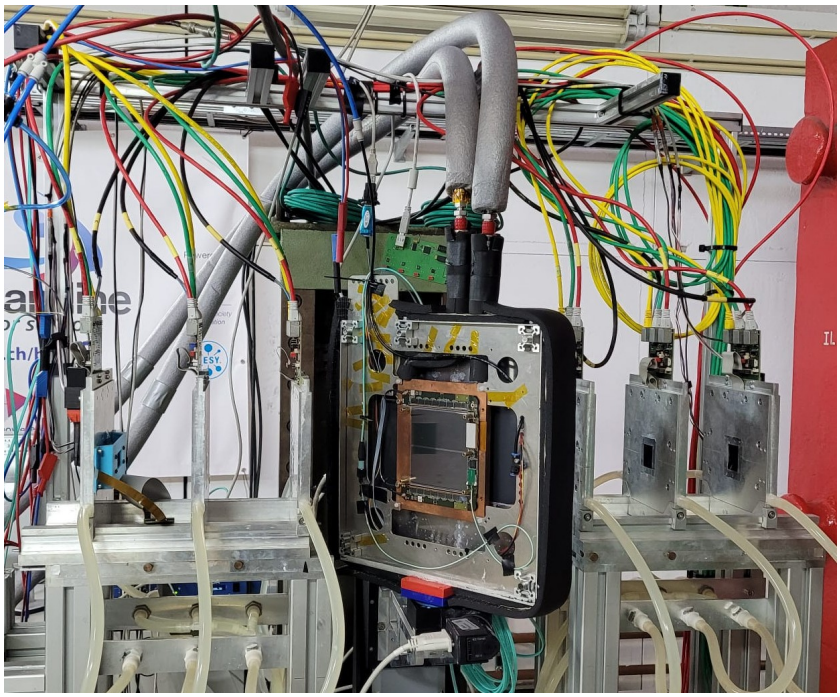

Figure C.3.: Picture of the setup used for the irradiated 2S module beam test at DESY. The module is mounted onto a copper cooling bridge that is integrated into the DUT box. Gray cooling pipes connect the bridge to an external chiller. The DUT box is mounted onto movement and rotation stages located at the telescope center. During the module operation the DUT box is closed light-tight and flooded with dry air.

List of Figures

List of Tables

Bibliography

[Ada+17] W. Adam et al. *P-Type Silicon Strip Sensors for the new CMS Tracker at HL-LHC*. In: Journal of Instrumentation 12.06 (June 2017), P06018. DOI: 10.1088/1748-0221/12/06/P06018 (cited on p. 53).

[Ada+20] W. Adam et al. *Experimental study of different silicon sensor options for the upgrade of the CMS Outer Tracker*. In: Journal of Instrumentation 15.04 (Apr. 2020), P04017. DOI: 10.1088/1748-0221/15/04/P04017 (cited on p. 53).

[Ada+21a] W. Adam et al. *Selection of the silicon sensor thickness for the Phase-2 upgrade of the CMS Outer Tracker*. In: Journal of Instrumentation 16.11 (June 2021), P11028. DOI: 10.1088/1748-0221/16/11/p11028 (cited on pp. 53, 144).

[Ada+21b] W. Adam et al. *The CMS Phase-1 pixel detector upgrade*. In: Journal of Instrumentation 16.02 (Feb. 2021), P02027. DOI: 10.1088/1748-0221/16/02/P02027 (cited on p. 10).

[Ada+21c] W. Adam et al. *The CMS Phase-1 pixel detector upgrade*. In: Journal of Instrumentation 16.02 (Feb. 2021), P02027–P02027. DOI: 10.1088/1748-0221/16/02/p02027 (cited on pp. 108, 112).

[ALI08] ALICE Collaboration. *The ALICE experiment at the CERN LHC*. In: Journal of Instrumentation 3.08 (Nov. 14, 2008), S08002–S08002. DOI: 10.1088/1748-0221/3/08/S08002 (cited on p. 8).

[Apl+09] S. Aplin et al. *A production system for massive data processing in ILCSoft*. In: (2009). URL: https://www.eudet.org/e26/e28/e42441/e70141/EUDET-MEMO-2009-12.pdf (cited on p. 109).

[Apo+17] G. Apollinari et al. *High Luminosity Large Hadron Collider HL-LHC*. Tech. rep. CERN, May 24, 2017. DOI: 10.5170/CERN-2015-005.1 (cited on pp. 15, 16, 139).

[ATL08] ATLAS Collaboration. *The ATLAS Experiment at the CERN Large Hadron Collider*. In: Journal of Instrumentation 3.08 (Aug. 14, 2008), S08003–S08003. DOI: 10.1088/1748-0221/3/08/s08003 (cited on p. 8).

[ATL12] ATLAS Collaboration. *Observation of a new particle in the search for the Standard Model Higgs boson with the ATLAS detector at the LHC*. In: Physics Letters B 716.1 (Sept. 2012), pp. 1–29. DOI: 10.1016/j.physletb.2012.08.020 (cited on p. 9).

[ATL17] ATLAS Collaboration. *Technical Design Report for the ATLAS Inner Tracker Strip Detector*. Tech. rep. Geneva: CERN, 2017. URL: https://cds.cern.ch/record/2257755 (cited on p. 102).

[Bar10] M. Barbero. *FE-I4 chip design*. In: PoS VERTEX 2009 (2010), p. 027. DOI: 10.22323/1.095.0027 (cited on pp. 108, 112).

[Beh+17] T. Behnke et al. *Test Beam at DESY*. Tech. rep. June 17, 2017. URL: https://www.eudet.org/e26/e28/e182/e283/eudet-memo-2007-11.pdf (cited on p. 107).

[Ber+22] G. Bergamin et al. *CIC2/2.1 Technical Specification*. 2022. URL: https://espace.cern.ch/Tracker-Upgrade/Electronics/CIC/Shared%20Documents/Specifications/CIC2_specs_v1p3.pdf (cited on pp. 23, 25).

[Bis+20] T. Bisanz et al. *EUTelescope: A modular reconstruction framework for beam telescope data*. In: Journal of Instrumentation 15.09 (Sept. 2020), P09020–P09020. DOI: 10.1088/1748-0221/15/09/p09020 (cited on pp. 110, 111).

[Blo07] V. Blobel. *Millepede II - Linear Least Squares Fits with a Large Number of Parameters*. In: (2007). URL: https://www.desy.de/~sschmitt/blobel/Mptwo.pdf (cited on p. 110).

[Bru+97] R. Brun et al. *ROOT — An object oriented data analysis framework*. In: Nuclear Instruments and Methods in Physics Research Section A: Accelerators, Spectrometers, Detectors and Associated Equipment 389.1 (1997). New Computing Techniques in Physics Research V, pp. 81–86. ISSN: 0168-9002. DOI: https://doi.org/10.1016/S0168-9002(97)00048-X (cited on p. 111).

[CER17a] CERN. *Macro Pixel ASIC user manual, A readout chip for the hybrid pixel sensor of the PS module.* 2017. URL: https://espace.cern.ch/CMS-MPA/SiteAssets/SitePages/Documents/MPA_UserManual_V0.pdf (cited on pp. 25, 26, 29).

[CER17b] CERN. *Short Strip ASIC specification document, A readout chip for the hybrid pixel sensor of the PS module.* 2017. URL: https://espace.cern.ch/CMS-MPA/SiteAssets/SitePages/Documents/SSA_Manual_V1.0.pdf (cited on p. 25).

[CER22a] CERN. *Accelerators*. 2022. URL: https://home.cern/science/accelerators (visited on 10/03/2022) (cited on p. 7).

[CER22b] CERN. *bPOL12V_V6 Radiation tolerant 10W Synchronous Step-Down Buck DC/DC converter*. 2022. URL: https://espace.cern.ch/project-DCDC-new/Shared%20Documents/bPOL12V_V6%20datasheet%20V1.5.pdf (cited on p. 25).

[CER22c] CERN. *bPOL2V5_V3.3 Radiation tolerant Synchronous Step-Down Buck DC/DC converter*. 2022. URL: https://espace.cern.ch/project-DCDC-new/Shared%20Documents/bPOL2V5_V3.3%20datasheet%20rev3.pdf (cited on p. 25).

[CER22d] CERN. *CMS Experiment*. 2022. URL: https://home.cern/science/experiments/cms (visited on 08/11/2022) (cited on p. 9).

[CER22e] CERN. *High Luminosity LHC Project*. 2022. URL: https://hilumilhc.web.cern.ch/content/hl-lhc-project (visited on 08/13/2022) (cited on pp. 15, 16, 18).

[CER22f] CERN. *New technologies for the High-Luminosity LHC*. 2022. URL: https://home.cern/science/accelerators/new-technologies-high-luminosity-lhc (visited on 08/13/2022) (cited on p. 16).

[Chi13] A. Chilingarov. *Temperature dependence of the current generated in Si bulk*. In: Journal of Instrumentation 8.10 (Oct. 2013), P10003–P10003. DOI: 10.1088/1748-0221/8/10/p10003 (cited on p. 37).

[CiK23] CiK Solutions GmbH. *Climatic chamber Kambic KK-190 CHLT*. 2023. URL: https://www.cik-solutions.com/content/files/en_climatic_chamber_kambic_kk-190_chlt_data_sheet.pdf (visited on 03/13/2023) (cited on pp. 102, 104).

[CMS00] CMS Collaboration. *CMS TriDAS project: Technical Design Report, Volume 1: The Trigger Systems*. Tech. rep. Dec. 15, 2000. URL: https://cds.cern.ch/record/706847 (cited on p. 13).

[CMS08] CMS Collaboration. *The CMS experiment at the CERN LHC*. In: Journal of Instrumentation 3.08 (Aug. 14, 2008), S08004–S08004. DOI: 10.1088/1748-0221/3/08/S08004 (cited on pp. 8, 9, 11, 12).

[CMS12] CMS Collaboration. *Observation of a new boson at a mass of 125 GeV with the CMS experiment at the LHC*. In: Physics Letters B 716.1 (2012), pp. 30–61. DOI: 10.1016/j.physletb.2012.08.021 (cited on p. 9).

[CMS17a] CMS Collaboration. *Particle-flow reconstruction and global event description with the CMS detector*. In: Journal of Instrumentation 12.10 (Oct. 2017), P10003–P10003. DOI: 10.1088/1748-0221/12/10/P10003 (cited on pp. 11, 12).

[CMS17b] CMS Collaboration. *Public CMS Luminosity Information*. Dec. 4, 2017. URL: https://twiki.cern.ch/twiki/bin/view/CMSPublic/LumiPublicResults (cited on p. 9).

[CMS17c] CMS Collaboration. *The CMS trigger system*. In: Journal of Instrumentation 12.01 (2017), P01020. DOI: 10.1088/1748-0221/12/01/p01020 (cited on p. 13).

[CMS17d] CMS Collaboration. *The Phase-2 Upgrade of the CMS Tracker*. Tech. rep. Geneva: CERN, June 2017. DOI: 10.17181/CERN.QZ28.FLHW (cited on pp. 16–23, 25–27, 58, 144, 151).

[CMS21] CMS Collaboration. *CMS Phase-2 Inner Tracker Upgrade*. Tech. rep. Geneva: CERN, June 2021. URL: https://cds.cern.ch/record/2816244 (cited on p. 17).

[CMS23a] CMS Collaboration. *CMS Phase 2 Tracker Layout*. 2023. URL: https://cms-tklayout.web.cern.ch/cms-tklayout/layouts-work/recent-layouts/OT616_200_IT404/index.html (visited on 01/20/2023) (cited on pp. 19, 121, 137, 138, 154).

[CMS23b] CMS Collaboration. *CMS Tracker Phase2 Acquisition & Control Framework*. 2023. URL: https://gitlab.cern.ch/cms_tk_ph2/Ph2_ACF (visited on 03/07/2023) (cited on p. 135).

[CMS23c] CMS Tracker Simulation Working Group. *Simulated tracking effciency as a function of the pseudorapidity and the particles' transverse momentum*. CMS internal. 2023 (cited on p. 134).

[CMS97a] CMS Collaboration. *The CMS electromagnetic calorimeter project: Technical Design Report*. Geneva, 1997. URL: http://cds.cern.ch/record/349375 (cited on p. 10).

[CMS97b] CMS Collaboration. *The CMS hadron calorimeter project: Technical Design Report*. Tech. rep. 1997. URL: http://cds.cern.ch/record/357153 (cited on p. 11).

[CMS97c] CMS Collaboration. *The CMS magnet project: Technical Design Report*. Technical design report. CMS. Geneva: CERN, 1997. DOI: 10.17181/CERN.6ZU0.V4T9 (cited on p. 11).

[CMS97d] CMS Collaboration. *The CMS muon project: Technical Design Report*. Tech. rep. Geneva, 1997. URL: http://cds.cern.ch/record/343814 (cited on p. 11).

[Col08] T. C. Collaboration. *The CMS experiment at the CERN LHC*. In: Journal of Instrumentation 3.08 (Aug. 2008), S08004. DOI: 10.1088/1748-0221/3/08/S08004 (cited on p. 10).

[Cus09] D. Cussans. *Description of the JRA1 Trigger Logic Unit (TLU), v0.2c*. Tech. rep. Sept. 11, 2009. URL: https://www.eudet.org/e26/e28/e42441/e57298/EUDET-MEMO-2009-04.pdf (cited on p. 108).

[Dav16] S. R. Davis. *Interactive Slice of the CMS detector*. In: (2016). URL: https://cds.cern.ch/record/2205172 (cited on p. 13).

[Deu07] Deutsches Elektronen-Synchroton DESY. *Gear A geometry description toolkit for ILC reconstruction software*. 2007. URL: https://ilcsoft.desy.de/portal/software_packages/gear (visited on 10/01/2022) (cited on p. 110).

[Die+19] R. Diener et al. *The DESY II test beam facility*. In: Nuclear Instruments and Methods in Physics Research Section A: Accelerators, Spectrometers, Detectors and Associated Equipment 922 (2019), pp. 265–286. ISSN: 0168-9002. DOI: https://doi.org/10.1016/j.nima.2018.11.133 (cited on pp. 107, 108).

[Dro21] A. Droll. *Performance Studies on 2S Module Prototypes for the Phase-2 Upgrade of the CMS Outer Tracker*. PhD thesis. Karlsruhe Institute of Technology (KIT), 2021 (cited on pp. 83, 111, 135, 143).

[EB08] L. Evans and P. Bryant. *LHC Machine*. In: Journal of Instrumentation 3.08 (2008), S08001–S08001. DOI: 10.1088/1748-0221/3/08/s08001 (cited on pp. 7, 8).

[EUD16] EUDAQ Development Team. *EUDAQ User Manual*. 2016. URL: http://eudaq.github.io/manual/EUDAQUserManual_v1.pdf (cited on p. 109).

[Fer+05] A. Ferrari et al. *FLUKA: A Multi-Particle Transport Code*. In: (Dec. 2005). DOI: 10.2172/877507 (cited on p. 19).

[Fis20] R. Fischer. *Bestrahlungstests an Siliziumstreifensensoren für das Phase-2-Upgrade des CMS-Spurdetektors*. Bachelor's thesis. Karlsruhe Institute of Technology (KIT), 2020 (cited on pp. 81, 95, 97).

[Gae+05] F. Gaede et al. *LCIO persistency and data model for LC simulation and reconstruction*. In: (2005). DOI: 10.5170/CERN-2005-002.471 (cited on p. 110).

[Gae+07] F. Gaede et al. *Marlin et al - A Software Framework for ILC detector R&D*. In: (2007). URL: https://www.eudet.org/e26/e27/e584/eudet-report-2007-11.pdf (cited on p. 110).

[Har09] F. Hartmann. *Evolution of Silicon Sensor Technology in Particle Physics*. Springer Cham, 2009. ISBN: 978-3-319-64436-3. DOI: https://doi.org/10.1007/978-3-319-64436-3 (cited on p. 41).

[Har17] F. Hartmann. *Evolution of Silicon Sensor Technology in Particle Physics*. 2nd ed. Springer, Nov. 3, 2017. ISBN: 978-3-319-64434-9. DOI: 10.1007/978-3-319-64436-3 (cited on pp. 33, 35, 38, 39, 41–43, 45–47, 49, 66, 85, 99, 131).

[Hen+16] J. Hendrik et al. *Performance of the EUDET-type beam telescopes*. In: EPJ Techniques and Instrumentation 3.1 (Oct. 2016). DOI: 10.1140/epjti/s40485-016-0033-2 (cited on pp. 108, 129).

[Hil19] U. Hilleringmann. *Silizium-Halbleitertechnologie : Grundlagen mikroelektronischer Integrationstechnik*. 7., überarbeitete und ergänzte Auflage. SpringerLinkSpringer eBook Collection. Wiesbaden: Springer Vieweg, 2019. ISBN: 9783658234447 (cited on p. 43).

[Hin17] V. Hinger. *Charge sharing studies of silicon strip sensors for the CMS phase II upgrade*. Diploma Thesis. Technische Universität Wien, 2017. URL: https://doi.org/10.34726/hss.2017.37400 (cited on pp. 34, 37, 59).

[HM18] W. Herr and B. Muratori. *Concept of luminosity*. Aug. 20, 2018. URL: https://cds.cern.ch/record/941318/files/p361.pdf (cited on p. 8).

[Hu-+10] C. Hu-Guo et al. *First reticule size MAPS with digital output and integrated zero suppression for the EUDET-JRA1 beam telescope*. In: Nuclear Instruments and Methods in Physics Research Section A: Accelerators, Spectrometers, Detectors and Associated Equipment 623.1 (2010). 1st International Conference on Technology and Instrumentation in Particle Physics, pp. 480–482. ISSN: 0168-9002. DOI: https://doi.org/10.1016/j.nima.2010.03.043 (cited on p. 108).

[Huh02] M. Huhtinen. *Simulation of non-ionising energy loss and defect formation in silicon*. In: Nuclear Instruments and Methods in Physics Research Section A: Accelerators, Spectrometers, Detectors and Associated Equipment 491.1 (2002), pp. 194–215. ISSN: 0168-9002. DOI: https://doi.org/10.1016/S0168-9002(02)01227-5 (cited on p. 47).

[Hun22] S. Hunklinger. *Solid state physics*. Berlin: De Gruyter, 2022. ISBN: 9783110666502 (cited on pp. 31, 33).

[Jun11] A. Junkes. *Influence of radiation induced defect clusters on silicon particle detectors*. PhD thesis. Hamburg University, 2011. URL: https://inspirehep.net/files/bc2a7c368e5b9a51e003ba1f032d4d22 (cited on pp. 48, 49).

[Kei11] Keithley. *Model 6485 Picoammeter User's Manual*. 2011. URL: https://download.tek.com/manual/6487-900-01(C-Mar2011)(User).pdf (visited on 12/21/2022) (cited on p. 72).

[Key19] Keysight Technologies. *Keysight E4980A/AL Precision LCR Meter*. 2019. URL: https://www.datatec.eu/media/pdf/65/ff/4c/Keysight-E4980A-HB-1_DE.pdf (visited on 12/31/2022) (cited on p. 74).

[Kit04] C. Kittel. *Introduction to Solid State Physics*. Wiley, 2004. ISBN: 9780471415268. URL: https://books.google.de/books?id=kym4QgAACAAJ (cited on p. 31).

[Kle+19] K. Klein et al. *Service hybrids for the silicon strip modules of the CMS Phase-2 Outer Tracker upgrade*. In: PoS TWEPP2018 (2019), p. 127. DOI: 10.22323/1.343.0127 (cited on p. 25).

[Kle12] C. Kleinwort. *General broken lines as advanced track fitting method*. In: Nuclear Instruments and Methods in Physics Research Section A: Accelerators, Spectrometers, Detectors and Associated Equipment 673 (2012), pp. 107–110. ISSN: 0168-9002. DOI: https://doi.org/10.1016/j.nima.2012.01.024 (cited on p. 110).

[Kön+16] A. König et al. *The impact and persistence of electrostatic charge on the passivation of silicon strip sensors*. In: Nuclear Instruments and Methods in Physics Research Section A: Accelerators, Spectrometers, Detectors and Associated Equipment 838 (2016), pp. 55–61. ISSN: 0168-9002. DOI: https://doi.org/10.1016/j.nima.2016.09.016 (cited on pp. 98, 101).

[Kop18] R. Koppenhöfer. *Conception and validation of test stations to electrically qualify silicon strip modules for the CMS Phase II Upgrade*. Master's thesis. Karlsruhe Institute of Technology (KIT), 2018 (cited on p. 139).

[Kop22] R. Koppenhöfer. *Noise and Detection Efficiency Studies on Full- Size 2S Module Prototypes for the Phase-2 Upgrade of the CMS Experiment*. PhD thesis. Karlsruhe Institute of Technology (KIT), 2022 (cited on pp. 5, 38, 104, 111, 112, 114, 135, 136, 142, 143, 148, 151, 154, 155, 178).

[LHC08] LHCb Collaboration. *The LHCb Detector at the LHC*. In: Journal of Instrumentation 3.08 (Aug. 14, 2008), S08005. DOI: 10.1088/1748-0221/3/08/S08005 (cited on p. 8).

[Liu+19] Y. Liu et al. *EUDAQ2—A flexible data acquisition software framework for common test beams*. In: Journal of Instrumentation 14.10 (Oct. 2019). DOI: 10.1088/1748-0221/14/10/p10033 (cited on p. 109).

[Lut07] G. Lutz. *Semiconductor Radiation Detectors*. Springer Heidelberg, 2007. ISBN: 978-0262035613. DOI: https://doi.org/10.1007/978-3-540-71679-2 (cited on pp. 34, 35, 37, 40, 46, 47).

[Mai19] S. Maier. *Assembly and qualification procedures of 2S modules and high rate tests of the CMS Binary Chip for the Phase 2 Upgrade of the CMS Outer Tracker*. PhD thesis. Karlsruhe Institute of Technology (KIT), 2019 (cited on pp. 20, 89, 136, 139, 151).

[Man+12] J. Mans et al. *CMS Technical Design Report for the Phase 1 Upgrade of the Hadron Calorimeter*. Tech. rep. Sept. 2012. URL: https://cds.cern.ch/record/1481837 (cited on p. 11).

[Mar+07] R. Marco-Hernández et al. *Alibava : A portable readout system for silicon microstrip sensors*. In: (2007). DOI: 10.5170/CERN-2007-001.412 (cited on p. 176).

[Mas+07] K. Masayoshi et al. *Advanced Dicing Technology for Semiconductor Wafer—Stealth Dicing*. In: IEEE Transactions on Semiconductor Manufacturing 20.3 (2007), pp. 259–265. DOI: 10.1109/TSM.2007.901849 (cited on p. 54).

[Met20] M. Metzler. *Irradiation studies on n-in-p silicon strip sensors in the course of the CMS Phase-2 Outer Tracker Upgrade*. PhD thesis. Karlsruhe Institute of Technology (KIT), 2020 (cited on p. 75).

[Mob19] E. Mobs. *The CERN accelerator complex. Complexe des accélérateurs du CERN*. July 29, 2019. URL: https://cds.cern.ch/record/2684277/?ln=de (cited on p. 9).

[Mol99] M. Moll. *Radiation Damage in Silicon Particle Detectors*. PhD thesis. Universtiy of Hamburg, 1999. URL: https://mmoll.web.cern.ch/thesis/ (cited on pp. 36, 46, 48–50).

[Mül21] J.-O. Müller-Gosewisch. *Investigation of Radiation Damage in Silicon Sensors for the Phase-2 Upgrade of the CMS Outer Tracker*. PhD thesis. Karlsruhe Institute of Technology (KIT), 2021 (cited on pp. 35, 59, 60, 81, 97, 176).

[Ope22] OpenCV. *OpenCV, Open Source Computer Vision*. 2022. URL: https://docs.opencv.org/4.x/d6/d00/tutorial_py_root.html (visited on 12/18/2022) (cited on p. 89).

[Pam23] H. Pamuła. *Dew Point Calculator*. 2023. URL: https://www.omnicalculator.com/physics/dew-point (visited on 03/14/2023) (cited on p. 104).

[Par20] Particle Data Group. *Review of Particle Physics*. In: Progress of Theoretical and Experimental Physics 2020.8 (Aug. 2020). 083C01. ISSN: 2050-3911. DOI: 10.1093/ptep/ptaa104. eprint: https://academic.oup.com/ptep/article-pdf/2020/8/083C01/34673722/ptaa104.pdf (cited on pp. 37–40).

[Pes+10] M. Pesaresi et al. *Simulating the performance of a pT tracking trigger for CMS*. In: Journal of Instrumentation 5.08 (Aug. 2010), pp. C08003–C08003. DOI: 10.1088/1748-0221/5/08/c08003 (cited on p. 18).

[Pes12] M. Pesaresi. *FC7 User Manual*. In: (2012). URL: https://espace.cern.ch/project-FC7/Documents/fc7_user_manual.pdf (cited on pp. 118, 135).

[Phi23] Philipp Laube. *Semiconductor Technology from A to Z - Wafer fabrication*. 2023. URL: https://www.halbleiter.org/pdf/en/Wafer%20fabrication/Wafer%20fabrication.pdf (visited on 07/02/2023) (cited on p. 44).

[Pra17] C. Pralavorio. *Record luminosity: well done LHC*. In: (Nov. 2017). URL: http://cds.cern.ch/record/2295027 (cited on p. 9).

[Pry19] M. Prydderch. *CBC3.1 user Manual*. 2019. URL: http://www.hep.ph.ic.ac.uk/ASIC/cbc3.1/CBC3p1_User_Manual_V1p4.pdf (cited on pp. 22, 24).

[Pyt22] Python Software Foundation. *Official Python website*. 2022. URL: https://www.python.org/ (visited on 12/12/2022) (cited on p. 63).

[Ras+20] N. Rasevic et al. *Development of an Optical Readout Hybrid for the CMS Outer Tracker Upgrade*. 2020. URL: https://pos.sissa.it/370/058/pdf (cited on p. 26).

[Sal22] A. Salameh. *Automatische Optische Defekterkennung an Siliziumstreifensensoren*. Bachelor's thesis. Karlsruhe Institute of Technology (KIT), 2022 (cited on p. 89).

[Sch19] D. Schell. *Development of a Macro-Pixel sensor for the Phase-2 Upgrade of the CMS experiment*. PhD thesis. Karlsruhe Institute of Technology (KIT), 2019 (cited on pp. 25, 57, 111, 117, 118, 120, 124, 128, 129).

[Sci22] Scipy. *Official Scipy website*. 2022. URL: https://scipy.org/ (visited on 12/12/2022) (cited on p. 66).

[SD19] D. Schell and A. Dierlamm. *Optimization of bias rail implementations for segmented silicon sensors*. In: Nuclear Instruments and Methods in Physics Research Section A: Accelerators, Spectrometers, Detectors and Associated Equipment 924 (2019). 11th International Hiroshima Symposium on Development and Application of Semiconductor Tracking Detectors, pp. 19–22. ISSN: 0168-9002. DOI: https://doi.org/10.1016/j.nima.2018.05.033 (cited on p. 120).

[Shv23] I. Shvetsov. *CMS tracker dew point*. personal communication. 2023 (cited on p. 104).

[Sin23] P. Singh. *Absolute Humidity Calculator*. 2023. URL: https://www.omnicalculator.com/physics/absolute-humidity (visited on 03/14/2023) (cited on p. 104).

[SL12] S. M. Sze and M. K. Lee. *Semiconductor Devices: Physics and Technology*. John Willey Sons, 2012. ISBN: 9780471415268 (cited on p. 33).

[Spi06] H. Spieler. *Semiconductor detector systems*. Repr. with corr. Series on semiconductor science and technology ; 12Oxford science publications. Oxfords: Oxford Univ. Press, 2006. ISBN: 0198527845; 9780198527848 (cited on pp. 34, 35).

[SR52] W. Shockley and W. T. Read. *Statistics of the Recombinations of Holes and Electrons*. In: Phys. Rev. 87 (5 Sept. 1952), pp. 835–842. DOI: 10.1103/PhysRev.87.835 (cited on p. 48).

[Tay11] L. Taylor. *CMS detector design*. Nov. 23, 2011. URL: http://cms.web.cern.ch/news/cms-detector-design (cited on p. 12).

[Tro+18] J. Troska et al. *The VTRx+, an Optical Link Module for Data Transmission at HL-LHC*. In: PoS TWEPP-17 (2018), p. 048. DOI: 10.22323/1.313.0048 (cited on p. 24).

[Wec+04] E. Weckert et al. *PETRA III: A New High Brilliance Synchrotron Radiation Source at DESY*. In: AIP Conference Proceedings 705 (May 2004). DOI: 10.1063/1.1757737 (cited on p. 107).

[Wit20] F. Wittig. *Characterization of Macro-Pixel Sensors for the Phase-2 Upgrade of the CMS Experiment*. Master's thesis. Karlsruhe Institute of Technology (KIT), 2020 (cited on pp. 117, 119, 120, 122–124, 133).

[Wol22] Wolfgang Warmbier. *Ionizer SMB60, portable and small benchtop unit*. 2022. URL: https://shop.warmbier.com/en/ionizer-smb60-portable-and-small-benchtop-unit.html?group=69 (visited on 12/23/2022) (cited on pp. 101, 102).

[ZAG22] ZAG. *Zyklotron AG (ZAG)*. 2022. URL: http://www.zyklotron-ag.de/ (visited on 12/31/2022) (cited on pp. 121, 137).

[Zie22] T. Ziemons. *Assembly and Test of Prototype 2S Modules for the Phase-2 Upgrade of the CMS Outer Tracker*. Presented 26-08-2022. PhD thesis. 2022. URL: https://cds.cern.ch/record/2836729 (cited on p. 151).

[Zog+22] A. Zografos et al. *Power, readout and service hybrids for the CMS phase-2 upgrade*. In: Journal of Instrumentation 17.03 (Mar. 2022), p. C03034. DOI: 10.1088/1748-0221/17/03/c03034 (cited on p. 26).

Acknowledgments — Danksagung

The present work would not have been possible without the support of many people, to whom I express my greatest thanks!
Die vorliegende Arbeit wäre ohne die Unterstützung zahlreicher Mitmenschen nicht möglich gewesen. Ihnen möchte ich an dieser Stelle meinen aufrichtigen Dank aussprechen.

An erster Stelle gilt mein Dank Herrn Prof. Dr. Ulrich Husemann für die Möglichkeit meine Promotion am Institut für Experimentelle Teilchenphysik durchführen zu können. Von seiner steten Unterstützung in jeglicher Hinsicht, sowie vielen gewinnbringenden Anregungen zur Arbeit habe ich sehr profitiert.
Herrn Prof. Dr. Günter Quast danke ich für die Übernahme des Korreferats.

Dr. Alexander Dierlamm danke ich für die hervorragende Betreuung während der letzten Jahre und das sorgfältige Korrekturlesen der Arbeit. Die vielen ausgiebigen Diskussionen zu verschiedensten Fragestellungen haben wesentlich zum Gelingen der Arbeit beigetragen.

Ein großer Dank gilt Dr. Roland Koppenhöfer für seine bedingungslose Hilfsbereitschaft in jeglicher Hinsicht, die enorme Unterstützung bei der Durchführung der Teststrahlenmessungen und die unzähligen Diskussionen über verschiedenste Themen. Außerdem bedanke ich mich herzlichst für das Korrekturlesen der Arbeit.

Weiterer Dank gebührt

- Dr. Stefan Maier für den Bau der im Teststrahl untersuchten 2S Modul Prototypen,
- Dr. Andreas Nürnberg für viele fruchtbare Diskussionen und die Unterstützung bei den Teststrahlmessungen,
- Dr. Hans Jürgen Simonis und Pia Steck für die zahlreichen und stets präzise platzierten Wire-Bond Verbindungen,
- Tobias Barvich, Bernd Berger, Marius Neufeld und Julian Stanulla für die durchweg zuverlässige Unterstützung bei mechanischen/elektronischen Konstruktionen sowie das Instandhalten und Überarbeiten diverser Messaufbauten,
- Umut Elicabuk für ein immer offenes Ohr und seine stete Hilfsbereitschaft in allen Belangen,
- Ronja Fischer, Gani Kösker, Rufa Rafeek und Thomas Vetter für die große Hilfe beim Messen der unzähligen Sensoren,
- Peichen Chen und Diana Fellner für die jederzeit schnelle und kompetente Hilfe bei jeglichen administrativen Angelegenheiten.

Allen aktuellen und ehemaligen Mitgliedern der ETP Hardware Gruppe die ich im Laufe der Arbeit am ETP kennenlernen durfte, insbesondere, Justus Braach, Dr. Alexander Droll, Umut Elicabuk, Christina Klauda, Dr. Roland Koppenhöfer, Dr. Stefan Maier, Dr. Marius Metzler, Dr. Jan-Ole Müller-Gosewisch, Dr. Andreas Nürnberg, Martin Pittermann, Dr. Daniel Schell, Lea Stockmeier, Bogdan Topko, danke ich für die durchweg angenehme und abwechslungsreiche Arbeitsatmosphäre!

Ein ganz besonderer Dank gilt meinen Eltern Regine und Klaus Wittig ohne deren bedingungslose und liebevolle Unterstützung mein Studium und die anschließende Promotion nicht möglich gewesen wäre.

Der Karlsruhe School of Elementary Particle and Astroparticle Physics: Science and Technology (KSETA) möchte ich für die Unterstützung während der Promotion danken.

I acknowledge funding by the Federal ministry of Education and Research of Germany in the framework of the project "Fortführung des CMS-Experiments zum Einsatz am HL-LHC: Verbesserung des Spurdetektors für das Phase-II-Upgrade des CMS-Experiments" under the grants 05H19VKCC9 and 05H21VKCC9.

The measurements leading to these results have been performed at the Test Beam Facility at DESY Hamburg (Germany), a member of the Helmholtz Association (HGF).

Declaration

I declare that the work in this dissertation was carried out in accordance with the requirements of the University's Regulations and that it has not been submitted for any other academic award. Except where indicated by specific reference in the text, the work is the candidate's own work. Work done in collaboration with, or with the assistance of, others is indicated as such.

Karlsruhe, April 2023

Florian Wittig